COUPLING PLASMONIC METAMATERIALS TO SINGLE-QUANTUM-WELL GAIN

Zur Erlangung des akademischen Grades eines
DOKTORS DER NATURWISSENSCHAFTEN
der Fakultät für Physik des Karlsruher Instituts für Technologie

genehmigte

DISSERTATION

von

Diplom-Physikerin Nina Meinzer
aus Karlsruhe

Tag der mündlichen Prüfung:	01. Juli 2011
Referent:	Prof. Dr. Martin Wegener
Korreferent:	Prof. Dr. Kurt Busch

To my father.

1947-2009

Publications

Parts of this work have already been published.

In scientific journals:

- N. Meinzer, M. Ruther, S. Linden, C.M. Soukoulis, G. Khitrova, J. Hendrickson, J.D. Olitzky, H.M. Gibbs, and M. Wegener, *Arrays of Ag split-ring resonators coupled to InGaAs single-quantum-well gain*, Opt. Express **18**, 24140 (2010)

- M. Wegener, J.-L. García-Pomar, C.M. Soukoulis, N. Meinzer, M. Ruther, and S. Linden, *Toy model for plasmonic metamaterial resonances coupled to two-level system gain*, Opt. Express **16**, 19785 (2008)

At conferences (own presentations only):

- N. Meinzer, M. Ruther, S. Linden, C.M. Soukoulis, G. Khitrova, J. Hendrickson, J.D. Olitzky, H.M. Gibbs, and M. Wegener, *Plasmonic Metamaterials Coupled to Single InGaAs-Quantum-Well Gain*, contributed talk, CLEO:QELS 2011, Baltimore, USA

- N. Meinzer, M. Ruther, S. Linden, C.M. Soukoulis, G. Khitrova, J. Hendrickson, J.D. Olitzky, H.M. Gibbs, and M. Wegener, *Plasmonic Metamaterials Coupled to Single InGaAs-Quantum-Well Gain*, invited talk, PQE 2011, Snowbird, USA

At special seminars (own presentations only):

- N. Meinzer, *Of Troughs and Horseshoes: Coupling Plasmonic Metamaterials to Quantum Wells*, invited talk, special seminar in January 2011, College of Optical Sciences, University of Arizona, Tucson, USA

- N. Meinzer, *Of Troughs and Horseshoes: Coupling Plasmonic Metamaterials to Quantum Wells*, invited talk, special seminar in January 2011, California Institute of Technology, Pasadena, USA

Additional work has been published.

In scientific journals:

- M.F.G. Klein, H. Hein, P.-J. Jakobs, S. Linden, N. Meinzer, M. Wegener, V. Saile, and M. Kohl, *Electron beam lithography of V-shaped silver nanoantennas*, Microelectron. Eng., **86**, 1078 (2008)

At conferences (own presentations only):

- N.Meinzer, M.Wegener, M.F.G. Klein, P.J. Jakobs, H. Hein, M. König, J. Niegemann, K. Busch, N. Feth, and S. Linden, *Spectroscopy of Individual V-shaped Silver Nanoantennas*, contributed talk, CLEO:QELS 2008, San Jose, USA

Contents

Chapter 1

Introduction

From early native mythology, over Shakespeare's plays right up to modern movies and TV shows, the most inspiring and most successful stories have always been the tales of overcoming obstacles. So far the story of metamaterials has been a very successful one of its own accord [1–3] but has now reached a point where it has to face a serious challenge:
Most of these artificial media, designed to have specially tailored properties not to be found in nature (e.g. a negative refractive index), exploit plasmonic effects and are therefore composed of metallic building blocks. Unfortunately, metal nanoparticles suffer from intrinsic losses due to absorption, which are especially severe in the optical wavelength regime. Many of the popular applications of plasmonic metamaterials like perfect lenses [4] or cloaking devices [5, 6] are therefore rendered impractical; after all, who is really interested in an invisibility cloak that itself casts a visible shadow?
Conclusively, it is currently one of the most important goals of the metamaterial and plasmonics community to compensate or at least reduce these intrinsic losses in the metal structures [7, 8]. Several approaches have been proposed to this end, ranging from the use of special low-loss alloys [9] to geometrically adjusting the plasmonic structures in order to reduce losses [10]. One of the most promising ideas, however, is the introduction of a medium providing optical gain which in turn could compensate for the loss of the metal [11].

The combination of a metamaterial with an optical gain medium has been studied by several theoretical investigations that prove the feasibility of this loss-compensation approach [12, 13]. This theoretical treatment relies on rigorous numerical calculations where the exact geometry of the metamaterial considered has to be implemented along with a sophisticated model of the gain medium (e.g. a four-level system). They show that loss-reduction can be reached for realistic parameters of both the metamaterial and the gain medium that are within experimentally accessible limits.
On the experimental side, however, only few results have been published on the hybrid system of metamaterial and gain medium. Nikolay Zheludev's group focuses on complementary split-ring resonators that are covered with a layer of lead-sulfide quantum dots. On these they observe an increase of transmittance by about 1% upon continuous-wave pumping [14] and a multifold enhancement of photoluminescence together with a narrowing of the photoluminescence spectrum [15].
Shumin Xiao *et al.* report on their results for a double-fishnet negative-index material that employs a dye-doped (Rh800) epoxy as spacer layer providing the gain [16]. They measure

an increase of relative transmittance on the order of 100% upon pumping and compare their experiments to detailed numerical calculations from which they infer complete loss-compensation for one particular wavelength.

Although loss-compensation is a very important aspect of current plasmonics research the combination of plasmonic particles with gain media - or, more generally speaking, with emitters - offers a multitude of other fascinating research topics as well. They range from fluorescence enhancement [17] over directing the emission of quantum dots by plasmonic antennas [18] to quantum-optical applications like the single-photon transistor [19].
The most prominent example of a device derived from plasmon-emitter interaction is the *spaser* (surface plasmon amplification by stimulated emission of radiation) proposed by Mark Stockman and David Bergman [20].
As the name already suggests, the spaser is the nanoplasmonic analogon to the laser where the cavitiy is replaced by a resonant nanoparticle and the plasmons take the part of photons. The energy for the amplification is, like with a conventional laser, provided by an externally pumped gain medium [21].
Yet the fundamental difference to a classical laser is that a spaser does not necessarily emit light. It can also make use of the dark plasmonic modes, which do not couple to the far field, and thus serve as an efficient energy source that is localised to a few nanometres. This energy can still be accessed by near-field interaction of, for instance, molecules with the spaser.
This concept has been experimentally realised by Mikhail Noginov *et al.* in 2009 [22] and expanded to a light-emitting variety, the so-called *lasing spaser* by Nikolay Zheludev [23]. The latter makes use of breaking the symmetry of a metamaterial building block that would otherwise support a dark mode, allowing it to weakly couple to the far field and eventually lead to emission of coherent light.

All these concepts, from loss-compensation in plasmonic metamaterials to spasing, fundamentally rely on the interaction between plasmonic materials and a gain medium. Without sufficient coupling, resulting in a significant energy transfer from the gain medium to the plasmon, no loss-compensation can be achieved, nor can plasmons be amplified. It is therefore essential to understand the way in which coupling between a plasmonic metamaterial and a gain medium occurs.
Most likely this coupling is mediated by the near fields of the plasmonic particles which can interact with the emitters of a gain medium. Since plasmons generate strongly enhanced near fields, this coupling can be rather efficient but their strong spatial confinement implies restrictions to the separation of the emitters from the particle to still observe significant coupling effects.
Although many propositions for efficient loss-compensation are based on dye molecules as gain media because they offer very high gain coefficients they are not necessarily suitable for a detailed study of the coupling mechanism between a plasmonic metamaterial and a gain medium. This goal demands a highly controllable, reproducible system that is ideally long-term photostable.
Therefore dye molecules in solution or embedded in some matrix are not our gain medium of choice. We rather turn to semiconductor nanostructures, more precisely to epitaxially-grown single quantum wells, whose physical properties can be precisely controlled in the growth

process and which still offer sufficiently high gain that can even be enhanced by cooling the sample to low temperatures. Furthermore, quantum wells hardly bleach and can thus be used even for time-consuming experiments without any change in their gain characteristics.
An additional advantage is the possibility of electrical charge-carrier injection in semiconductor structures, which is likely essential if active metamaterial devices are the final goal of our research because optical pumping is certainly not suitable for technological applications.

Outline of this Thesis

We start with a summary of the most important properties of plasmonic metamaterials in Chapter 2. This includes a review of basic light-matter interaction followed by an introduction to the physics of particle plasmons. We then present the concept of metamaterials and give a brief overview over the different possibilities this offers before we discuss the split-ring resonator (SRR) in some detail because it serves as the example of metamaterial building blocks throughout this thesis. The chapter closes with a review on the losses of plasmonic particles and on how they can be compensated.
Chapter 3 introduces the fundamentals of semiconductors with a special focus on the optical properties of single quantum wells (QWs). Here, we also discuss the physics of a two-level system (2LS) with the different mechanisms of absorption and emission and we deduce the optical Bloch equations which are the relevant equations of motion for charge carriers in a 2LS.
Next, we present the experimental and numerical methods used in this thesis (Chapter 4). We describe the fabrication of the QWs by molecular-beam epitaxy (performed in Tucson) and that of the metamaterials electron-beam lithography. An illustration of the optical setups for photoluminescence and pump-probe measurements follows, together with a brief explanation of the pump-probe method. Finally, we sketch the principle of the discontinuous Galerkin time-domain method used (in the group of Prof. Kurt Busch) for numerical near-field calculations.
In Chapter 5 we develop a simple analytical toy model based on the near-field coupling between a bosonic plasmon resonance and a fermionic gain resonance of a two-level system. We use this model to theoretically study the influence of the coupling strength and of the spectral detuning between the two resonances on the behaviour of the coupled system. Thus we can make some predictions on the outcome of our experiments and get an impression of the important parameters of the system.
The following two chapters are dedicated to our experimental results. First (in Chapter 6) we present pump-probe measurements that clearly prove the coupling between arrays of SRRs and a single quantum well. We find a distinct change in relative differential transmittance of the the SRR+QW (-8%) compared to that of the bare QW ($+2\%$) together with a pronounced decay-rate enhancement, which we compare to numerical near-field calculations and explain by the Purcell effect. We then proceed to studying how the coupling between metamaterial and quantum well changes upon growing distance between the two (Chapter 7). We find an explicit dependence of the strength of coupling - represented by the strength of the resulting effects - on the SRR-QW separation. Again, we compare our results to numerical near-field calculations and find overall agreement. We therefore conclude the interaction between the SRR arrays and the QW to be dominated by the plasmonic near fields.
In the end we summarise our results and the conclusions drawn from them and give a brief outlook on further research regarding plasmon-emitter interaction.

Chapter 2

Plasmonic Metamaterials

Many of the applications usually mentioned for metamaterials seem to belong into the world of science fiction rather than into actual science to most people. Indeed, a negative refractive index [24], a perfect lens [4] and the notion of cloaking [5, 6] all contradict our every-day experiences and more likely appeal to our imagination. But as sometimes "truth is stranger than fiction" (M. Twain), most of them have already been realised to some extent and are still an active field of research [1–3, 7]
This has only been possible because of the underlying concept of metamaterials: artificial materials whose optical properties can be specially tailored to such an extent that they cannot be found in any natural material. As the properties of the building blocks - the analogue of atoms in normal substances - mainly govern the properties of the metamaterial as a whole, we can design them to generate the properties we intend.
Most often this is achieved by exploiting the concept of particle plasmons, collective oscillations of the free electron gas, in metallic nanostructures. Their resonances can be tuned by altering the shape of the particles, leading to a high degree of flexibility and a broad range of applications their properties can be adjusted to. On the other hand, plasmonic metamaterials have one major drawback: they suffer from intrinsic losses due to the dissipative metal they are composed of. Especially in the near-infrared and optical spectral region metals have very high losses that to this day hinder real applications of photonic metamaterials.

In this chapter we are concerned with the basic concepts of plasmonic metamaterials and the losses they suffer. We start with a general introduction to the light-matter interaction, in the course of which we discuss the Lorentzian oscillator and the dielectric response of metals as described by the Drude model. Next, we turn to the fundamentals of particle plasmons and continue with a brief overview of metamaterials in general, followed by a more detailed study of the split-ring resonator, which is the metamaterial building block we use in this thesis. The chapter closes with a discussion of losses in plasmonic metamaterials and in how we can compensate for them.

2.1 Light-Matter Interaction: The Dielectric Response

When an electromagnetic wave interacts with matter it is mainly the electric field $\boldsymbol{E}$ displacing the electrons (or other charge carriers) inside the material from their equilibrium positions [25,

26]. This leads to charge separation because the lattice ions are much heavier than the electrons and can therefore be considered to stay at rest. The resulting dipoles yield a polarisation of the whole material given by

$$\boldsymbol{P} = N\boldsymbol{p} = -Ne\boldsymbol{x}, \tag{2.1}$$

where N is the number of electrons and $\boldsymbol{p}$ is the dipole moment of a single atom which is given by the product of the elementary electron charge e and the average displacement $\boldsymbol{x}$ of an electron with respect to its equilibrium position. Assuming the material to be linear and isotropic we can use the material equation for the electric displacement field

$$\boldsymbol{D} = \epsilon_0\boldsymbol{E} + \boldsymbol{P} = \epsilon_0\left(1+\chi\right)\boldsymbol{E} = \epsilon_0\epsilon\boldsymbol{E} \tag{2.2}$$

to find the dielectric response which is contained in the susceptibility χ and the dielectric function ϵ, both of which are, in general, not constant but depend on frequency. Instead of these functions, however, we often use the refractive index

$$n(\omega) = \sqrt{\epsilon(\omega)} \tag{2.3}$$

which is sometimes the more intutitive observable.
No matter which of these three functions we use to describe the dielectric response of a material, we generally deal with complex functions:

$$\begin{aligned}
\chi(\omega) &= \mathrm{Re}\left[\chi(\omega)\right] + i\mathrm{Im}\left[\chi(\omega)\right] && (2.4)\\
\epsilon(\omega) &= \mathrm{Re}\left[\epsilon(\omega)\right] + i\mathrm{Im}\left[\epsilon(\omega)\right] && (2.5)\\
n(\omega) &= \mathrm{Re}\left[n(\omega)\right] + i\mathrm{Im}\left[n(\omega)\right]. && (2.6)
\end{aligned}$$

The material is therefore not only dispersive but also dissipative as the imaginary part of the refractive index is related to the absorption coefficient δ in Beer's law by

$$\delta = \frac{2\omega}{c}\mathrm{Im}\left[n(\omega)\right]. \tag{2.7}$$

In the following we discuss two classical models, the Lorentzian-oscillator model and the Drude model, from which we can derive the dielectric response functions. The former is suitable for dielectrics, the latter describes free charge carriers and is therefore applicable to metals and doped semiconductors.

2.1.1 Lorentzian-Oscillator Model

Starting again from the assumption that an external electric field $\boldsymbol{E}(t)$ displaces the electrons in a material from their equilibrium position and taking into account the attractive force between an electron and a lattice ion, which acts as a restoring force, we arrive at a driven harmonic oscillator with resonance frequency Ω. This, of course, implies the displacement to be small and is therefore only true if the electrons are still bound to the atoms. In a solid, the oscillation is further damped, e.g. by interaction of the electrons with phonons. We can consequently describe the response of the electrons to the external field by the following classical equation of motion:

$$m_\mathrm{e}\ddot{\boldsymbol{x}}(t) + m_\mathrm{e}\gamma\dot{\boldsymbol{x}}(t) + m_\mathrm{e}\Omega^2\boldsymbol{x}(t) = -e\boldsymbol{E}(t). \tag{2.8}$$

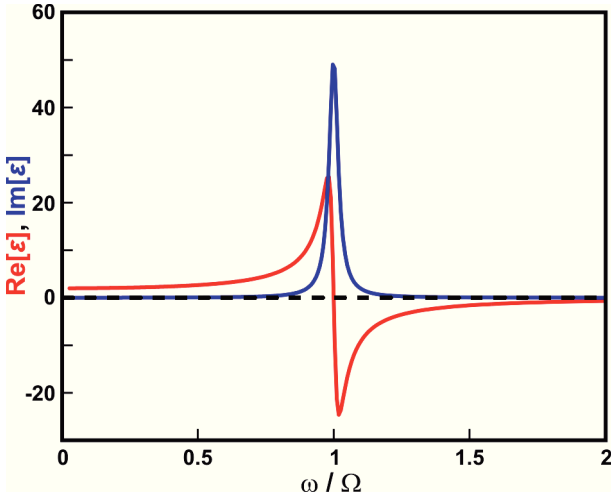

Figure 2.1: Real and imaginary part of the dielectric function $\epsilon(\omega)$ of a Lorentzian oscillator. The parameters are $\Omega = 2\pi \times 1.6 \times 10^{13}\,\mathrm{s}^{-1}$, $\gamma = 2\pi \times 7.9 \times 10^{11}\,\mathrm{s}^{-1}$, $(Ne^2)/(\epsilon_0 m_\mathrm{e}\Omega^2) = 2$, chosen to be realistic values for a typical ionic crystal [25]. Frequencies are normalised to the resonance frequency Ω.

Here, we have introduced the damping frequency γ and the electron mass m_e. Equation (2.8) can be readily solved to yield

$$\boldsymbol{x}(t) = -\frac{e}{m_\mathrm{e}} \cdot \frac{1}{\Omega^2 - \omega^2 - i\gamma\omega} \cdot \boldsymbol{E}(t). \tag{2.9}$$

Using equations (2.1) and (2.2) we deduce the following dielectric function (compare Fig. 2.1)

$$\epsilon(\omega) = \epsilon_\infty + \frac{Ne^2}{\epsilon_0 m_\mathrm{e}} \cdot \frac{1}{\Omega^2 - \omega^2 - i\gamma\omega}, \tag{2.10}$$

where ϵ_∞ is the dielectric constant the material approaches in the limit of high frequencies, which contains non-resonant contributions like lattice vibrations. To refine our picture of the dielectric response we can explicitly take these contributions into account by treating them as additional Lorentzian oscillators. We assign to each of them a specific oscillator strength f_j to model their influence on the complete response and then take the sum over all contributions:

$$\epsilon(\omega) = 1 + \frac{Ne^2}{\epsilon_0 m_\mathrm{e}} \sum_j \frac{f_j}{\Omega_j^2 - \omega^2 - i\gamma_j\omega}. \tag{2.11}$$

Note, that the classical model will lead to $f_j = 1$ for every oscillator but that a quantum mechanical treatment rather yields the condition $\sum_j f_j = 1$ for each electron. This paradox can be resolved by assuming that one particular electron is involved in several transitions and the absorption strength is divided amongst them [25].

2.1.2 Drude Model

For the treatment of metals where the electrons are no longer bound to the lattice atoms we need to modify the Lorentzian oscillator model. We now consider a gas of quasifree electrons (electron plasma) which is distributed over the whole crystal [28]. If we excite this gas with

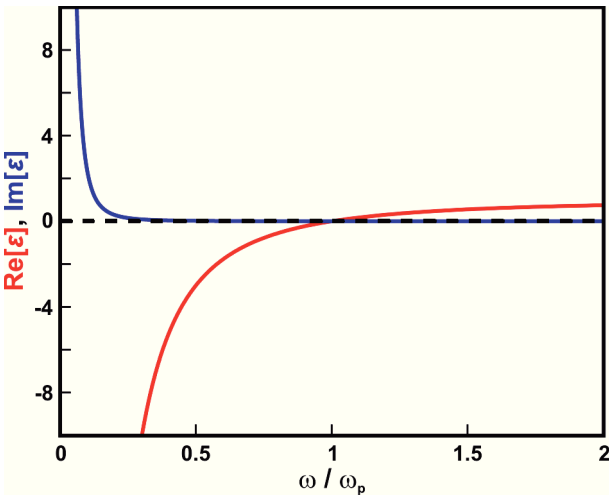

Figure 2.2: Real and imaginary part of the dielectric function $\epsilon(\omega)$ of a Drude metal. The parameters have been chosen to match those of silver ($\omega_\mathrm{p} = 2\pi \times 2.2 \times 10^{15}\,\mathrm{s}^{-1}$, $\omega_\mathrm{c} = 2\pi \times 5.2 \times 10^{12}\,\mathrm{s}^{-1}$) found by a fit to the experimental data of Johnson and Christy [27]. Frequencies are normalised to the plasma frequency ω_p.

an external electric field $\boldsymbol{E}(t) = \boldsymbol{E}_0 e^{-i\omega t}$ a free electron will be displaced by $\boldsymbol{x}$ and follow the equation of motion

$$m_\mathrm{e}\ddot{\boldsymbol{x}}(t) + m_\mathrm{e}\gamma \cdot \boldsymbol{x}(t) = -e\boldsymbol{E}(t), \tag{2.12}$$

where all interactions have been merged into the effective electron mass m_e. In the free-electron case there is no restoring force from the lattice ions because the interaction between electrons and lattice is negligible (thus equation (2.12) resembles equation (2.8) for a vanishing resonance frequency $\Omega = 0$). All interaction between the electrons and the lattice is described by the frictional damping from collisions of the electrons with, mainly, phonons and defects. The damping frequency γ of a Drude metal is therefore often referred to as collision frequency ω_c. Solving equation (2.12) yields

$$\boldsymbol{x}(t) = \frac{e}{m_\mathrm{e}} \cdot \frac{1}{\omega^2 - i\gamma\omega} \cdot \boldsymbol{E}(t), \tag{2.13}$$

which can be used to calculate the dielectric response with the help of equations (2.1) and (2.2):

$$\epsilon(\omega) = 1 - \frac{Ne^2}{\epsilon_0 m_\mathrm{e}} \cdot \frac{1}{\omega^2 - i\gamma\omega} = 1 - \frac{\omega_p^2}{\omega^2 - i\gamma\omega}. \tag{2.14}$$

Here we have introduced the plasma frequency

$$\omega_\mathrm{p} = \sqrt{\frac{Ne^2}{\epsilon_0 m_\mathrm{e}}}, \tag{2.15}$$

which is the natural resonant frequency of the whole electron gas and marks the transition from negative to positive real parts of the dielectric constant of a Drude metal (compare Fig. 2.2).
Let us note in passing that a real metal can never be fully described with the Drude model because it does not account for interband transitions. For most metals these transitions occur in the UV (e.g. $3.9\,\mathrm{eV} = 320\,\mathrm{nm}$ for silver) and can thus be neglected for the visible and near-infrared spectral region. Notable exceptions to this rule are gold and copper, which have an

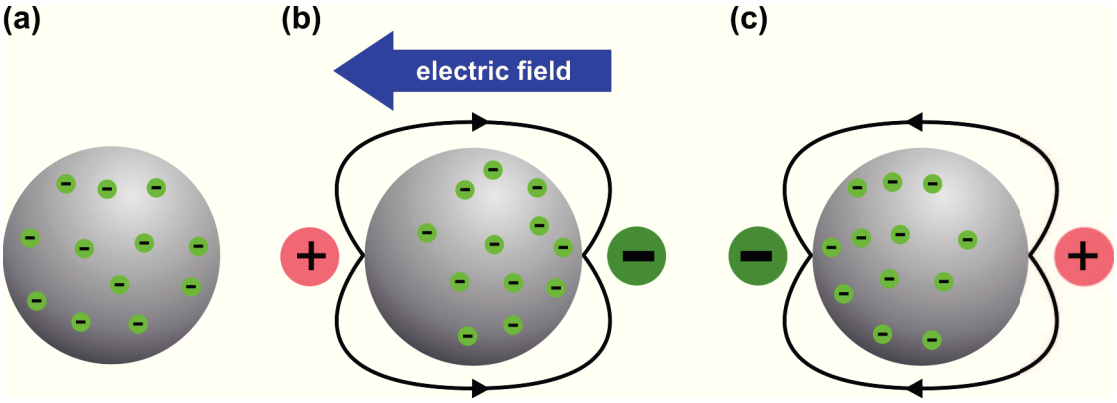

Figure 2.3: Electronic origin of a particle plasmon: (a) equilibrium distribution, (b) induced dipole at $t = 0$, (c) dipole distribution at $t = T_0/2$.

interband transition in the visible spectrum [25] ($2.4\,\mathrm{eV} = 520\,\mathrm{nm}$ for gold). This transition drastically increases absorption around this frequency, which is why gold and copper have a reddish shine to the spectator's eye.

2.1.3 Kramers-Kronig Relations

From the dielectric functions derived above (equations (2.10) and (2.14)) we see that their real and imaginary parts depend on the same quantities, most notably on the resonance and the damping frequency. This infers that we cannot change either part of the complex number without changing the other.
In fact, this is not unique to refractive indices within the Lorentz or Drude model but is a universal statement that can be deduced directly from the law of causality; the exact interdependence is formulated by the Kramers-Kronig relations [25, 29]:

$$\mathrm{Re}\left[n(\omega)\right] = 1 + \frac{1}{\pi}\mathcal{P}\int_{-\infty}^{\infty}\frac{\mathrm{Im}\left[n(\omega')\right]}{\omega' - \omega}\mathrm{d}\omega' \tag{2.16}$$

$$\mathrm{Im}\left[n(\omega)\right] = -\frac{1}{\pi}\mathcal{P}\int_{-\infty}^{\infty}\frac{\mathrm{Re}\left[n(\omega')\right] - 1}{\omega' - \omega}\mathrm{d}\omega' \tag{2.17}$$

2.2 Particle Plasmons

We have seen above how the electrons in bulk matter react to an external electric field $\boldsymbol{E}$. Especially for metals this behaviour changes when we substitute the bulk sample by a small particle whose size is comparable to the skin depth. In this case the electric field can penetrate the volume of the particle, which gives rise to an electronic response unlike that of a simple Drude metal.
Let us first consider a spherical metal nanoparticle: Without an external field the electron gas in the metal is in equilibrium and evenly distributed over the particle volume (Fig. 2.3 a). If, however, we introduce an external electric field the whole gas is somewhat shifted with respect to its equilibrium position, thus leading to charge separation by accumulating negative charges (Fig. 2.3 b). This induced dipole produces an internal electric field which points in the opposite

direction than the external field. It therefore acts as a restoring force on the electrons and leads to a charge oscillation (Fig. 2.3 c). We call this collective oscillation of valence electrons a *particle plasmon* or *localised surface plasmon*[1]. Since the mechanism it originates from is very similar to that of the Lorentzian oscillator model (section 2.1.1) we can use the same equation of motion as equation (2.8).

Yet the picture of a plasmon as an induced dipole is only valid if we assume the electric field to have a constant phase over the whole particle and thus neglect retardation. Within this quasistatic approximation we can find an analytic expression for the polarisability $\alpha(\omega)$ of a metal nanosphere by solving the Laplace equation [30]:

$$\alpha(\omega) = 4\pi r^3 \frac{\epsilon(\omega) - \epsilon_\mathrm{s}}{\epsilon(\omega) + 2\epsilon_\mathrm{s}}, \tag{2.18}$$

where $r << \lambda$ is the radius of the sphere, $\epsilon(\omega)$ is the dielectric function of the (Drude) metal and ϵ_s the dielectric constant of the surrounding material. This term shows a resonance when the real part of the denominator vanishes, that is, when

$$|\mathrm{Re}\left[\epsilon(\omega)\right]| = -2\epsilon_\mathrm{s}. \tag{2.19}$$

The non-vanishing imaginary part $\mathrm{Im}\left[\epsilon(\omega)\right]$, however, causes this resonance to be finite and not a pole in the polarisability. It is manifest - and clearly visible - in the resonantly enhanced scattering and absorption cross-sections [30]

$$\sigma_\mathrm{scat} = \tfrac{k^4}{6\pi}\left|\alpha(\omega)\right|^2 \quad \text{and} \quad \sigma_\mathrm{abs} = k\mathrm{Im}\left[\alpha(\omega)\right], \tag{2.20}$$

which is the origin of the bright colours in transmittance and reflectance of metal-stained glasses.
Remarkably, beyond the quasistatic approximation the spectral position of the particle plasmon resonance does not solely depend on the materials of the sphere and its surrounding but also on the size (or more generally the shape) of the particle. Plasmon resonances can therefore be tuned to almost arbitrary spectral positions by adjusting the geometry of the particle.

If we now want to study larger spherical particles, which do not satisfy the conditions of the quasistatic approximation, we have to return to the rigorous analytical approach of Mie theory [31]. Here, the internal and scattered fields of a metal sphere are expanded into a set of normal modes. We can then in turn expand the absorption into a power series and truncate it at an appropriate order. For instance, if we only take the first - the dipolar - term of this expansion into account we arrive at the above result for the quasistatic approximation and the two descriptions become completely analogous.
More complex shapes than a sphere can, in prinicple, not be studied analytically. Although the quasistatic approach can be extended to elliptical particles by the introduction of geometrical factors, we generally have to resort to numerical calculations to find the optical properties associated with arbitrarily shaped metal particles.

[1] As these are the only kind of plasmons we deal with in this thesis, we refer to particle plasmons whenever we use the simplified term plasmon.

Modern research efforts on particle plasmons are not so much concerned with the resonance spectra but, to a large extent, rather focus on the enhanced near fields associated with these resonances. Returning to the quasistatic approximation we can describe the near field of a spherical particle as the electric near field of a dipole known from classical electrodynamics [29]

$$\boldsymbol{E}_{\mathrm{dipole}} = \frac{1}{4\pi\epsilon_0}\left[3\boldsymbol{n}(\boldsymbol{n}\cdot\boldsymbol{p}) - \boldsymbol{p}\right]\frac{1}{r^3}. \tag{2.21}$$

Since the dipole moment $\boldsymbol{p}$ is connected with the polarisability α by $\boldsymbol{p} = \epsilon_0\epsilon_\mathrm{s}\alpha\boldsymbol{E}$ a particle plasmon resonance is always accompanied by a resonantly enhanced near field. Again, for more complex particle shapes or outside the quasistatic limit we rely on numerical calculations to find the exact field distributions generated by a plasmon (compare section 4.3).

2.3 Metamaterials

The basic principles of optics allow for a lot of interesting optical properties that are physically possible but do not occur in natural materials. One of the most striking examples of this is the possibility of a negative refractive index proposed by Victor Veselago in 1968 [24]. Since John Pendry found an application for these negative-index materials (NIMs) in the form of his perfect lens in 2000 [4] the research interest in this direction is undiminished [1–3, 7, 32, 33].
To arrive at materials with specially tailored artificial properties, which we call metamaterials, we use an analogy to real substances in form of the effective medium approach: the optical properties of a crystal are crucially influenced by the properties of the individual atoms while both the size of and the distance between the atoms is much smaller than optical wavelengths. In this case the incident wave cannot resolve the lattice structure and therefore reacts to the crystal as a whole.
Translating this concept of an effective medium to artificial media we find the condition that the grating period a of the medium must be much smaller than the wavelength λ for which the medium is designed. Furthermore, we can make use of the fact that it is the physical properties of the individual building blocks that dominate the optical properties of the whole effective material. From this we draw the freedom to design building blocks that are tailored to the problem at hand.
We have already met the first example of a metamaterial for which the effective medium approach is valid in form of metal-stained glasses where the plasmonic resonances of the artificially-added particles cause the glass to have a certain colour by significantly changing its scattering and absorption behaviour. In general, metamaterial building blocks do not need to be based on plasmonic particles and therefore do not have to be metallic. If the artificial properties of a metamaterial do, however, rely on plasmon resonances we sometimes refer to them specifically as plasmonic metamaterials.

Let us now return to negative-index materials as the most prominent example of metamaterials. As Veselago states, a negative refractive index requires both the permittivity ϵ and the permeability μ to be negative. This is the reason why there are no natural negative-index materials. Although a negative ϵ is readily found in metals (see section 2.1.2), natural substances show a negligible magnetic response at optical frequencies and therefore have a permeability $\mu = 1$.

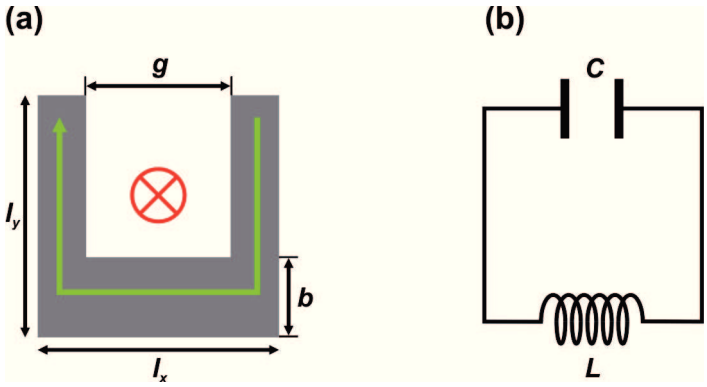

Figure 2.4: (a) Sketch of the split-ring resonator geometry and its relevant size parameters; the green arrow indicates the ring current induced by an external field. (b) Analogous representation of the resonator as an electrical LC circuit.

The goal of designing a building block for a negative-index material is therefore to find structures that exhibit a magnetic dipole moment when excited with an external field. The component that provides this magnetic response in the quintessential NIM in the optical region, the fishnet structure [34–36], is a so-called cut-wire pair [37, 38]. It consists of two parallel metal strips separated by a dielectric spacer. Owing to retardation effects this configuration can support a ring current from one wire to the other, leading to a magnetic moment.
Yet when it comes to magnetic response the workhorse of the metamaterial community is still the first structure proposed to this end [39]: the split-ring resonator which we describe in detail below.

2.3.1 The Split-Ring Resonator

John Pendry and co-workers first suggested the split-ring resonator (SRR) as a "magnetic atom" in 1999 [39] and the first experimental realisation in the microwave regime followed soon after by David Smith and co-workers [32]. Using electron-beam lithography the same concept could be extended to the near-infrared and optical spectral region by Stefan Linden and co-workers [40, 41].
The SRR is basically a U-shaped metal particle along which an external field can excite a ring current following the shape of the SRR (Fig. 2.4 a). This ring current, in turn, induces a magnetic moment perpendicular to the plane of the resonator and thus provides a magnetic response and the possibility of a permeability unequal to unity.
Essentially, the split-ring resonator can be understood as an analogue of the classical electrodynamic LC circuit: the bent metal wire is one winding of a coil, the upper parts of the two vertical arms, separated by a gap, act as capacitor (Fig. 2.4 b). The inductivity L and the capacitance C of this circuit can then also be calculated from electrostatics:

$$L = \epsilon_0 \epsilon \frac{A_{\text{plate}}}{d} = \epsilon_0 \epsilon \frac{t \cdot b}{g}, \qquad C = \mu_0 \frac{A_{\text{coil}}}{l_{\text{coil}}} = \mu_0 \frac{l_{\text{x}} \cdot l_{\text{y}}}{t}, \tag{2.22}$$

where l_{x}, l_{y}, g and b are the geometry parameters of the SRR as depicted in Fig. 2.4 a and t is the metal thickness. We therefore expect the resonance frequency corresponding to this LC (or magnetic) resonance to be

$$\omega_{\text{LC}} = \frac{1}{\sqrt{LC}} = \frac{c}{\epsilon} \sqrt{\frac{g}{l_{\text{x}} l_{\text{y}} b}}, \tag{2.23}$$

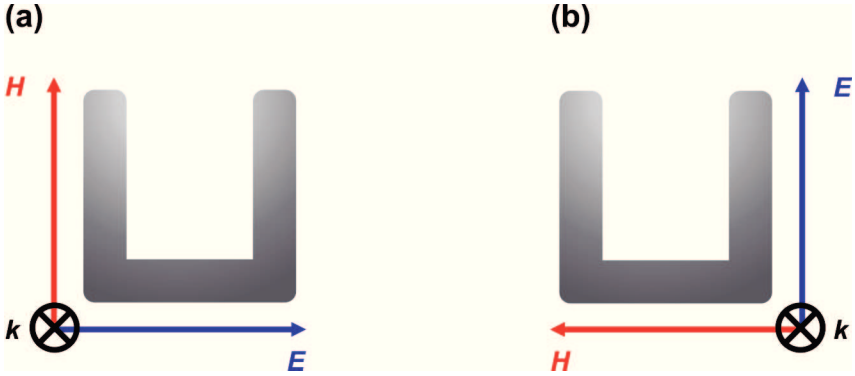

Figure 2.5: Possible orientations of the electric and the magnetic field along the arms of an SRR under normal incidence. For the polarisation in (a) the magnetic mode is excited, for the one in (b) it is not.

which depends only on the geometry of the split-ring resonator and on the dielectric constant of the surrounding. Much like plasmonic resonances, we can thus tune the position of the magnetic resonance by altering the absolute and relative sizes of the arms of the SRR. There is, of course, a limit to this procedure when the height b of the horizontal arm becomes so small that it vanishes or so large that the SRR turns into a rectangle; in both cases the magnetic resonance can no longer be observed.

Polarisation Dependence

When a light wave impinges onto a split-ring resonator it is, in principle, possible for both the electric and the magnetic field component to couple to the SRR. As we are mainly interested in the magnetic resonance it would be the obvious approach to induce the necessary ring current by a magnetic field vector $\boldsymbol{H}$ normal to the plane of the SRR. In most optical experiments, however, we want to work under normal incidence where neither $\boldsymbol{H}$ nor $\boldsymbol{E}$ are perpendicular to the substrate. The two principal orientations of the fields to the SRR for this case are shown in Fig. 2.5.
Since the electric field $\boldsymbol{E}$ does not couple to the coil but rather to the capacitor, it is still possible to induce the desired ring current *via* the electric field if it has a component perpendicular to the capacitor plates, i.e. parallel to the gap of the resonator [42]. For this configuration, as shown in Fig. 2.5 a, the ring current flows through the SRR because the external field has to be compensated and therefore charge has to be transferred from one plate to the other.
If $\boldsymbol{E}$ is oriented along the vertical arms (Fig. 2.5 b) it does not couple to the internal field of the capacitor to which it is perpendicular. Thus there is no need for charge transfer to compensate for an additional field and no magnetic mode is observed.
In what follows we stick to the terminology of horizontal and vertical polarisation and by these refer to the alignment of the electric field with respect to the gap of the SRR. Thus horizontal polarisation (Fig. 2.5 a) can excite the fundamental resonance whereas vertical (Fig. 2.5 b) cannot; this is why we sometimes also use the terms resonant and non-resonant polarisation.

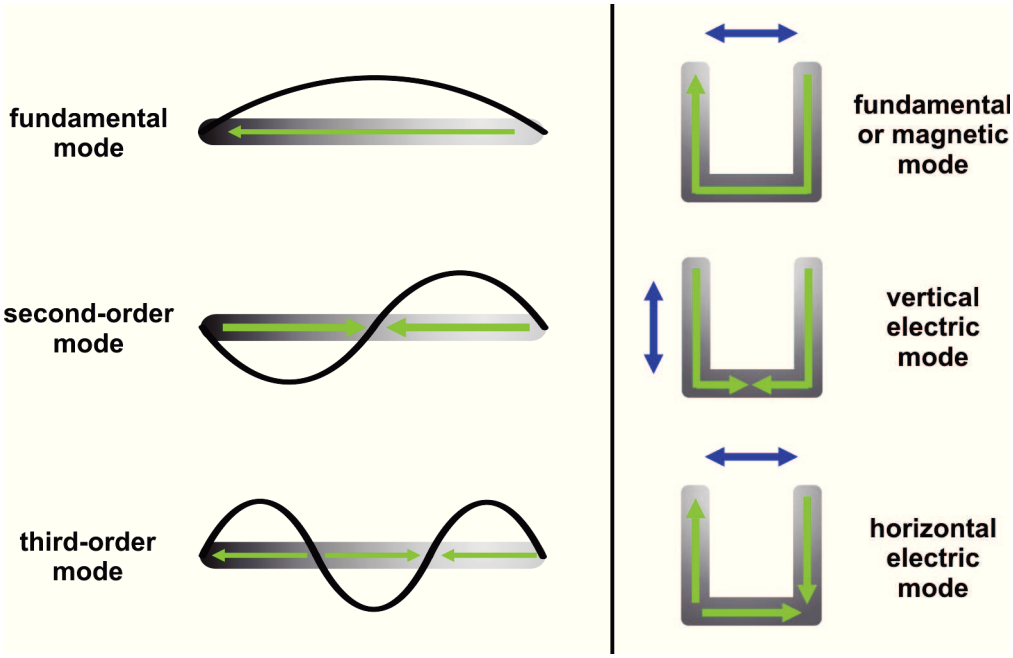

Figure 2.6: Correspondence between the resonant modes of a rod antenna (left panel) and a split-ring resonator (right panel). The blue arrows indicate the polarisation for which the SRR modes can be excited.

Higher-Order Resonances

We have already described the split-ring resonator as a wire bent into a U-shape and now take a closer look at this picture. It illustrates the plasmonic point of view on an SRR and helps to understand the higher-order resonances.
If we fold the two vertical arms back to the baseline of the resonator we obtain a rod antenna whose excitation modes are well-known: the fundamental mode occurs when the current is distributed over the complete length of the antenna with one maximum in the middle and two nodes at the ends. An additional node is present, along with a second maximum, for the second-order mode. The third-order excitation exhibits yet another node and maximum in the current distribution and so forth (Fig. 2.6, left panel).
Folding the antenna back into a split ring, we find the same current distributions and can relate them to the SRR resonances. The fundamental mode gives rise to the ring current and can therefore be identified as the magnetic mode. The second- and third-order resonances do not lead to a dominant magnetic moment. We consequently call them electric resonances and further classify them according to the polarisation by which they can be excited as vertical and horizontal electric mode (Fig. 2.6, right panel).
Figure 2.7 shows calculated spectra of a split-ring-resonator array for horizontal and vertical incident polarisation. The long-wavelength fundamental mode can only be observed for horizontal polarisation. For this excitation geometry we also observe the third-order or horizontal electric mode at shorter wavelength. At almost the same spectral position but with a significantly larger linewidth we find the second-order mode for vertical incident polarisation.

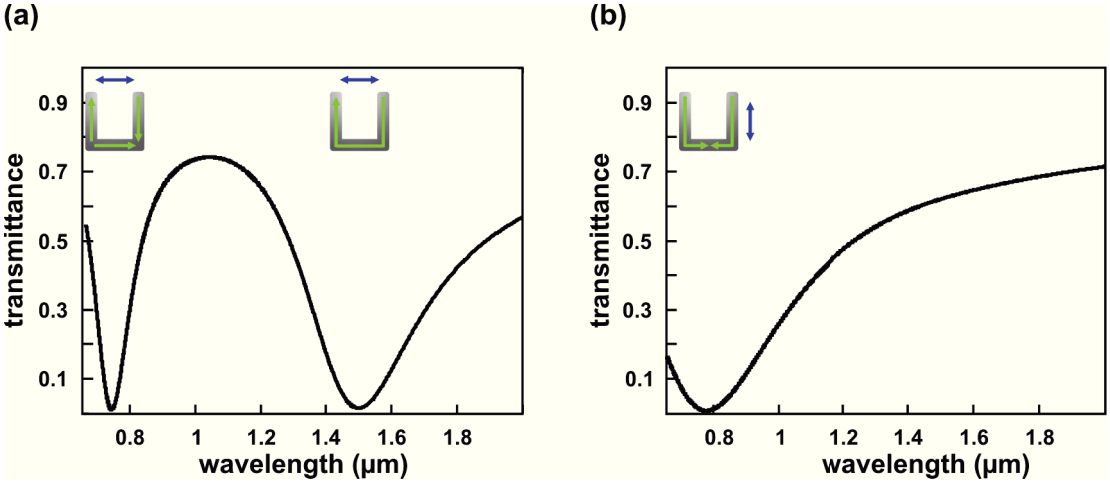

Figure 2.7: Calculated transmittance spectra of an array of split-ring resonator for (a) horizontal and (b) vertical incident polarisation. The SRR cartoons show which modes the resonances correspond to.

2.4 Loss and Loss-Compensation

One of the big challenges plasmonic metamaterials research, indeed any plasmonics research, faces today is that of overcoming the intrinsic losses of the dispersive metals they are based on. These losses are the main obstacle to most applications that scientists and engineers are working on. For instance, a plasmonic waveguide has to be able to support a surface plasmon for more than a few microns [43], otherwise it is just as useless as a cloaking device that casts a shadow due to absorption losses [6].
Since this thesis aims at taking a step towards loss-compensation by investigating the coupling between plasmonic metamaterials and quantum wells, we take a closer look at these losses and how they can possibly be compensated, in this section.

2.4.1 Losses in Metallic Nanostructures

As we have seen in section 2.1, metals described by the Drude model are highly dissipative for frequencies well below the plasma frequency ω_p (compare $\mathrm{Im}\left[\epsilon\right]$ in Fig. 2.2). Using equation (2.7) we can link the imaginary part of the refractive index, ultimately the imaginary part of the dielectric response, to absorption in the metal. This absorptive loss is often referred to as *Ohmic loss* because the electron energy is dissipated into heat in the same way that is responsible for electric resistance.
These Ohmic losses present a severe challenge for many possible applications of plasmonics and metamaterials, especially in the visible or in the near-infrared spectral region where typical telecomunication wavelengths are located.

Dealing with metallic nanoparticles instead of extended films or bulk metal, however, we cannot use a pure Drude description for the optical behaviour of the particle. Especially when approaching a plasmonic resonance the response of a metal nanoparticle to an external electromagnetic field differs considerably from that of a Drude metal (see section 2.2).
We can find an instructive analytical formula for this behaviour if we return to the polarisability

of a metallic nanosphere in equation (2.18): let the sphere be composed of a perfect Drude metal following the dispersion relation $\epsilon(\omega)$ given by equation (2.14) and let it be surrounded by vacuum, thus $\epsilon_\mathrm{s} = 1$. In this simple case we can rewrite the polarisability as

$$\alpha(\omega) = \frac{4\pi r^3}{3} \cdot \frac{Ne^2}{\epsilon_0 m_\mathrm{e}} \cdot \frac{1}{\tilde{\Omega}^2 - \omega^2 - i\gamma\omega}, \tag{2.24}$$

where we have substituted the resonance frequency $\tilde{\Omega} = \omega_\mathrm{p}/\sqrt{3}$. This term already resembles the functional form of a Lorentzian oscillator. We continue with an evaluation of the scattering and absorption cross-sections by inserting the above result into equation (2.20).

$$\sigma_\mathrm{scat} = A \cdot \frac{\omega^4}{(\tilde{\Omega}^2 - \omega^2)^2 + \gamma^2\omega^2}, \tag{2.25}$$

$$\sigma_\mathrm{abs} = B \cdot \frac{\gamma\omega^2}{(\tilde{\Omega}^2 - \omega^2)^2 + \gamma^2\omega^2}, \tag{2.26}$$

where we have condensed all constants into the prefactors A and B. The scattering and absorption cross-sections, or more precisely their sum, is directly linked to the extinction spectrum resulting from a plasmonic particle. Thus we find the particle plasmon resonance to have a Lorentzian lineshape, centred around $\tilde{\Omega}$. And a full-width at half-maximum (FWHM) $\Delta\omega = 2\gamma$. Since γ quantifies the damping of the oscillator we can use it to define a quality factor Q of the plasmon, which can be directly derived from the spectrum:

$$Q = \frac{\tilde{\Omega}}{\Delta\omega}. \tag{2.27}$$

As a rule of thumb we can therefore state: the narrower and the larger the peak in the extinction spectrum, the higher is the Q factor of the plasmon and the higher is its oscillator strength f.
The above, however, is only strictly true for the natural linewidth of a plasmon. In most experiments we deal with an ensemble of particles which are not exactly identical in shape and size. This results in a further broadening of the spectral line owing to the multitude of slightly differing resonance positions; this effect is called inhomogeneous broadening.

Loss Channels of Particle Plasmons

At this point it is important to have a closer look at the loss channels we observe for particle plasmons. Generally speaking, we can divide losses into two categories: radiative and non-radiative ones. The former are due to energy transfer to the environment by radiative processes. The latter originate from internal dissipation of energy (compare Fig. 2.8).
Radiative losses of plasmons are related to the coupling of the plasmon to the external electromagnetic field. An efficient coupling of the plasmon to the light field goes along with high radiative losses and therefore with a broad spectral line. This "loss" channel is, in fact, highly desirable for a lot of experiments and applications where the plasmonic particle is used as an antenna.
Non-radiative ohmic losses, however, hinder most applications because the conversion of energy to internal processes renders this amount of energy inaccessible by optical means. In

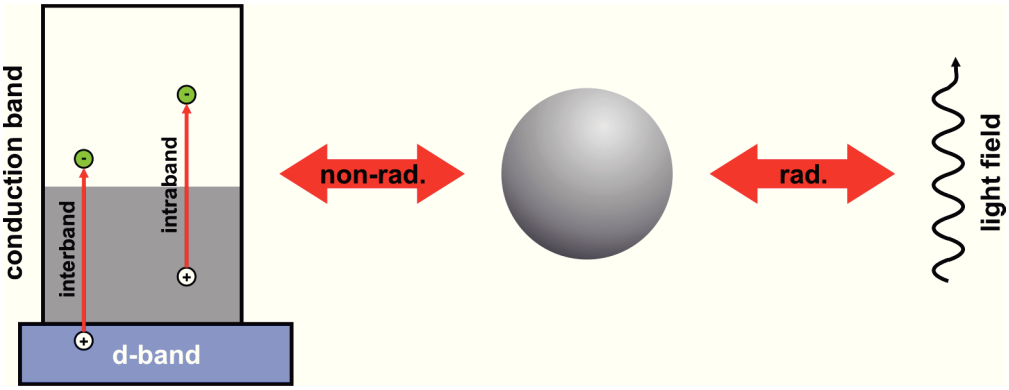

Figure 2.8: Decay channels of a particle plasmon: radiative losses by coupling to the light field and non-radiative losses by creation of an electron-hole pair; adapted from [44]

.

plasmonic particles the energy is mainly dissipated due to the production of electron-hole pairs, either *via* interband transitions from the d-band to the conduction band or *via* intraband transitions within the conduction band [44].

2.4.2 Loss-Compensation

To make devices based on optical metamaterials feasible we need to compensate the high Ohmic losses of the metal building blocks to a great extent. There are several approaches by which absorptive losses can be reduced: by selecting low-loss materials [36, 45, 46], by tailoring the geometry [10] or by introducing a gain medium [11]. We describe these concepts in the following paragraphs.

The first idea is simple: to find a conducting material, supporting plasmons, that has the lowest possible losses in the spectral region of interest. For optical and near-infrared wavelengths this turns out to be silver. Indeed, the negative-index metamaterial with the lowest losses in this regime is a silver fishnet structure [36]. For this structure Gunnar Dolling *et al.* report a figure of merit $FOM = -\mathrm{Re}(n)/\mathrm{Im}(n) = 3$ with $\mathrm{Re}(n) = 1$ at a wavelength of $1400\,\mathrm{nm}$. Using equation (2.7) we find a corresponding absorption coefficient of $\delta \approx 3 \times 10^4\,\mathrm{cm}^{-1}$.
The use of superconducting materials for metamaterials is another obvious idea in this direction because in the superconducting phase all resistive losses vanish. However, this approach is not feasible for plasmonic applications because the superconducting energy gap is well below the near-infrared region but the superconducting phase exists only for energies lower than this gap. Even for more suitable spectral regions it is not the solution of choice for applications because of the low temperatures required for operation. Even the best high-temperature superconductors to date still require liquid-nitrogen cooling, making them unfit for use in many devices.
New material systems like metal-alloys [9], intermetallics [47] or graphene [48] have also been proposed as a possible solution by way of material engineering. Experimental realisations of these ideas, however, have not passed the stage of being proof-of-principle, yet.

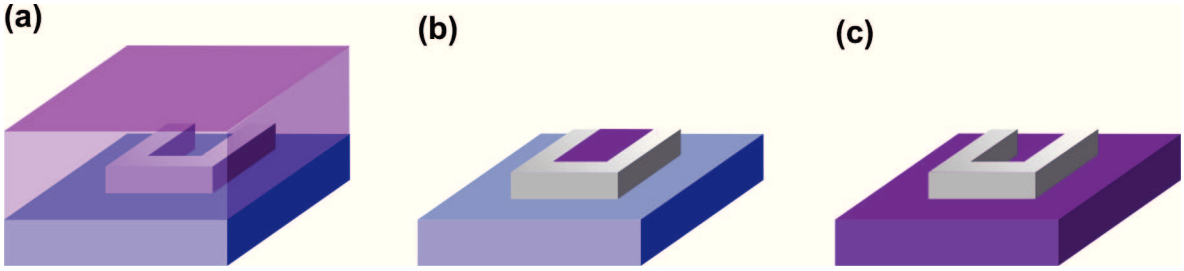

Figure 2.9: Three possibilities of positioning a gain medium (purple) with respect to a plasmonic metamaterial: (a) imbed the whole sample in the gain medium, (b) selectively position the gain medium at special locations, (c) use a gain medium as substrate.

.

A second way of minimising absorptive losses is the convenient design of the building blocks to this end. Durdu Güney *et al.* have numerically studied the influence of geometric parameters of split-ring resonators for different frequency regions [10]. For the high frequencies of interest to us they find a means of lowering Ohmic losses by reducing the geometric skin depth and simultaneously enlarging the cross section of the SRR arms. The key idea behind this is to geometrically approach the bulk limit and come closer to the bulk value of the skin depth which is smaller than the value found for particles.
This approach has the advantage of starting from well-studied and already controllable material systems and only adjusting the design parameters. However, if we aim at an application for a specific wavelength geometrical tailoring can only be performed within narrow boundaries because every change in geometry results in an altered resonance frequency. How well this idea can be transported to real samples has also not been demonstrated experimentally, so far.

The third approach is the one we follow in this thesis: the compensation of absorptive losses by the introduction of optical gain [11]. Optical gain is, naively speaking, the opposite of absorption. We can therefore use the excess energy provided by the gain medium to compensate for the energy lost due to dissipation in the metallic nanostructure. Theoretical investigation has proved the introduction of gain a promising method for loss-compensation [12, 13, 49].
Although the *gain solution* to the problem of loss sounds straightforward we have to make certain considerations:
We have found above that low-loss metamaterials have an absorption coefficient of $\delta \approx 3 \times 10^4\,\mathrm{cm}^{-1}$, which is on the same order of magnitude as the gain coefficients of typical semiconductors. We can therefore be confident to find a gain medium that is, in principle, strong enough to compensate the loss of a metamaterial.
Most importantly, though, the energy transfer between the nanostructure and the gain medium requires cross-talk between the two components. We have shown in [49] that the behaviour of the combined system depends crucially on the coupling strength between the plasmon and the gain. Before aiming at full compensation of absorptive losses, we therefore first have to prove substantial coupling between the plasmonic metamaterial and the gain medium we intend to use.

Finally, we need to decide how to experimentally incorporate the gain medium into an active metamaterial. Figure 2.9 shows the three basic possibilities: we can completely imbed the metamaterial in the gain medium, which is feasible for dyes or quantum dots or polymers

doped with either [14]. For certain types of metamaterials, e.g. fishnets or cut-wire pairs, it is favourable to position the active medium at a specific location where we expect the highest coupling efficiency. In case of a fishnet or a cut-wire pair the gain medium can be efficiently used as spacer between the two metal layers [16]. If, however, we choose a semiconductor as gain material the obvious incorporation is the use as active substrate [50]. Although this is not the position where we expect maximum coupling efficiency, semiconductors have two advantages: they are long-term photostable and they offer the possibility of electrical pumping, which is especially important regarding applications.

We have so far discussed loss-compensation approaches from a purely plasmonic point of view, deliberately disregarding what happens to a negative index of refraction. Because a negative index implies a negative phase velocity we have to regard causality as expressed in the Kramers-Kronig relations (see section 2.1.3), thus imposing restrictions on how far losses can be reduced in negative-index materials without violating causality [51, 52].

Chapter 3

Semiconductor Optics

The optical properties of semiconductors ceased to be of purely scientific interest many years ago: light-emitting semiconductor devices have arrived in our every-day lives, e.g. in the form of semiconductor lasers [53, 54] powering CD players and disk drives. This capability to produce light when excited with an electrical source, which makes them so interesting for use in compact devices, is the reason why we use semiconductors as gain media, keeping in mind future applications[1].
We want to exploit this optical gain of a semiconductor nanostructure to aim at compensating the absorptive losses of a plasmonic metamaterial, in which we follow theoretical suggestions [20, 55]. However, in order for this concept to work the two systems have to exchange energy and thus have to couple significantly.
To achieve substantial coupling between a semiconductor substrate and a plasmonic structure maximum overlap of the electronic wave function in the semiconductor and the plasmonic near field is crucial. This renders control over the distribution of the wave function desirable. Such is, however, not possible in bulk semiconductors because the electrons can move freely in all three spatial directions. Quasi-two-dimensional structures like quantum wells [56] confine the movement of electrons to a plane, leading to bound quantised states in the third dimension. As this confinement depends not only on the materials but also on the exact geometry of the quantum well the wave function can be engineered to some extent.
In this chapter we summarise the basic concepts of semiconductors before we go on to consider in more detail the optical properties of single quantum wells. We conclude this introduction by studying how semiconductors can be modelled as optical two-level systems. In this framework we describe different light-emission processes and derive the optical Bloch equations as the relevant equations of motion. Here, we also review the Purcell effect and Förster transfer as examples of how (two-level) emitters interact with their environment.

3.1 Semiconductors

In crystalline solids the electronic states form bands and are not considered as individual levels [57]. Occupied states below the Fermi energy form the valence band, unoccupied ones above

[1] Within the scope of this thesis, however, we only use optical pumping.

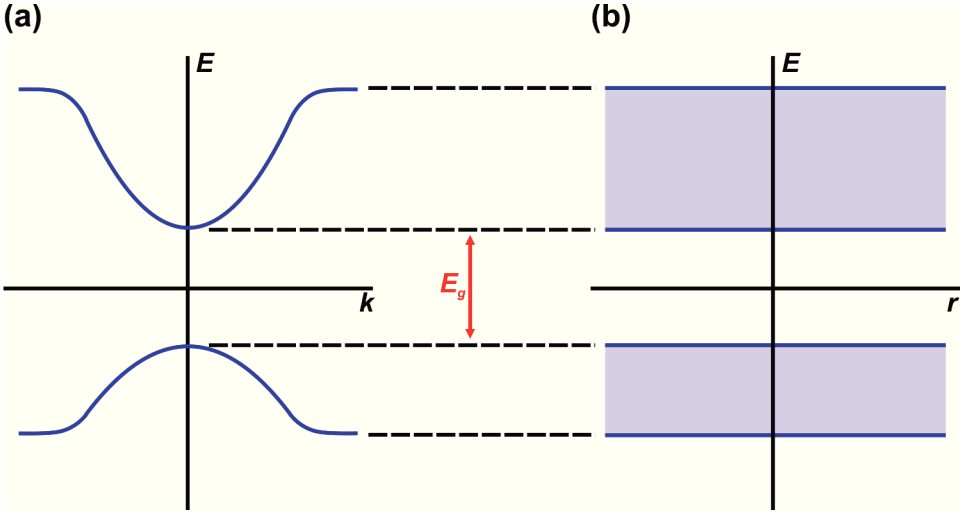

Figure 3.1: Schematic band structure of a semiconductor (a) in momentum space - energy versus wave vector $\boldsymbol{k}$ - and (b) real space - energy versus space coordinate $\boldsymbol{r}$.

the Fermi energy form the conduction band[2]. These two bands can either overlap, when the electron levels form a continuum, or they can be energetically separated by a region in which no states exist. This region is called a band gap and is characterised by its width in energy space, the band gap energy E_g. As a rule of thumb, we generally speak of a semiconductor if the band gap energy is $0 < E_\mathrm{g} \leq 4\ \mathrm{eV}$ [58].

We further divide semiconductors into two classes according to their band structure: If the maximum of the valence band and the minimum of the conduction band occur at the same momentum vector $\boldsymbol{k}$ we call this a direct semiconductor (e.g. GaAs, see Fig. 3.2 a). If, however, the band minima and maxima have some separation in momentum space the semiconductor is considered indirect (e.g. silicon, see Fig. 3.2 b) because an additional momentum component is needed for the lowest-energy transition from the valence to the conduction band. In general, a semiconductor material has a more complex band structure and can have both direct and indirect band gaps at once. It is then classified by the one with the lowest band-gap energy.

3.1.1 Charge Carriers

The optical properties of semiconductors are mainly governed by electronic interband transitions. We therefore take a closer look at the relevant charge carriers and discuss a simple model of the transitions and related optical effects later, in section 3.3.

The Concept of Effective Mass

Speaking about the basic concepts of semiconductor optics we usually operate in the so-called one-electron approximation. This means, we condense the potential of the crystal atoms and

[2]Note that these sharp filling conditions are only true for $T = 0\,\mathrm{K}$; for temperatures $T > 0$ K the electronic distribution is smeared out within an energy interval of about $k_\mathrm{B}T$ according to the Fermi-Dirac statistics. For the sake of simplicity, we stick to the zero-temperature case throughout the text.

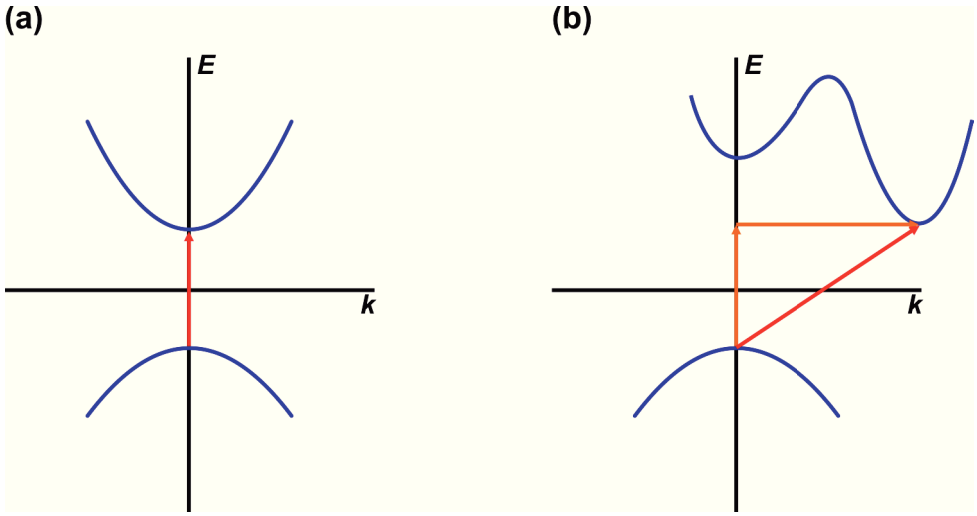

Figure 3.2: Schematic bandstructure of (a) a direct semiconductor like gallium arsenide and (b) of an indirect semiconductor like silicon.

the interaction potentials between all the electrons into one periodic potential [58]. If we now want to describe the influence of an external field acting on the electrons, we need to account for the interactions with the lattice and with other electrons by introducing the effective mass m^* given by

$$\frac{1}{m^*} = \frac{1}{\hbar^2}\frac{\partial^2 E}{\partial k^2} = \frac{1}{\hbar^2}\frac{\partial^2 E}{\partial k_i \partial k_j}, \tag{3.1}$$

where $i, j = x, y, z$ refer to the spatial coordinates. Equation (3.1) shows that the effective mass reflects the curvature of the band a charge carrier is located in and that it is, in general, a tensor depending on the direction the particle is moving in.
For interband transitions we often only need to consider events close to the band extrema, where the dispersion is usually parabolic, leading to a constant effective mass. We can therefore apply the effective-mass approximation and describe the charge carriers as free particles with effective mass m^*.

The Concept of Holes

In interband transitions electrons are excited from the valence band to the conduction band. While it is straightforward to describe the movement of the few excited electrons in the conduction band, this direct approach becomes impractical for the multitude of occupied states in the valence band. We therefore turn to considering the *defect electrons* or *holes* left by the excitation of electrons. The properties of such a hole are closely connected to the ones of the electron that was removed from the valence band and are given below.

electric charge:	q_h	$=$	$-q_\mathrm{e} = e$
wave vector:	$\boldsymbol{k}_\mathrm{h}$	$=$	$-\boldsymbol{k}_\mathrm{e,VB}$
effective mass:	m^*_h	$=$	$-m^*_\mathrm{e,VB}$
	$m^*_\mathrm{h} > 0$		$m^*_\mathrm{e,VB} < 0$

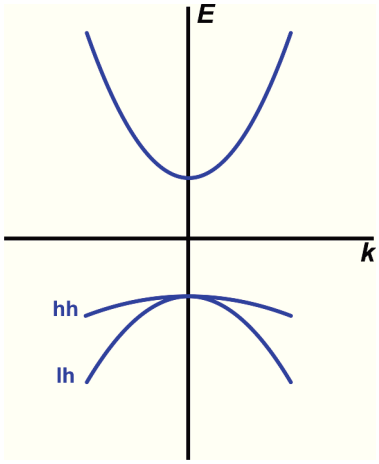

Figure 3.3: Schematic band structure of a semiconductor including the spin-orbit splitting of the valence band into a heavy hole (hh) band and a light hole (lh) band.

The concept of holes allows for a description of the valence band, which is simple and completely equivalent to that of the few electrons in the conduction band. These quasiparticles are therefore the second relevant charge carriers in a semiconductor, alongside the electrons.
In many semiconductors the valence bands show spin-orbit splitting, that is, they are split into two subbands degenerate at the Γ-point [59]. These two subbands differ significantly (see Fig. 3.1.1) in their dispersion, which leads to the holes having substantially different effective masses. We therefore speak of the *heavy hole* band and the *light hole* band and also refer to the respective charge carriers as heavy holes and light holes.

The Concept of Excitons

Since electrons and holes are oppositely charged particles they interact *via* their Coulomb potentials and form a bound pair similar to positronium. We can describe this bound state as one quasiparticle and then call it an *exciton*. In most semiconductors the Coulomb interaction between an electron in the conduction band and the corresponding hole is strongly screened by the valence electrons. This results in a weak binding of the electron-hole pair and is often referred to as Wannier-Mott exciton. The less-frequent tightly bound case, as it exists in ionic semiconductors, is called Frenkel exciton.
As any two-particle system, the Wannier-Mott exciton can be described by a center-of-mass motion and a relative motion of the two particles. The former leads to the picture of an exciton as one quasiparticle with an effective mass $m^*_{\mathrm{exc}} = m^*_{\mathrm{e}} + m^*_{\mathrm{h}}$; the latter is similar to the well-known case of a hydrogen atom: The relative motion thus has quantised bound states and a continuum of states, where we can describe the excitons as ionised into free electrons and free holes. Still, the wave functions of the "free" particles are modified by their Coulomb interaction. In principle, the absorption spectra of excitons can be calculated from their eigenenergies and wave functions if we introduce an interaction term accounting for the Coulomb interaction. However, the underlying concept of excitonic absorption is different from optical absorption in the one-electron picture [59]. In the two-particle picture optical absorption is the conversion of a

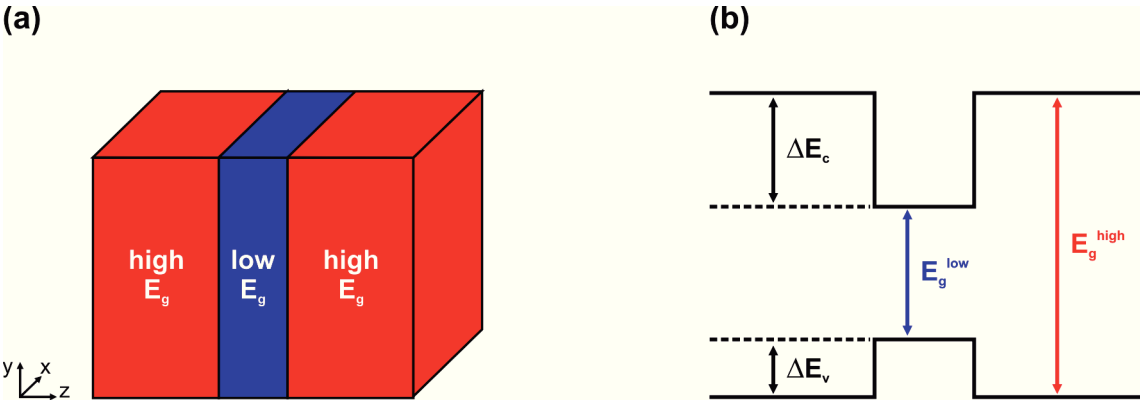

Figure 3.4: (a) Schematics of a single quantum well. (b) Corresponding band structure in real space.

photon into an exciton leading to an exciton-polariton. Using this conceptionally strict approach usually makes approximations necessary if we want to calculate the absorption spectra. We will therefore not go into further detail of exciton-polaritons, which can be found in textbooks on semiconductors [59] and semiconductor optics [58].

3.2 Semiconductor Quantum Wells

Single quantum wells (QWs) are semiconductor heterostructures consisting of a thin layer of one semiconductor with a lower band-gap energy $E_\mathrm{g}^\mathrm{low}$ sandwiched between two thicker layers of another semiconductor material whose band gap energy $E_\mathrm{g}^\mathrm{high}$ is higher (see Fig. 3.4). Usually, one refers to the middle layer as the quantum well or the quantum film and to the two surrounding high-band-gap layers as the barriers.
This configuration confines the charge carriers in the stacking direction (z) if the confinement energy

$$E_\mathrm{conf} = \frac{(\Delta p_z)^2}{2m} \sim \frac{\hbar^2}{2m(\Delta z)^2}$$

is comparable to the kinetic energy of the (quasi-)particle. For semiconductors this is the case when the layer thickness Δz of the well is smaller or equal to the exciton Bohr radius $a_{0,\mathrm{exc}}$ of the low-band-gap material. For the material system used in this work (InAlAs/InGaAs/InAlAs) this leads to a quantum-well layer that must be smaller than the exciton Bohr radius of InGaAs $a_{0,\mathrm{InGaAs}} \approx 18\,\mathrm{nm}$ [60]. If this confinement condition is fulfilled the charge carriers behave like particles in a box potential resulting in quantised states with well-defined energies and wave functions, which are derived in detail below.
In the plane of the well itself (xy-plane) the electrons (and holes) can still move freely, undisturbed by the confinement in z-direction. A single QW therefore is an example of a two-dimensional electron gas with the corresponding step-like functional form of its density of states (see Fig. 3.5).

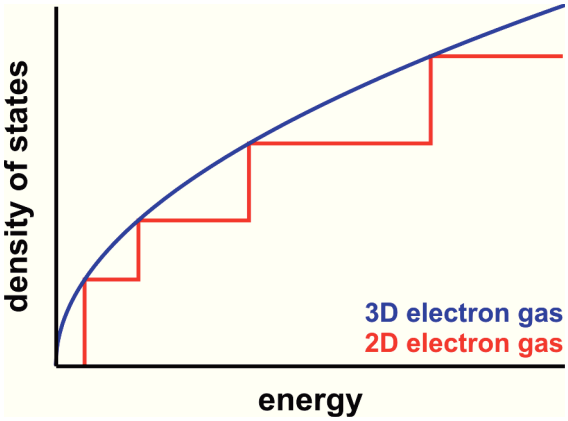

Figure 3.5: Density of states for a free electron gas in three (bulk) and in two dimensions (quantum well).

3.2.1 Electronic States of an Infinite Potential Well

Having introduced the basic concept of a single quantum well (QW) we now derive the energy levels and wave functions by modelling the confinement of the electrons[3] in z-direction by an infinite potential, which corresponds to the textbook problem of a particle in a one-dimensional box. This potential describes the situation in a single QW for large differences of the two band gaps $\Delta E_\mathrm{g} = E_\mathrm{g}^\mathrm{high} - E_\mathrm{g}^\mathrm{low}$, for smaller ΔE_g a refinement of the model towards a finite potential well may be necessary. For the quantum wells used in this thesis the larger band gap of InAlAs ($E_\mathrm{g}^\mathrm{high} \approx 2\,\mathrm{eV}$) is more than twice as high as that of InGaAs ($E_\mathrm{g}^\mathrm{high} \approx 0.75\,\mathrm{eV}$) and the barriers can therefore be considered infinitely high. We thus restrict the following discussion to the case of an infinite potential.

This confinement potential $V(z)$ for a quantum well of width w is given by

$$V(z) = \begin{cases} 0 & \text{for} \quad 0 < z < w \\ \infty & \text{else} \end{cases}$$

Since there is no further potential acting on the electrons in x- and y-direction we can write the Schrödinger Equation for the electrons as

$$\left[-\frac{\hbar^2}{2m_\mathrm{e}^*} \nabla^2 + V(z) \right] \psi(x,y,z) = \mathcal{E}\psi(x,y,z), \tag{3.2}$$

where m_e^* is the effective mass of the electron, $\psi(x,y,z)$ and $\mathcal{E}$ are the wave functions and energy eigenvalues.
This equation can be separated into two independent problems for the potential $V(z)$ in the z-direction and for a free movement (zero potential) in the xy-plane. The complete wave function $\psi(x,y,z)$ can then be found as the product

$$\psi(x,y,z) = \phi(x,y) \cdot \zeta(z)$$

[3] In this section we only consider the electronic states explicitly but the same formalism holds true for holes if we substitute the effective mass of the electron m_e^* by that of the hole m_h^*.

of the wave functions $\phi(x, y)$ and $\zeta(z)$ resulting from the separated equations:

$$\left[-\frac{\hbar^2}{2m_{\mathrm{e}}^*}\nabla_{xy}^2\right]\phi(x,y) = \mathcal{E}_{\mathrm{xy}}\phi(x,y) \tag{3.3}$$

with $\nabla_{xy}^2 = \frac{\partial^2}{\partial x^2} + \frac{\partial^2}{\partial y^2}$ and

$$\left[-\frac{\hbar^2}{2m_{\mathrm{e}}^*}\frac{\partial^2}{\partial z^2} + V(z)\right]\zeta(z) = \mathcal{E}_z\zeta(z). \tag{3.4}$$

Equation (3.3) describes the movement of a free particle in two dimensions and (3.4) is the Schrödinger equation of a one-dimensional infinite potential well. The solutions to both problems are well-known and can readily be found in standard textbooks on quantum mechanics, e.g. [61] or semiconductor optics, e.g. [58, 62]:
The wave function of a free particle is known to be a plane wave

$$\phi(x,y) = e^{i(k_x x + k_y y)} \equiv e^{i\mathbf{k}_{xy}\cdot\mathbf{r}_{xy}} \tag{3.5}$$

with the corresponding continuous eigenvalues

$$\mathcal{E}_{xy} = \frac{\hbar^2}{2m_{\mathrm{e}}^*}(k_x^2 + k_y^2) = \frac{\hbar^2}{2m_e^*}k_{xy}^2. \tag{3.6}$$

The particle-in-a-box problem in equation (3.4) leads to perfect confinement of the electrons within the width of the well. Therefore the wave function $\zeta(z)$ is strictly zero outside the well and at its boundaries, owing to the continuity condition. Inside the potential well ($0 < z < w$) the electrons have symmetric wave functions

$$\zeta^{(j)}(z) = \sqrt{\frac{2}{w}}\sin\left(\frac{j\pi}{w}z\right), \tag{3.7}$$

which are individually related to the quantised energy eigenvalues denoted by $j = 1, 2, ...$ and given by

$$\mathcal{E}_z^{(j)} = \frac{\hbar^2}{2m_{\mathrm{e}}^*}\left(\frac{j\pi}{w}\right)^2. \tag{3.8}$$

Together, equations (3.5) to (3.8) describe a set of j two-dimensional parabolic subbands whose minimum corresponds to the j^{th} eigenvalue of the infinite quantum well as illustrated in Fig. 3.6. In the x- and y- direction a particle can thus move in much the same way no matter what band it is located in, but its energy - even at rest - is raised by the eigenenergy $\mathcal{E}_z^{(j)}$ of the particular band. The complete energy eigenvalues of a single quantum well are therefore given by the sum of $\mathcal{E}_{xy}$ and $\mathcal{E}_z^{(j)}$

$$\mathcal{E}^{(j)} = \frac{\hbar^2}{2m_e^*}\left(k_x^2 + k_y^2 + \frac{j^2\pi^2}{w^2}\right). \tag{3.9}$$

From this energy quantisation in one dimension follow the distinct optical properties of semiconductor quantum wells, which we discuss next.

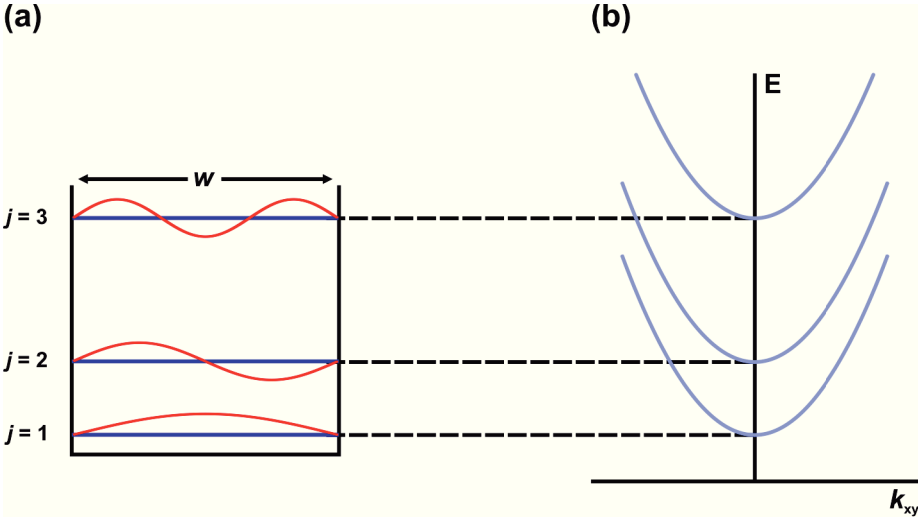

Figure 3.6: (a) Energy eigenvalues and wave functions for a one-dimensional infinite potential well and the corresponding (b) parabolic subbands of the free electron gas in the xy-plane.

3.2.2 Optical Properties: Absorption

In order to understand the absorption of light by a single quantum well we consider in the following the transitions that can occur between the valence and the conduction band when the charge carriers are subject to the confinement condition in z-direction given by equation (3.8). To evaluate the rate of absorption we have to evaluate Fermi's golden rule

$$w_{i\to f} = \frac{2\pi}{\hbar} \left|\langle f \left| -e\boldsymbol{r}\cdot\boldsymbol{E}\right| i\rangle\right|^2 g(\hbar\omega), \tag{3.10}$$

where $\boldsymbol{r}$ is the position vector of the electron, $\boldsymbol{E}$ is the amplitude of the incident electric field and $g(\hbar\omega)$ is the density of states, which for the case of a quantum well has to be considered in two dimensions. If we want to find the absorption spectrum we first need to evaluate the matrix elements in equation (3.10). For a polarisation vector in the xy-plane these take the form

$$M_{\mathrm{jj'}} = \langle j' \left| x \right| j\rangle = \int \psi^*_{\mathrm{j'}} x \psi_{\mathrm{j}} \mathrm{d}^3\boldsymbol{r}. \tag{3.11}$$

For the wave functions of a single quantum well (given by equation (3.7)) this term is only non-zero if the quantum number j of the inital state is equal to the number j' of the final state as the wave functions are orthonormal. Interband transitions in quantum wells therefore need to obey the selection rule

$$\Delta j = 0 \tag{3.12}$$

and can only occur between hole states and electron states with the same quantum number j as illustrated in figure 3.7. Each of these transitions corresponds to a specific energy

$$\hbar\omega = E_{\mathrm{g}} + \mathcal{E}_{\mathrm{e}}^{(j)} + \mathcal{E}_{\mathrm{h}}^{(j)} = E_{\mathrm{g}} + \frac{\hbar^2 j^2 \pi^2}{2w^2}\left(\frac{1}{m_e^*} + \frac{1}{m_h^*}\right) \tag{3.13}$$

depending on the band gap energy E_{g} and the two energy levels $\mathcal{E}_{\mathrm{e}}^{(j)}$ and $\mathcal{E}_{\mathrm{h}}^{(j)}$ for the j^{th} electron and hole state. The absorption spectrum of a quantum well therefore consists of a series of

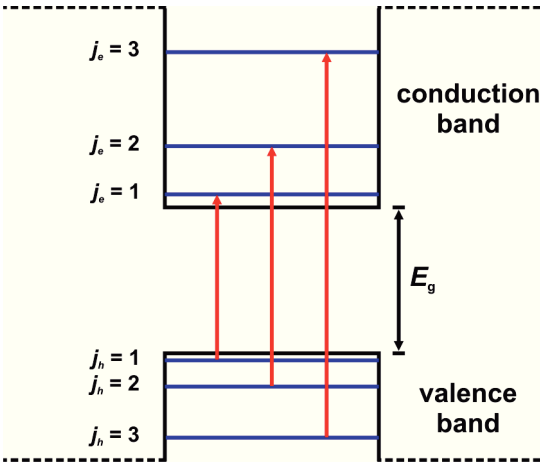

Figure 3.7: Allowed transitions with $\Delta j = 0$ between the valence and conduction band of a single quantum well.

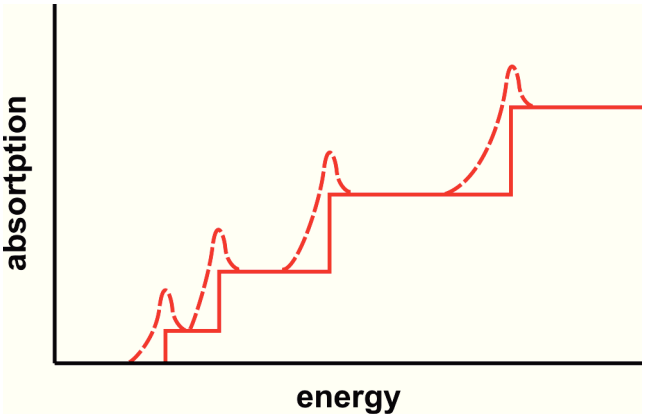

Figure 3.8: Schematics of the step-like absorption spectrum of a single quantum well. The peaks (dashed lines) show the influence of the excitonic interaction.

steps corresponding to the allowed transitions for $\Delta j = 0$. Taking into account the Coulomb interaction between electrons and holes every step is further modified by its own excitonic series. Figure 3.8 shows a sketch of the resulting absorption spectrum [62].

For light polarised in z direction, i.e. in quantisation direction of the quantum well, we need to find different selection rules. Their derivation relies on symmetry arguments in a group theory approach [63], so we only sketch an outline here and give some results.
Like above we need to evaluate the matrix element in equation (3.10) for electronic eigenstates of the QW. We obtain non-zero solutions of the matrix element that do not simply depend on the quantum number j but rather on parity π and on the eigenstates m of the angular momentum L_z. Transitions are allowed if either

$$\Delta m = 0 \quad \text{and} \quad \Delta\pi = 1 \tag{3.14}$$

or

$$\Delta m = 1 \quad \text{and} \quad \Delta\pi = 0. \tag{3.15}$$

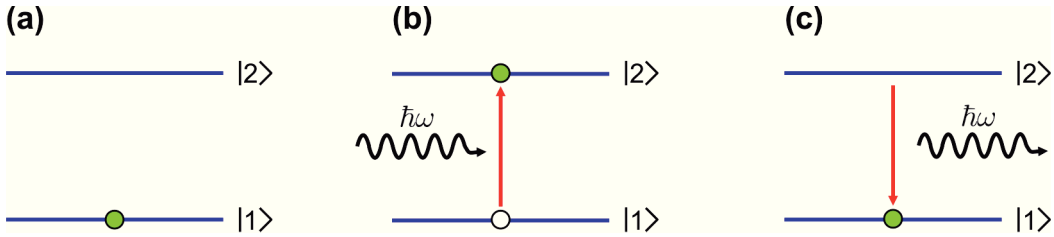

Figure 3.9: Diagram of different states of a two-level system: (a) the electron rests in its ground state $|1\rangle$, (b) an incident photon excites the electron to the upper state $|2\rangle$, (c) the electron relaxes back to its ground state emitting a photon in the process.

In particular, this renders the dipole transition between the heavy-hole (hh2) and the conduction (c1) band forbidden. However, these restrictions only hold true for plane-wave excitation if there is no gradient of the electric field over the width of the quantum well. They can also be excited, if only weakly, owing to tetrahedral symmetry in many real semiconductors.

3.3 Two-Level Systems

To understand optical transitions in a semiconductor it is instructive to limit considerations to only two levels, a ground state $|1\rangle$ with energy E_1 and an excited state $|2\rangle$ with energy $E_2 > E_1$ (compare Fig. 3.9). This approximation is valid for absorption and emission processes in semiconductors as long as they occur at or around the band extrema, where the dispersion of the bands can be neglected; it is relatively accurate for the discrete levels in quantum wells. It does, however, reach its limit at the explanation of gain and lasing because the necessary population inversion cannot be achieved in a two-level system. Still, the formalism of a two-level system can be applied to a gain medium if we introduce an external pump rate, like we do in the toy model described in chapter 5.

3.3.1 Absorption, Spontaneous and Stimulated Emission

In a two-level system a photon can only be absorbed or emitted if the electron "jumps" from one of the levels to the other. The photon is needed to fulfil energy conservation and therefore has to carry an energy $\hbar\omega = E_2 - E_1$ equivalent to the energetic difference of the two levels [25].
If an electron has been excited to the upper level it has the natural tendency to relax back to an energetically more favourable, i.e. lower, state. In the process of jumping from level $|2\rangle$ to level $|1\rangle$ it emits a photon[4]. As this happens without an external stimulus we call it *spontaneous emission* or *luminescence*. The spontaneous emission rate is governed by the Einstein A coefficient and is given by

$$\frac{dN_2}{dt} = -A_{21}N_2, \tag{3.16}$$

[4]The emission of radiation is, of course, not the only way in which an excited system can decay back to its ground state. There are also non-radiative channels allowing for the release of energy, which shall not be described here (compare 2.4.1).

where N_2 is the population of state $|2\rangle$ and A_{21} describes the transition from the upper to the lower level. From this we can deduce the radiative decay rate τ_{rad} for spontaneous emission to be

$$\tau_{\mathrm{rad}} = A_{21}^{-1}. \tag{3.17}$$

The opposite transition, that is the excitation of an electron from the lower to the upper state, cannot occur spontaneously. The electron needs to gain energy from an external field to cross the gap between the two levels. This can be achieved by the *absorption* of a photon. For processes stimulated by an external field the transition rates are described by the Einstein B coefficient. Therefore absorption accompanied by an excitation of the electron from $|1\rangle$ to $|2\rangle$ is described by the following rate equation:

$$\frac{dN_1}{dt} = -B_{12}N_1u(\omega) \tag{3.18}$$

with N_1 being the population of the lower level, B_{12} being the Einstein coefficient for excitation and $u(\omega)$ being the energy density of the external electric field of the incident photon.

However, an external field can not only yield absorption if the electron is in the lower state, it can also stimulate an electron in state $|2\rangle$ to jump down to state $|1\rangle$. For this relaxation the electron needs to release its excess energy and consequently emits another photon. We therefore call this process *stimulated emission*. It can formally be described analogously to absorption with the Einstein coefficient B_{21} for the opposite transition, i.e. from the upper to the lower level:

$$\frac{dN_2}{dt} = -B_{21}N_2u(\omega) \tag{3.19}$$

The three processes of absorption, spontaneous and stimulated emission are not independent and neither are the corresponding Einstein coefficients. The two Einstein B coefficients for absorption and emission are related *via* the degeneracies g_1 and g_2 of the two levels involved

$$g_1B_{12} = g_2B_{21}. \tag{3.20}$$

The relation between the coefficients A_{21} and B_{21}, respectively, governing spontaneous and stimulated emission is given by

$$A_{21} = \frac{2\hbar}{\pi} \cdot \left(\frac{\omega n}{c}\right)^3 B_{21}, \tag{3.21}$$

where c is the speed of light in vacuum and n is the refractive index of the medium. From equations (3.20) and (3.21) we see that the B_{12} coefficient for absorption is directly proportional to the two emission coefficients A_{21} and B_{21}. We can thus conclude that a high absorption coefficient yields a high probability for emission, leading to a short radiative lifetime τ_{rad} (see Eq. (3.17)). This, however, does not mean that the absorption and emission spectra are the same. The spectral shapes cannot be explained by rate equations but by the thermal distribution of the charge carriers in their bands [25]. The absorption spectrum of a quantum well is, for example, a step function (Fig. 3.8) whereas its luminescence spectrum is generally a Lorentzian.

The above relations also contain the reason why a strict two-level system cannot reach population inversion and thus not serve as a gain material. In this case the degeneracies in equation (3.20) are both unity and the two coefficients for absorption and stimulated emission are the same. An incident photon will thus stimulate absorption and emission with equal probability. It is therefore not possible that more electrons are in the upper state $|2\rangle$ than there are in the lower state $|1\rangle$, unless the system is driven coherently.

3.3.2 Optical Bloch Equations

Having introduced the relevant absorption and emission processes, we now take a closer look at the dynamics of a two-level system interacting with an external field $\boldsymbol{E}(\boldsymbol{r}, t)$. We further limit our considerations to fermionic charge carriers (like electrons and holes) in the one-particle approximation and only allow dipolar transitions between the two levels.
These assumptions lead to the following Hamiltonian [64]

$$\mathcal{H} = E_1 c_1^\dagger c_1 + E_2 c_2^\dagger c_2 - \boldsymbol{E}(\boldsymbol{r}, t)\left(d_{21} c_2^\dagger c_1 + d_{21}^* c_1^\dagger c_2\right), \tag{3.22}$$

where E_1 and E_2 are again the energies of the two levels and d_{21} is the dipole matrix element of the transition from level $|2\rangle$ to level $|1\rangle$. We have also introduced the creation operator $c_j^\dagger$ and the annihilation operator c_j, which respectively describe the creation and annihilation of an electron in level $|j\rangle$.

The dynamics of the optical transition amplitudes

$$p_{ij} = \langle c_i^\dagger c_j \rangle \tag{3.23}$$

for a transition from level $|j\rangle$ to $|i\rangle$ and the occupation factor of level $|i\rangle$

$$f_i = \langle c_i^\dagger c_i \rangle \tag{3.24}$$

can then be deduced straightforwardly from the Heisenberg equation of motion, which is given by

$$-i\hbar \frac{\partial}{\partial t}\mathcal{O} = [\mathcal{H}, \mathcal{O}] \tag{3.25}$$

for an arbitrary operator $\mathcal{O}$. If we want to evaluate this equation for the transition amplitudes p_{ij} and the occupation factors f_i, we first solve equation (3.25) for the four creation and annihilation operators with the help of the commutator relation for Fermions

$$\left[c_i, c_j^\dagger\right] = \delta_{ij}. \tag{3.26}$$

Inserting the results into equations (3.23) and (3.24) and employing charge carrier conservation ($f_1 + f_2 = 1$) directly leads to the optical Bloch equations for a fermionic two-level system:

$$-i\hbar \frac{\partial}{\partial t} p_{12} = (E_1 - E_2)\, p_{12} + \boldsymbol{d}_{21}\boldsymbol{E}(\boldsymbol{r}, t)\,(1 - 2f_2) \tag{3.27}$$

and

$$-i\hbar \frac{\partial}{\partial t} f_2 = \boldsymbol{d}_{21}\boldsymbol{E}(\boldsymbol{r}, t) p_{12}^* - \boldsymbol{d}_{21}^*\boldsymbol{E}(\boldsymbol{r}, t) p_{12} \tag{3.28}$$

In order to complete the picture of charge-carrier dynamics in a two-level system we add two phenomenological damping rates [64]: the longitudinal damping Γ for the occupation number f_i describes the relaxation of an initial distribution back to the equilibrium Fermi function. On the other hand, the transverse damping rate γ characterises the damping of the oscillation of the transition amplitude p_{ij}. Introducing these rates into equations (3.27) and (3.28) and some rearrangement yields the final form of the optical Bloch equations

$$-i\hbar\frac{\partial}{\partial t}p_{12} + (E_2 - E_1 + i\hbar\gamma)\, p_{12} = \boldsymbol{d}_{21}\boldsymbol{E}(\boldsymbol{r},t)\,(1-2f_2) \tag{3.29}$$

and

$$-i\hbar\frac{\partial}{\partial t}f_2 - i\hbar\Gamma f_2 = \boldsymbol{d}_{21}\boldsymbol{E}(\boldsymbol{r},t)p_{12}^* - \boldsymbol{d}_{21}^*\boldsymbol{E}(\boldsymbol{r},t)p_{12}. \tag{3.30}$$

Linear Optical Properties

The optical Bloch equations are the equations of motion for the charge carriers in a semiconductor. We should therefore be able to derive the optical properties directly from them in a similar way as we have done in section 2.1. This task is most straightforwardly achieved by rewriting equations (3.27) and (3.28) with the help of the *Bloch vector*

$$\begin{pmatrix} u \\ v \\ w \end{pmatrix} \equiv \begin{pmatrix} 2\mathrm{Re}\,[p_{12}] \\ 2\mathrm{Im}\,[p_{12}] \\ f_2 - f_1 \end{pmatrix}. \tag{3.31}$$

We additionally define the transition frequency $\Omega = \hbar^{-1}\,(E_2 - E_1)$ and the Rabi frequency $\Omega_\mathrm{R}(t) = \hbar^{-1}d_{21}E(t)$ and arrive at the matrix form of the (undamped) optical Bloch equations:

$$\begin{pmatrix} \dot{u} \\ \dot{v} \\ \dot{w} \end{pmatrix} = \begin{pmatrix} 0 & \Omega & 0 \\ -\Omega & 0 & -2\Omega_\mathrm{R}(t) \\ 0 & 2\Omega_\mathrm{R}(t) & 0 \end{pmatrix} \begin{pmatrix} u \\ v \\ w \end{pmatrix}. \tag{3.32}$$

Since we are interested in the linear optical properties we only need to consider the uninverted two-level system, which means the occupation of the upper level is zero ($f_2 = 0$) and therefore $w = -1$. We can now simplify equation (3.32) to

$$\ddot{u} + \Omega^2 u = 2\Omega_\mathrm{R}(t)\Omega. \tag{3.33}$$

This equation is formally equivalent to the equation of motion for the Lorentzian oscillator (compare (2.8)) - in the undamped case - if we interpret $u = x/x_0$ as a relative displacement of the electrons[5] normalised to an arbitrary value x_0. The transition frequency Ω describes the eigenfrequency of the system. Inserting the definition of the dipole matrix element $d_{21} = -e\hbar/\,(2x_0 m_\mathrm{e}\Omega)$, where m_e is the (effective) mass of the electron, we arrive at the well-known equation of motion for a Lorentzian oscillator

$$m_\mathrm{e}\ddot{x} + m_\mathrm{e}\Omega^2 x = -eE(t). \tag{3.34}$$

Starting from this equation we can derive the linear optical properties as we have done in section 2.1.1, which we will not repeat here as the results are already given therein.

[5]Here again, we use electrons as one example of charge carriers in a semiconductor, where the same formalism could be used for holes as well.

3.3.3 Interaction of Emitters and their Environment

Two-level systems describe many types of optical emitters fairly well but this picture only treats them as isolated entities. Their interaction with the surrounding is, however, important for many applications where resonant interaction effects are exploited. Since our investigation of the coupling between a quantum well and a plasmonic metamaterial is a similar problem to the interaction of an emitter with its surroundings, we think it worthwile to revisit two of the most common mechanisms associated with this issue: the Purcell effect and resonant Förster transfer.

The Purcell Effect

The Purcell effect, as originally stated by Edward M. Purcell in 1946, describes the enhancement of the spontaneous decay rate[6] Γ of a single emitter when it is coupled to a resonant cavity [65] with a quality factor Q by the Purcell factor

$$F = \frac{3Q}{4\pi^2 V}\left(\frac{\lambda}{n}\right)^3 \quad \text{with} \quad V = \frac{\int \epsilon |E|^2 d\boldsymbol{r}}{\max\left(\epsilon |E|^2\right)}, \tag{3.35}$$

where V is the effective mode volume in a cavity resonant at wavelength λ with a host medium of refractive index n.
More generally, we can relate the spontaneous decay rate Γ to the local density of photonic states (LDOS) g_L by

$$\Gamma = \frac{\pi p^2 \omega}{3\hbar\epsilon_0} g_\mathrm{L}, \tag{3.36}$$

where p is the dipole moment and ω is the frequency of the optical transition [66]. We can therefore also express the Purcell factor as the enhancement of the LDOS. This is especially important because the conventional Purcell factor defined in equation (3.35) is a disputable quantity if we deal with plasmonic particles instead of dielectric cavities. In the following we discuss some of the concerns raised on this subject [67, 68].

Most obviously, the definition of the mode volume in equation (3.35) presents a problem for plasmonic particles because the energy density $\epsilon |E|^2$ therein becomes negative for metals with $\epsilon < 0$. Stefan A. Maier therefore proposed to redefine the energy density in such a way that it accounts for the energy stored in the metal [67], for instance by $\left(\mathrm{Re}\left[\epsilon\right] + 2\omega \mathrm{Im}\left[\epsilon\right]/\gamma\right)|E|^2$, which remains positive and real [69].
A more general objection to the Purcell factor based on mode volume and quality factor was raised by A. Femius Koenderink [68]. Equation (3.35) can be derived from the more general formulation using the LDOS when we make two assumptions: firstly, that normal modes can be defined and that the LDOS can be expressed as the sum over all normal modes. Secondly, that this sum is dominated by a single term.
For metallic particles, however, both these assumptions do, generally, not hold and the derivation of Eq. (3.35) therefore breaks down. Firstly, dispersive absorbing media usually do not allow for the definition of a set of normal modes. Secondly, even if this expansion can be performed, it is not dominated by a single term, although in many cases the resonance itself results from one term only.

[6] Not to be confused with the longitudinal damping Γ in the previous section.

Whenever we talk about the Purcell effect in this work, we therefore refer to the enhancement of the LDOS and relate changes in decay rate directly to a change in the LDOS.

Förster Transfer

While the Purcell effect deals with the interaction of an emitter and a cavitiy, Förster resonant energy transfer (FRET) describes the non-radiative transfer of energy from one emitter (donor) to another (acceptor) *via* non-radiative dipole-dipole interaction [70].
Suppose a donor in its excited state D^* can be described as a radiating dipole. If we now put an acceptor A in close proximity, the electric field of the donor dipole acts on the electrons of the acceptor and induces a dipole A^*. We can write this as a reaction equation

$$\mathrm{A} + \mathrm{D}^* \rightarrow \mathrm{A}^* + \mathrm{D}$$

that clearly shows the energy transfer from the excited donor to the acceptor.
This energy transfer is mediated by the dipole-dipole interaction without any real photons being transferred from donor to acceptor. Thus the transfer rate Γ_T is proportional to the square of the dipole-dipole interaction potential $V_{\mathrm{dipole-dipole}}$ and consequently proportional to the sixth power of the dipole-dipole separation R:

$$\Gamma_\mathrm{T} \propto \left|V_{\mathrm{dipole-dipole}}\right|^2 \propto \frac{1}{R^6}. \tag{3.37}$$

The overall efficiency of energy transfer E_T can now be expressed as a relation between the transfer rate Γ_T and the relaxation rate Γ_0 of the acceptor without the donor:

$$E_\mathrm{T} = \frac{\Gamma_\mathrm{T}}{\Gamma_\mathrm{T} + \Gamma_0} = 1 - \frac{\Phi_0}{\Phi_\mathrm{F}}. \tag{3.38}$$

Here, we have also rearranged the expression to depend solely on the quantum yields Φ_0 and Φ_F of the acceptor on its own and in the presence of the donor, respectively.

Generally speaking, the Förster transfer is most efficient if two conditions are met [71]: The separation between donor and acceptor should be as small as possible (less than $10\,\mathrm{nm}$) because the dipole interaction is governed by the near fields. Furthermore, there must be sufficient overlap between the emission spectrum of the donor and the absorption spectrum of the acceptor, otherwise energy transfer is not possible at all.

Chapter 4

Experimental and Numerical Methods

Before we turn to the theoretical discussion and the experimental investigation of plasmonic metamaterials coupled to gain media, we first want to introduce the methods we employ for these purposes. We start with the fabrication of our samples. Within the scope of this thesis we concentrate on epitaxially grown single semiconductor quantum wells as gain medium, which we incorporate into the metamaterial system by using them as substrate in our standard fabrication procedure based on electron-beam lithography.
Following this section on fabrication, we present the two measurement setups that have been assembled and are used for characterising our gain materials and for investigating the coupling between plasmonic metamaterials and quantum wells. Here, we also shortly recap the measurement principle of pump-probe spectroscopy, which is the central method we use for studying the coupling behaviour.
Finally, we give a brief introduction to the discontinuous Galerkin time-domain method. This numerical tool is employed to access the near-field distributions created by the plasmonic resonances of the metamaterial, from which we seek to understand details in the coupling mechanism between the metamaterial and the gain substrate.

4.1 Sample Fabrication

Our single quantum wells are specially designed for this thesis and grown using molecular-beam epitaxy by Profs. Galina Khitrova and Hyatt M. Gibbs at the College of Optical Sciences at the University of Arizona. On top of these wafers we fabricate arrays of silver split-ring resonators by a standard electron-beam-lithography process with subsequent metal evaporation and a final lift-off procedure. The principles of both these fabrication steps towards our final samples are described below, together with the special parameters used to arrive at the specific samples shown in this thesis.

4.1.1 Molecular-Beam Epitaxy

Molecular-beam epitaxy (MBE) is a very precise technique for growing thin layers or layered (semiconductor) nanostructures. The molecular (or atomic) beams needed for this method are usually produced in Knudsen cells by thermal evaporation of ultrapure material sources. These beams are introduced into an ultra-high vacuum chamber where they react on the surface of a

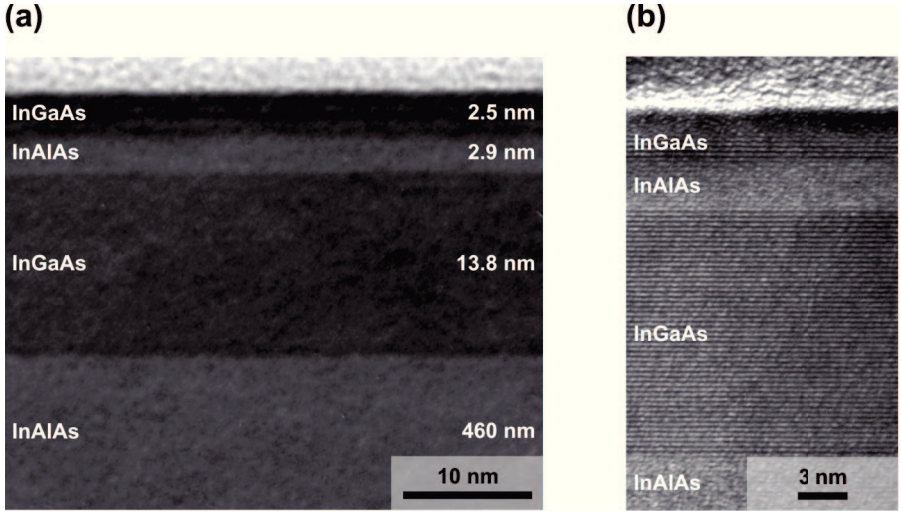

Figure 4.1: (a) TEM image of the HSG 37 InGaAs-quantum well and (b) high-resolution TEM image of the same wafer, indicating the low surface roughness and the smooth layer boundaries. The numbers on the right-hand side of panel (a) give the measured thicknesses of the individual layers.

heated crystalline substrate to form monolayers of the intended material, e.g. doped, ternary or quaternary semiconductors. This allows for controlled growth concerning both the composition and the thickness of the layers.
Such precision is, however, subject to certain preconditions: Achieving pure and clean epilayers is only possible if the concentration of contaminants, mainly residual gases, is as low as possible. To assure this the components of an MBE system are built of materials that show little outgassing and can withstand high temperatures. The latter is neccessary because regular bakeouts are important for the system to remain clean and remove any residual gases from the chamber. Aditionally, we minimise interaction of leftover gas molecules with the substrate by assuring that their mean free path is larger than the complete size of the MBE chamber by establishing ultra-high vacuum conditions.
Having cleared the chamber of all contaminants we still need a means of control to adjust the thickness and the crystal stoichiometry in the intended layer. By opening and closing mechanical shutters to switch the molecular beams on and off we can modulate the relative growth times and thus control the layer thickness to monolayer precision. At the same time this sets the relative amounts of materials in one layer. Still, precise handling of the shutters is only possible if we can monitor the layer thickness and its stoichiometry during growth. Owing to the already established ultra-high vacuum we can use electronic or ionic methods like mass spectroscopy, reflection high-energy electron diffraction or Auger electron spectroscopy [59].

The quantum-well wafer we use for most of this thesis (HSG 37) was grown in a Riber 32P MBE machine. The semi-insulating Fe-doped InP substrate was first heated to $175°\mathrm{C}$ for degassing overnight. Afterwards we heated it to $490°\mathrm{C}$ under an As_4 flux of $1.4 \times 10^{-5}\,\mathrm{Torr}$ and then performed the epitaxy at the same As_4 flux but at slightly lower temperature ($480-485°\mathrm{C}$). The layer structure of InAlAs and InGaAs was grown lattice matched to the InP substrate without interruptions to the following target thicknesses (from substrate to top): $400\,\mathrm{nm}$ $In_{0.52}Al_{0.48}As$ as buffer and lower barrier $12.7\,\mathrm{nm}$ $In_{0.53}Ga_{0.47}As$ for the QW layer, $2.5\,\mathrm{nm}$ $In_{0.52}Al_{0.48}As$ upper barrier followed by a $2.3\,\mathrm{nm}$ thick $In_{0.53}Ga_{0.47}As$ cap layer to prevent oxidation.

Figure 4.1 shows transmission electron microscope (TEM) images of the resulting quantum-well wafer HSG 37. From these we can measure the layers to be slightly thicker than intended; the $In_{0.53}Ga_{0.47}As$ layers are by about 8.7% larger, the $In_{0.52}Al_{0.48}As$ layers by 15%. We can also see the smooth surface, which was measured by atomic-force microscopy to be $0.37\,\mathrm{nm}$ root mean square in the centre of the $51\text{-}\mathrm{mm}$ diameter wafer, and also the smooth interfaces between the individual layers.

4.1.2 Electron-Beam Lithography

For the fabrication of planar nanostructures electron-beam lithography (EBL) is the method of choice because it combines high resolution with high flexibility regarding structure design as long as the structures are essentially two-dimensional. Its superior resolution in comparison to optical lithography results from the much shorter wavelength of the electrons.
To perform electron-beam lithography we need a scanning-electron microscope (SEM) that is equipped with a computer-controlled beam-deflection unit and a beam blanker: in the SEM a beam of electrons from a cathode is accelerated - for lithographic purposes typically between 10 to $100\,\mathrm{kV}$ - and focused onto the image plane.
If we put a resist-covered substrate in the image plane the focused electron beam will expose the resist locally. Finally, the deflection unit and the blanker allow for moving the electron beam along a pre-defined path where the resist will be exposed. We can therefore use the lithography SEM to write almost arbitrary patterns with a resolution of a few nanometers. This limit of EBL resolution is, however, not the spot size we can focus the electron beam to but is rather given by the resist.
After the writing process we develop the sample, making use of the fact that the solubilities of the exposed and the unexposed areas of the resist in a specific developer are significantly different. For a positive-tone photoresist, like the one used for this thesis, the exposed parts are highly soluble whereas the unexposed parts are not. In this case, development leaves a mask of the written pattern which can be used for postprocessing like metallisation.

The nanostructures used for our experiments are all fabricated by the same procedure of electron-beam lithography and subsequent metallisation which is described in detail below. Figure 4.2 illustrates the individual steps of sample fabrication.

Starting from a clean $5\,\mathrm{mm} \times 5\,\mathrm{mm}$ piece of the quantum-well wafer we spin-coat an approximately 200-nm thick layer of the positive-tone photoresist poly-methyl-metacrylate (PMMA[1]) and afterwards remove the remaining solvent by heating the sample to $165^\circ\mathrm{C}$ for at least 30 minutes.
Into this resist layer we write the patterns of our intended nanostructure arrays using a Raith eLine[2] lithography SEM. For the EBL we apply an acceleration voltage of $30\,\mathrm{kV}$ together with a basic area dose of $180\,\mu\mathrm{C/cm^2}$ to write the nanostructures. In order to modify the geometric features of the structures to a certain degree, the actually deposited dose is adjusted to vary from this basic value by up to 25% for every array.
The electron beam has cracked the polymer chains of the PMMA where the resist was exposed

[1] PMMA 950k A4 by MicroChem. Corp., Newton (USA)
[2] Raith GmbH, Dortmund (Germany)

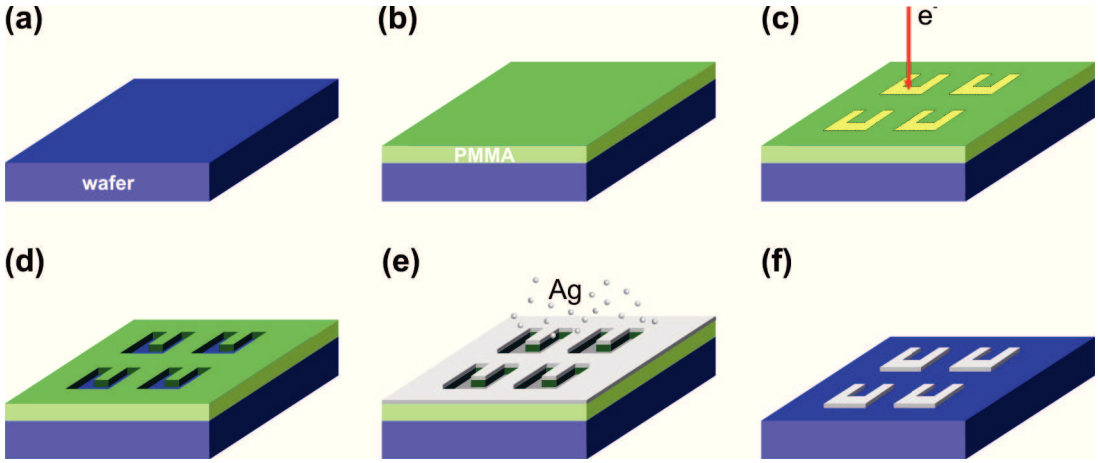

Figure 4.2: Fabrication of SRR arrays: (a) The quantum-well wafer is used as a substrate which is (b) spin-coated with PMMA-resist. (c) SRR arrays are written by electron-beam lithography and (d) developed resulting in a PMMA mask. (e) Onto this we evaporate silver and (f) perform an acetone lift-off leaving behind the silver nanostructures on the wafer.

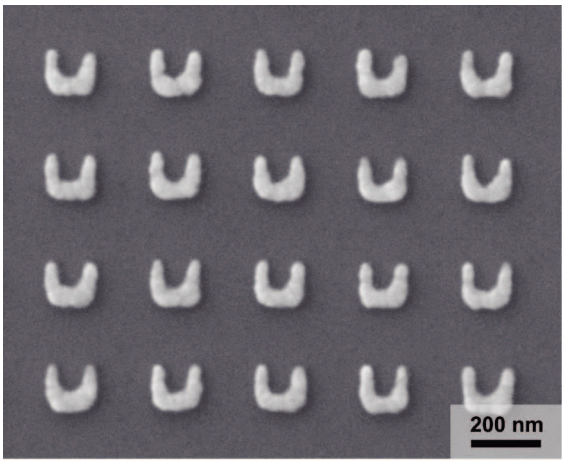

Figure 4.3: Electron micrograph of a typical silver split-ring-resonator array on a quantum-well wafer.

and we develop the sample in a 1:3 mixture of methyl-isobutyl ketone and isopropanole for $8\,\mathrm{s}$ and, additionally, for $20\,\mathrm{s}$ in pure isopropanole. This leaves a negative PMMA structure of our sample design, which we can use for metallisation.
Under vacuum conditions (pressures below $2 \times 10^{-6}\,\mathrm{mbar}$) we apply $\sim 30\,\mathrm{nm}$ of silver onto the sample by electron-beam evaporation. Finally, we perform a lift-off in hot ($65°\mathrm{C}$) acetone to remove excess metal and obtain a sample with arrays of silver nanostructures on top of the quantum-well wafer. An example of the resulting metal structures is shown in Fig. 4.3.

To adjust the separation of the quantum well from the surface for the samples discussed in section 7 we completely cover the piece of wafer with an additional layer of magnesium flouride before it is coated with resist. Like the metallisation, this is done by electron-beam evaporation where the thickness of the layers can easily be varied by only a few nanometers.

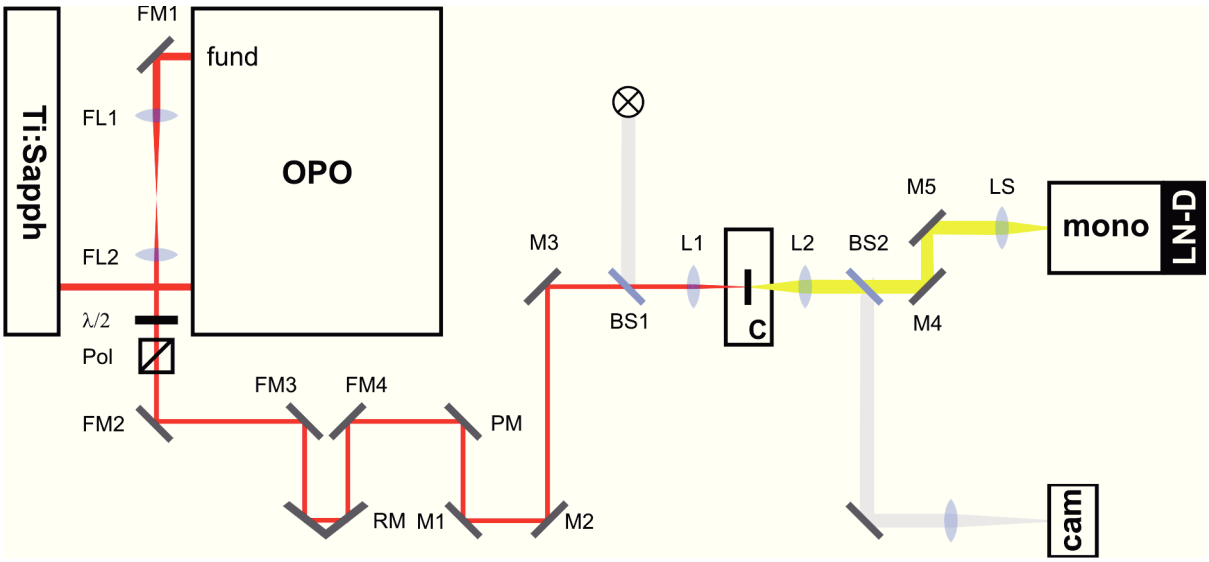

Figure 4.4: Diagram of the low-temperature photoluminescence setup. Note, that many components are only present in the setup because the same laser system is used for pump-probe spectroscopy as well.

4.2 Measurements

In this thesis we use standard linear spectroscopy, more precisely a fourier-transform spectrometer[3], only to pre-characterise our samples, which is not explicitly described here. To investigate the coupling of a plasmonic metamaterial with the gain of a quantum-well we employ measurement techniques where the active material is pumped and we then detect its emission properties. For all experiments we cool the samples to less than $10\,\mathrm{K}$ to minimise thermal effects and to provide maximum gain from the quantum wells.

4.2.1 Photoluminescence Spectroscopy

Photoluminescence (PL) is the spontaneous emission from an active material after excitation with an optical source (compare section 3.3.1). In our measurement setup (see Fig. 4.4) this source is a mode-locked titanium:sapphire oscillator[4] with a repetition rate of $81\,\mathrm{MHz}$ and a pulse length of $150\,\mathrm{fs}$; its output wavelength is set to $810\,\mathrm{nm}$. In the standard configuration we only use a maximum of $200\,\mathrm{mW}$ of the original $2.1\,\mathrm{W}$ average output power because we derive our pump beam from the backreflection from the optical parametric oscillator (OPO; we do this for practical reasons because the same laser system is also used for pump-probe spectroscopy (see section 4.2.2)).
To continuously adjust the pump power for the PL measurements we use a combination of a half-wave plate and a linear polariser. We also reduce the diameter of the laser beam[5] with a system of two lenses (FL1 and FL2) whose focal lengths are $f = 150\,\mathrm{mm}$ and $f = 50\,\mathrm{mm}$,

[3]Equinox 55 by Bruker Optics GmbH, Ettlingen (Germany)
[4]Tsunami by Spectra-Physics GmbH, Darmstadt (Germany)
[5]This is not essential for the PL measurements but for pump-probe spectroscopy (see 4.2.2) for which the same laser system and components are used.

respectively. The pump beam is then focused onto the sample by a 50-mm lens (L1) resulting in a pump spot of $\sim 20\,\mu\text{m}$ diameter. The sample itself is kept in a helium-flow cryostat[6] (C) and cooled to $T_{\text{sample}} < 10\,\text{K}$.
We collect the photoluminescence in forward direction with a second identical 50-mm lens (L2) and eventually send it into a spectrometer[7] (mono) equipped with a 150-lines-per-cm grating optimised for $1200\,\text{nm}$. A liquid-nitrogen-cooled InGaAs array[8] (LN-D) is mounted on the exit port of the spectrometer as a detector. We can thus take a complete spectrum over a spectral range of roughly $200\,\text{nm}$ in one run.
The setup is further equipped with an imaging arm to control the position of the pump spot on the sample with the help of a PbS-CCD camera[9] working in the near infrared.

Photoluminescence measurements offer a fast way to investigate active samples but for the combined system of a metamaterial on a quantum film the results proved to be uninstructive. We have therefore discontinued the use of PL spectroscopy for this purpose and have limited the approach to the characterisation of the bare quantum-well wafers and their emission properties.

4.2.2 Pump-Probe Spectroscopy

Our discussion of the two-level system (section 3.3) has already shown that the optical properties of such systems depend on their inversion state described by the inversion factor $f_2 - f_1$ or simply by the occupation factor f_2 of the upper state. In a pump-probe experiment we can directly measure the resulting change in transmittance or reflectance - depending on the experimental setup:
We hit a sample with a pump beam whose energy suffices to lift electrons to an excited state leading to a population of the upper state ($f_2 > 0$) resulting in altered optical properties. If then a second beam (the probe) hits the excited sample a different proportion of the light is transmitted than for the unpumped case. By employing a lock-in technique we can directly measure the often relatively small change ΔT of transmittance induced by the pump.
If we now delay the arrival of the probe beam by a time interval Δt compared to the pump beam we allow the charge carriers to relax back to the ground state in the meantime. Consequently, we detect less change in transmittance because the system is in a less strongly inverted state. By continuously varying the time delay Δt we can thus monitor the relaxation behaviour of the charge carriers involved.
For negative time delays, when the probe hits the sample before the pump, we expect no pump-probe signal because all electrons are still in their ground state. In practice, however, we always see a background signal stemming from photoluminescence which occurs independently from the probe.

The centre piece of our pump-probe setup (Fig. 4.5) is an optical parametric oscillator[10] (OPO) from which we derive both the pump and the probe beam. We use the backreflection off the OPO crystal to pump our samples; the crystal reflects approximately $200\,\text{mW}$ average power of

[6] CryoVac, Troisdorf (Germany)
[7] HR 460 by Jobin Yvon GmbH, Grasbrunn (Germany)
[8] OMA V by Roper Scientific GmbH, Trenton (USA)
[9] IR Vidikon by Hamamatsu, Hersching (Germany)
[10] Opal by Spectra-Physics GmbH, Darmstadt (Germany)

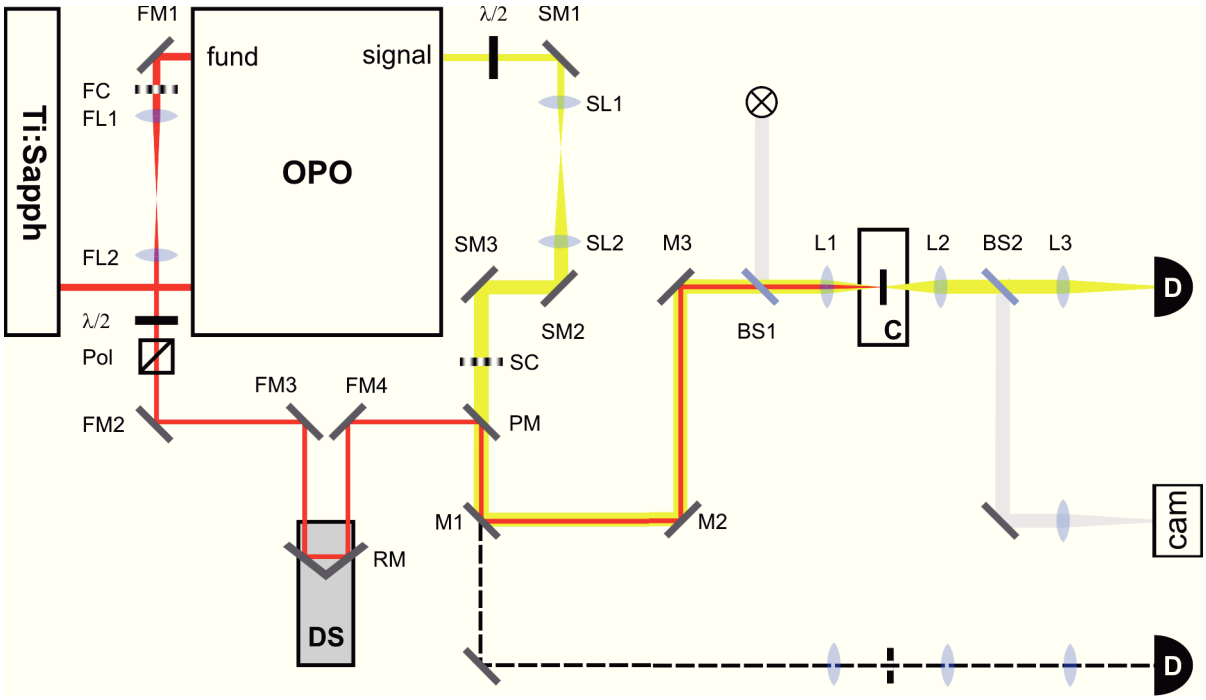

Figure 4.5: Diagram of the pump-probe setup that was assembled and used for this thesis. The 810 nm-pump beam is derived from the ti:sapphire backreflection off the OPO crystal, the probe beam is the OPO's signal and can be tuned between roughly 1.4 µm and 1.6 µm.

the pump laser which is a mode-locked titanium:sapphire oscillator[11] with a repetition rate of 81 MHz at a centre wavelength of 810 nm with a pulse duration of 150 fs and a beam diameter of 2 mm. If necessary, the pump beam power can be freely attenuated with a combination of a half-wave plate ($\lambda/2$) and a linear polariser (Pol). In order to ensure a sufficiently large pump spot on the sample the pump beam passes through two lenses (FL1 and FL2) with focal lengths of $f = 150\,\mathrm{mm}$ and $f = 50\,\mathrm{mm}$, respectively, by which the beam diameter is reduced. It then hits a retro reflector (RM) mounted on a motorised delay line (DS) with a travel range of 4 cm before it is combined with the probe beam at the pick-up mirror (PM) which reflects the pump wavelength but allows the probe to pass through.
The signal output of the OPO, tunable between 1.4 µm and 1.6 µm, serves as the probe in our setup. As continuous tuning of the probe power is not necessary we attenuate it to the desired value of $\sim 70\,\mu\mathrm{W}$ with a set of neutral-density filters. The probe beam passes through a telescope (SL1 and SL2) consisting of an $f = 25\,\mathrm{mm}$ lens and an $f = 100\,\mathrm{mm}$ lens, by which the beam is expanded before it reaches the pick-up mirror (PM) where it meets the pump beam. The probe polarisation can be turned with a half-wave plate ($\lambda/2$) inserted into the beam if necessary.

The two arms of the setup have to be adjusted in such a way that both pump and probe have travelled the same distance from the OPO crystal when they reach the pick-up mirror and the delay stage is set to its $\Delta t = 0$ position. From this point on they are guided colinearly and focused with an $f = 50\,\mathrm{mm}$-lens onto the sample which is cooled to $T_{\mathrm{sample}} < 10\,\mathrm{K}$

[11] Tsunami by Spectra-Physics GmbH, Darmstadt (Germany)

in a helium-flow cryostat[12] (C). The spot sizes on the sample are $20\,\mu\mathrm{m}$ for the pump and $10\,\mu\mathrm{m}$ for the probe spot. This ratio is necessary to ensure the probed part of the sample to be homogeneously pumped.
We collect the transmitted light with an $f = 50\,\mathrm{mm}$-lens (L2), filter the remaining pump light (most of it is already absorbed by the InP substrate) and image (L3, $f = 100\,\mathrm{mm}$) the remaining probe onto a germanium diode (D). The transmittance change ΔT resulting from the pump is directly measured with a lock-in technique when the pump beam is chopped (i.e. blocked and unblocked) at $400\,\mathrm{Hz}$ frequency. In much the same way we can record the reference, i.e. the transmittance of the probe without the pump, by blocking the pump beam, modulating the probe beam and measuring the lock-in signal thereof.
Finally, the temporal information results from stepping the motorised delay line and recording the pump-probe signal ΔT with respect to its position. We usually record 100 steps over a travel range of $3\,\mathrm{cm}$ in a double-pass geometry, resulting in a time-delay window of $200\,\mathrm{ps}$ and a temporal resolution of $2\,\mathrm{ps}$.

In order to ensure spatial overlap of the two beams we can use an alignment arm (dashed beam path in Fig. 4.5) equipped with the same set of lenses as L1 and L2 and a $25\,\mu\mathrm{m}$ pinhole in the focal plane through which both beams have to be focused. We also use this arm to check the alignment of the delay line by comparing the signal transmitted through the pinhole over the whole travel range of the stage. During measurements we monitor the position of both beams on the sample with a PbS-CCD camera[13] (cam).

4.3 Numerical Calculations

To obtain a theoretical understanding of the coupling mechanism between metamaterial and quantum well we need information about the three-dimensional field distributions around the metal nanostructures, which are not accessible from our experiments. We therefore rely on numerical simulations of the field distributions. These calculations are performed by Michael König in the group of Prof. Kurt Busch at Karlsruhe Institute of Technology and are based on the discontinuous Galerkin time-domain method.
We give a brief introduction to this method below. In our reasoning we follow a related review by Kurt Busch *et al.* [72] and refer to this article and the references therein for a more detailled description of the method.

4.3.1 Discontinuous Galerkin Time-Domain Method

To numerically solve nanophotonic problems we can usually stick to a classical description of the electromagnetic fields given by Maxwell's equations. Numerous methods exist for this task but two of them are most notable because they are most flexible: these are the finite difference time-domain method (FDTD) and the finite element method (FEM).
The former is a fast time-domain approach, which allows for calculating a whole spectrum in one simulation by exciting the system with a short - thus spectrally broad - pulse instead of a

[12] CryoVac, Troisdorf (Germany)
[13] IR Vidikon 2741 by Hamamatsu, Hersching (Germany)

plane wave. The speed of FDTD, however, is the result of a rather simple stepping algorithm that relies on the rigid, rectangular Yee grid. This turns spatial discretisation into a problem if objects are not parallel to the grid axes and can lead to slow convergence and staircasing effects which are especially relevant for metallic nanostructures.
Finite element methods, on the other hand, allow efficient discretisation of almost arbitrary geometries by a flexible, unstructured mesh. The electromagnetic field is formulated for each individual element and every element is in turn coupled to its neighbours, leading to a sparse system of linear equations, which is then solved. However, FEM is a frequency-based method. We therefore need to solve this system of equations for a series of frequencies if we want to obtain a spectrum that can be compared with measurements. It is thus often slower and computationally more costly than a comparable FDTD calculation.

The discontinuous Galerkin time-domain method (DGTD) essentially combines the advantages of both approaches resulting in a versatile and efficient simulation technique for nanophotonic problems. Like in FEM we divide the computational domain into a set of elements that can be of arbitrary shape but for three-dimensional calculations are often chosen to be tetrahedral. On each of these elements we expand the electromagnetic fields in terms of a set of basis functions. In case of DG(TD) these basis functions are restricted to one specific element and strictly zero on all others - hence the *discontinuous* in DGTD. This allows for an individual treatment of the linear algebra on each element and therefore reduces computational cost. In the end, we have to combine all elements by reintroducing coupling between neighbouring elements again. We achieve this by the concept of numerical flux and by modifying the physical equations on each element to incorporate the continuity conditions from Maxwell's equations. Note, that the necessary modifications depend on the fields on neighbouring elements.
We start from Maxwell's curl equations

$$\begin{aligned} \epsilon(\boldsymbol{r}) \cdot \partial_t \boldsymbol{E}(\boldsymbol{r},t) &= \nabla \times \boldsymbol{H}(\boldsymbol{r},t) \\ \mu(\boldsymbol{r}) \cdot \partial_t \boldsymbol{H}(\boldsymbol{r},t) &= -\nabla \times \boldsymbol{E}(\boldsymbol{r},t) \end{aligned} \tag{4.1}$$

where we have absorbed ϵ_0 and μ_0 into the fields to have dimensionless units. Employing the discontinuous Galerkin procedure to discretise the electromagnetic fields in space, we find a system of coupled, first-order ordinary differential equations for the expansion coefficients of the electromagnetic field:

$$\partial_t \begin{pmatrix} \tilde{\boldsymbol{E}}(t) \\ \tilde{\boldsymbol{H}}(t) \end{pmatrix} = \mathcal{H} \cdot \begin{pmatrix} \tilde{\boldsymbol{E}}(t) \\ \tilde{\boldsymbol{H}}(t) \end{pmatrix} + \begin{pmatrix} \tilde{\boldsymbol{E}}^{source}(t) \\ \tilde{\boldsymbol{H}}^{source}(t) \end{pmatrix}, \tag{4.2}$$

where $\mathcal{H}$ is the explicitly known system operator acting on the current expansion coefficients and where source terms have been included.
Having accomplished the spatial discretisation of our problem, we need to find a time stepping scheme for the time-domain. For DGTD the algorithm of choice are low-storage Runge-Kutta methods because they are comparable in accuracy to the spatial discretisation and because they are storage-efficient. To obtain spectral information from DGTD calculations, we again do not repeat the whole procedure for a set of plane waves at discrete frequencies but rather use an ultra-short excitation pulse and thus draw a complete spectrum from a single run.

In conclusion, the discontinuous Galerkin time-domain method is well-suited to problems in nanophotonics and is therefore employed to determine the plasmonic near-field distribution

of split-ring resonator arrays. Using DGTD we can perform these calculations of the real geometry of the structures, including the rounded edges, and do not run into problems with the discretisation of the high-index substrates. Still, the calculations can be completed in a reasonable amount of time.

Chapter 5

Toy Model for a Plasmonic Resonance Coupled to a Two-Level System

A coupled system never behaves like the simple sum of its parts. This is impressively demonstrated by the beating of two coupled pendula. Depending on the initial conditions, they each change their amplitude and oscillation frequency in such a way that a naive observer of only one pendulum would likely not perceive it as a harmonic oscillator.
When dealing with coupled systems it is therefore always desirable to have a theoretical model of the system which helps to predict and understand its often complicated and unexpected behaviour. Such a model can also give insight into the important parameters driving the system to one response or another.
Many theoretical studies of the coupled metamaterial-with-gain system rely on numerical calculations [13, 20, 23] and use some model (e.g. a four-level system) for the gain medium involved. Apart from the high computational cost of this time-consuming approach, it also calls for an exact implementation of the plasmonic structure. Although such a treatment can help to understand particular experiments or test their feasibility in advance, we can hardly draw general conclusions from it.
We therefore propose a simple but general toy model of a plasmonic resonance coupled to the gain resonance of a two-level system, which is the appropriate equivalent to the coupled-oscillator model. The key difference, however, is the fact that our toy model deals with two different kinds of resonances: a bosonic plasmon resonance and a fermionic gain resonance of an inverted two-level system [49].

The present chapter gives an overview of this toy model and over the main conclusions we can draw from it. We start with the definition of the model, leading to a set of equations resembling the optical Bloch equations (compare 3.3.2). From these we derive linear spectra for fixed inversion of the two-level system and preview what kind of response we expect from the pump-probe measurements presented in the following chapters. Finally, we review the limits of this simple model, in the course of which we briefly investigate in how far this model is capable of reproducing lasing (or rather spasing) predicted for a plasmon-and-gain system [20, 23].

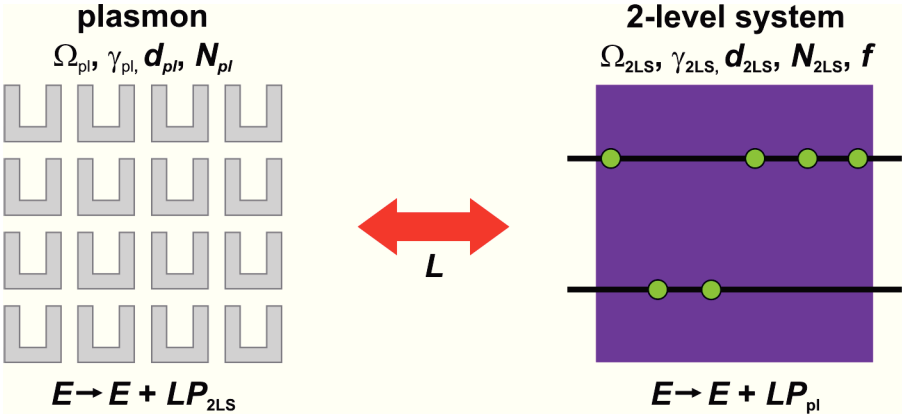

Figure 5.1: Illustration of the toy model: a plasmonic resonance (SRR array on the left) with resonance frequency Ω_{pl}, damping frequency γ_{pl}, dipole matrix element d_{pl} and dipole density N_{pl} is coupled to a two-level system (on the right) with resonance frequency Ω_{2LS}, damping frequency γ_{2LS}, dipole matrix element d_{2LS} and dipole density N_{2LS} with an inversion factor f. The coupling is described by a phenomenological parameter L.

5.1 Definition

To arrive at a general toy model for a particle plasmon coupled to gain we first have to simplify the description of both constituents based on their resonant behaviour:
The plasmonic resonance, which is a Lorentzian, is characterised by its lineshape *via* the centre frequency Ω_{pl} and the spectral width correlated with the damping frequency γ_{pl} and a dipole matrix element d_{pl} of the oscillation. Furthermore, we can describe the bosonic system by its transition amplitude p_{pl}. Knowing the volume density of plasmonic resonators N_{pl} in our sample, we can calculate the macroscopic polarisation P_{pl} as the product of the latter three quantities: $P_{\mathrm{pl}} = N_{\mathrm{pl}} d_{\mathrm{pl}} p_{\mathrm{pl}} + \mathrm{c.c.}$, where c.c. denotes the complex conjugate of the first term.
The two-level system (2LS) gain resonance is described by a fermionic mode with centre frequency Ω_{2LS} and transverse damping frequency γ_{2LS}. The dipole matrix element d_{2LS} and the transition amplitude p_{2LS} characterise the transition, and the occupation factor f of the upper level quantifies the state of inversion of the system. We further introduce the longitudinal damping Γ_{2LS} which determines the relaxation of the two-level inversion. Again, the macroscopic polarisation $P_{\mathrm{2LS}} = N_{\mathrm{2LS}} d_{\mathrm{2LS}} p_{\mathrm{2LS}} + \mathrm{c.c.}$ can be calculated with the help of the volume density of oscillators N_{2LS} in the gain material.

As sketched in figure 5.1 the coupling between the plasmonic resonance and the gain resonance is defined by a phenomenological parameter L. We model the coupling by the interaction of the (evanescent) near fields, which modify the local electric field [1]:
We first consider the local field of the two-level system. For the isolated system this is given by the external electric field

$$E(t) = \tilde{E}\cos(\omega t) = \frac{\tilde{E}}{2}\left(\mathrm{e}^{-i\omega t} + \mathrm{c.c.}\right). \tag{5.1}$$

To account for the influence of the plasmonic near-field we have to introduce an additional term consisting of the (macroscopic) polarisation of the plasmon P_{pl} times the phenomenological

[1] For the sake of simplicity, we omit any vectorial properties of the electric field and all other quantities here.

coupling parameter L

$$E \to E + LP_{\mathrm{pl}}. \tag{5.2}$$

The same reasoning leads to an equivalent alteration of the local field for the plasmon by the near field of the two-level system

$$E \to E + LP_{\mathrm{2LS}}. \tag{5.3}$$

In section 3.3.2 we have already derived the optical Bloch equations (3.29) and (3.30) as the equations of motion for a fermionic two-level system. We can use the same formal result for the bosonic plasmon mode if we remove the Fermi blocking factor $(1-2f)$; for this case the second Bloch equation is not relevant because the inversion of the bosonic system is zero. This leads to the following three equations

$$\begin{aligned}
\dot{p}_{\mathrm{2LS}} + \left(i\Omega_{\mathrm{2LS}} + \gamma_{\mathrm{2LS}}\right) p_{\mathrm{2LS}} &= i\hbar^{-1} d_{\mathrm{2LS}} E \left(1-2f\right) && (5.4)\\
\dot{p}_{\mathrm{pl}} + \left(i\Omega_{\mathrm{pl}} + \gamma_{\mathrm{pl}}\right) p_{\mathrm{pl}} &= i\hbar^{-1} d_{\mathrm{pl}} E && (5.5)\\
\dot{f} + \Gamma_{\mathrm{2LS}} f &= i\hbar^{-1} \left(p^*_{\mathrm{2LS}} d_{\mathrm{2LS}} E - p_{\mathrm{2LS}} d^*_{\mathrm{2LS}} E^*\right). && (5.6)
\end{aligned}$$

Within the toy model the electric fields need to be modified according to equations (5.2) and (5.3) to account for the near-field coupling between the plasmon and the gain mode. We thus arrive at the defining equations of the model:

$$\begin{aligned}
\dot{p}_{\mathrm{2LS}} + \left(i\Omega_{\mathrm{2LS}} + \gamma_{\mathrm{2LS}}\right) p_{\mathrm{2LS}} &= i\left[\hbar^{-1} d_{\mathrm{2LS}} E + V_{\mathrm{2LS}} p_{\mathrm{pl}}\right] \left(1-2f\right) && (5.7)\\
\dot{p}_{\mathrm{pl}} + \left(i\Omega_{\mathrm{pl}} + \gamma_{\mathrm{pl}}\right) p_{\mathrm{pl}} &= i\left[\hbar^{-1} d_{\mathrm{pl}} E + V_{\mathrm{pl}} p_{\mathrm{2LS}}\right] && (5.8)\\
\dot{f} + \Gamma_{\mathrm{2LS}} f &= i\left[p^*_{\mathrm{2LS}} \left(\hbar^{-1} d_{\mathrm{2LS}} E + V_{\mathrm{2LS}} p_{\mathrm{pl}}\right) - \mathrm{c.c.}\right]. && (5.9)
\end{aligned}$$

To simplify notation we have introduced the coupling frequencies

$$V_{\mathrm{2LS}} = \hbar^{-1} d_{\mathrm{2LS}} L N_{\mathrm{pl}} d_{\mathrm{pl}} \quad \text{and} \quad V_{\mathrm{pl}} = \hbar^{-1} d_{\mathrm{pl}} L N_{\mathrm{2LS}} d_{\mathrm{2LS}}. \tag{5.10}$$

Toy Model in the Rotating-Wave Approximation

For resonant experimental situations we can further simplify the above result using the well-known rotating-wave approximation (RWA). Here, the fast oscillating non-resonant term is neglected as it almost averages out to zero [58], justifying a harmonic *ansatz* for the electric field

$$E(t) = \frac{\tilde{E}}{2}\left(\mathrm{e}^{-i\omega t} + c.c.\right) \tag{5.11}$$

and for the complex transition amplitudes

$$p_{\mathrm{2LS}} = \tilde{p}_{\mathrm{2LS}} \cdot \mathrm{e}^{-i\omega t} \quad \text{and} \quad p_{\mathrm{pl}} = \tilde{p}_{\mathrm{pl}} \cdot \mathrm{e}^{-i\omega t}. \tag{5.12}$$

In this way we can rewrite the defining equations of the toy model as follows:

$$\begin{aligned}
i\left(\Omega_{\mathrm{2LS}} - \omega\right) \tilde{p}_{\mathrm{2LS}} + \gamma_{\mathrm{2LS}} \tilde{p}_{\mathrm{2LS}} &= i\left[\hbar^{-1} d_{\mathrm{2LS}} \frac{\tilde{E}}{2} + V_{\mathrm{2LS}} \tilde{p}_{\mathrm{pl}}\right] \left(1-2f\right) && (5.13)\\
i\left(\Omega_{\mathrm{pl}} - \omega\right) \tilde{p}_{\mathrm{pl}} + \gamma_{\mathrm{pl}} \tilde{p}_{\mathrm{pl}} &= i\left[\hbar^{-1} d_{\mathrm{pl}} \frac{\tilde{E}}{2} + V_{\mathrm{pl}} \tilde{p}_{\mathrm{2LS}}\right] && (5.14)\\
\dot{f} + \Gamma_{\mathrm{2LS}} f &= i\left[\tilde{p}^*_{\mathrm{2LS}} \left(d_{\mathrm{2LS}} \frac{\tilde{E}}{2} + V_{\mathrm{2LS}} \tilde{p}_{\mathrm{pl}}\right) - c.c.\right]. && (5.15)
\end{aligned}$$

5.2 Analytical Solution for Fixed Inversion

The pump-probe measurements we show in the following chapters present the special case of a coherently driven system under transient conditions, which can be described by a fixed and given population inversion f of the two-level system[2].
We therefore limit our considerations to a constant inversion f and to situations where the RWA is valid. In this case we can analytically solve equations (5.13) and (5.14). The transition amplitudes then follow as

$$\tilde{p}_{\mathrm{2LS}} = \frac{(1-2f)\left[\hbar^{-1} d_{\mathrm{2LS}} \frac{\tilde{E}}{2} + \frac{\hbar^{-1} V_{\mathrm{2LS}} d_{\mathrm{pl}} \frac{\tilde{E}}{2}}{\left(\Omega_{\mathrm{pl}} - \omega\right) - i\gamma_{\mathrm{pl}}}\right]}{(\Omega_{\mathrm{2LS}} - \omega) - i\gamma_{\mathrm{2LS}} - (1-2f)\,\frac{V_{\mathrm{pl}} V_{\mathrm{2LS}}}{\left(\Omega_{\mathrm{pl}} - \omega\right) - i\gamma_{\mathrm{pl}}}} \tag{5.16}$$

for the two-level-gain resonance and

$$\tilde{p}_{\mathrm{pl}} = \frac{\hbar^{-1} d_{\mathrm{pl}} \frac{\tilde{E}}{2} + V_{\mathrm{pl}} \tilde{p}_{\mathrm{2LS}}}{(\Omega_{\mathrm{pl}} - \omega) - i\gamma_{\mathrm{pl}}} \tag{5.17}$$

for the plasmon resonance.

Although these are solutions for a special case they are well suited to illustrate some aspects of the behaviour of a coupled plasmon-and-gain system. Both $\tilde{p}_{\mathrm{2LS}}$ and $\tilde{p}_{\mathrm{pl}}$ do not only depend on the quantities describing either the two-level-system gain or the plasmon resonance but on a mixture of both. It is therefore no longer appropriate to consider the two as separate resonances but rather as one combined mode, unless the coupling factor L is strictly zero.
We further expect complicated spectra to be derived from equations (5.16) and (5.17), which - in general - are not simply Lorentzian. A sure sign of this is the denominator of (5.16) which leads to the general resonance in $\tilde{p}_{\mathrm{2LS}}$ but has a resonance itself.

In the following we derive linear spectra from equations (5.16) and (5.17) and study the influence that the parameters entering the toy model have on the spectra. We choose to do this for three experimentally relevant parameters, namely the occupation factor f, the coupling strength described by L and the spectral detuning between the two resonances.

5.2.1 Linear Spectra

If we want to extract linear transmittance spectra from the above transition amplitudes we first need to calculate the macroscopic polarisations

$$P_{\mathrm{2LS}} = N_{\mathrm{2LS}} d_{\mathrm{2LS}} p_{\mathrm{2LS}} + \mathrm{c.c.} \quad P_{\mathrm{pl}} = N_{\mathrm{pl}} d_{\mathrm{pl}} p_{\mathrm{pl}} + \mathrm{c.c.} \tag{5.18}$$

from them. These translate into complex refractive indices for the two layers *via* equation (2.2) and (2.3). Although we essentially deal with one coupled resonance, as we have stated

[2] At this point we must note that a strict two-level system cannot reach inversion factors greater than $f = 0.5$ for steady-state conditions. We resolve this restriction by imagining the gain medium to be pumped *via* additional levels, which are not explicitly treated within the toy model.

above, the toy model still assigns two separate refractive indices n_{2LS} and n_{pl} to the two layers, representing the gain layer influenced by the plasmon and the nanostructure layer influenced by the gain medium.
We thus arrive at a multilayer system for which the transmittance can be extracted in several ways: We can either follow an effective-medium approach described by Maxwell-Garnett theory [73, 74] where the whole sample is described as one slab; or we can calculate the transmittance spectrum from a transfer-matrix algorithm [26], retaining the layer structure of our sample.

In the Maxwell-Garnett effective-medium approach we calculate a single polarisation P for the complete slab by weighting the separate polarisations P_{2LS} and P_{pl} with the relative thickness of the respective layer:

$$P = \frac{l_{\mathrm{2LS}}}{l_{\mathrm{2LS}} + l_{\mathrm{pl}}} P_{\mathrm{2LS}} + \frac{l_{\mathrm{pl}}}{l_{\mathrm{2LS}} + l_{\mathrm{pl}}} P_{\mathrm{pl}}, \tag{5.19}$$

where the absolute thickness of the layers is given by l_{2LS} and l_{pl}. Employing equations (2.2) and (2.3) we can calculate the effective refractive index n of this layer and then calculate the amplitude transmission coefficient t of the slab with the help of the Airy formula [26]

$$t = \frac{4n \cdot e^{i\delta/2}}{(n+1)^2 - (n-1)^2 \cdot e^{i\delta}}. \tag{5.20}$$

Here, $\delta = 2nl\frac{\omega}{c}$ denotes the phase delay caused by the transition through the slab. Knowing the surrounding media of the effective slab, this value translates into the intensity transmittance T and we can calculate effective transmittance spectra.

For the transfer-matrix approach we first calculate the two refractive indices n_{2LS} and n_{pl} of the two layers by way of equations (2.2) and (2.3) and insert these into the matrices $M_{\mathrm{pr}}(n)$ describing the propagation through a homogeneous slab with refractive index n and $M_{\mathrm{tr}}(n_1, n_2)$ accounting for the transition from one layer with refractive index n_1 to another with index n_2. The propagation and transition matrices are given by

$$M_{\mathrm{pr}}(n) = \begin{pmatrix} e^{i\delta} & 0 \\ 0 & e^{i\delta} \end{pmatrix} \quad \text{and} \quad M_{\mathrm{tr}}(n_1, n_2) = \begin{pmatrix} n_1 + n_2 & n_2 - n_1 \\ n_2 - n_1 & n_1 - n_2 \end{pmatrix}, \tag{5.21}$$

where the phase delay is again $\delta = 2nl\frac{\omega}{c}$ if l is the layer thickness.
We can calculate the complete matrix of the transmission through a layered stack by sequentially multiplying the matrices for transition and propagation with the correct refractive indices for the individual layers. The resulting matrix TM consists only of combinations of the amplitude transmission coefficients t_{b}, t_{f} in forward and backward direction and the amplitude reflection coefficient r_{b}.

$$TM = \frac{1}{t_{\mathrm{b}}} \begin{pmatrix} t_{\mathrm{f}} t_{\mathrm{b}} - r_{\mathrm{f}} r_{\mathrm{b}} & r_{\mathrm{b}} \\ -r_{\mathrm{b}} & 1 \end{pmatrix} \tag{5.22}$$

Therefore the matrix TM contains all necessary information we need to calculate linear transmittance (or reflectance) spectra.

In figure 5.2 we present a comparison of the transmittance spectra calculated from the toy model *via* the two approaches described above. We have chosen the parameters that enter the model

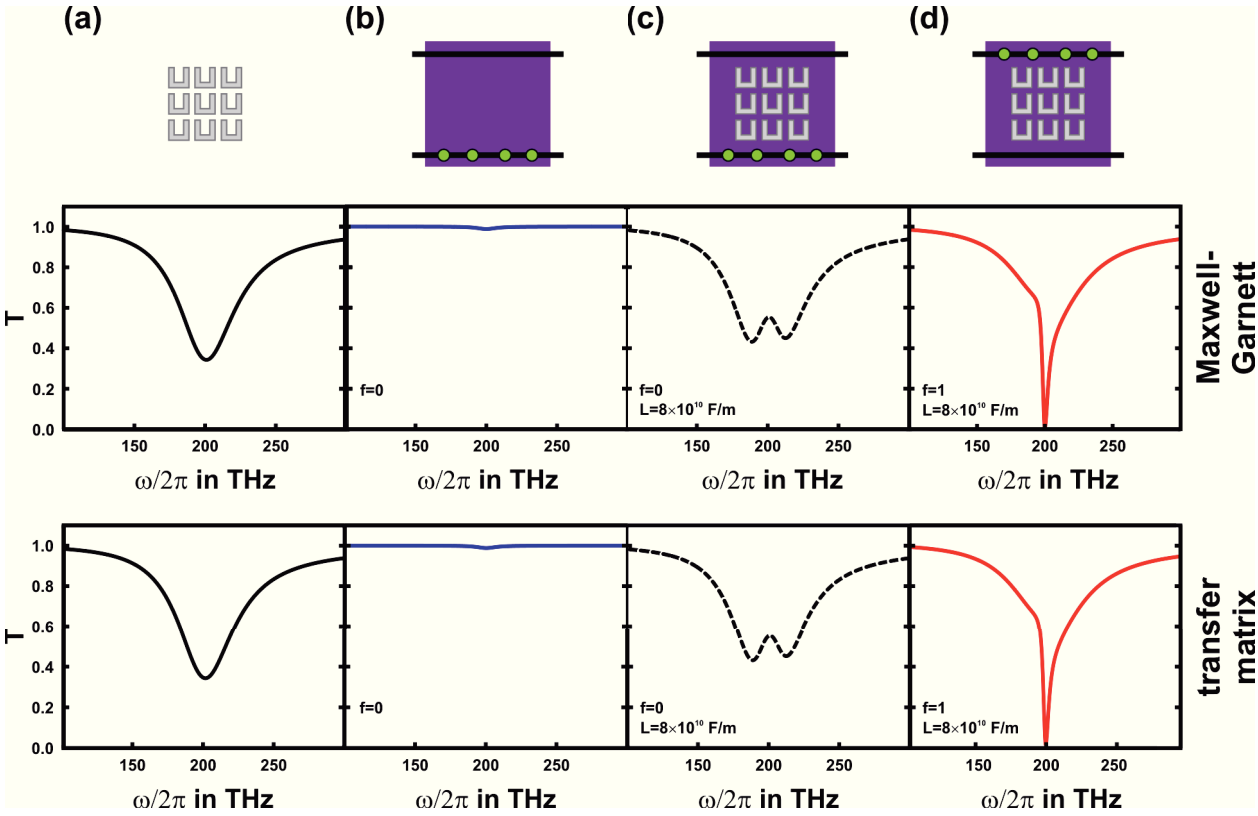

Figure 5.2: Comparison of transmittance spectra calculated from the toy model with either a Maxwell-Garnett effective-medium approach (upper row) or a transfer-matrix formalism (lower row): column (a) shows the spectra for the plasmonic resonance alone, column (b) for the pure two-level system in its ground state, column (c) gives the spectra for the coupled resonances for an unpumped gain medium, column (c) the same for a completely inverted two-level system. Parameters are: $\Omega_{2\mathrm{LS}} = 2\pi \times 200\,\mathrm{THz}$, $\gamma_{2\mathrm{LS}} = 50\,\mathrm{THz}$, $d_{2\mathrm{LS}} = 6.5 \times 10^{-29}\,\mathrm{Cm}$, $N_{2\mathrm{LS}} = 2.1 \times 10^{24}\,\mathrm{m}^{-3}$; $\Omega_{\mathrm{pl}} = 2\pi \times 200\,\mathrm{THz}$, $\gamma_{\mathrm{pl}} = 90\,\mathrm{THz}$, $d_{\mathrm{pl}} = 4.2 \times 10^{-26}\,\mathrm{Cm}$, $N_{2\mathrm{LS}} = 5.3 \times 10^{20}\,\mathrm{m}^{-3}$; $L = 8 \times 10^{10}\,\mathrm{Fm}^{-1}$.

to be roughly comparable to the samples we present in the experimental section following this chapter. The gain medium is described by $\Omega_{2\mathrm{LS}} = 2\pi \times 200\,\mathrm{THz}$, $\gamma_{2\mathrm{LS}} = 50\,\mathrm{THz}$, $d_{2\mathrm{LS}} = 6.5 \times 10^{-29}\,\mathrm{Cm}$, $N_{2\mathrm{LS}} = 2.1 \times 10^{24}\,\mathrm{m}^{-3}$; the parameters for the plasmonic resonance are $\Omega_{\mathrm{pl}} = 2\pi \times 200\,\mathrm{THz}$, $\gamma_{\mathrm{pl}} = 90\,\mathrm{THz}$, $d_{\mathrm{pl}} = 4.2 \times 10^{-26}\,\mathrm{Cm}$, $N_{2\mathrm{LS}} = 5.3 \times 10^{20}\,\mathrm{m}^{-3}$; finally, the phenomenological coupling parameter is chosen to be $L = 8 \times 10^{10}\,\mathrm{Fm}^{-1}$.
For these calculations we have limited the system under consideration to a two-layer geometry: the plasmonic metamaterial of thickness $l_{\mathrm{pl}} = 30\,\mathrm{nm}$ and the two-level gain medium with a thickness $l_{2\mathrm{LS}} = 15\,\mathrm{nm}$. We have not introduced a substrate or any additional spacer layer separating the metamaterial from the gain medium and we have set the background refractive index to unity.
Figure 5.2 shows that under these conditions both the effective-medium approach and the rigorous transfer-matrix approach lead to the same transmittance spectra. For more complicated geometries, especially for a thick spacer between the metamaterial- and the gain layer, the effective-medium approach can become obsolete and we have to resort to transfer-matrix calculations. For the parameter study in the following section, however, we use the effective-medium approach for the simple two-layer geometry described above.

Here, we also see how different the optical properties, represented by the transmittance spectra, of the coupled system can be compared to those of the two constituting resonances: For the coupled case where the two-level system rests in its ground state (Fig. 5.2 c) we observe the typical mode-splitting for strongly coupled resonances. However, if the two-level system is inverted (Fig. 5.2 d) the spectral lineshape changes significantly from the (split) Lorentzian we find in cases a to c.
This is first evidence of how sensitively the coupled system reacts to a change in the model parameters. We therefore study the influence of the coupling strength described by L and of the spectral detuning between Ω_{2LS} and Ω_{pl} in the following section.

5.3 Influence of Toy-Model Parameters

Ten parameters enter into the definition of the toy model: each resonance is characterised by four of them (Ω, γ, d and N). We additionally need the occupation factor f to fully describe the two-level system. Finally, to model the coupling between the two resonances we have introduced the phenomenological local-field coupling parameter L.
Under experimental conditions most of these parameters are fixed by the materials of the samples. For instance, the transition matrix element d_{2LS} and the dipole density N_{2LS} are material parameters depending on the specific gain medium we choose for our samples. Other parameters, however, can easily be varied in an experiment. Especially the plasmon resonance frequency can be adjusted by geometrical tuning and we can also deliberately change the coupling strength, e.g. by varying the distance between the metamaterial and the gain medium. Of course, these parameters are fixed for one sample once we have chosen them for our experiments. One parameter we can directly adjust in the measurement is the occupation factor f which we can influence by changing the pump power we use.
This section is therefore dedicated to a theoretical investigation of how the transmittance spectra change upon variation of f, L or Ω_{pl}. Since from this parameter study we intend to develop a feeling for our experiments (Chapters 6 and 7), which happen under transient conditions, we can use the analytical solution for fixed inversion derived above.

5.3.1 Occupation Factor f

We start with the influence of the occupation factor f, which represents the pump intensity used in the experiment. This factor has no direct effect on the plasmonic resonance, only on the 2LS resonance and by this also on the coupled system. We thus want to compare the transmittance spectra derived from the toy model for both the gain medium and for the hybrid sample if the two-level system is inverted to different extents (Fig. 5.3) while we keep all other parameters (apart from f) the same as for Fig. 5.2.
From Fig. 5.3 we immediately see that the coupled system (red curves) is influenced far more significantly by a change in the occupation factor f than the two-level system alone. The 2LS spectrum changes from a slight dip in transmittance for $f < 0.5$ to a slight peak for $f > 0.5$. The gain material is therefore absorbing if the 2LS is not inverted and becomes active, i.e. amplifying, if the occupation of the upper level exceeds that of the lower level. The change in transmittance itself is, of course, not very large because we have adjusted the 2LS parameters to our experimental gain medium which shows an increase in transmittance of 2% upon pumping.

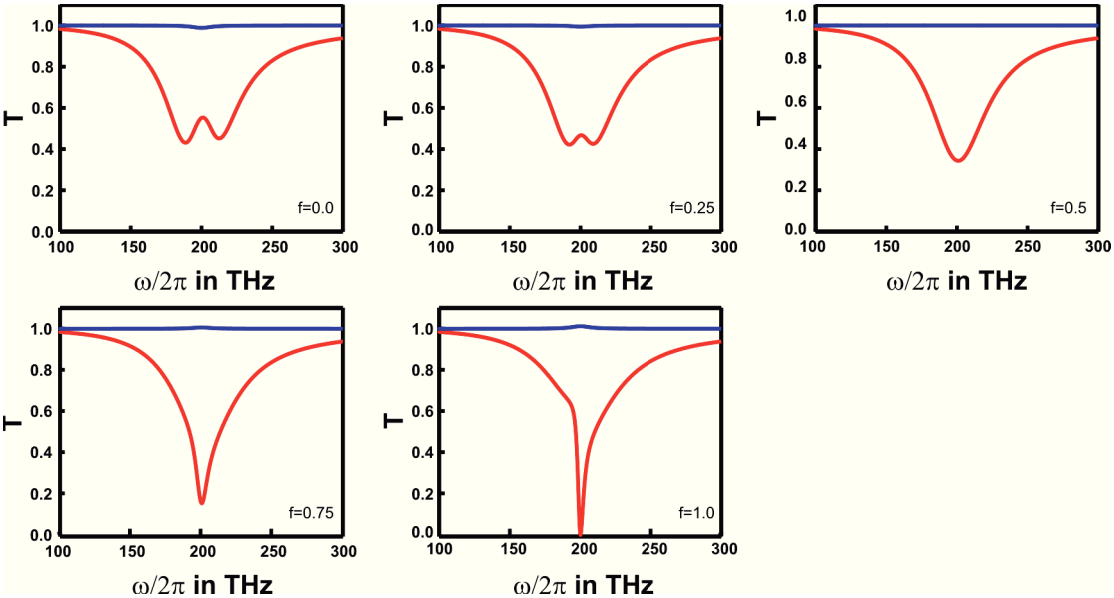

Figure 5.3: Change in transmittance spectra upon variation of the occupation factor f. Blue curves correspond to the bare two-level system, red curves are for the coupled system of gain medium and plasmonic resonance ($L = 8 \times \times 10^{10}\,\mathrm{Fm}^{-1}$).

For the coupled system, however, a change of the occupation factor generates qualitatively different spectra: If the two-level system is in the ground state ($f = 0$) we clearly see the two split modes expected for two sufficiently strongly coupled resonances. This splitting becomes less and less pronounced if we increase the occupation factor until the coupled resonance is indistinguishable from the uncoupled case (compare Fig. 5.2 a) at $f = 0.5$. For larger values of f - we now deal with an inverted 2LS because more electrons occupy the upper than the lower state - the resonance becomes both deeper and narrower, indicating a reduction of damping in the coupled plasmon-2LS system compared to the plasmon alone. In the extreme case of a completely inverted gain medium transmittance even becomes zero at the common resonance frequency.
It is therefore desirable to invert the gain medium as much as possible in order to compensate for plasmonic losses. In the following, we consequently compare a completely inverted two-level system ($f = 1$) to an uninverted one ($f = 0$) and investigate how other experimentally accessible parameters change the transmittance of our system.

5.3.2 Coupling Strength L

The second influential parameter we want to study is the coupling strength described by the phenomenological parameter L. To this end we calculate transmittance spectra for different values of L while leaving the other parameters fixed at $\Omega_{2\mathrm{LS}} = 2\pi \times 200\,\mathrm{THz}$, $\gamma_{2\mathrm{LS}} = 50\,\mathrm{THz}$, $d_{2\mathrm{LS}} = 6.5 \times 10^{-29}\,\mathrm{Cm}$, $N_{2\mathrm{LS}} = 2.1 \times 10^{24}\,\mathrm{m}^{-3}$, $\Omega_{\mathrm{pl}} = 2\pi \times 200\,\mathrm{THz}$, $\gamma_{\mathrm{pl}} = 90\,\mathrm{THz}$, $d_{\mathrm{pl}} = 4.2 \times 10^{-26}\,\mathrm{Cm}$, $N_{2\mathrm{LS}} = 5.3 \times 10^{20}\,\mathrm{m}^{-3}$ and do this for an occupation factor of $f = 0$ (unpumped system) and $f = 1$ (completely inverted system), respectively. Figure 5.4 shows the resulting spectra for a coupling parameter varying between $L = 0$ and $L = 11 \times 10^{10}\,\mathrm{Fm}^{-1}$.

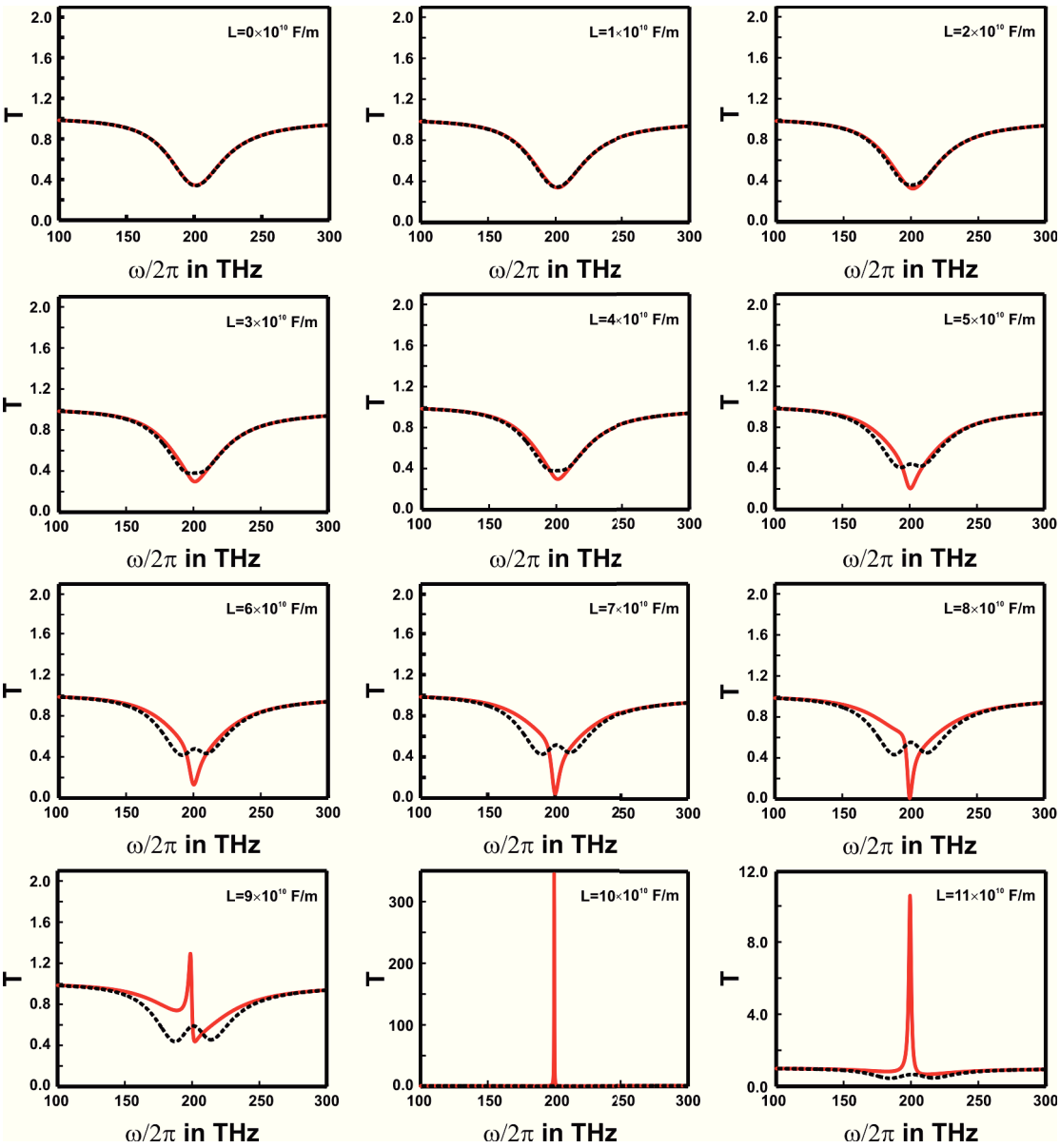

Figure 5.4: Change in transmittance spectra upon variation of the coupling parameter L. Dashed black curves correspond to the unpumped case ($f = 0$), solid red curves are for a completely inverted two-level system ($f = 1$).

Let us first look at the passive case when the two-level system is in its ground state ($f = 0$, dashed black curves in Fig. 5.4): Without coupling ($L = 0$) the transmittance spectrum resembles the plasmon resonance. If we increase the coupling there is at first no visible change but the resonance broadens slightly owing to mode-splitting, which is not very pronounced yet. At $L = 5 \times 10^{10}\,\mathrm{Fm}^{-1}$ the split modes become clearly visible; they are distributed symmetrically about the common centre frequency of the plasmon and the gain resonance at $\omega = 2\pi \times 200\,\mathrm{THz}$. For even higher coupling parameters the split increases, i.e. the spectral separation between the two modes becomes larger and larger. The depth of both transmittance dips, however, remains roughly the same with a minimum value of $T_{\min} = 0.4$, regardless of the coupling strength. This behaviour is typical for coupled modes and can be found in many coupled systems.

A more dramatic dependence on the coupling strength can be found for the coupled system in case the two-level system is excited. To maximise this effect we consider a completely inverted 2LS ($f = 1$, solid red curves in Fig. 5.4): Again, for no or low coupling the spectrum is given by the resonance of the plasmonic metamaterial. If, however, we now increase the coupling strength, we do not find a broadening and subsequent splitting of the spectrum but rather the opposite. The transmittance dip narrows down to increasingly smaller linewidth and becomes deeper and deeper with the minimum transmittance value reaching its lowest position of $T_{\min} = 0$ for a coupling parameter of $L = 8 \times 10^{10}\,\mathrm{Fm}^{-1}$. Note that this does not happen absolutely symmetrically around the centre frequency as was the case for the mode-splitting when $f = 0$; the spectra rather develop a certain asymmetry which is manifest in the kink on the low-frequency side of the transmittance dip for $L = 8 \times 10^{10}\,\mathrm{Fm}^{-1}$.
For even higher coupling factors the system becomes unstable and shows a Fano-like lineshape before the transmittance dip turns into a delta peak reaching values of $T > 300$ for $L = 10 \times 10^{10}\,\mathrm{Fm}^{-1}$. The latter can be interpreted as the onset of lasing or rather lasing spasing [23]. However, yet higher coupling does not lead to an increase of this effect (see bottom right panel in Fig. 5.4). This clearly shows how sensitive the plasmon-and-gain system with an inverted gain medium reacts to changes in coupling. Obviously, not only the overall strength of coupling can be important but also the exact value of the coupling parameter, especially for the unstable lasing (spasing) case.

5.3.3 Spectral Detuning of Ω_{2LS} and Ω_{pl}

A second important parameter which is easily accessible in an experiment is the spectral detuning $\Delta\Omega$ of the two resonance frequencies Ω_{2LS} and Ω_{pl}. To develop a feeling for the influence of the detuning on the transmittance of the coupled system, we choose a coupling strength exhibiting a specific spectral feature ($L = 8 \times 10^{10}\,\mathrm{Fm}^{-1}$), keep the resonance position of the two-level system constant at $\Omega_{\mathrm{2LS}} = 2\pi \times 200\,\mathrm{THz}$ and vary the resonance frequency Ω_{pl} of the plasmonic metamaterial; again we examine the spectra for the umpumped ($f = 0$) and the fully inverted ($f = 1$) case. This approach closely resembles the way we conduct the experiments. The results of these calculations are shown in figure 5.5.

Again, the behaviour in the passive case is that of two classical coupled oscillators. We start from the degenerate situation, i.e. $\Delta\Omega = 0$ (central panel in Fig. 5.5), where the resonance is split into two modes, symmetrically with respect to the centre frequency $\Omega_{\mathrm{pl}} = \Omega_{\mathrm{2LS}}$.
If we now move to larger detunings $\Delta\Omega$ - either to the blue or to the red - we find the original plasmon resonance to re-emerge. The further Ω_{pl} is removed from Ω_{2LS} the more weight does it gain; this becomes visible in the corresponding transmittance dip, which is much deeper compared to the second dip in the spectrum; the latter meanwhile becomes more and more shallow. We can identify the more pronounced of the two modes to belong to the plasmon because this feature moves through the spectrum when we alter the plasmonic resonance frequency and it is located at Ω_{pl} for larger detunings.
The changes to the transmittance spectra owing to detuning of the two resonances with an inverted two-level system are somewhat more complicated. In general, we can state that the transmittance spectrum is the more similar to the $f = 0$ case the larger the detuning becomes

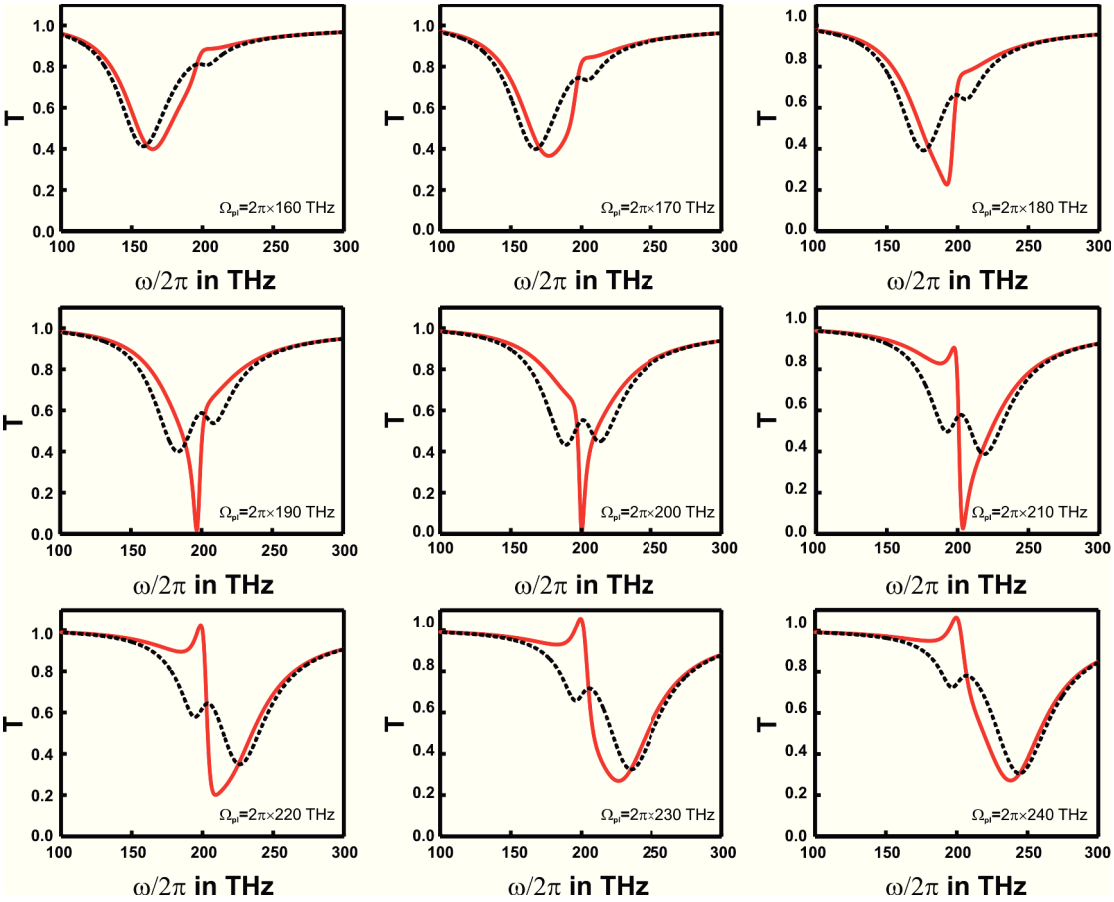

Figure 5.5: Change in transmittance spectra upon variation of the plasmon resonance frequency Ω_{pl} while the centre frequency of the two-level system resonance remains fixed at $\Omega_{\mathrm{2LS}} = 2\pi \times 200\,\mathrm{THz}$. Dashed black curves correspond to the unpumped case ($f = 0$), solid red curves are for a completely inverted two-level system ($f = 1$).

(compare top left and bottom right panels in Fig. 5.5). Here too, the two individual resonances are revealed when their centre frequencies differ; naturally, the two-level-system resonance appears as a peak instead of a dip when the system is inverted. This peak, however, is more pronounced for blueshifts of Ω_{pl} than it is for redshifts.
One big difference to the unpumped situation is the way in which the plasmonic resonance emerges: the narrow dip for the degenerate case (Fig. 5.5, central panel) does not immediately split into a broad dip from the plasmon and a small peak from the two-level system. It rather develops a more pronounced asymmetry in form of a broadening of the resonance to the side of the spectrum the plasmonic resonance is shifted to. That is the dip "opens up" towards lower frequencies if we redshift Ω_{pl} or to higher frequencies for a blueshift. For even larger detunings the spectrum is reshaped gradually towards the unpumped case while the steep feature at Ω_{2LS} is maintained for a certain range of $\Delta\Omega$, leading to non-Lorentzian lineshapes in the transmittance spectra.

Overall, general predictions for a given experimental situation turn out to be difficult when dealing with a coupled system consisting of a plasmonic metamaterial and a gain medium. Especially for the pump-probe experiments presented in Chapters 6 and 7, where we do not deal with transmittance spectra but rather with the difference between the pumped and unpumped

system for one spectral point, it is crucial to know the parameters of a given sample.
For the degenerate case $\Omega_{\mathrm{2LS}} = \Omega_{\mathrm{pl}}$ we expect the inversion of the gain medium to result in a decrease of transmittance around the centre frequency and to an increase for frequencies removed from it - provided the system is not yet in its unstable (lasing) state. For non-degenerate situations, however, no such simple prediction can be made and we have to calculate the difference of the spectra for an inverted and a passive two-level system.

5.4 Limits of the Toy Model

The mode-coupling model presented in this chapter is called *toy model* for a reason: it is an extreme simplification of a system exhibiting complicated physics. We consequently do not expect the model to cover all aspects of the real system in detail. In this section we aim to find the boundaries within which we can use the toy model by exploring possible limitations.

One case where we expect such a simple model to cause problems is the extreme situation when the coupled system becomes unstable and starts to lase (or lasing spase). We have, however, seen in section 5.3 that the calculations for a fixed occupation factor of $f = 1$ do already show the onset of lasing. Still, this is not sufficient evidence for the toy model being able to describe lasing (spasing) as here especially the constant inversion factor is an improper oversimplification.
In this case of net-gain, i.e. when the gain exceeds the loss, the probability of the upper level population described by f will be reduced by stimulated emission. Eventually, a stady-state emerges and the occupation is fixed to some value $f < 1$; in laser theory this phenomenon is known as gain-pinning [64].
If we want to treat lasing dynamics with the toy model we therefore have to go back to the defining equations (5.13) to (5.15) remaining in the rotating-wave approximation and adjust them accordingly. We now eliminate all effects from external electric fields by setting $E = 0$ and introduce an additional pump rate $\Gamma_{\mathrm{pump}} = \Gamma_0 (1 - f)$ to account for the inversion of the two-level system, which would otherwise not be possible. We also abbreviate the effective rate of stimulated emission on the left-hand side of Eq. (5.15) with Γ_{stim}. Overall, this leads to a rate equation describing the dynamics of the coupled system.

$$\dot{f} + \Gamma_{\mathrm{2LS}} f = i \left[\tilde{p}^*_{\mathrm{2LS}} V_{\mathrm{2LS}} \tilde{p}_{\mathrm{pl}} - c.c. \right] + \Gamma_{\mathrm{pump}} = -\Gamma_{\mathrm{stim}} + \Gamma_{\mathrm{pump}}. \tag{5.23}$$

If we now establish non-zero initial conditions from which lasing can start in some way and solve this equation numerically we can monitor the switch-on behaviour of a lasing spaser including the typical relaxation oscillations of a laser. Further details on this treatment can be found in reference [49] and will not be discussed here because this work is not concerned with the details of lasing spasing.
In conclusion, the special case of a lasing spaser can be described with the help of the toy model and does not present severe problems.

The fact that we need to feed some non-zero initial conditions into the model is, however, a first hint towards one of its constraints. We have to impose these initial conditions because the model does not contain any spontaneous emission from which lasing could start. The model is therefore incapable of describing any phenomena related to spontaneous emission. We cannot

use it to analyse photoluminescence measurements and we cannot account for changes in the emission rates owing to an enhancement of spontaneous emission, i.e. for the Purcell effect.

In the toy model both the plasmonic metamaterial and the two-level system are described by a single resonance each, which are subsequently coupled *via* their near-field interaction. There is no means of introducing coupling effects between the individual plasmonic particles or the set of emitters that make up the gain medium.
Especially when the gain material is inhomogeneously distributed over the metamaterial in the real sample a description where this spatial distribution is not averaged out might become important. Here, modifications to the present toy model can become necessary in such a way that we first couple an individual plasmonic particle resonance to a gain resonance and let a set of these systems interact afterwards.

Finally, the toy model is based on near-field interactions but does not provide a possibility of modelling the spatial distribution of these. For instance, we can only account for less overlap of the evanescent fields of the metamaterial with the gain due to increasing spatial separation of the two by lowering the phenomenological coupling parameter L. There is no method to adjust it systematically, even if we know how the field decays.
Furthermore the near-field coupling parameter in the model does not explicitly account for the fact that only a small percentage of the dipoles in the gain medium are reached by the plasmonic near fields. This too can only be described by lowering L to a value averaging over the emitters that are affected and the ones that are not.
In both cases we can only adjust the local-field parameter by fitting to experimental results and not predict its value or its dependence on, for instance, separation *a priori*. Considering the altogether ten parameters we need to determine, this procedure becomes somewhat questionable if the other parameters cannot be fixed by different means (additional spectroscopic data, literature values etc.). This turns the coupling parameter L into a difficult observable to draw conclusions from.

On the whole, the toy model presented in this chapter is surprisingly well suited for a qualitative description of a plasmonic metamaterial coupled to a gain medium - as we will see later in comparison to our experimental data - especially considering the high degree of simplification it is based on. Although this simplicity can be of advantage for understanding important aspects of the system, we have to be aware of the limits of this model. However, it turns out to be a convenient tool for predicting or checking experimental data qualitatively but the numerical values of the model parameters can only be derived from a fit (with up to ten parameters for the worst case) and should therefore not be taken too seriously.

Chapter 6

Experimental Proof of Coupling between Split-Ring Resonators and Quantum Wells

We are now set and ready to turn to the experimental investigation of a hybrid system consisting of a plasmonic metamaterial and a gain medium. The specific system we consider in this thesis is an array of silver split-ring resonators (SRR) on top of a single InGaAs-quantum well (QW), which we study by means of low-temperature femtosecond pump-probe spectroscopy as described in section 4.2.2.
In this first experimental section we focus on one sample (NA1) and present detailed experimental evidence for the existence of substantial coupling between the metamaterial and the quantum well. Our measurements show a significant difference both in the magnitude of the pump-probe signals and in the dynamics of the system when we compare the bare quantum well to the well with an array of SRRs on top. This claim is further supported by fitting the spectroscopic data with the toy model introduced in Chapter 5 and by estimating the Purcell factors derived from the dynamics with the help of numerically acquired field enhancements.

We start by giving the specific design of sample NA1 and by outlining the exact set of measurements and control measurements we perform. Thereafter we choose a representative set of measurements which we discuss in detail before we give an overview over the remaining experimental data and show how all these can be consistently analysed with the help of the toy model. The chapter closes with a theoretical approach to the description of the decay-rate enhancement we observe in our measurements; here, we use near-field calculations to estimate the corresponding Purcell factor for our experimental situation.

6.1 Outline of the Experiments

Although this section deals with only one sample, we need to present a considerable amount of data to draw reliable conclusions from the experiments. This involves a set of control experiments whose purpose we outline in this section. First, however, we present some details on sample NA1, which is the one we investigate here.

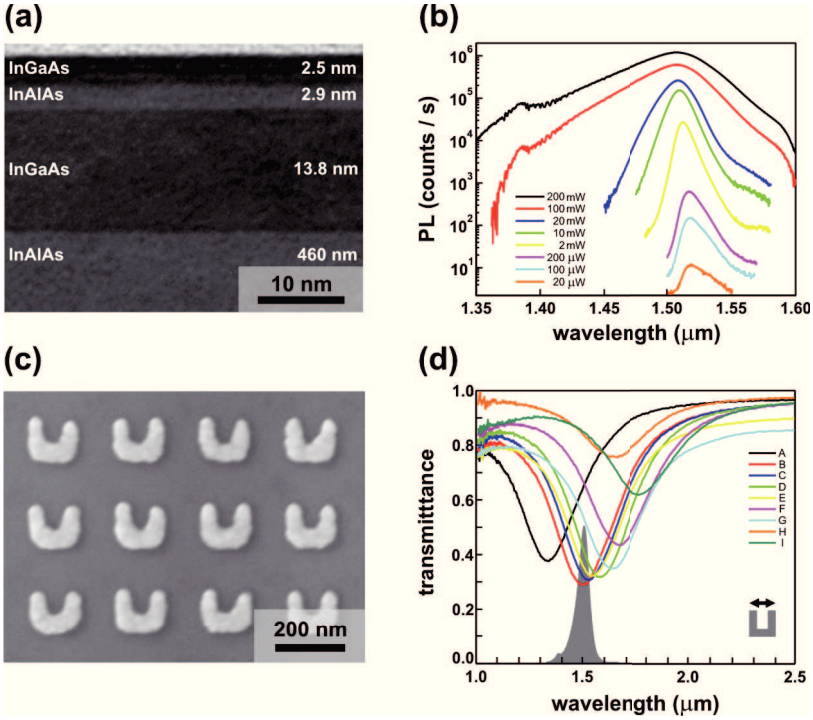

Figure 6.1: (a) TEM image of the quantum well HSG 37. (b) Low-temperature photoluminescence (PL) measurements for increasing pump power P, taken on a part of NA1 without SRRs. (c) SEM image of a typical SRR array (D) on NA1. (d) Room-Temperature transmittance spectra of the SRR arrays on NA1 for horizontally incident polarisation; the grey curve marks the spectral position of the low-temperature PL for $P = 200\,\mathrm{mW}$.

6.1.1 Sample Design

Sample NA1 is fabricated on a piece of the epitaxially grown wafer HSG 37 containing a single $In_{0.53}Ga_{0.47}As$ quantum well which is $13.8\,\mathrm{nm}$ thick and starts $5.3\,\mathrm{nm}$ below the surface (Fig. 6.1 a). The barriers consist of $In_{0.52}Al_{0.48}As$ and the whole sample is capped by a further thin layer of $In_{0.53}Ga_{0.47}As$ to prevent oxidation of the aluminium content. Further details on the fabrication and composition of HSG 37 are given in section 4.1.1.
HSG 37 is designed to have its low-temperature $(5 - 10\,\mathrm{K})$ gain to be centred around $1.5\,\mu\mathrm{m}$. The corresponding photoluminescence (PL) measurements - which are taken under identical conditions as the pump-probe measurements - are presented in Fig. 6.1 b and show a PL maximum around the desired wavelength and a linewidth for low excitation powers of about $25\,\mathrm{nm}$, which further proves the quality of the quantum well. This spectral width significantly broadens with increasing pump power, so we conclude that the pump power used for the time-resolved measurements $(200\,\mathrm{mW})$ suffices to saturate the inversion of the gain medium.

To produce arrays of silver SRRs which serve as the plasmonic metamaterial we perform a standard electron-beam lithography procedure (section 4.1.2) with HSG 37 as substrate. On one sample we fabricate a whole set of arrays where the SRRs are geometrically adjusted to exhibit different spectral positions of their fundamental resonance. In this way we can examine the spectral detuning between the gain resonance and the plasmonic resonance. On NA1 the metal structures are $30\,\mathrm{nm}$ thick and their fundamental resonances vary between $1.20\,\mu\mathrm{m}$ and $1.80\,\mu\mathrm{m}$; corresponding room-temperature transmittance spectra are given in Fig. 6.1 d.

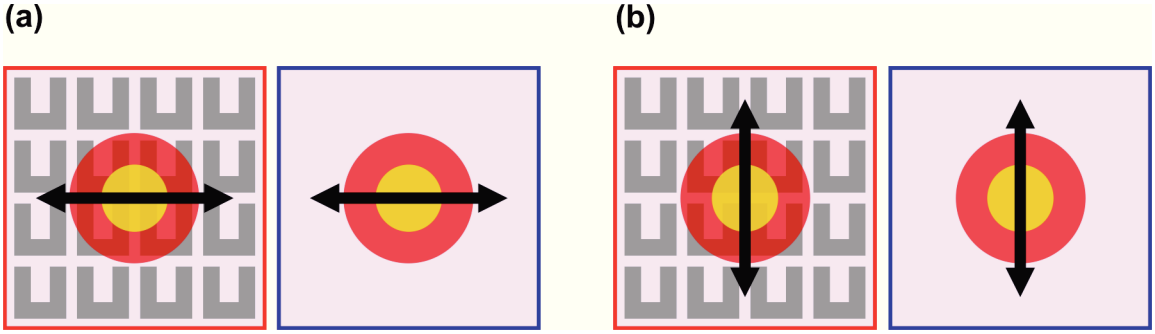

Figure 6.2: Sketch (not to scale) of the set of four experiments we perform on each field and for every wavelength. (a) pump-probe measurement on the SRR field (red) and on the bare quantum well (blue) for horizontal probe polarisation, where the fundamental mode is excited; (b) the same for vertical probe polarisation, for which the fundamental mode cannot be excited.

6.1.2 Experimental Procedure

The pump-probe setup described in section 4.2.2 is used to obtain time-resolved spectroscopic data on our samples, with which we investigate the coupling between SRRs and quantum wells. We pump the samples at $810\,\mathrm{nm}$ with an average power of $200\,\mathrm{mW}$ focused to a spot of $22\,\mu\mathrm{m}$ full width at half maximum (FWHM). To ensure that a homogeneously pumped area of the sample is measured, the probe spot has about half the diameter ($10\,\mu\mathrm{m}$ FWHM); the average probe power is set to $70\,\mu\mathrm{W}$. Having verified that the measurements are not sensitive to pump polarisation, we have chosen the polarisation of the pump beam to be horizontal (with respect to the bottom arm of the SRRs) for all further experiments.
While we leave the pump conditions constant for all measurements, we change the wavelength of the probe beam between $1.4\,\mu\mathrm{m}$ and $1.6\,\mu\mathrm{m}$ to obtain some spectral information. We can also turn its polarisation to provide some control measurements, which are described in the following paragraph.

For every probe wavelength and every SRR array we perform a set of four pump-probe measurements which are illustrated in Fig. 6.2.
The most interesting experiment is the one where we expect to see coupling. This is the case when the fundamental resonance of the split-ring resonators is excited, i.e. for probe polarisation horizontal with respect to the SRR gap (Fig. 6.2 a). We take this measurement on the SRR field (red box) and on a region of the sample close by where there are no metal structures (blue box). Thereby we can directly compare the pump-probe signal of the bare QW and of the coupled SRR-QW system and determine the changes from coupling to the metamaterial.
The same pair of measurements on and off the SRR field is taken for vertical probe polarisation (Fig. 6.2 b). For this configuration the fundamental mode, which is the one that has spectral overlap with the gain resonance, cannot be excited. We can therefore determine if the effects we observe in the experiment corresponding to the red box in Fig. 6.2 a are caused by resonant coupling or purely by the presence of metal on top of the well.

6.2 Time-Resolved Spectroscopy on Sample NA1

On sample NA1 we have performed time-resolved spectroscopic measurements on several fields of SRRs with different resonance positions owing to variations in their geometrical design. Here, we will not present all of them in detail but rather focus on two selected arrays: field D which shows the strongest effects ($\lambda_{\mathrm{SRR}} = 1540\,\mathrm{nm}$); field A, whose fundamental resonance ($\lambda_{\mathrm{SRR}} = 1270\,\mathrm{nm}$) has no spectral overlap with the QW gain resonance.
For the remaining arrays we condense the data into spectra for one particular time delay and compare these with fits from the toy model (section 5). Finally, we return to the time-resolved data and take a closer look at the decay-rate enhancement we find in our experiments.

6.2.1 Measurements for Selected SRR-Resonance Positions

Figure 6.3 shows time-resolved measurements for SRR array D whose fundamental resonance at low-temperatures is centred around $1540\,\mathrm{nm}$.
The blue curves depict the relative differential transmittance $\Delta T/T$ on the bare quantum well close to field D. They are positive over the whole spectrum of probe wavelengths and reach their maximum of about 2% around $\lambda_{\mathrm{probe}} = 1480\,\mathrm{nm}$. We find the pump-probe signal of the quantum well to decay single-exponentially with a lifetime $\tau_{\mathrm{QW}} = 670\,\mathrm{ps}$ for all wavelengths. Both the spectral and the temporal behaviour of the quantum well show no dependence on the polarisation of the probe beam.
This resembles the behaviour expected of quantum wells in a pump-probe experiment [75] when pumped to saturation: The pump lifts electrons from their ground to an excited state so that the the probability for absorption of the probe beam is reduced, leading to an increase in transmittance. The relaxation of the excited electrons is governed by standard quantum statistics and is therefore expected to be exponential.

For horizontal probe polarisation (column a) we find a distinct difference for the measurements on the SRR arrays (red curves) compared to the control measurements on the bare quantum well (blue curves):
Most notably, the majority of on-field signals for this configuration are negative, corresponding to a lowering of the transmittance upon pumping. Only for probe wavelengths at the very edges of our measurement window ($\lambda_{\mathrm{probe}} = 1420\,\mathrm{nm}$, $\lambda_{\mathrm{probe}} = 1440\,\mathrm{nm}$ and $\lambda_{\mathrm{probe}} = 1560\,\mathrm{nm}$) do we find positive $\Delta T/T$ values at all.
The magnitude of this (negative) differential transmittance changes with probe wavelength. It reaches its maximum value of $\Delta T/T = -8\%$ for a probe wavelength of $1480\,\mathrm{nm}$, corresponding to the spectral maximum position of the quantum-well-gain spectrum. For both lower and higher wavelengths the magnitude of $\Delta T/T$ decreases down to less than $\pm 1\%$.
Apart from the pure value of the signals we observe a significant change in the dynamics of the combined SRR-QW system compared to that of the quantum well alone. Especially for wavelengths between $1460\,\mathrm{nm}$ and $1520\,\mathrm{nm}$ a single-exponential decay is not suitable to describe the dynamics of the on-field signals. When fitting the experimental data with a sum of two exponentials we find two time constants that are both shorter ($\tau_1 = 15\,\mathrm{ps}$, $\tau_2 = 180\,\mathrm{ps}$) than the lifetime of the quantum well. This decay rate enhancement will be discussed in detail below (section 6.2.3).

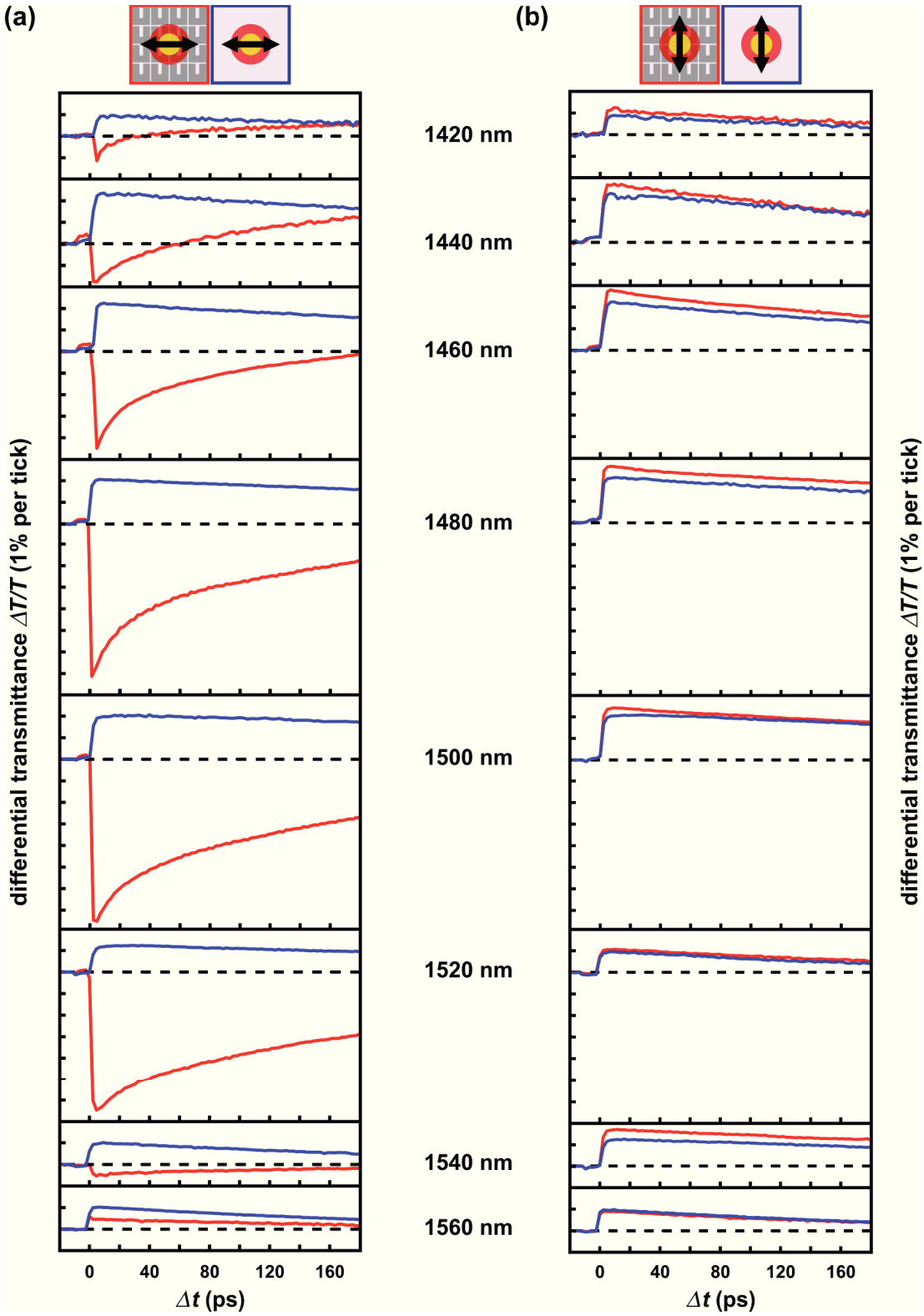

Figure 6.3: Time-resolved pump-probe measurements on field D ($\lambda_{\mathrm{SRR}} = 1540\,\mathrm{nm}$). Red lines correspond to measurements on the SRR array, blue ones to measurements on the bare quantum well. (a) Differential transmittance over time delay for horizontal probe polarisation; (b) the same for vertical probe polarisation.

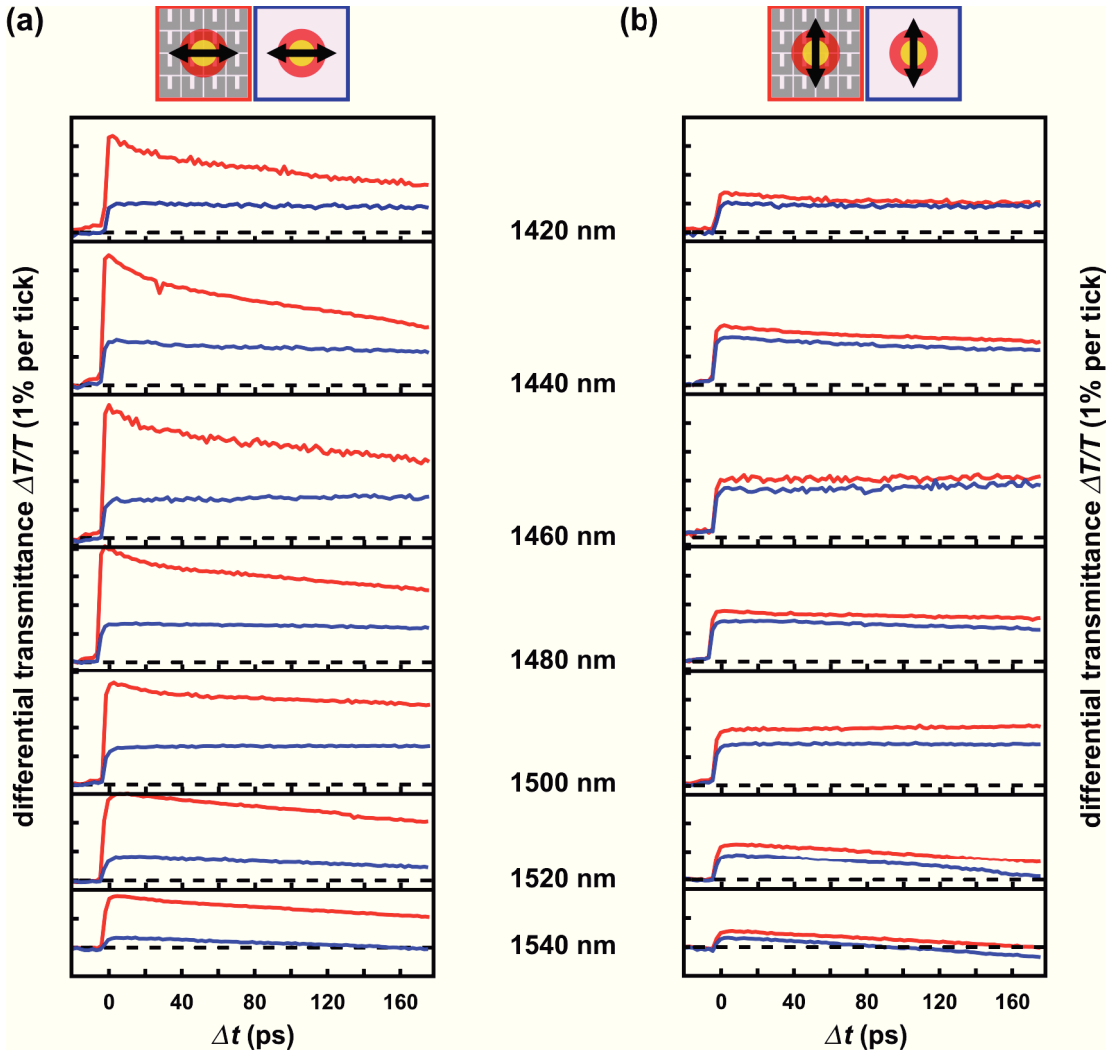

Figure 6.4: The same as Fig. 6.3 for field A whose fundamental resonance is located around $\lambda_{\mathrm{SRR}} = 1270\,\mathrm{nm}$, thus representing an off-resonant situation of plasmon and gain resonance.

Throughout the accessible wavelength range the signals on the arrays for horizontal probe polarisation are significantly different from those on the bare quantum well.

If, on the other hand, we look at the data for vertical probe polarisation (Fig. 6.3 b) we find the measurement on the array (red curves) to be hardly distinguishable from the ones on the bare well (blue curves):
The differential transmittance on the field is positive over the whole spectral range and its magnitude varies on the same scale as the signal of the quantum well alone, i.e. roughly between 1% and 2%. There is also no detectable change in the dynamics of the pump-probe signals on the array for this polarisation. We still find a single-exponential decay with a lifetime of $\tau = 670\,\mathrm{ps}$, which is identical to the dynamics of the bare wafer.
We can therefore conclude that all effects found on the split-ring arrays for horizontal polarisation can be attributed to a coupling of the fundamental resonance to the gain resonance of the quantum well. A dominant influence of the metal in proximity to the semiconductor

nanostructure can be ruled out on the basis of this control experiment for vertical polarisation.

We now compare the above observations to the measurements on the off-resonant field A ($\lambda_{\mathrm{SRR}} = 1280\,\mathrm{nm}$) presented in figure 6.4. Although the signals on field A for horizontal polarisation also differ from the ones on the bare well the difference is not as dramatic as it is for field D.
Here, we do not observe the differential transmittance to become negative but we find the magnitude of $\Delta T/T$ on the arrays to be larger than on the quantum well alone. Over the whole spectral range of our measurements the ratio between the maximum $\Delta T/T$ value on the array and the maximum on the bare well is roughly constant with the on-field signal being about three times as high. There is no significant dependence of this change on the probe wavelength. The same holds true for the dynamics of the combined system. We find a single exponential decay whose lifetime $\tau_1 = 530\,\mathrm{ps}$ is not much different from the lifetime of the well alone. Neither the single-exponential dynamics nor the lifetime show any significant variation with the probe wavelength.

For vertical probe polarisation we again find no veritable difference between the pump-probe data on the array and on the bare quantum well, neither in the magnitude nor in the dynamics of the differential transmittance.

6.2.2 Summary and Comparison with Toy Model

In general, the pump-probe data of the other arrays measured on sample NA1 show the same qualitative behaviour as the fields A and D described above, depending on the spectral position of their fundamental resonance. To ease comparison we here condense data to a spectral representation by taking the differential transmittance values at a fix time delay of $\Delta t = +5\,\mathrm{ps}$ and plotting them against the probe wavelength for horizontal probe polarisation (Fig. 6.5); the full time-resolved data for all fields can be found in Appendix B.

We find the relative differential transmittance on the bare quantum well (blue dots) to not vary much over the whole sample; it reaches its maximum of $\Delta T/T = 2\%$ for a probe wavelength of $1.46\,\mu\mathrm{m}$ and falls off to either side of the accessible spectral range.
Comparing the measurements on different fields with different resonance wavelengths we also observe a shift in the spectral position of the maximum $|\Delta T/T|$ value; if the resonance is further in the blue this maximum is also shifted to the blue. For higher resonance wavelengths the width of the differential transmittance spectrum also broadens compared to the cases for lower resonance wavelengths. Together with this broadening the maximum value of $|\Delta T/T|$ decreases.
For resonant on-field measurements we generally find negative values of $\Delta T/T$ around the resonance and values close to zero or even positive towards both lower and higher wavelengths. How does this change the original line shape of the plasmonic resonance on the passive substrate? The resonance occurs as a Lorentzian dip in the transmittance spectrum; a negative value of ΔT around the resonance therefore further deepens the resonance whereas the positive values on the spectral edges push the lobes of the Lorentzian closer to unity. The overall

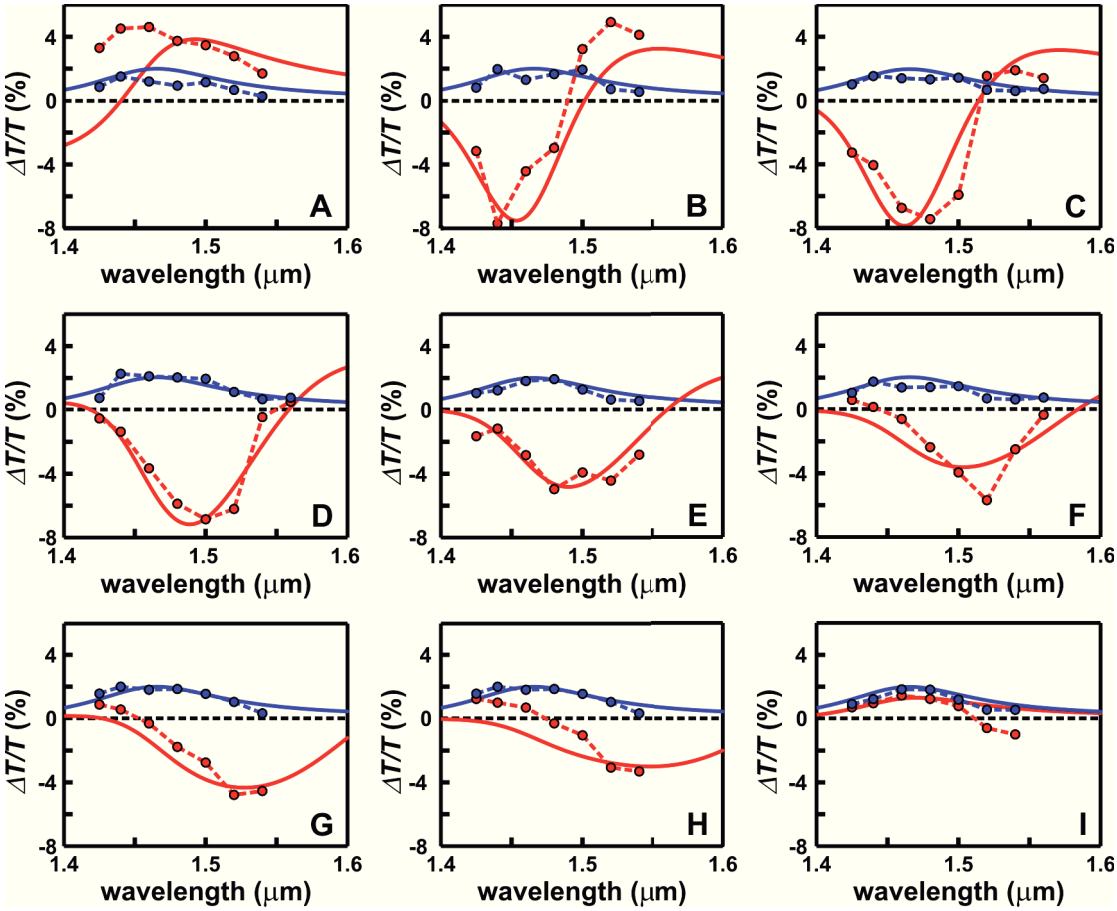

Figure 6.5: Summary of the measurements on sample NA1 for horizontal probe polarisation: Dots represent measured values for a fix time delay of $\Delta t = +5\,\mathrm{ps}$, dashed lines are guides to the eyes. Solid lines show the corresponding toy-model fits for fields A to I. The colour code is the same as in the figures before: blue are data for the bare QW, red for QW+SRR. Table 6.1 gives the resonance wavelengths and the coupling parameters L of the individual fields.

result is a spectral narrowing of the resonance, which in turn corresponds to a reduction of the damping frequency γ describing the Lorentzian (compare Chapter 2). We therefore find evidence of a slight loss-compensation in our pump-probe data, the extent of which is further discussed in 6.2.4.

Fields A and I represent off-resonant fields which have their fundamental resonance at $\lambda_{\mathrm{SRR}} = 1270\,\mathrm{nm}$ and $\lambda_{\mathrm{SRR}} = 1740\,\mathrm{nm}$, respectively. Here, the $\Delta T/T$ values are generally positive, we observe neither the change in sign of the signal nor the drastic change in magnitude we find for resonant conditions.

We now want to compare these measurements with the predictions from our toy model (Chapter 5). To this end we need to generate differential transmittance data from the toy-model spectra. We thus calculate the spectra for an array both for a passive two-level system ($f = 0$) and for a completely inverted one ($f = 1$). To arrive at the relative differential transmittance we then

field	λ_{SRR}	Ω_{pl}	L
A	$1270\,\mathrm{nm}$	$2\pi \times 241\,\mathrm{THz}$	$1.8 \times 10^{10}\,\mathrm{F/m}$
B	$1460\,\mathrm{nm}$	$2\pi \times 205\,\mathrm{THz}$	$1.7 \times 10^{10}\,\mathrm{F/m}$
C	$1480\,\mathrm{nm}$	$2\pi \times 203\,\mathrm{THz}$	$1.8 \times 10^{10}\,\mathrm{F/m}$
D	$1540\,\mathrm{nm}$	$2\pi \times 195\,\mathrm{THz}$	$2.1 \times 10^{10}\,\mathrm{F/m}$
E	$1550\,\mathrm{nm}$	$2\pi \times 193\,\mathrm{THz}$	$1.8 \times 10^{10}\,\mathrm{F/m}$
F	$1580\,\mathrm{nm}$	$2\pi \times 190\,\mathrm{THz}$	$2.1 \times 10^{10}\,\mathrm{F/m}$
G	$1610\,\mathrm{nm}$	$2\pi \times 187\,\mathrm{THz}$	$2.2 \times 10^{10}\,\mathrm{F/m}$
H	$1640\,\mathrm{nm}$	$2\pi \times 183\,\mathrm{THz}$	$2.1 \times 10^{10}\,\mathrm{F/m}$
I	$1740\,\mathrm{nm}$	$2\pi \times 175\,\mathrm{THz}$	$0.1 \times 10^{10}\,\mathrm{F/m}$

Table 6.1: Resonance positions λ_{SRR} and Ω_{pl} and local-field parameter L used for the toy-model calculations for the different fields on sample NA1.

take the difference of the two values and normalise this to the passive system:

$$\left(\frac{\Delta T}{T}\right)_{\mathrm{TM}} = \frac{T(f=1) - T(f=0)}{T(f=0)}. \tag{6.1}$$

The resulting calculated differential-transmittance spectra are presented in figure 6.5 by the solid lines; solid blue lines show the calculations without the SRRs, i.e. for the bare two-level system, solid red lines show the calculations for the complete, coupled system.

For all these calculations we keep most of the ten model parameters constant and choose them to fit our experimental conditions as well as possible. The quantum well is modelled by a two-level system with

$$\begin{array}{ll} \Omega_{\mathrm{2LS}} = 2\pi \times 205\,\mathrm{THz}, & \gamma_{\mathrm{2LS}} = 50\,\mathrm{THz}, \\ d_{\mathrm{2LS}} = 6.5 \times 10^{-29}\,\mathrm{Cm}, & N_{\mathrm{2LS}} = 2.1 \times 10^{24}\,\mathrm{m}^{-3} \end{array} \tag{6.2}$$

and the fundamental split-ring mode with a plasmonic resonance described by

$$\begin{array}{ll} \Omega_{\mathrm{pl}} \text{ depends on array} & \gamma_{\mathrm{pl}} = 90\,\mathrm{THz}, \\ d_{\mathrm{pl}} = 4.2 \times 10^{-26}\,\mathrm{Cm}, & N_{\mathrm{pl}} = 5.3 \times 10^{20}\,\mathrm{m}^{-3}. \end{array} \tag{6.3}$$

The remaining local-field parameter L is left as a free fit parameter to adjust the calculations to our measurements. The resulting values for L are given in table 6.1 for all nine arrays together with the respective resonance frequencies Ω_{pl}.

We see in Fig. 6.5 that the general agreement of the toy-model fits with the measured data is excellent considering how very simplified the model is and how complex the experimental behaviour turns out. The two most notable observations - that the signals are mainly negative in the observed spectral range and that the maximum of $|\Delta T/T|$ shifts with the central wavelength of the plasmonic resonance - are reproduced in the calculations.
The toy-model fits can even be made consistently with most of the toy model parameters being kept at the same values for all arrays. Even the only real free parameter L only varies by about $\pm 10\%$ from the average over the whole range of arrays. Note, that the off-resonant field I is excluded from this rule because the fitting procedure for this field results in an ambiguity.

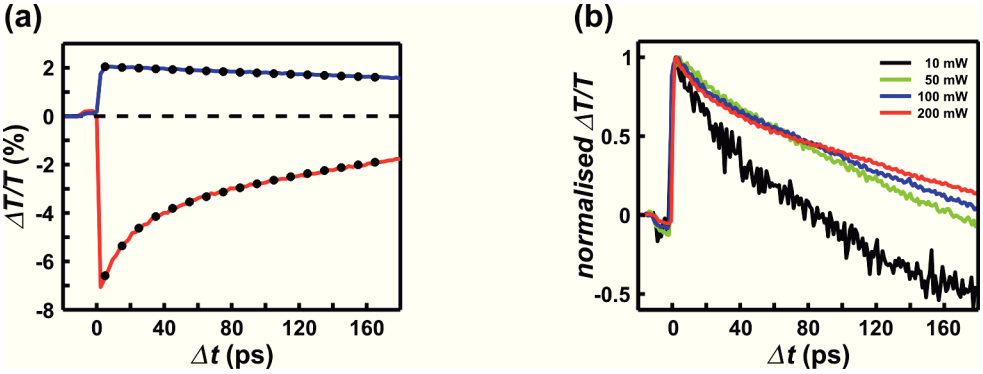

Figure 6.6: (a) Temporal dynamics of field D for $\lambda_{\mathrm{probe}} = 1480\,\mathrm{nm}$; the black dots show the fits to the experimental data, a single-exponential decay for the bare quantum well (blue curve) and a sum of two exponentials for SRR+QW (red curve). (b) Dynamics of field F at $\lambda_{\mathrm{probe}} = 1500\,\mathrm{nm}$ for different pump powers; the ratio of pump to probe power is kept constant over all measurements.

In conclusion, we regard all this as evidence of substantial coupling between the split-ring-resonator arrays and the single quantum well underneath, which we propose to be mediated by the plasmonic near fields of the metamaterial. We therefore proceed with an investigation of how the coupling effects vary when we alter the distance between the quantum well and the split-ring resonators in Chapter 7.
Before we turn to this second step, however, we take a closer look at the decay-rate enhancements we observed in the time-resolved measurements on sample NA1 and discuss their origin.

6.2.3 Decay-Rate Enhancement

From the time-resolved data in Fig. 6.3 we have found a pronounced difference in the dynamics of the measurements on the fields compared to those on the bare wafer. From these data we find the signals on the bare quantum well to decay single-exponentially with a time constant of $\tau_{QW} = 670\,\mathrm{ps}$; the signal on array D cannot be fitted with a single exponential but a sum of two exponential functions describes the decay in the measured time window rather well. From this fit we extract two time constants $\tau_1 = 15\,\mathrm{ps}$ and $\tau_2 = 180\,\mathrm{ps}$. These fits to the experimental data are given by the black dots in figure 6.6 a. There are, basically, three explanations to the more rapid decay times in the presence of the plasmonic nanostructures:

(i) Quenching due to the presence of metal.

(ii) The onset of lasing.

(iii) Enhancement of the spontaneous emission rate as described by the Purcell effect.

We can rule out explanation (i) from the control measurements we performed for vertical probe polarisation: any effect that arises directly from the presence of metal in close proximity to the gain medium should not depend on polarisation, and thus on the excitation of a plasmonic resonance. Since we do not observe any decay-rate enhancements for vertical probe polarisation this cannot be the cause of the more rapid decays.

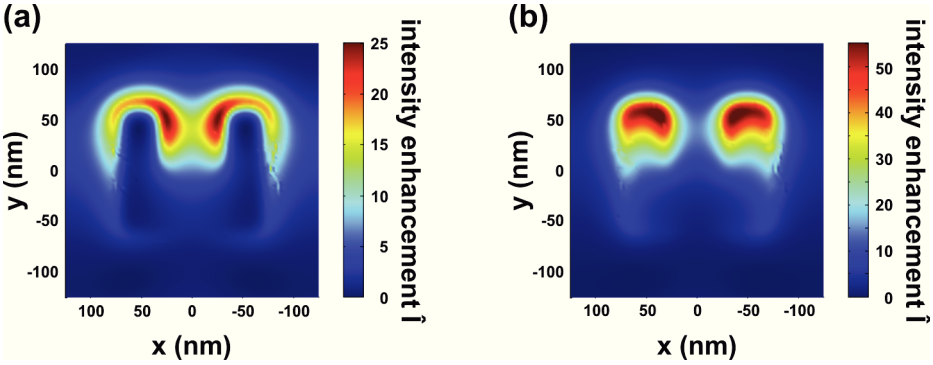

Figure 6.7: Intensity $|\mathbf{E}|^2$ enhancements calculated by DGTD for an SRR representing the ones of field D in the central plane of the quantum well ($z = -12.5\,\mathrm{nm}$): (a) Enhancement of the in-plane components of $\mathbf{E}$, (b) intensity enhancements of all field components.

If the decay-rate enhancement marks the onset of lasing we expect the decay to be faster with higher pump powers. Since we already use the maximum pump power we can derive from our experimental setup ($P_{\mathrm{pump}} = 200\,\mathrm{mW}$) we can only check what happens for lower powers. In this case we would expect the fast decay to slow down and resort back to the single-exponential decay with $\tau \approx \tau_{\mathrm{QW}}$ eventually.
We therefore repeat the measurements on field F for pump powers of $100\,\mathrm{mW}$, $50\,\mathrm{mW}$ and $10\,\mathrm{mW}$ and also reduce the original probe power of $70\,\mu\mathrm{W}$ so that the ratio of pump and probe power is kept constant at $20000 : 7$ ($\lambda_{probe} = 1500\,\mathrm{nm}$). We can see from the results presented in Fig. 6.6 b that the temporal dynamics of the pump-probe signals on the array do not change significantly with the pump power. They especially do not follow our expectation that the fast component vanish when we decrease the pump power.
From this we conclude that our system is not on the brink of lasing and that the decay-rate enhancements must be explained otherwise.

We are thus left with the Purcell effect as the most probable cause of this observation. We check this assumption in the following paragraph with the help of numerical calculations.
As we have stated in section 3.3.3 the Purcell effect leads to a decay-rate enhancement which is correlated with an increase in the local density of states (LDOS). In the presence of a resonant plasmonic particle we can in turn link the increased LDOS to the near-field-intensity enhancement resulting from the plasmon resonance. As we have no direct experimental access to the near-fields generated by the SRR metamaterial we derive this information from numerical calculations *via* a discontinuous Galerkin time-domain (DGTD) method (compare section 4.3) that is implemented by the group of Prof. Kurt Busch.
Michael König performed DGTD calculations for silver ($\omega_{\mathrm{pl}} = 1.37 \times 10^{-16}\,\mathrm{s}^{-1}$, $\omega_{\mathrm{c}} = 0.84 \times 10^{-14}\,\mathrm{s}^{-1}$) SRRs ($l_{\mathrm{x}} = 145\,\mathrm{nm}$, $l_{\mathrm{y}} = 125\,\mathrm{nm}$, $t = 35\,\mathrm{nm}$, $g = 61\,\mathrm{nm}$, $b = 60\,\mathrm{nm}$, edges are rounded with a radius of $12.5\,\mathrm{nm}$.) arranged in an array with a grating constant $a = 250\,\mathrm{nm}$ on a homogeneous substrate with a refractive index of $n = 2.8$ which is modelled by a half-space. He first determined the wavelength of the fundamental resonance and then calculated the electric fields in the unit cell of the array for different cut planes (z coordinate) of the SRR and the substrate. We can thus calculate the field or intensity enhancement $\hat{I} = I/I_0$ for one particular z plane by taking the ratio of the intensities (or fields)

$I = |\mathbf{E}|^2$ with the SRR to the fields without, i.e. for the substrate alone, $I_0 = |\mathbf{E}_0|^2$.
Figure 6.7 shows the calculated intensity enhancements for a cut plane $z = -12\,\mathrm{nm}$ corresponding to the middle plane of the quantum well. In Fig. 6.7 a we present the enhancement of the in-plane intensity, that is we only take into account the x- and y components of the electric field, so the in-plane intensity becomes $|E_x|^2 + |E_y|^2$. Panel (b) gives the enhancement of the complete intensity where the z component is not eliminated.
For the middle plane of the quantum well ($z = -12.5\,\mathrm{nm}$) and compare the in-plane with the complete intensity enhancement because of the physics of a single quantum well (compare section 3.2): In an infinite quantum well the ground state ($n = 1$) wave function has a maximum at the centre of the well and therefore the probability of presence for an electron is highest there. We thus consider the LDOS enhancement in this plane to be dominant for the Purcell factors we find in our experiments. To better match the experimental conditions we should average over the whole width of the quantum well, ideally weighting this average with the electronic wave function. Since we only aim at an approximation to back our thesis of the origin of rate enhancement we only consider the fields in the symmetry plane.
We know from the selection rules that the heavy-hole exciton in a quantum well cannot couple to an electric field in z direction if excited with a plane wave where there is no strong field gradient over the width of the quantum well. Therefore the in-plane intensity enhancement (Fig. 6.7 a) would be relevant for an estimation of the Purcell factor. The near-fields of a plasmonic nanostructure, however, cannot be described with plane waves; moreover, their decay into the substrate happens on the same scale as the width of the quantum well ($\hat{z} = 20\,\mathrm{nm}$ where $I_z = I_{z=0}/2$, taken from the calculations). We thus do not expect the selection rule stated above to hold true for this case and expect the quantum well to also couple to the z component of the electric field.

In conclusion, the enhanced LDOS and with this the Purcell factor resulting from the presence of the SRRs can be estimated from the complete intensity enhancement as it occurs in the central plane of the quantum well. From Fig. 6.7 b we therefore approximate the maximum Purcell factor to $F \approx 50$. This is in good agreement with the experimental decay-rate enhancement for the fast time component, where $F = \tau_{\mathrm{QW}}/\tau_1 = 670\,\mathrm{ps}/15\,\mathrm{ps} = 44.6$.
The plasmonic intensity enhancement presented in Fig. 6.7 is obviously not distributed uniformly over the whole unit cell but rather exhibits certain *hot spots*, that is areas of high enhancement factors, and large areas with much lower enhancement factors. This, we presume, is the cause of the two different lifetimes we find in our experiments: because the low-enhancement regions lead to a lower Purcell factor than the high-enhancement regions the original lifetime τ_{QW} of the quantum well is influenced differently, resulting in a multi-exponential decay instead of a single-exponential one.
There is, of course, no general reason why there should be exactly two different decay constants and not an arbitrarily high number of them. However, this simplest of the more complex decay dynamics fits our experimental data rather well (Fig. 6.6 a) and we see no reason to complicate matters further since the scope of these calculations does not go beyond first-order approximations, anyway.

Overall, we prove substantial coupling between a plasmonic metamaterial and a single quantum well by time-resolved pump-probe measurements. We find a significant difference in sign

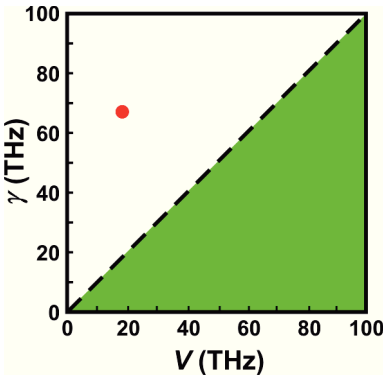

Figure 6.8: Illustration of the extent of loss-compensation we have achieved for field D given by the red dot. The dashed line marks the limiting condition of $\gamma = V$ between the white triangle, for which no permissible solution of equation (6.4) exists and the green triangle where such a solution can be found, thus losses can be compensated completely.

and magnitude of the differential transmittance for the measurements on the resonant arrays compared to all reference measurements. Furthermore, we observe a dramatic change in the dynamics of the system in form of a double-exponential instead of a single-exponential decay with much shorter lifetimes than for the quantum well alone. We attribute this decay-rate enhancement to the Purcell effect, i.e. an enhanced LDOS due to the plasmonic near-field enhancements.

6.2.4 Extent of Loss-Compensation

As the ultimate goal of coupling metamaterials to gain media is the compensation of Ohmic losses in the metal structures we briefly want to examine in how far we succeed in doing so and evaluate if, from our experimental data, we can consider such loss-compensation feasible.
From our pump-probe data we have already found qualitative evidence of some loss-compensation but we now want to quantify this effect. We therefore first derive a measure to judge the extent of loss-compensation in relation to a metamaterial in which losses are completely compensated. For this reason we return to the toy model (Chapter 5) for the best-case scenario when the two resonance frequencies Ω_{pl} and Ω_{2LS} are equal. For this degenerate case the condition where the loss exactly compensates the gain is given by the occupation factor f of the upper level

$$f = \frac{1}{2}\left(1 + \frac{\gamma_{\mathrm{pl}}\gamma_{\mathrm{2LS}}}{V_{\mathrm{pl}}V_{\mathrm{2LS}}}\right) \equiv \frac{1}{2}\left(1 + \frac{\gamma^2}{V^2}\right) \in [0,1] \tag{6.4}$$

where we have introduced the effective damping and the coupling frequencies γ and V (for a detailed derivation of this equation see Appendix A). If the zero-loss condition - where the gain equals the loss - can be fulfilled, equation (6.4) has a solution in the allowed interval $[0,1]$ (green triangle in Fig. 6.8); if such a solution does not exist, the zero-loss criterion cannot be met for the given set of toy model parameters (white triangle in Fig. 6.8).
For the toy model parameters from the fit to the experimental data (compare Fig. 6.5) of field D on sample NA1 we can calculate the effective damping and coupling frequencies as

$$\gamma = 67\,\mathrm{THz} \quad \text{and} \quad V = 18\,\mathrm{THz}. \tag{6.5}$$

Figure 6.8 illustrates the extent of loss-compensation with respect to the limiting case of $\gamma = V$ (dashed line) for field D. With this sample we are still in the region where equation (6.4) has no solution in the permitted interval and the zero-loss condition can therefore not be fulfilled. It also shows how far away we are from completely compensating the losses: to arrive at the $\gamma = V$ line we would have to increase the coupling (L) by a factor of three to four or increase the quantum-well gain (i.e. the dipole matrix element $d_{2\mathrm{LS}}$) by the same factor. Alternatively we could also decrease the damping of either the SRRs or the QW or perform any possible combination of these strategies.

Chapter 7

Influence of the SRR-QW Separation on Coupling Strength

In the previous chapter we have thoroughly studied if observably strong coupling exists between a plasmonic metamaterial - represented by an array of silver split-ring resonators - and a gain medium, namely an InGaAs-single-quantum well. Having accumulated sufficient evidence for the existence of coupling we now investigate the nature of this coupling in more detail.
Both in the definition of the toy model (Chapter 5) and for the theoretical (section 6.2.3) estimation of Purcell factors we have already assumed the coupling to be mediated by the plasmonic near fields of the metamaterial. We therefore expect the strength of the coupling to significantly depend on the spatial separation of the SRRs from the quantum well. This distance can be adjusted experimentally to a certain degree by introducing an additional spacer layer before we fabricate the metal structures on the quantum-well wafer.
In this way we can, of course, only achieve larger separations of the SRRs and the quantum well, leading to weaker coupling between them. We therefore expect all the effects presented in chapter 6 (large negative values of $\Delta T/T$ together with an enhancement of the decay-rates) as evidence of a coupled system to become less and less pronounced with growing separation.

We start with a brief overview of how we expect the distance between SRR and QW to influence the coupling between them and then define the five samples we have fabricated and investigated in order to study this dependence. Afterwards we pick one particular sample (NA7) and discuss the effects we find there in comparison to sample NA1 presented in the previous chapter. Finally, we assemble the experimental data of all five samples to reveal the behaviour of the SRR-QW coupling with growing separation. To test our assumption of the coupling being mediated by plasmonic near fields we compare the experimental results with intensity enhancements derived from DGTD calculations and find good agreement.

7.1 Changing the Distance

We are interested in how the coupling changes with the distance between the metamaterial and the quantum well because we expect its strength to depend strongly on the spatial overlap

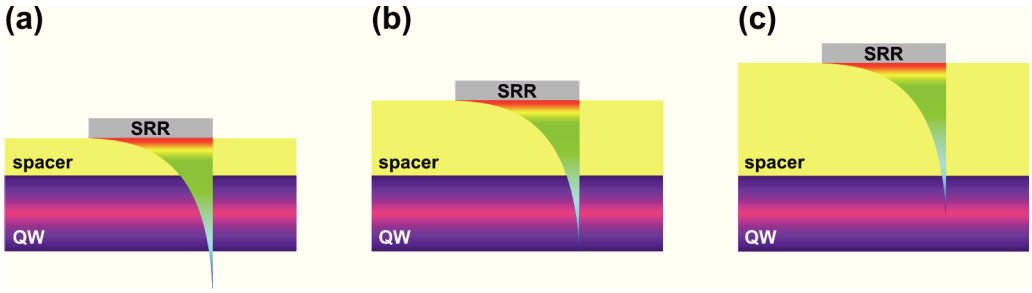

Figure 7.1: Sketch of the spatial overlap of the exponentially decaying plasmonic near field (colour map from blue to red) with the electronic wave function of the single quantum well (colour map purple to pink) with increasing spacer thickness from (a) to (c). The geometry in (a) corresponds to sample NA1, the one in (c) to NA62.

between the plasmonic near field of the SRR and the electronic wave function in the quantum well as depicted in Fig. 7.1. Ideally, the maximum of the plasmonically enhanced near field is at the same z position as the maximum of the electronic wave function, i.e. in the symmetry plane of the well. In an experiment we cannot straightforwardly arrive at such a configuration because the upper barrier, together with the width of the well itself, present a lower boundary to the separation for our standard fabrication procedure.

To investigate in what way the coupling changes with separation we have fabricated five samples where the split-ring resonators are situated at different distances from the centre of the quantum well. The sample with the smallest separation is sample NA1, which we have already presented in Chapter 6; its basis is the quantum-well wafer HSG 37 and no additional spacer layer has been introduced. From the same wafer (HSG 37) we have fabricated three further samples where we have evaporated a defined layer of magnesium flouride (MgF_2) onto the wafer before the lithography step. Samples NA7, NA5 and NA62 thus have additional spacers of $15\,\mathrm{nm}$, $20\,\mathrm{nm}$ and $40\,\mathrm{nm}$ thickness, respectively.
Since this evaporated MgF_2 layers do not form homogeneous closed films for smaller thicknesses we have also used one sample that is based on a different wafer (HSG 33). The quantum well in HSG 33 is of the same nominal thickness as that in HSG 37; their photoluminescence spectra are comparable and the gain is centred around the same wavelengths. The upper barrier of HSG 33 is, however, $9.5\,\mathrm{nm}$ larger than that of HSG 37, which increases the separation of the well from the metamaterial on top.
The details on the wafers and spacer layers of all five samples we use for the investigation of the distance-dependence of SRR-QW coupling are given in table 7.1. Comparing these samples, we have to keep in mind that the refractive index of magnesium flouride ($n_{\mathrm{MgF_2}} = 1.3$) is significantly smaller than that of the semiconductors the QW is made up of ($n_{\mathrm{SC}} \sim 3$). Therefore the near fields decay more rapidly (with distance) in the semiconductor than they do in the dielectric spacer.
Before we now turn to a comparison of all five samples we first look in more detail at sample NA5, whose separation of the SRR from the middle of the QW is roughly twice that of NA1 and see how the effects we found earlier change in this particular case.

sample	QW wafer	cap and barrier	MgF_2 layer	complete top layer
NA1	HSG 37	5.5 nm	0 nm	5.5 nm
FA3	HSG 33	15.0 nm	0 nm	15.0 nm
NA7	HSG 37	5.5 nm	15 nm	20.5 nm
NA5	HSG 37	5.5 nm	20 nm	25.5 nm
NA62	HSG 37	5.5 nm	40 nm	45.5 nm

Table 7.1: Samples used for distance-dependent measurements. Note, that all - apart from one - are based on the same quantum-well wafer HSG 37.

7.1.1 Sample NA7: Doubling the Distance between SRR and QW

The separation of the SRR from the centre of the QW in NA7 is roughly twice as large as for sample NA1. The latter we discussed in some detail in Chapter 6. We therefore want to pick NA7 as reference of the samples with an additional spacer layer and discuss it to a greater extent than the others. It also serves as a start to the comparison with sample NA1, where the metamaterial is closest to the quantum well of all the five samples investigated.

Figure 7.2 shows pump-probe data collected on field C with a fundamental resonance at $\lambda_{\mathrm{SRR}} = 1500\,\mathrm{nm}$; it thus corresponds directly to the measurements presented in Fig. 6.3 and taken on sample NA1. For sample NA7 we also find evidence of coupling in the significant difference of the horizontally probed measurements taken on the arrays (red lines) to those on the bare quantum well (blue lines). Again, no such difference occurs for vertical probe polarisation.
However, the signals we observe on NA7 for the coupled case are smaller in the magnitude of $\Delta T/T$ than that of the bare wafer and do not change dramatically with wavelength. For all accessible probe wavelengths the magnitude of the differential transmittance on the fields is well below $\pm 0.5\%$ whereas the signal on the bare QW varies between 0.4% and 1.9%.
Although we still observe some negative values of $\Delta T/T$ for the on-field measurements they are far from being as pronounced as they are on the resonant fields of NA1; neither are they as frequent and rather present the exception on NA7. Actually, field C here can be seen as the limiting case where the pump-probe signals of a resonant array change from negative to positive, thus being hardly different from zero.

On sample NA1 the dynamics of the system are also changed dramatically - from a slow single-exponential decay on the bare QW to a double-exponential decay with two faster time constants on the SRR arrays. This effect, too, is hardly observable on field C of sample NA7 where the decay on the arrays is a single exponential one and happens at the same time scale as that of the quantum well alone.

A direct comparison of sample NA7 with NA1 distinctly shows how sensitive the coupling between a plasmonic metamaterial and a quantum well underneath is on the relative separation of the two. Despite the additional spacer layer being only $15\,\mathrm{nm}$ thick - thus doubling the distance between SRR and the mid-plane of the QW - the coupling effects are dramatically reduced: we still observe a significant difference between the differential transmittance on the

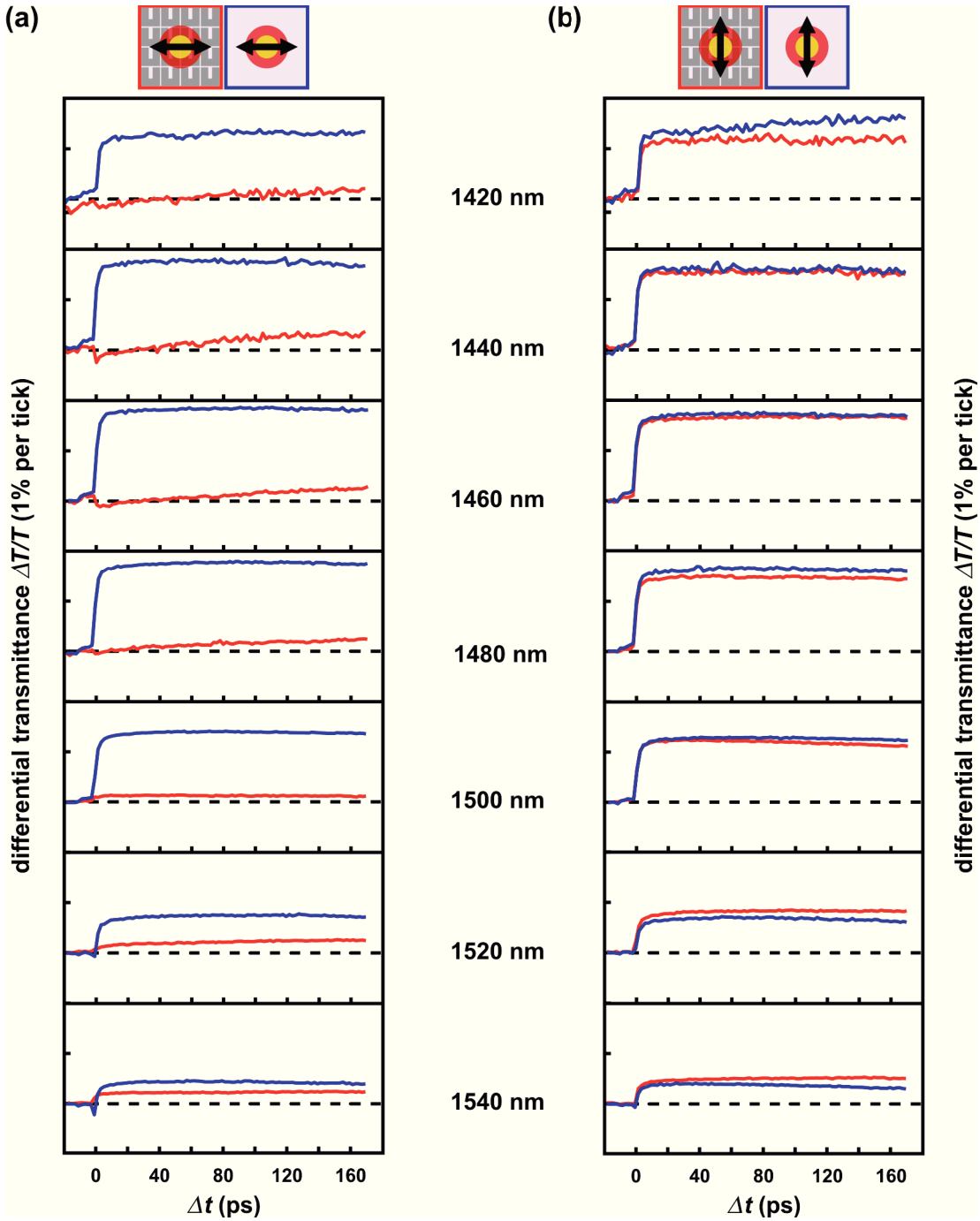

Figure 7.2: Time-resolved pump-probe measurements on field C ($\lambda_{\mathrm{SRR}} = 1500\,\mathrm{nm}$). Red lines correspond to measurements on the SRR array, blue ones to measurements on the bare quantum well. (a) Differential transmittance over time delay for horizontal probe polarisation; (b) the same for vertical probe polarisation. We observe that all effects found on NA1 have decreased significantly (compare Fig. 6.3).

SRR array compared to that on the bare QW but neither large negative signals nor pronounced changes in the system dynamics can be observed.

From the DGTD calculations we have already used in the previous chapter we know that the near fields of the SRRs decay to half their initial strength on the order of $20\,\mathrm{nm}$. In sample

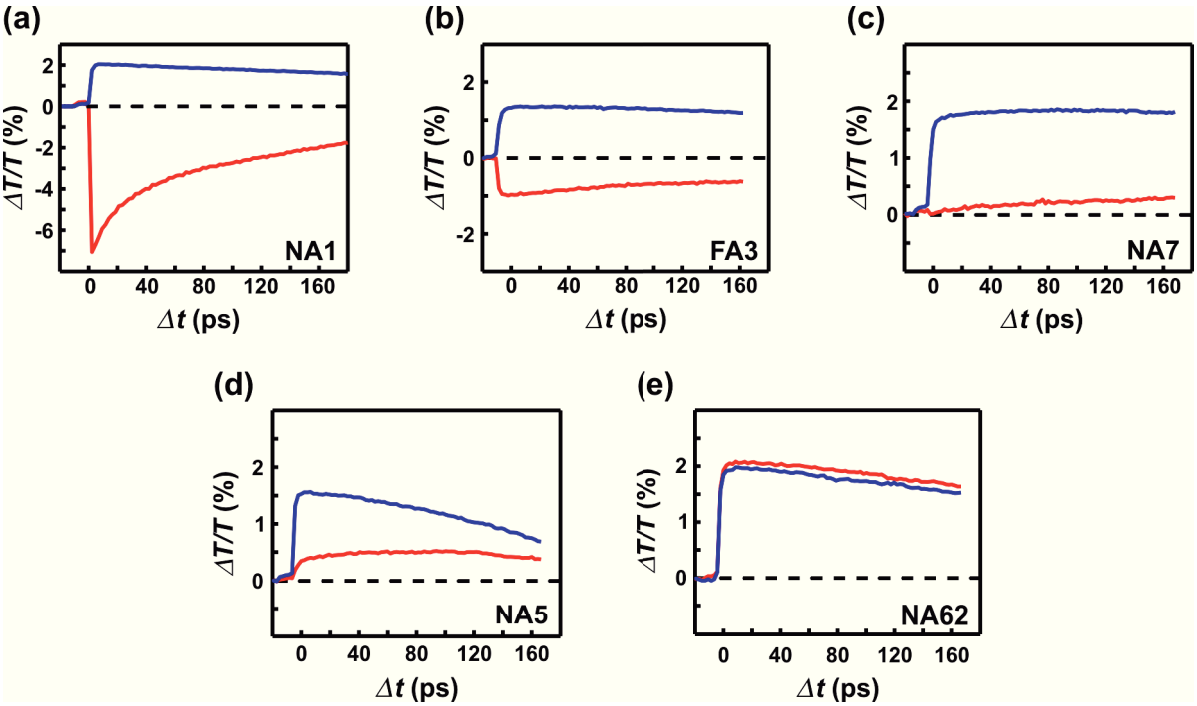

Figure 7.3: Pump-probe measurements for all five samples at a probe wavelength of $\lambda_{\mathrm{probe}} = 1480\,\mathrm{nm}$ taken on SRR arrays whose fundamental resonance is centred around $1540\,\mathrm{nm}$.

NA7 we have artificially enlarged the separation between SRR and QW by $15\,\mathrm{nm}$, which is not far from the decay length of the near fields and find the coupling effects to have reduced significantly. This meets our expectation that the coupling is mainly governed by the overlap of the plasmonic near fields with the quantum-well wave function (Fig. 7.1).

In the following we proceed to a comparison of all five samples (see table 7.1) for which we only use the measurements on one resonant field for the same probe wavelength on each sample.

7.1.2 Different SRR-QW Separations

In the previous chapter we found the most pronounced effects, resulting from the coupling between the SRR array and the single QW, on field D of sample NA1 at a probe wavelength of $\lambda_{\mathrm{probe}} = 1480\,\mathrm{nm}$. The fundamental SRR resonance of this field is centred around $\lambda_{\mathrm{SRR}} = 1540\,\mathrm{nm}$ for low temperatures.
We therefore choose an array of SRRs on each of the five samples[1], which shows a magnetic resonance at approximately the same centre wavelengths $\lambda_{\mathrm{SRR}} = 1540\,\mathrm{nm}$ and compare the differential transmittance we measure on these fields for a probe wavelength of $\lambda_{\mathrm{probe}} = 1480\,\mathrm{nm}$. The resulting time-resolved measurements are assembled in figure 7.3 with growing distance between SRR and QW from (a) to (e).
While we do not observe a significant difference in the differential transmittance of the bare quantum well (blue lines) for the five different samples, we find a distinct dependence of the

[1]The full set of measurements for all fields and all probe wavelength on these five samples can be found in Appendix B.

signal on the arrays (red lines) on the separation of the SRRs from the QW.
The variations we find for the off-field measurements are likely due to slight changes in the measurement parameters (like the maximum accessible pump power) or to diminished quality of the QW when a sample is cut from close to the edge of the wafer.
For the on-field measurement, however, the change in the signals of the different samples is much more prominent and cannot be explained by mere experimental imperfections: For samples NA1 and FA3, where the metamaterial is located relatively close to the quantum well and the overlap between near field and wave function is large, we observe a negative sign of $\Delta T/T$ together with a visible acceleration of the decay compared to the bare well. This decay-rate enhancement is extremely pronounced for NA1 (factor 50 for the fast decay constant) but only slight for FA3 (factor 4).
Like already discussed above, sample NA7 marks the transition from negative to positive differential transmittance signals. Here, for twice the distance from the QW compared to NA1, the on-field signal is hardly different from zero and no significant decay-rate enhancement can be derived from the measurement. If the metamaterial is separated even further from the quantum well (sample NA5) $\Delta T/T$ turns clearly positive with a single-exponential but its magnitude is still different from the measurement on the quantum well alone.
Finally, for an additional $40\,\mathrm{nm}$-spacer (sample NA62) the measurement on the split-ring array is almost indistinguishable from that on the QW close by. This corresponds to the uncoupled case where we do not expect changes in the pump-probe signal stemming from the SRR resonance. The latter will lead to a resonant decrease in the absolute transmittance T of the probe beam but this will not be affected by the pump; the increase in transmittance therefore originates solely from the quantum well. The overlap between the plasmonic near field and the QW wave function is therefore found to be negligibly small for a separation of approximately $52\,\mathrm{nm}$ between SRR and the mid-plane of the QW, which is more than twice the decay length of the plasmonic near fields we derived from the DGTD calculations.

We further condense the above measurements to yield the distance-dependent plot shown in figure 7.4. To this end we introduce the *lift* Δ in the differential transmittance signal, which we define as the difference between the maxima of the pump-probe signals on the bare quantum well to those on the SRR array (compare Fig. 7.4(a)):

$$\Delta = \left(\frac{\Delta T}{T}\right)^{(\mathrm{QW})}\Bigg|_{\Delta t=+5\,\mathrm{ps}} - \left(\frac{\Delta T}{T}\right)^{(\mathrm{SRR+QW})}\Bigg|_{\Delta t=+5\,\mathrm{ps}}. \tag{7.1}$$

This lift from the relative differential transmittance on the array to that on the bare quantum well is an experimental observable that is capable of quantifying the strength of the near-field coupling between SRR and QW. We have already found in section 5.3 that the difference between the pumped and unpumped coupled system, i.e. the differential transmittance, becomes larger when coupling gets stronger (L is larger). For the bare gain medium, however, without any metamaterial resonance to couple to, the coupling strength has no influence on the pump-probe signal. For the extreme case of zero coupling we further expect the relative differential transmittance to be the same on the array and on the bare wafer. Overall, the magnitude of Δ is therefore directly correlated with the strength of the near-field coupling.
The experimentally determined dependence of the coupling strength - described by the lift Δ - on the spatial separation of the SRR and the QW is clearly not linear and resembles the

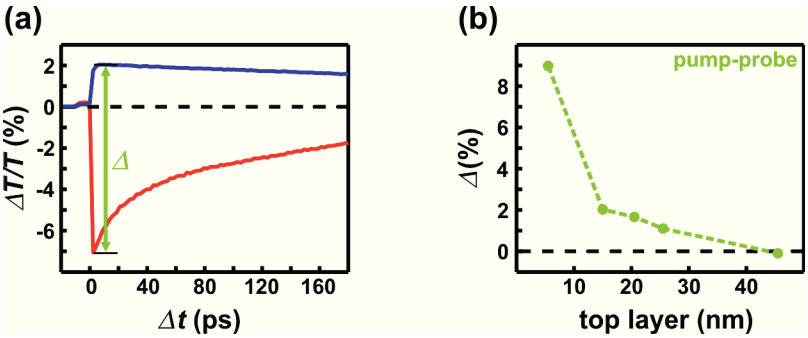

Figure 7.4: (a) Definition of the lift Δ in differential transmittance; as an example we use a set of measurements on sample NA1 (Fig. 7.3 a). (b) Lift Δ in relative differential transmittance (green dots) plotted against the thickness of the complete top layer; the dashed line has been added as a guide to the eye.

exponential decay we expect from near-field effects rather well, as far as this conclusion can be drawn from a set of five distances only.

To further support the relation between the strength of the coupling of the metamaterial to the quantum well and the intensity enhancement of the plasmonic near fields, we return to the DGTD calculations we have already used for this purpose in Chapter 6 in the following section.

7.1.3 Comparison to DGTD Calculations

Still assuming it is the magnitude of the intensity enhancement $\hat{I} = I/I_0$ of the plasmonic near fields that determines the coupling strength between the metamaterial and the QW we first survey in what way this enhancement decays with growing distance from the split-ring resonators. To this end we compare the calculated near-field enhancements which we derive from the same DGTD calculations we use in Chapter 6 in different cut planes. We choose them such that their separation from the bottom of the metal structure is the same as that of the quantum well symmetry plane in the five samples we experimentally study. Since the quantum wells in HSG 33 and HSG 37 are both roughly $14\,\mathrm{nm}$ thick, this means adding another $7\,\mathrm{nm}$ to the *complete top layer* values in table 7.1. The resulting intensity-enhancement distributions for the five samples are presented in figure 7.5.

From these calculations we clearly see how strongly the intensity enhancement depends on the distance from the plasmonic particle. Where the maximum enhancement for the QW mid-plane of NA1 is $\hat{I} = 55$ we only find a maximum value of 22 for that of FA3, which is only $10\,\mathrm{nm}$ further away. This trend of a super-linear decay continues for even larger distances from the SRR, complying with the expectation of an exponential decay we have for plasmonically enhanced near fields.
For sample NA62 (Fig. 7.5 e) we find almost no enhancement of the fields compared to the situation without the SRRs. This fact matches the experimental observation that coupling between the SRR and the QW is almost absent for this sample (compare Fig. 7.3 e). We can therefore conclude that the strength of the coupling is directly correlated with the strength of intensity enhancement generated by the plasmon.

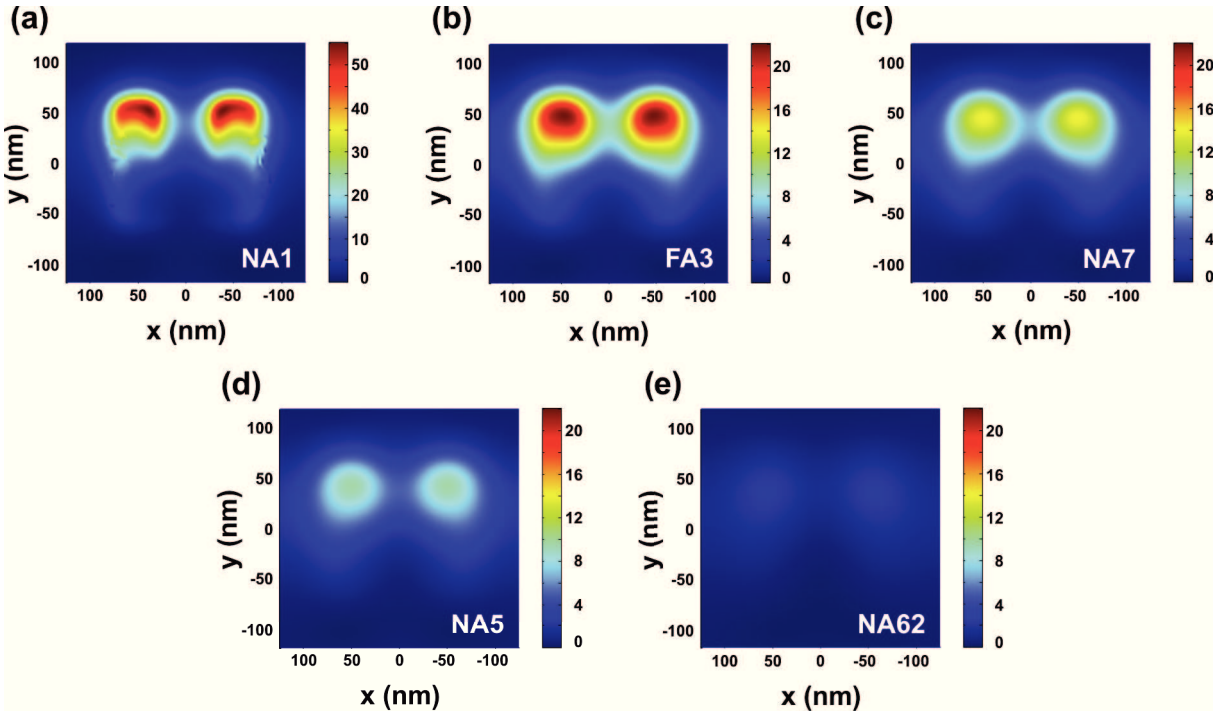

Figure 7.5: Intensity enhancements calculated *via* DGTD for z planes corresponding to the depth of the symmetry planes of the quantum well for each of the five samples. Except for (a) the colour coding is identical in all plots.

The picture we use above, where we only take the maximum value of $\hat{I}$ for one distinct plane, is subject to simplifications: firstly, the calculations do not account for the different refractive index we introduce with the MgF_2 layer. Secondly, we overemphasise the maximum of the wave function in the central plane of the quantum well.
The first simplification is inherent in the way we performed the calculations and only leads to minor digressions from a full treatment, which will lead to the decay length with a lower-index (MgF_2) spacer being slightly longer than for the high-index version in our calculations. The reduction of our considerations to only one point instead of sampling the whole quantum well, however, is significant and we deal with it in the following.

To account for all the different intensity enhancements over the quantum well we simply average the $\hat{I}$ values over the whole unit cell and over a layer of $13.8\,\mathrm{nm}$, which is the thickness of the QW. We thus end up with only one value $\hat{I}_{\mathrm{avg}}$ for every sample configuration, allowing for a direct comparison of how the intensity enhancement varies with distance. Figure 7.6 b shows the resulting plot of $\hat{I}_{\mathrm{avg}}$ against the thickness of the complete top layer, clearly revealing the super-linear dependence on distance; panel a of the same figure repeats the corresponding relation derived from the measurements.
To ease comparison between measured and calculated distance-dependences, which are considered for different observables, we normalise both data sets to the value for the smallest distance from the SRR, i.e. for a complete top layer of $5.5\,\mathrm{nm}$ (sample NA1). We present the resulting graphs in figure 7.6 c and find excellent qualitative agreement: the curves for measurement (green) and calculation (orange) show the same overall behaviour although

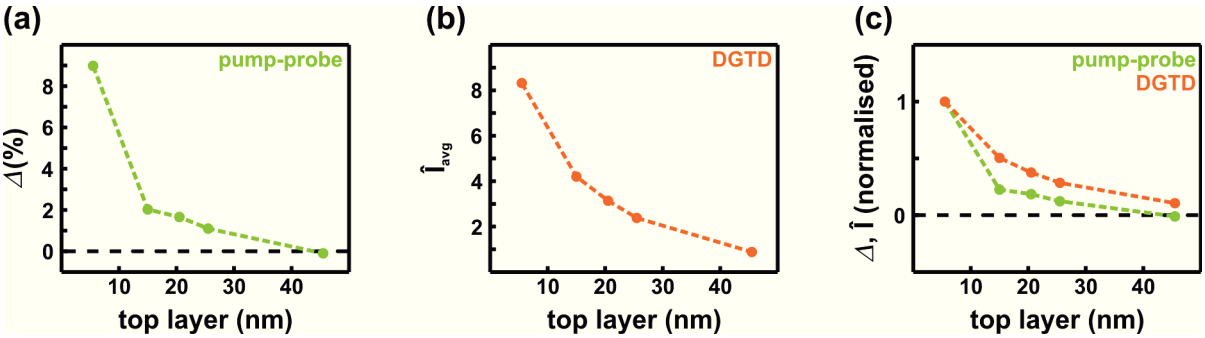

Figure 7.6: (a) Experimentally determined lift Δ in relative differential transmittance (green dots) plotted against the thickness of the complete top layer. (b) Calculated intensity enhancement $\hat{I}_{\mathrm{avg}}$ averaged over one unit cell and the complete thickness of the QW for different depths. (c) Comparison of experimental and theoretical results in (a) and (b); both are normalised to their maximum values to ease comparison. Dashed lines are guides to the eye.

the calculated values are always larger than the measured ones, indicating that the coupling strength decays more slowly in the calculations than it does in the experiments.
Part of this discrepancy results from the particles in the calculations being more perfect than the measured ones; therefore they will likely suffer less losses and thus support stronger, more long-range plasmonic near fields. Furthermore, upon averaging over all intensity enhancements in the whole well, we have used an unweighted average and thereby assume that the coupling strength scales strictly linear with the intensity enhancement and also that every (z) position of the well contributes equally to the coupling. However, we know that in real quantum wells the wave functions can be distorted from the ideally symmetric case by disorder, asymmetry and the finite potential barriers of the QW. The latter assumption does therefore not necessarily hold for a real QW structure but as we do not know the details of these deviations from an ideal QW we choose to consider an ideal, infinite well.

Overall, the agreement between our distance-dependent pump-probe measurements and the DGTD calculations for the plasmonic intensity-enhancement is excellent, especially considering the simplicity of the theoretical model. We take this accordance as evidence of the fact that the coupling between a plasmonic metamaterial and a gain medium is dominated by near-field interactions.
We have assumed this correlation throughout this thesis, starting with the near-field coupling in the toy model (Chapter 5), but we can now rely on experimental data undermining this assumption to be justified.

Chapter 8

Conclusions and Outlook

The scope of this thesis has been to take first steps towards the compensation of ohmic losses in plasmonic structures by introducing a gain medium. This is certainly one of the most pressing issues in metamaterial research because the intrinsic losses hinder all applications suggested for these artificial media. However, the fundamental prerequisite, without which this loss-compensation principle does not work, is a substantial coupling between the plasmon and the gain medium. This thesis has therefore focused on the coupling between a plasmonic metamaterial and a gain medium.

Furthermore, the coupling between plasmonic systems and an emitter or gain medium is of an even more general interest to current research because hybrid systems of plasmonic particles and gain media offer a multitude of fascinating possibilities:
Most closely related to loss-compensation is the concept of the spaser as the plasmonic analogue to the laser as proposed by Mark Stockman and David Bergman in 2003 [20]. As the original spaser operates with dark optical modes Nikolay Zheludev and co-workers have expanded this idea to the lasing spaser where coherent optical emission is possible [23]. In 2009 Mikhail Noginov *et al.* have experimentally realised a spaser-based nanolaser and thus proved the feasibility of this approach [22].
In general, plasmonic antennas can siginificantly influence the radiative properties of emitters. Besides enhancing the efficiency of emission of, for example, fluorescent molecules [17], correctly-designed antennas can also control the direction of emission [18]. Like the aforementioned work a lot of current research focusses on the interaction of plasmonic antennas with single emitters because this system promises interesting quantum-optical phenomena [76] and devices like the generation of single photons and plasmons [77] or the single-photon transistor [19].
The work presented in this thesis has therefore contributed to a vibrant field of optics that offers a wide range of promising research topics and applications because all the above-mentioned effects are essentially based on this interaction mediated by the plasmonic near fields.

For our study, however, we have focused on only one material system: we have chosen arrays of silver split-ring resonators (SRRs) as a suitable example of a plasmonic metamaterial and have employed epitaxially-grown single InGaAs-quantum wells (QWs) as gain medium that we have used as substrate for electron-beam lithography, thus essentially placing the gain underneath the metamaterial.

We have experimentally studied this hybrid system of SRRs and QW - whose fundamental resonance and gain resonance are respectively centred around $1.5\,\mu\mathrm{m}$ - by means of low-temperature femtosecond pump-probe spectroscopy. This method provides a well-defined excitation and de-excitation situation, which has allowed us to arrive at conclusive evidence of coupling between an array of SRRs and a single QW underneath.
This experimental evidence is supported by theoretical studies of the hybrid system, both by numerically acquired near-field calculations and by comparison with a general analytical toy model for the coupling of a plasmon resonance to a two-level-system gain resonance, which we have developed as part of this thesis.

The first step towards understanding the coupling between a plasmonic metamaterial and a gain medium has been the development of a specific but general theoretical model of this very complex hybrid system. Instead of relying on numerical implementations of the plasmonic particle and a suitable three- or four-level-system description of the gain medium used [13, 23], this toy model (Chapter 5) simply couples a bosonic plasmon resonance to a fermionic gain resonance of a two-level system (2LS) *via* near-field interactions. For this approach we neither need to know the geometry of the metamaterial building blocks nor the exact term schemes of the gain medium. It is therefore far less demanding in terms of time and computational resources.
The defining equations of the toy model take the mathematical form of the optical Bloch equations with an additional term that accounts for the coupling between the two resonances. Under transient conditions for a fixed occupation factor f of the upper level of the 2LS, this basic system of equations can be solved analytically within the rotating-wave approximation, which is appropriate for comparison with our experimental situation.
From this solution we have derived transmittance spectra for toy model parameters that were adjusted as to fit the composition of our samples: The plasmonic resonances have been chosen to roughly resemble those of the fabricated SRR arrays in spectral position and lineshape (centre frequency, depth and width of the Lorentzian) and the 2LS has been defined such that it is in accordance with the physical properties of typical InGaAs quantum wells whose gain is centred around $1.5\,\mu\mathrm{m}$.
By systematically changing the centre frequency Ω_{pl} of the plasmon resonance in one case and the value of the near-field-coupling parameter L in another, we have have performed parameter studies of this realistic hybrid plasmon-gain system for both a passive (unpumped) gain medium ($f = 0$) and a fully inverted (pumped) 2LS ($f = 1$). These have shown that the behaviour of the coupled system is very complex and sensitively depends on both the coupling strength and on the relative spectral detuning of the two resonances involved. Comparing the spectra of the pumped 2LS with those of the passive one we find transmittance to generally decrease around the resonance upon pumping, which gives a first impression of the signals we expect from the pump-probe measurements.
For the degenerate case ($\Omega_{\mathrm{pl}} = \Omega_{\mathrm{2LS}}$) we have also found the system to become unstable for strong enough coupling. In this case transmittance rises to values far larger than one in a sharp peak at the common resonance frequency; this can be interpreted as lasing - or rather as lasing spasing since the feedback is provided by the plasmon mode and not by a usual cavity.

In the first experimental section (Chapter 6) of this work we have concentrated on the pump-probe measurements performed on one specific sample (NA1) where the single InGaAs quantum well is situated only $5.5\,\mathrm{nm}$ below the surface and is $13.8\,\mathrm{nm}$ thick (compare Fig. 4.1) with a gain spectrum centred around $1.46\,\mu\mathrm{m}$. On this sample we have fabricated a set of silver SRR arrays that are geometrically adjusted to have their fundamental resonances centred at various spectral positions between $1.20\,\mu\mathrm{m}$ and $1.80\,\mu\mathrm{m}$, which has allowed us to experimentally study the influence of the spectral detuning between the SRR resonance and the gain resonance.

On this sample we have found substantial evidence for the coupling between the quantum well and the plasmonic metamaterial on top of it. We have directly compared the time-resolved relative differential transmittance $\Delta T/T$ on the SRR arrays with that on the bare QW next to the array for several probe wavelengths and have found them to be distinctly different: while the QW shows a maximum $\Delta T/T$ of $1-2\%$ (depending on the probe wavelength) which decays single-exponentially with a lifetime of $\tau_{\mathrm{QW}} = 668\,\mathrm{ps}$ the signals on the arrays are generally negative and differ in magnitude both from that of the QW and for different probe wavelengths.

For the field with the most pronounced effects we have found a maximum $\Delta T/T = -8\%$ at a probe wavelength of $1480\,\mathrm{nm}$ compared to $+2\%$ on the QW in the corresponding experiment. The magnitude of the differential transmittance depends on the spectral position of the probe and is generally larger around the resonance of the QW and smaller for wavelengths away from it. We have been able to fit this behaviour with the toy model described above consistently for all fields measured on this sample, keeping most significant parameters constant and only changing the position of the plasmon resonance to match the array and adjusting the coupling parameter to a certain degree.

Furthermore, the dynamics of the measurements on the arrays are also significantly different from that of the well alone. Most obviously, the temporal behaviour cannot be expressed with a single-exponential decay, like for the bare QW, but follows a more complicated function. We have found the sum of two exponentials with decay constants $\tau_1 = 15\,\mathrm{ps}$ and $\tau_2 = 180\,\mathrm{ps}$ to approximate the dynamics well.

We have thus observed a decay-rate enhancement of 50 times for the fast and of 4 times for the slow time component. These more rapid decays could either originate from quenching to non-radiative modes due to the presence of metal or signify the onset of lasing or result from an enhanced local density of states (LDOS) in the sense of the Purcell effect.

We have ruled out the first explanation by a pump-probe control experiment for a probe polarisation turned by 90° where the fundamental SRR resonance cannot be excited. In this measurement we have seen no significant difference between the measurements on the SRR arrays and those on the bare wafer, neither in the magnitude of the signal nor in the dynamics of the system. We have thus concluded that quenching is not the origin of the more rapid decay times.

The second hypothesis has been tested by an additional experiment where we have varied the pump power. The lifetimes in these time-resolved measurements have not changed with pump power and have especially not become shorter with an increase in power. Lasing can therefore also be excluded as the cause of the decay-rate enhancements observed.

Conclusively, we have been left with the Purcell effect to explain these more rapid decays. Since the Purcell effect describes a decay-rate enhancement by an increase in the LDOS, which

in turn is correlated with the intensity enhancement in the quantum well by the presence of the plasmonic particle, we have employed numerical near-field calculations performed in the group of Prof. Kurt Busch to support this claim. The calculated intensity enhancements reach factors of up to 55, which fits the enhancement factor of the fast decay component surprisingly well. We therefore attribute the rapid decays to the Purcell effect and the two time components to contributions from areas with high intensity enhancements and areas with low intensity enhancements.
Finally, we have developed a means of characterising how far we are still from the goal of complete loss-compensation in the plasmonic metamaterial based on the solution of the toy model for the case of degenerate resonances. Although we have compensated some of the intrinisic losses of the SRRs, we have concluded to be "a factor of three to four" below this goal for the most effectively compensated array on sample NA1. This means we would either need to increase the coupling or the gain by a factor of three to four or decrease the effective damping of the system by this factor or use any combination of these approaches to arrive at the same values in order to reach a zero-loss metamaterial.

In the last part of this thesis (Chapter 7) we have investigated how the coupling strength and the resulting effects in the pump-probe data change if we increase the distance between the quantum well and the split-ring resonators. To this end we have fabricated five samples with differently thick spacer layers on top of the QW. Apart from one sample we have used the same quantum well and have added an additional layer of magnesium flouride to increase this distance.
On these samples we have found the coupling effects described above to be less and less pronounced with increasing distance between the QW and the SRR array. We have observed negative $\Delta T/T$ values less frequently and the decay-rates have been enhanced by smaller factors. Overall, the measurements on the arrays have increasingly resembled those on the bare quantum well the further we have separated the SRRs from the QW. In fact, we would expect the two signals to be identical for a completely uncoupled system, so this observation agrees well with our expectations.
To further support our assumption of the coupling between metamaterial and gain medium to be mediated by the plasmonically enhanced near fields we have again compared our measurements to numerically calculated intensity enhancements. Averaging these enhancements over the complete dimensions of the quantum well underneath one array and examining the dependence of the resulting $\hat{I}_{\mathrm{avg}}$ value on the distance of the well from the surface has yielded a super-linear decay of the intensity enhancement.
We have compared this result to the experimentally found decay of the *lift* Δ of differential transmittance, i.e. the difference of the signal on the field to that on the bare wafer, with growing distance of the QW from the SRR. The two curves are in excellent qualitative agreement and the relative decays from the initial maximum value over distance are also comparable (the actual values cannot be compared directly because Δ and $\hat{I}_{\mathrm{avg}}$ have different dimensions). This has confirmed our expectation that the plasmonic near fields play a dominant and crucial part in the coupling between a plasmonic metamaterial and a gain medium.

By this thorough experimental study of silver SRR arrays on top of single InGaAs quantum wells and comparison of the results with both an analytical toy model and numerical near-field calculations we have proved the existence of significant coupling between the plasmonic metamaterial and the gain medium. This coupling is the essential prerequisite to compensate the intrinsic Ohmic losses of the metamaterial by incorporating gain.
In addition our distance-dependent experiments have confirmed the assumption that this coupling is dominated by near-field interactions between the plasmonic mode and the gain medium. This observation is further supported by numerical near-field calculations that show the same distance-dependent behaviour as our measurements.
This proof can, however, only be the first step towards an applicable loss-compensation scheme. To achieve a zero-loss metamaterial one will have to find a way to increase the coupling between the metamaterial and the active medium, either by designing the plasmonic particles such that they yield higher near-field enhancements or by positioning the gain closer to the particles, preferrably in the plane of maximum field enhancement. This can readily be done by using a different sort of gain medium, for instance molecules in a host matrix [16], but if one wants to stick to semiconductor structures because of their advantages for possible technological applications this means a considerable effort regarding fabrication.

Appendix A

A Loss-Compensation Criterion Derived from the Toy Model

We want to derive a criterion with which to judge the extent of loss-compensation from the simple toy model described in Chapter 5. We start from the defining equations of the toy model in the rotating-wave approximation

$$i\left(\Omega_{\mathrm{2LS}}-\omega\right)\tilde{p}_{\mathrm{2LS}}+\gamma_{\mathrm{2LS}}\tilde{p}_{\mathrm{2LS}} = i\left[\hbar^{-1}d_{\mathrm{2LS}}\frac{\tilde{E}}{2}+V_{\mathrm{2LS}}\tilde{p}_{\mathrm{pl}}\right](1-2f) \tag{A.1}$$

$$i\left(\Omega_{\mathrm{pl}}-\omega\right)\tilde{p}_{\mathrm{pl}}+\gamma_{\mathrm{pl}}\tilde{p}_{\mathrm{pl}} = i\left[\hbar^{-1}d_{\mathrm{pl}}\frac{\tilde{E}}{2}+V_{\mathrm{pl}}\tilde{p}_{\mathrm{2LS}}\right], \tag{A.2}$$

where we have neglected the third equation because we do not need it here. Without an external light field ($\tilde{E}=0$) and for steady-state gain (i.e. f is pinned to a steady-state value) we can readily combine these two coupled equations to

$$\omega^2-\left[\left(\Omega_{\mathrm{2LS}}+\Omega_{\mathrm{pl}}\right)-i\left(\gamma_{\mathrm{2LS}}+\gamma_{\mathrm{pl}}\right)\right]\omega=-\left(\Omega_{\mathrm{2LS}}-i\gamma_{\mathrm{2LS}}\right)\left(\Omega_{\mathrm{pl}}-i\gamma_{\mathrm{pl}}\right)+V_{\mathrm{2LS}}V_{\mathrm{pl}}\left(1-2f\right). \tag{A.3}$$

This quadratic equation straightforwardly leads to the solutions

$$\omega=\frac{\Omega_{\mathrm{2LS}}+\Omega_{\mathrm{pl}}-i\gamma_{\mathrm{2LS}}+\gamma_{\mathrm{pl}}}{2} \pm\sqrt{\left(\frac{\Omega_{\mathrm{2LS}}+\Omega_{\mathrm{pl}}-i\gamma_{\mathrm{2LS}}+\gamma_{\mathrm{pl}}}{2}\right)^2-\left(\Omega_{\mathrm{2LS}}-i\gamma_{\mathrm{2LS}}\right)\left(\Omega_{\mathrm{pl}}-i\gamma_{\mathrm{pl}}\right)+V_{\mathrm{2LS}}V_{\mathrm{pl}}\left(1-2f\right)}, \tag{A.4}$$

which can be simplified to yield

$$\omega=\frac{\Omega_{\mathrm{2LS}}+\Omega_{\mathrm{pl}}}{2}-i\frac{\gamma_{\mathrm{2LS}}+\gamma_{\mathrm{pl}}}{2}\pm\sqrt{\left(\frac{\Omega_{\mathrm{2LS}}-\Omega_{\mathrm{pl}}}{2}-i\frac{\gamma_{\mathrm{2LS}}-\gamma_{\mathrm{pl}}}{2}\right)^2+V_{\mathrm{2LS}}V_{\mathrm{pl}}\left(1-2f\right)}. \tag{A.5}$$

For the zero-loss case when the gain exactly cancels out the loss of the system, the polarisation envelops need to be constant, therefore the imaginary part of equation (A.5) has to be strictly

zero. We can therefore use this fact to arrive at a general gain-equals-loss condition:

$$\frac{\gamma_{2\mathrm{LS}}+\gamma_{\mathrm{pl}}}{2}=\pm\mathrm{Im}\left[\sqrt{\left(\frac{\Omega_{2\mathrm{LS}}-\Omega_{\mathrm{pl}}}{2}-i\frac{\gamma_{2\mathrm{LS}}-\gamma_{\mathrm{pl}}}{2}\right)^2+V_{2\mathrm{LS}}V_{\mathrm{pl}}\left(1-2f\right)}\right]. \tag{A.6}$$

To get a slightly more simple criterion we restrict ourselves to the special case of degenerate resonance frequencies $\Omega_{2\mathrm{LS}}=\Omega_{\mathrm{pl}}$ for which equation (A.6) can easily be solved leading to a criterion for the steady-state occupation factor f

$$f=\frac{1}{2}\left(1+\frac{\gamma_{\mathrm{pl}}\gamma_{2\mathrm{LS}}}{V_{\mathrm{pl}}V_{2\mathrm{LS}}}\right)\equiv\frac{1}{2}\left(1+\frac{\gamma^2}{V^2}\right)\in[0,1]\,. \tag{A.7}$$

Here we have introduced the effective damping and the coupling frequencies $\gamma=\gamma_{\mathrm{pl}}\gamma_{2\mathrm{LS}}$ and $V=V_{\mathrm{pl}}V_{2\mathrm{LS}}$. Since the inversion factor f can only take values in the interval $[0,1]$ we can judge the possibility of complete loss-compensation by the solution of equation (A.7): If a given set of toy-model parameters represented by γ and V yields a solution in the permitted interval zero loss is possible; if the solution does not fall into this interval complete loss-compensation cannot be achieved under these conditions.

Appendix B

Experimental Data: Full Record

The interpretations presented in the main part of this thesis are based on a vast set of experimental data and have therefore not been shown completely within the text. Here, however, we want to present all experimental information gathered from the five samples discussed in sections 6 and 7: These include room-temperature FTIR spectra, scanning-electron microscopy (SEM) images taken after the measurements and the complete time- and wavelength-dependent pump-probe measurements.
In the figures presenting the pump-probe results we stick to the colour code used in the main text, i.e. red lines denote measurements on the split-ring resonator arrays, blue curves correspond to measurements on the bare quantum well. Again, the data for a probe polarisation horizontal with respect to the SRR gap are presented in the left column, those for vertical probe polarisation on the right. The polarisation of the pump beam is always oriented horizontally.

Sample NA1 (HSG 37)

FTIR Spectra

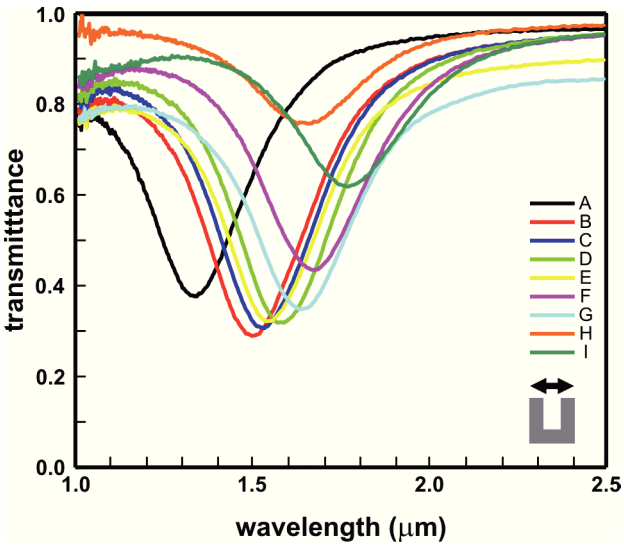

SEM Micrographs

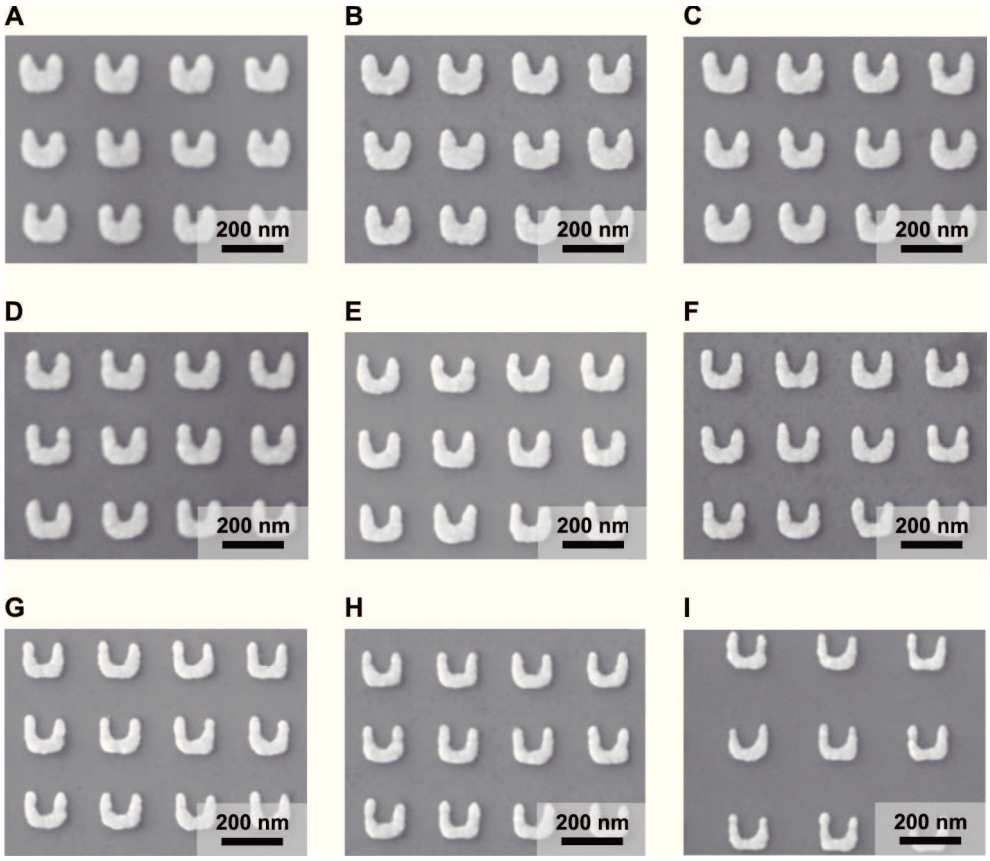

Pump-Probe Data

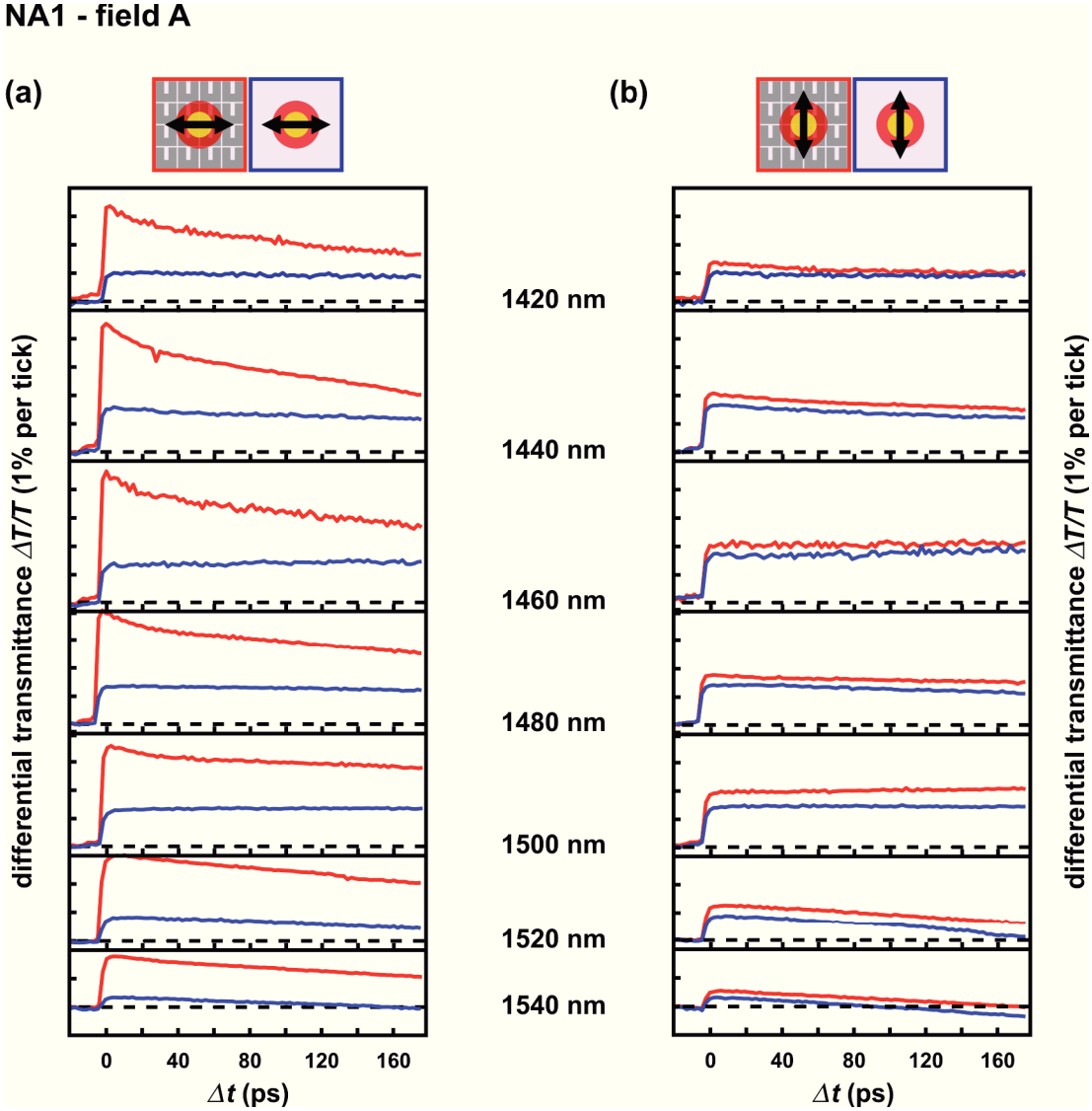

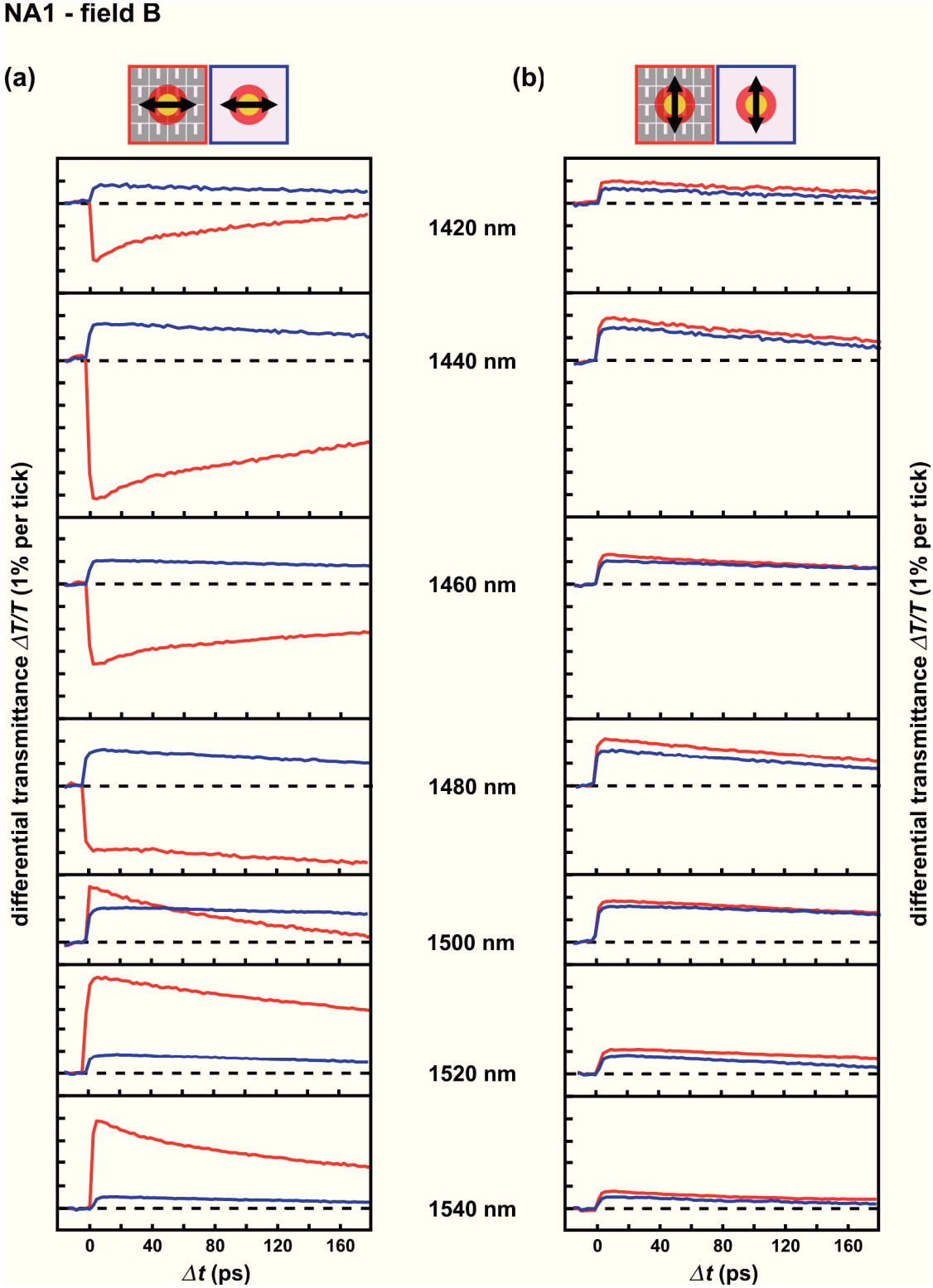
NA1 - field B
(a)
(b)
1420 nm
1440 nm
1460 nm
1480 nm
1500 nm
1520 nm
1540 nm
differential transmittance ΔT/T (1% per tick)
differential transmittance ΔT/T (1% per tick)
0
40
80
120
160
Δt (ps)
0
40
80
120
160
Δt (ps)

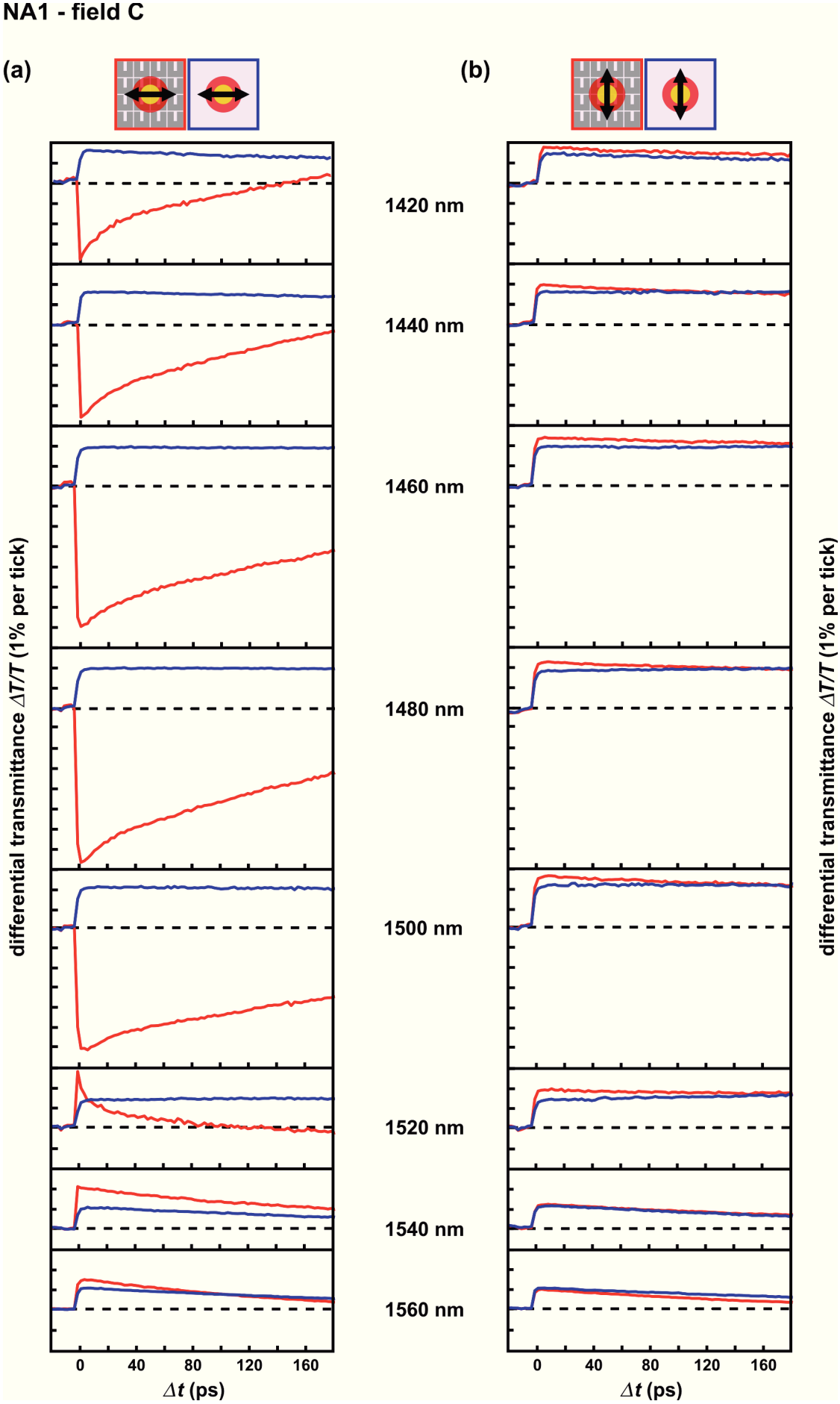
NA1 - field C
(a)
(b)
1420 nm
1440 nm
1460 nm
1480 nm
1500 nm
1520 nm
1540 nm
1560 nm
differential transmittance ΔT/T (1% per tick)
differential transmittance ΔT/T (1% per tick)
0
40
80
120
160
Δt (ps)
0
40
80
120
160
Δt (ps)

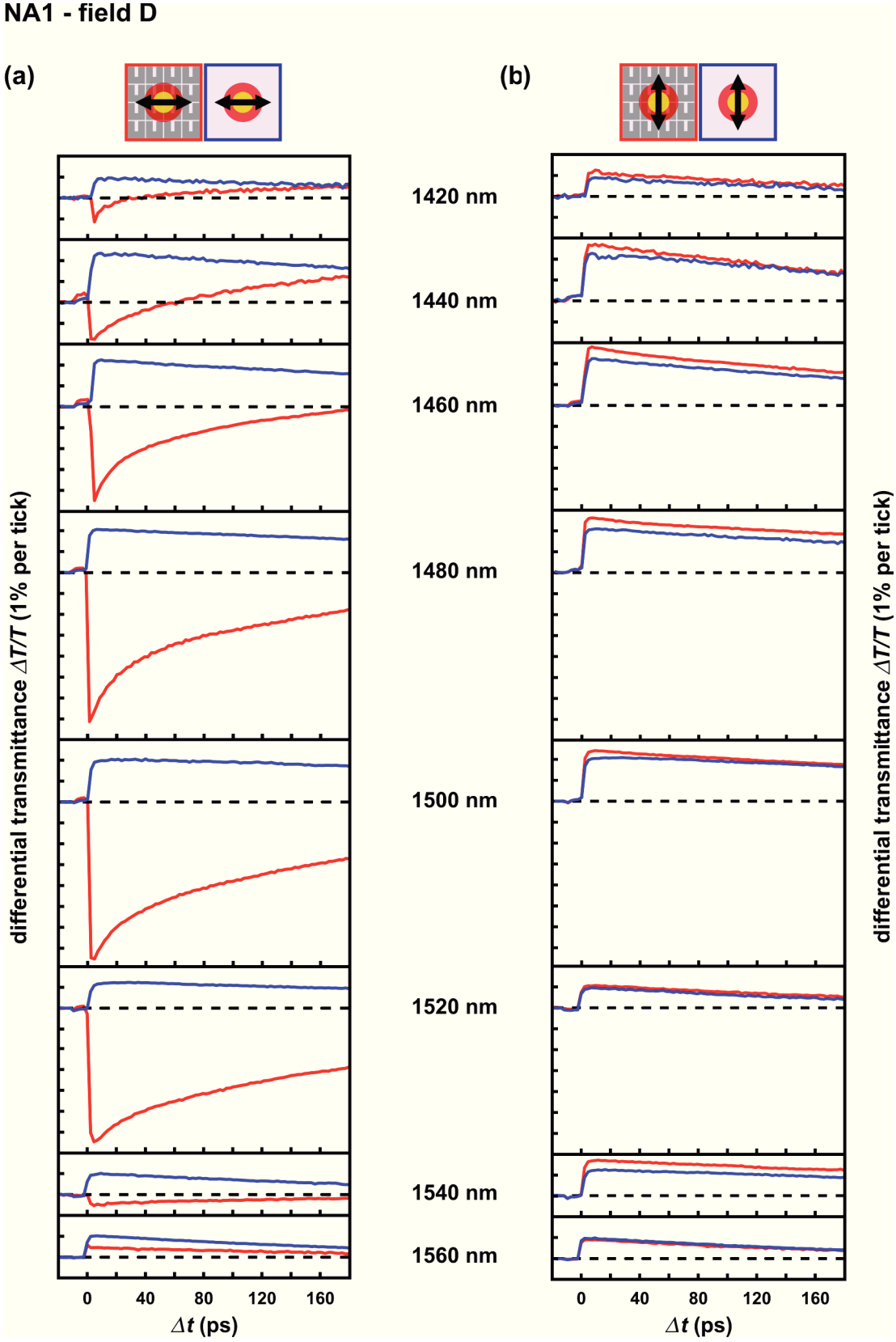
NA1 - field D
(a)
(b)
1420 nm
1440 nm
1460 nm
1480 nm
1500 nm
1520 nm
1540 nm
1560 nm
differential transmittance ΔT/T (1% per tick)
differential transmittance ΔT/T (1% per tick)
0
40
80
120
160
Δt (ps)
0
40
80
120
160
Δt (ps)

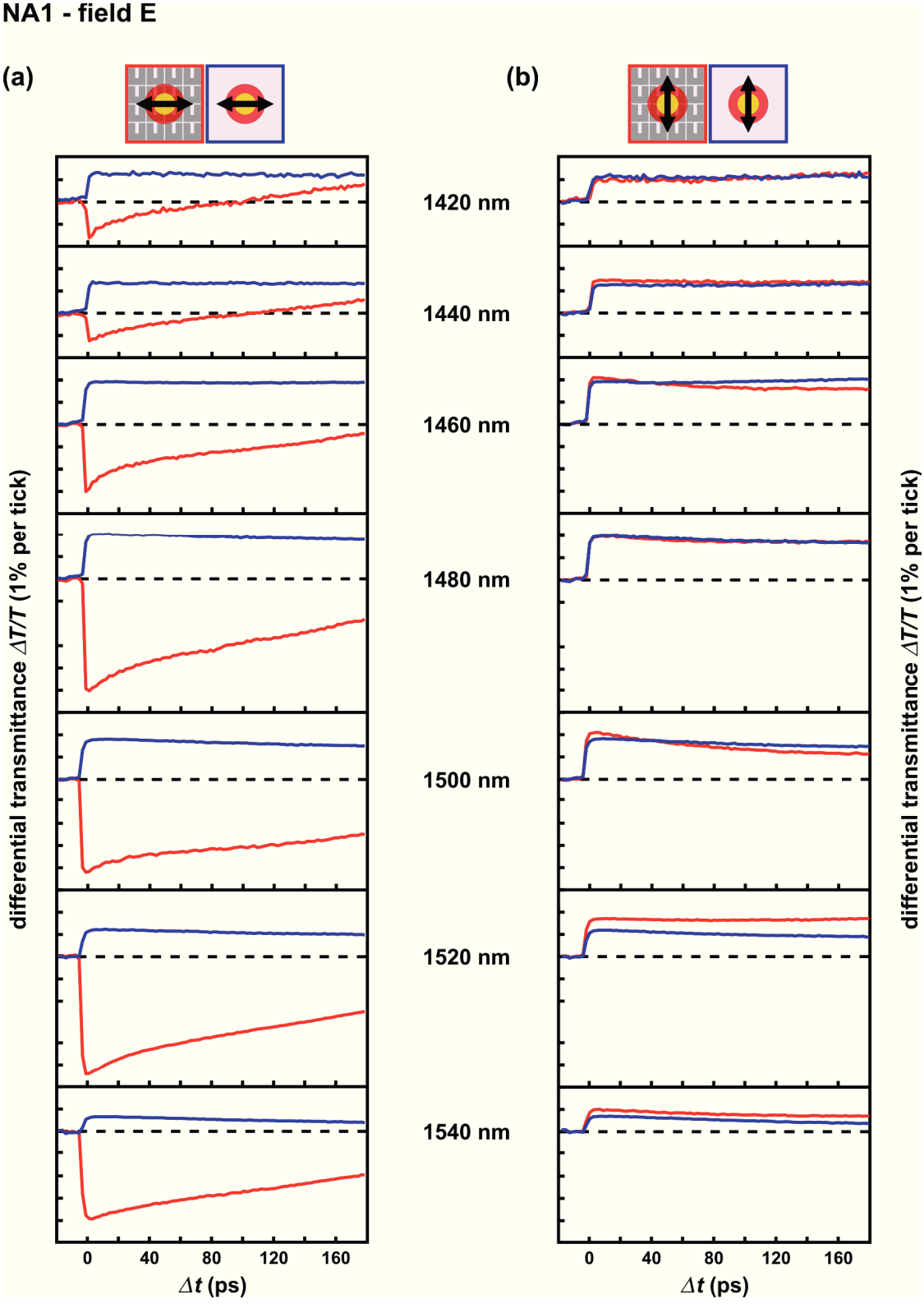
NA1 - field E
(a)
(b)
1420 nm
1440 nm
1460 nm
1480 nm
1500 nm
1520 nm
1540 nm
differential transmittance ΔT/T (1% per tick)
differential transmittance ΔT/T (1% per tick)
0
40
80
120
160
Δt (ps)
0
40
80
120
160
Δt (ps)

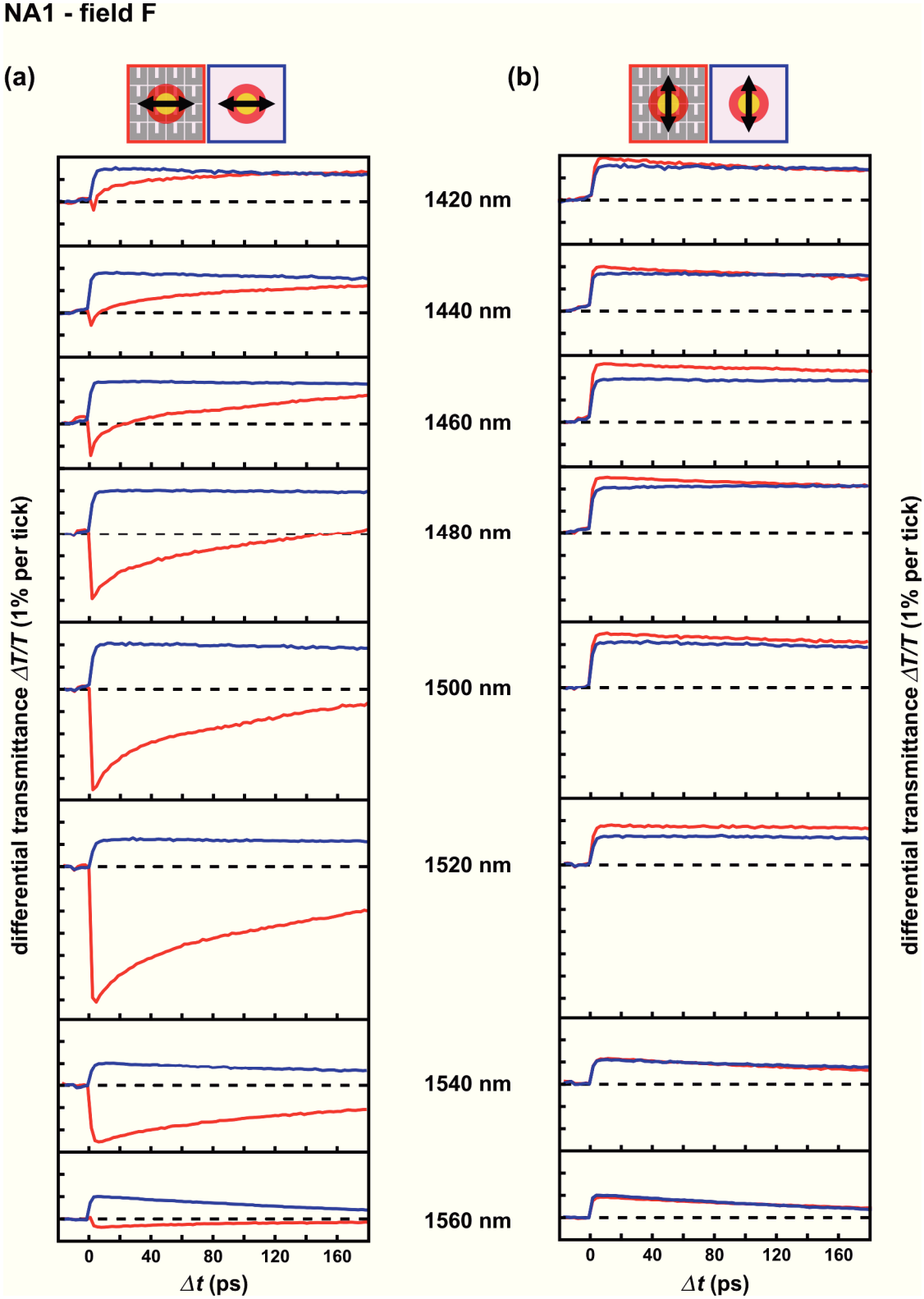
NA1 - field F
(a)
(b)
1420 nm
1440 nm
1460 nm
1480 nm
1500 nm
1520 nm
1540 nm
1560 nm
differential transmittance ΔT/T (1% per tick)
differential transmittance ΔT/T (1% per tick)
0
40
80
120
160
Δt (ps)
0
40
80
120
160
Δt (ps)

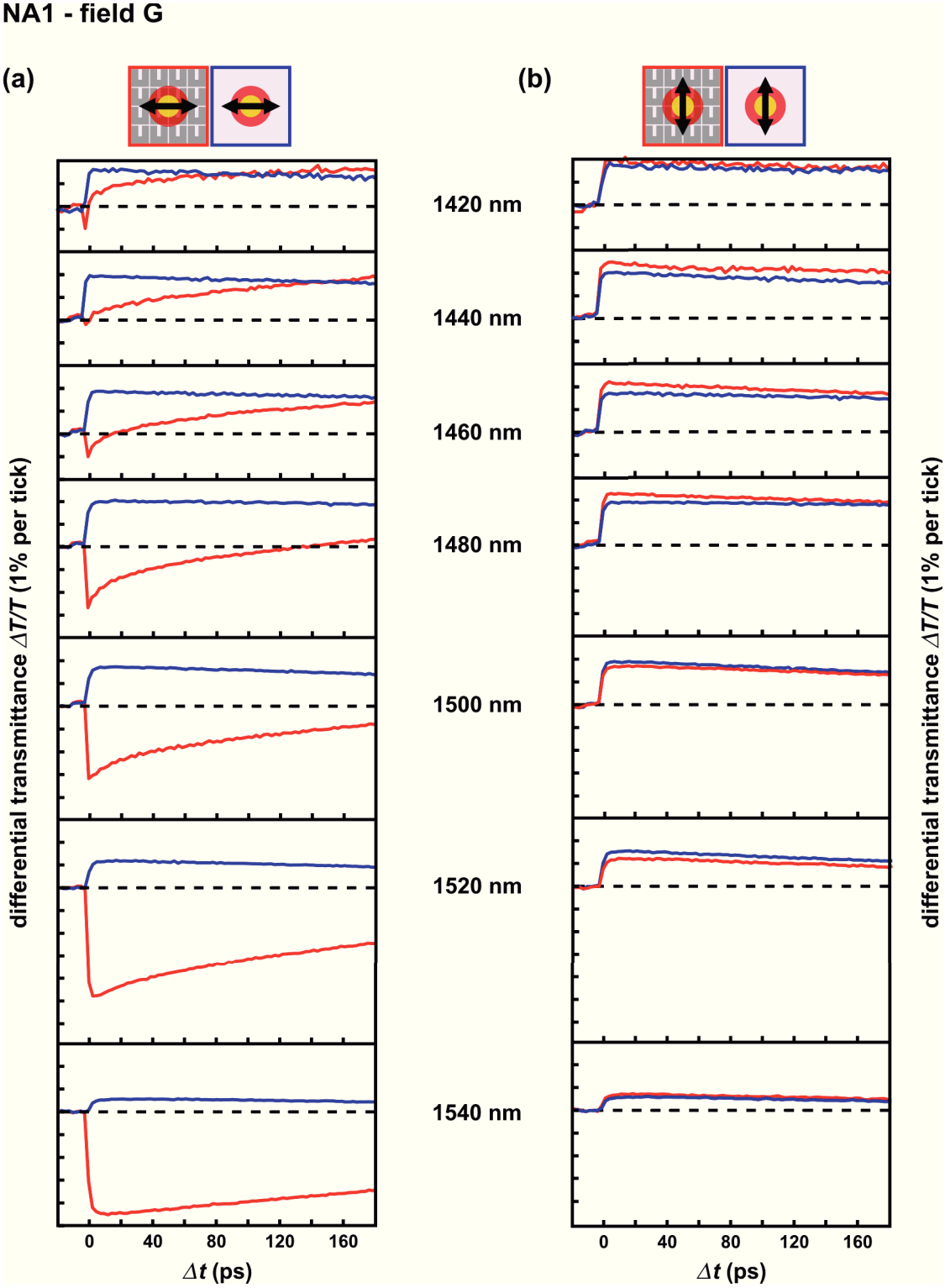
NA1 - field G
(a)
(b)
1420 nm
1440 nm
1460 nm
1480 nm
1500 nm
1520 nm
1540 nm
differential transmittance ΔT/T (1% per tick)
differential transmittance ΔT/T (1% per tick)
0
40
80
120
160
Δt (ps)
0
40
80
120
160
Δt (ps)

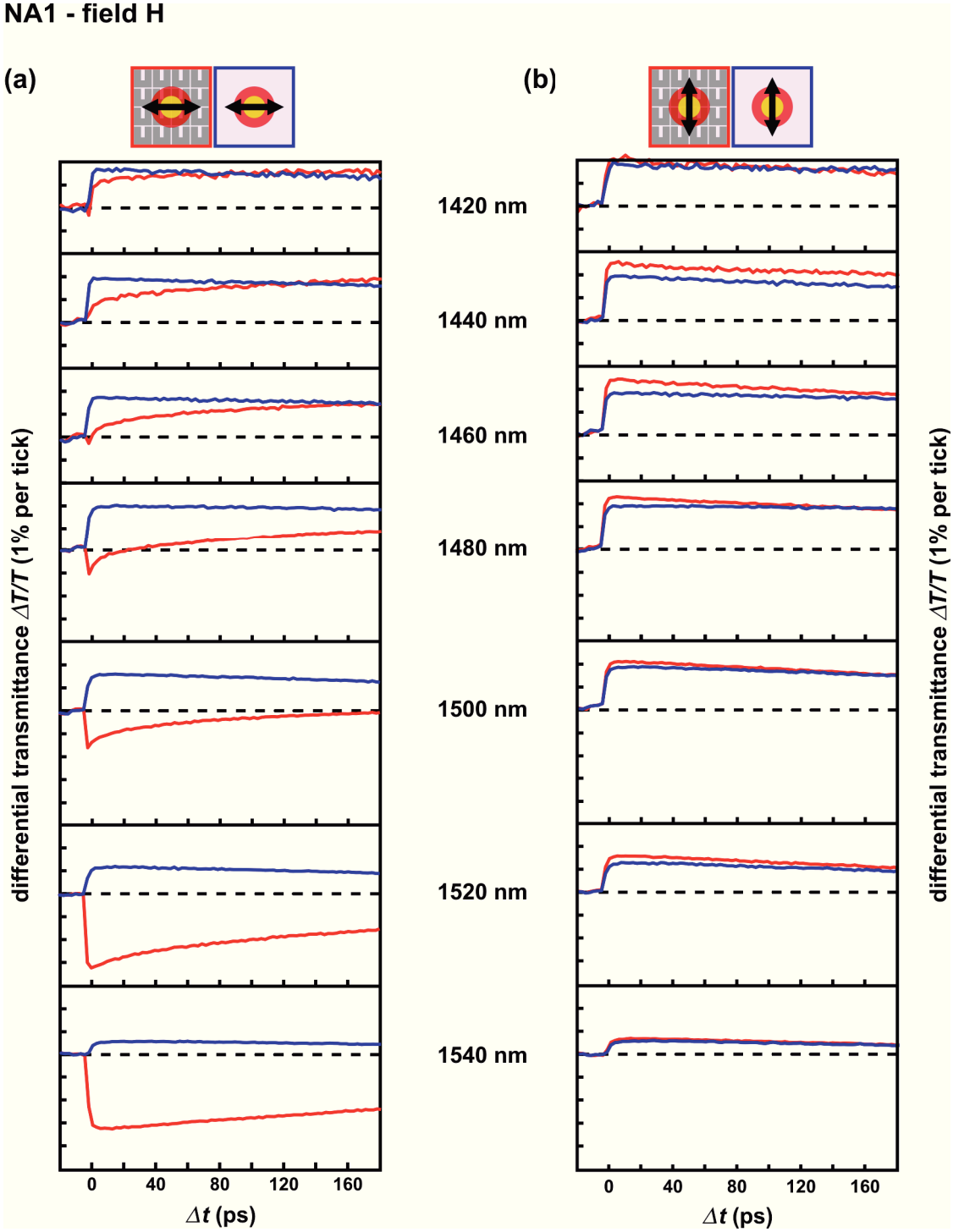
NA1 - field H
(a)
(b)
1420 nm
1440 nm
1460 nm
1480 nm
1500 nm
1520 nm
1540 nm
differential transmittance ΔT/T (1% per tick)
differential transmittance ΔT/T (1% per tick)
0
40
80
120
160
Δt (ps)
Δt (ps)

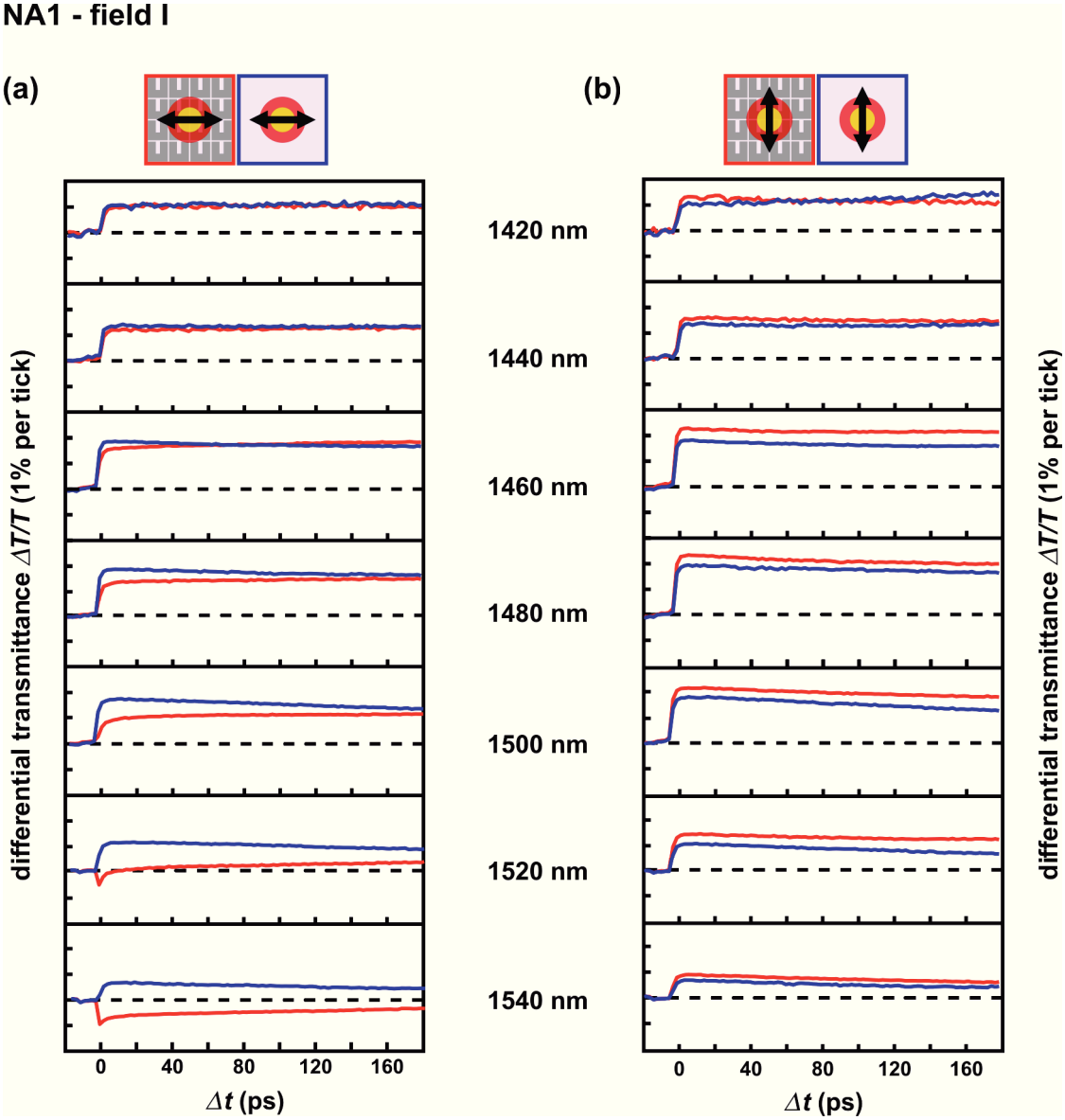
NA1 - field I
(a)
(b)
1420 nm
1440 nm
1460 nm
1480 nm
1500 nm
1520 nm
1540 nm
differential transmittance ΔT/T (1% per tick)
differential transmittance ΔT/T (1% per tick)
0
40
80
120
160
Δt (ps)
0
40
80
120
160
Δt (ps)

Sample FA3 (HSG 33)

FTIR Spectra

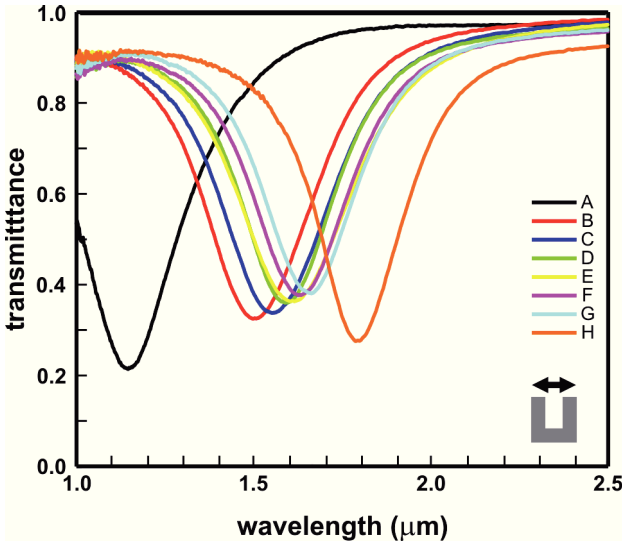

SEM Micrographs

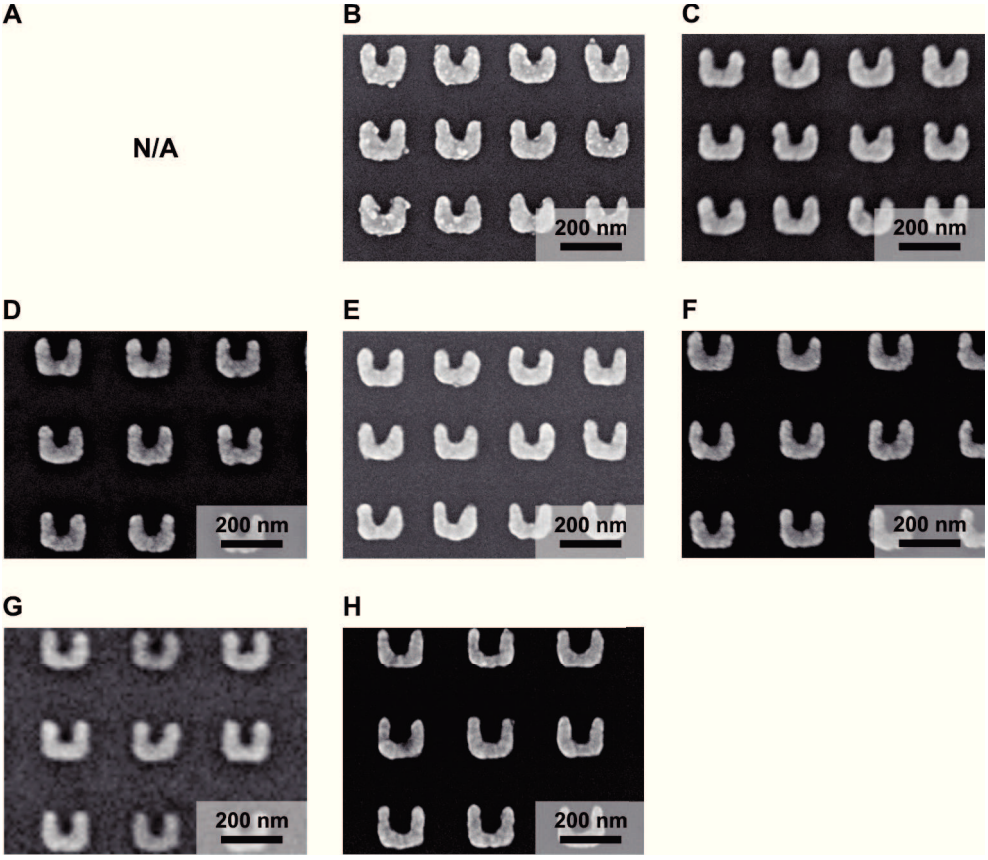

Pump-Probe Data

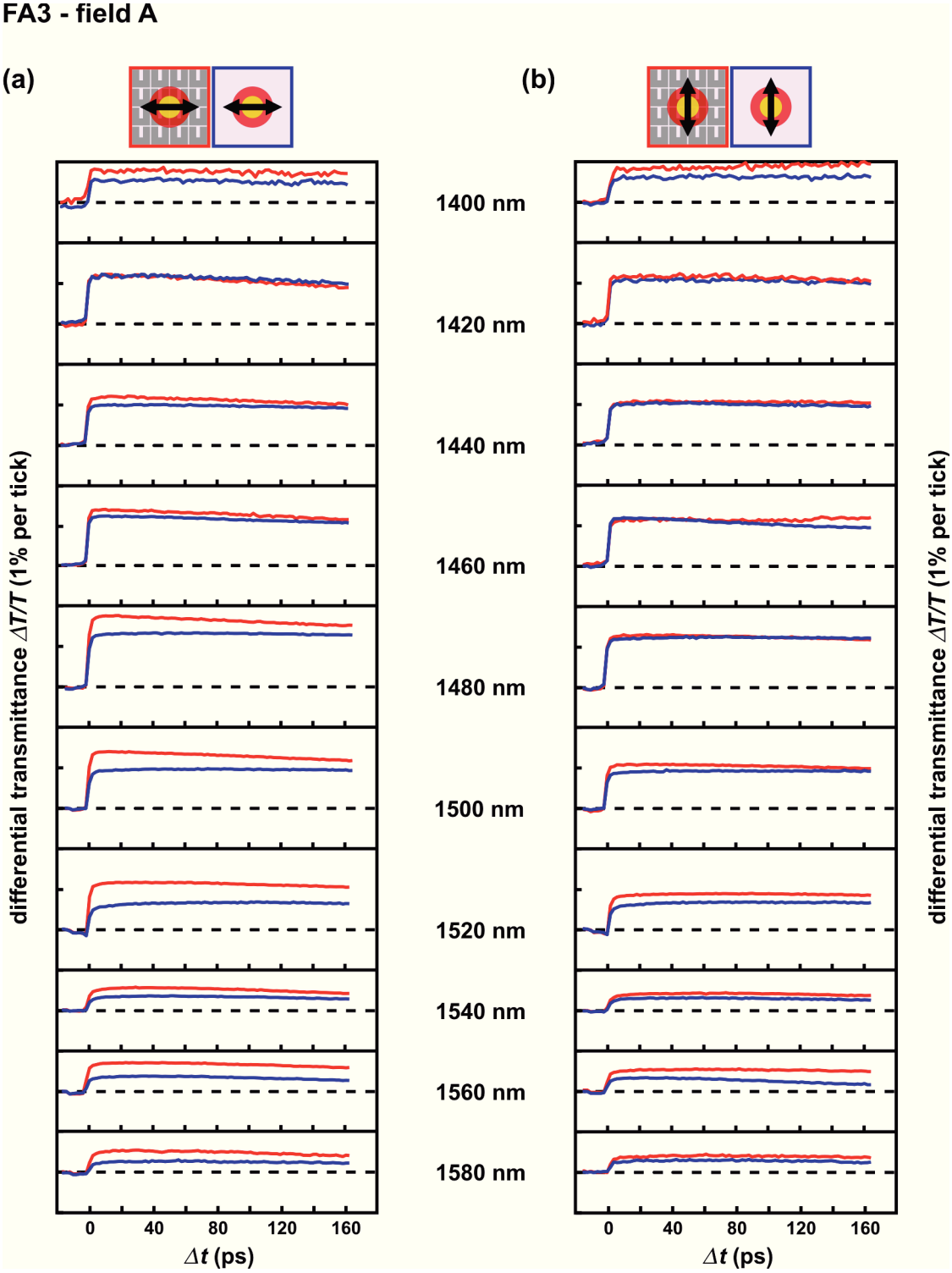

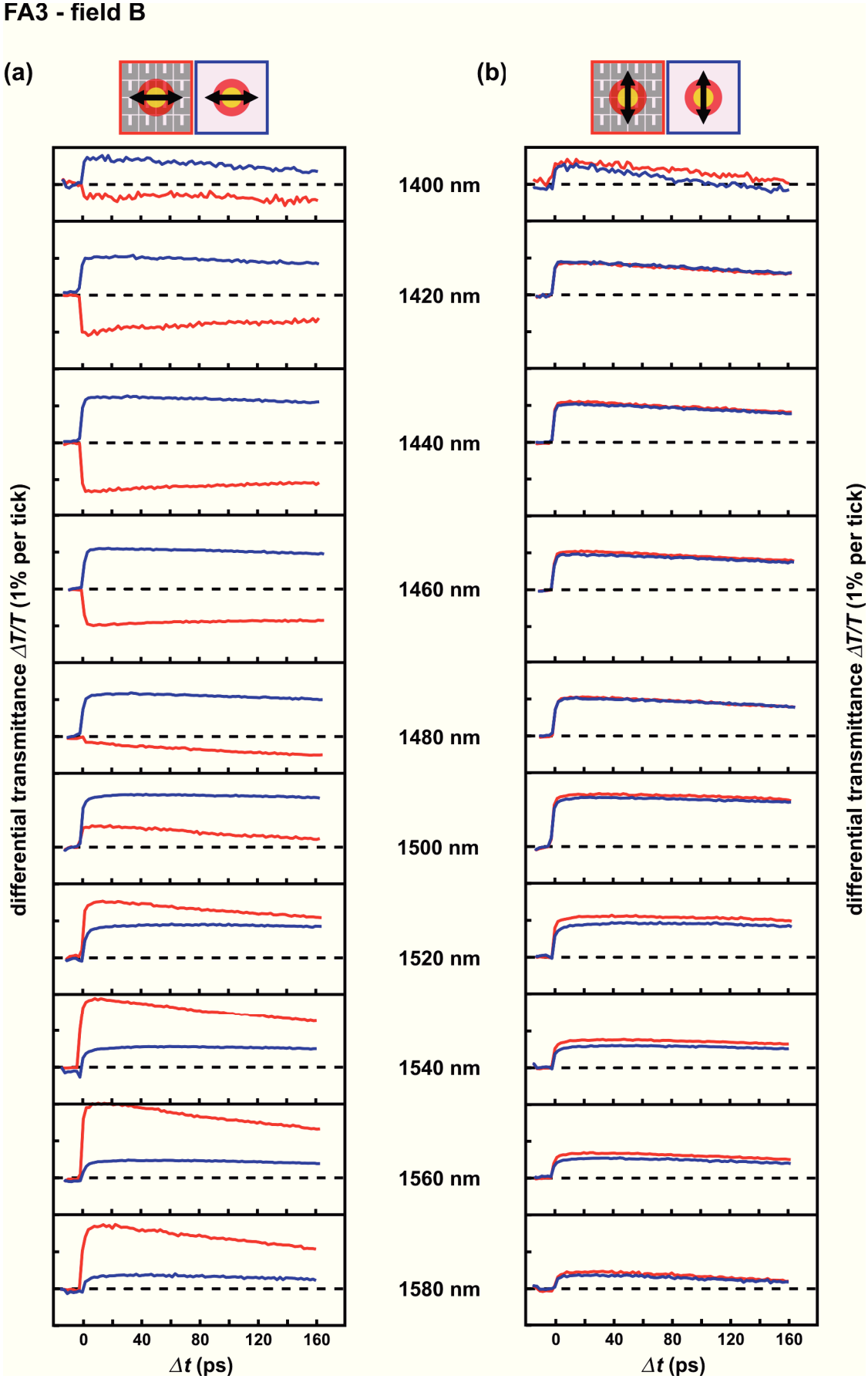
FA3 - field B
(a)
(b)
1400 nm
1420 nm
1440 nm
1460 nm
1480 nm
1500 nm
1520 nm
1540 nm
1560 nm
1580 nm
differential transmittance ΔT/T (1% per tick)
differential transmittance ΔT/T (1% per tick)
0
40
80
120
160
Δt (ps)
0
40
80
120
160
Δt (ps)

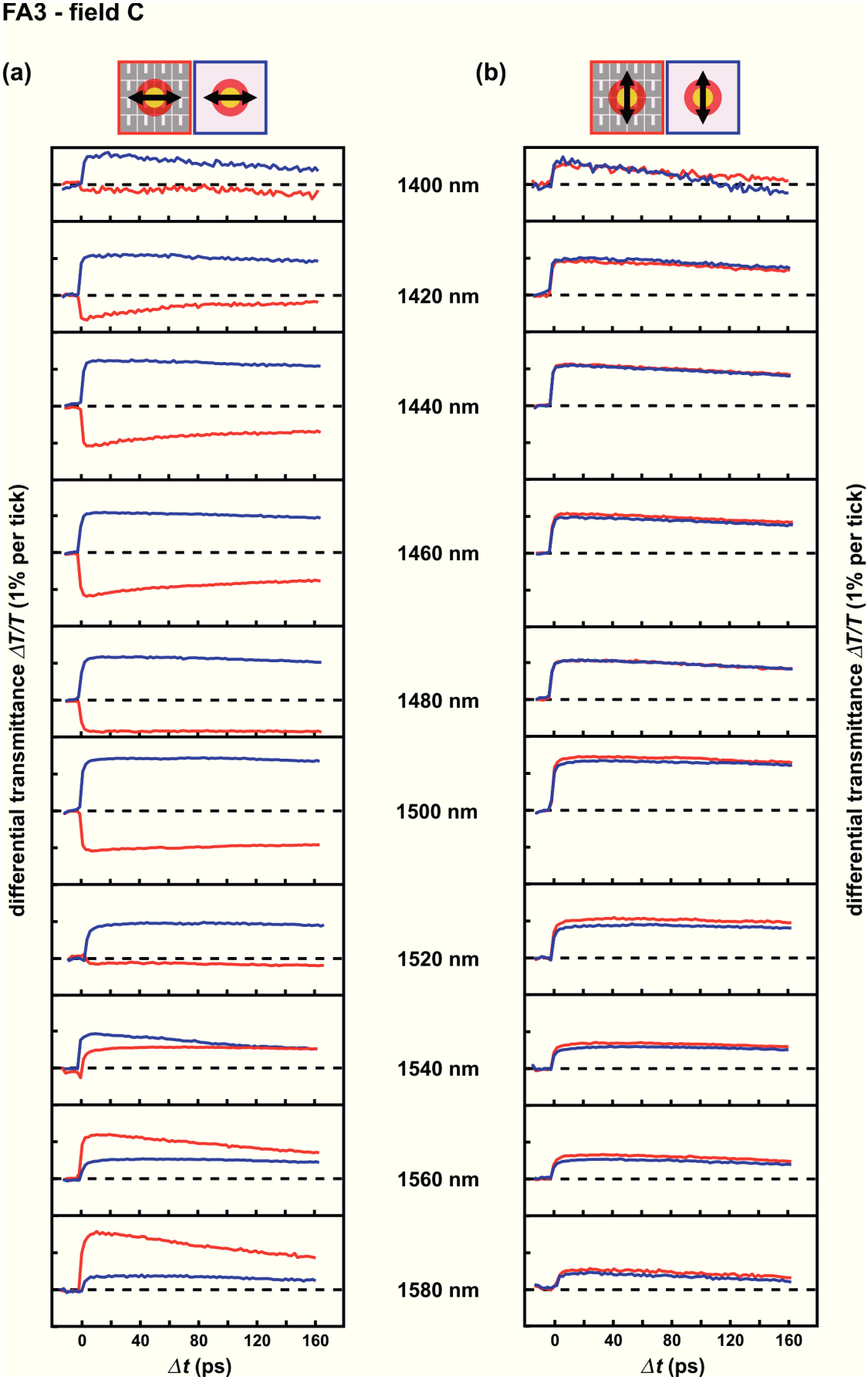
FA3 - field C
(a)
(b)
1400 nm
1420 nm
1440 nm
1460 nm
1480 nm
1500 nm
1520 nm
1540 nm
1560 nm
1580 nm
differential transmittance ΔT/T (1% per tick)
differential transmittance ΔT/T (1% per tick)
0
40
80
120
160
Δt (ps)
0
40
80
120
160
Δt (ps)

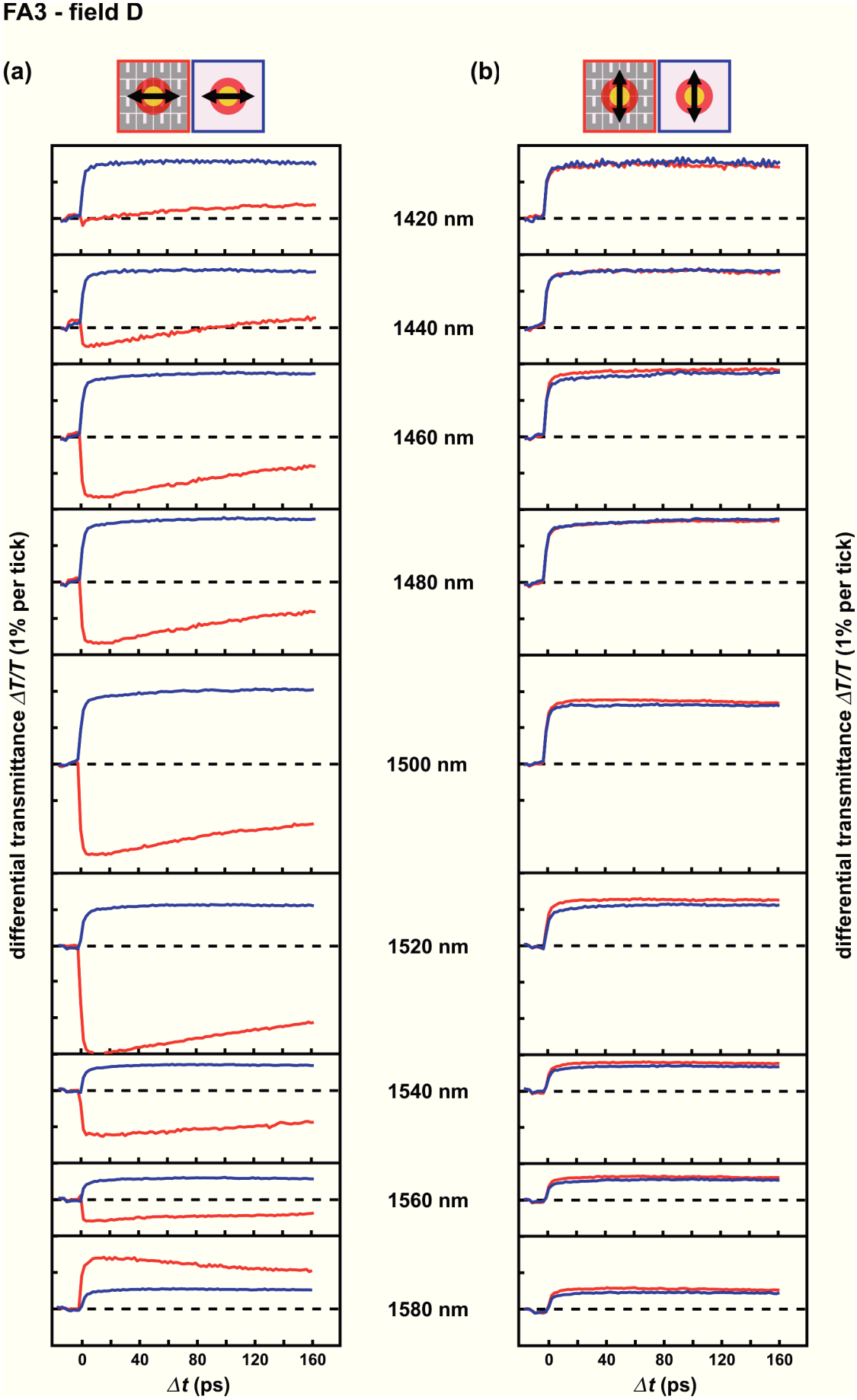
FA3 - field D
(a)
(b)
1420 nm
1440 nm
1460 nm
1480 nm
1500 nm
1520 nm
1540 nm
1560 nm
1580 nm
differential transmittance ΔT/T (1% per tick)
differential transmittance ΔT/T (1% per tick)
0
40
80
120
160
Δt (ps)
0
40
80
120
160
Δt (ps)

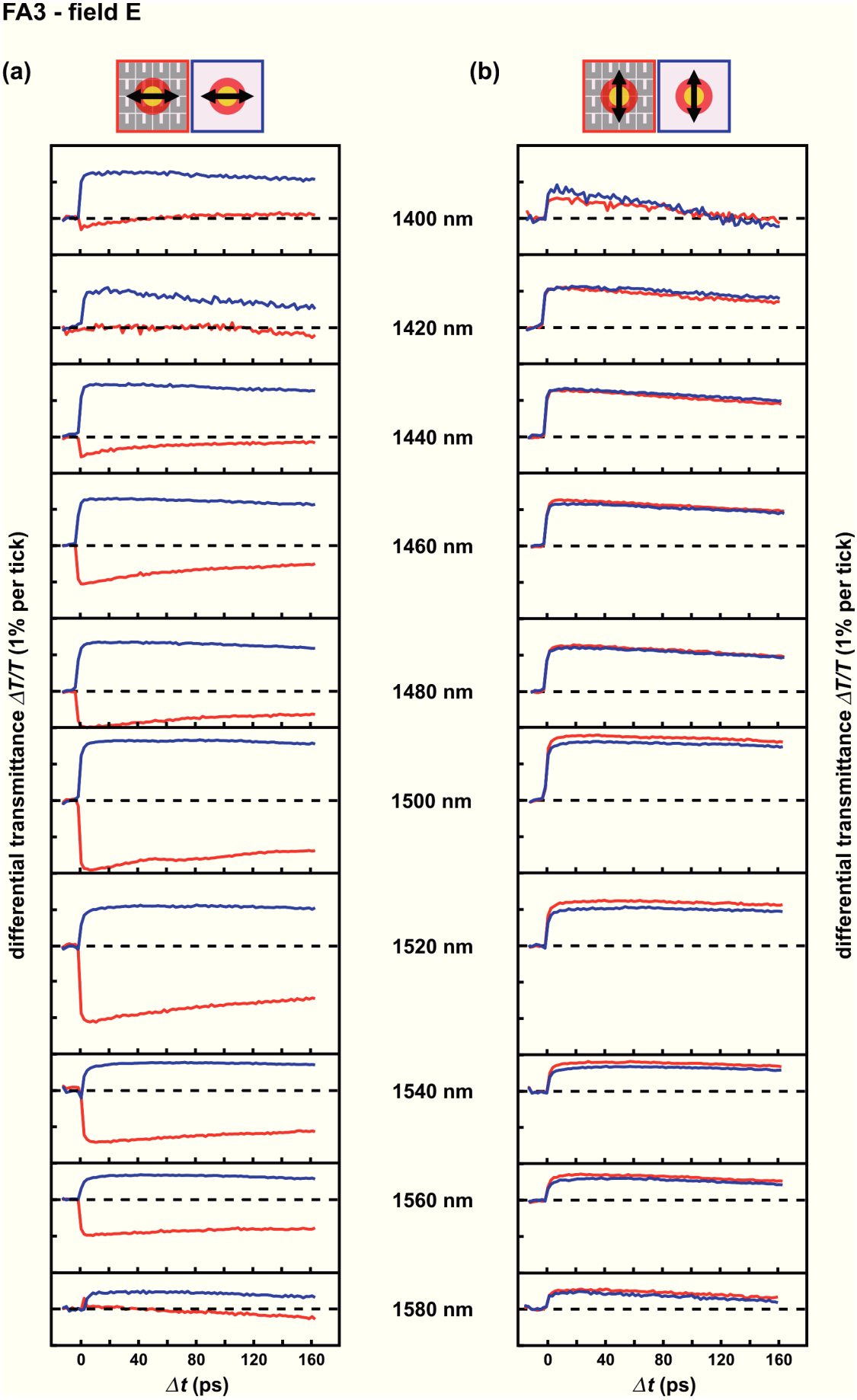
FA3 - field E
(a)
(b)
1400 nm
1420 nm
1440 nm
1460 nm
1480 nm
1500 nm
1520 nm
1540 nm
1560 nm
1580 nm
differential transmittance ΔT/T (1% per tick)
differential transmittance ΔT/T (1% per tick)
0
40
80
120
160
Δt (ps)
0
40
80
120
160
Δt (ps)

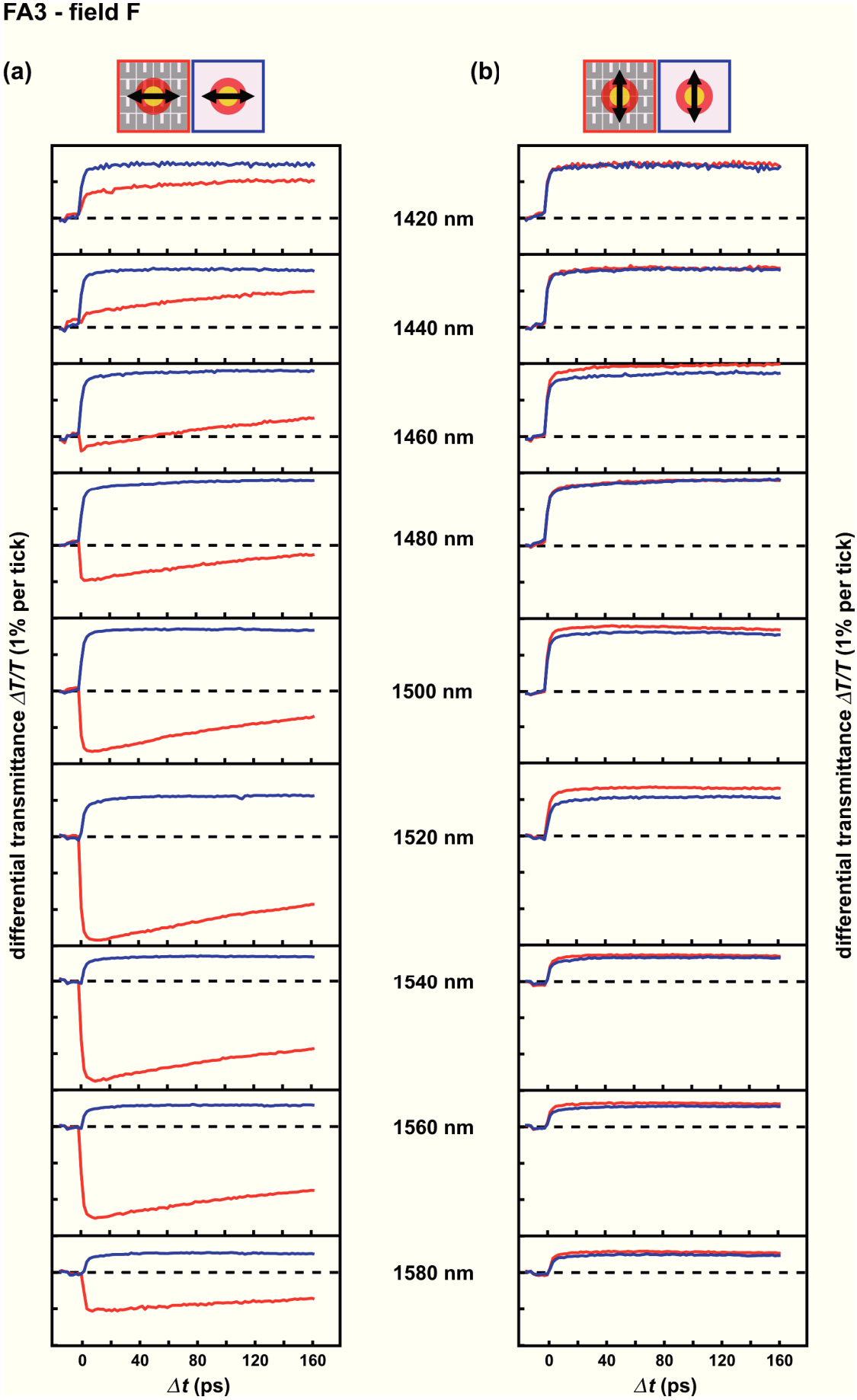
FA3 - field F
(a)
(b)
1420 nm
1440 nm
1460 nm
1480 nm
1500 nm
1520 nm
1540 nm
1560 nm
1580 nm
differential transmittance ΔT/T (1% per tick)
differential transmittance ΔT/T (1% per tick)
0
40
80
120
160
Δt (ps)
Δt (ps)

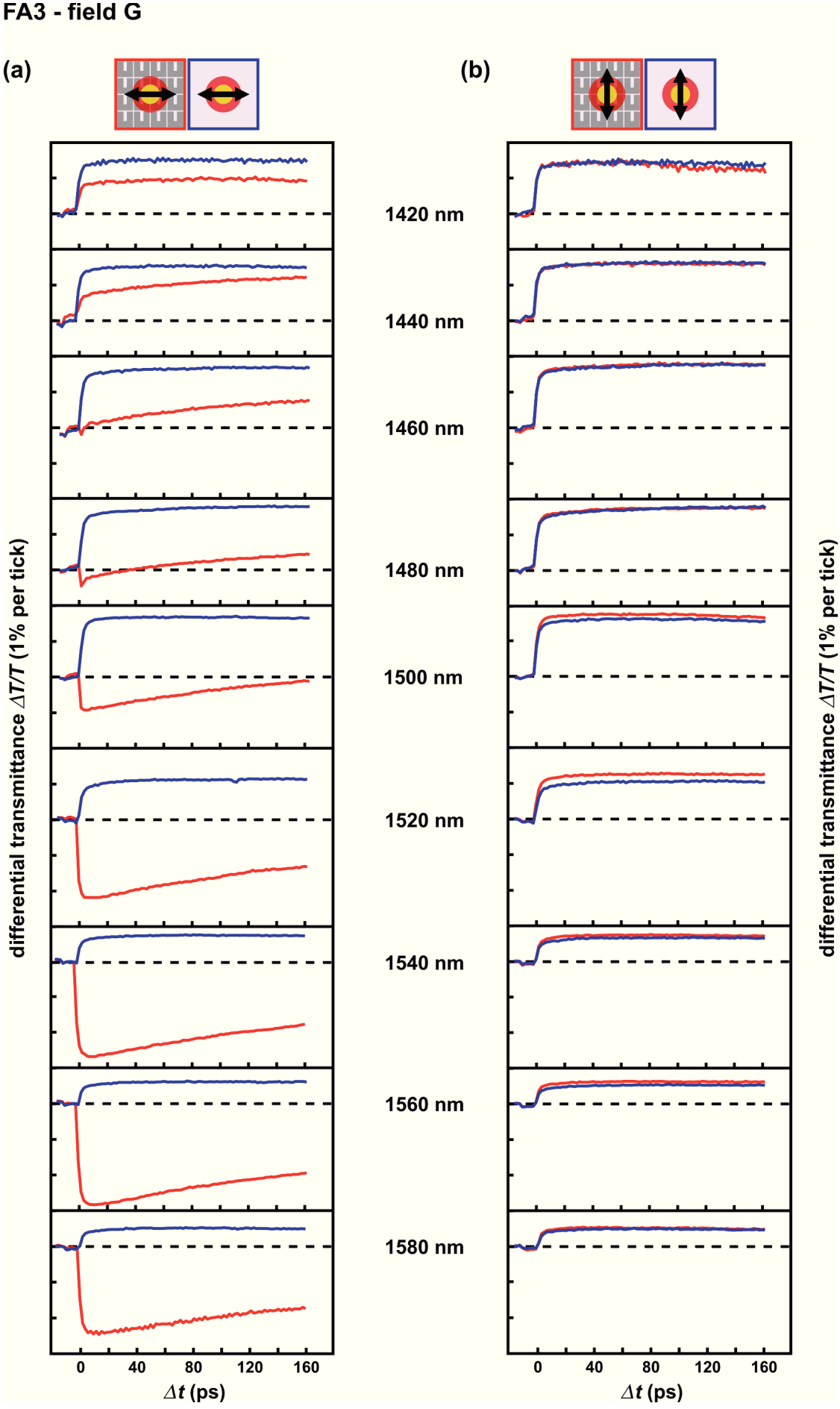
FA3 - field G
(a)
(b)
1420 nm
1440 nm
1460 nm
1480 nm
1500 nm
1520 nm
1540 nm
1560 nm
1580 nm
differential transmittance ΔT/T (1% per tick)
differential transmittance ΔT/T (1% per tick)
0
40
80
120
160
Δt (ps)
0
40
80
120
160
Δt (ps)

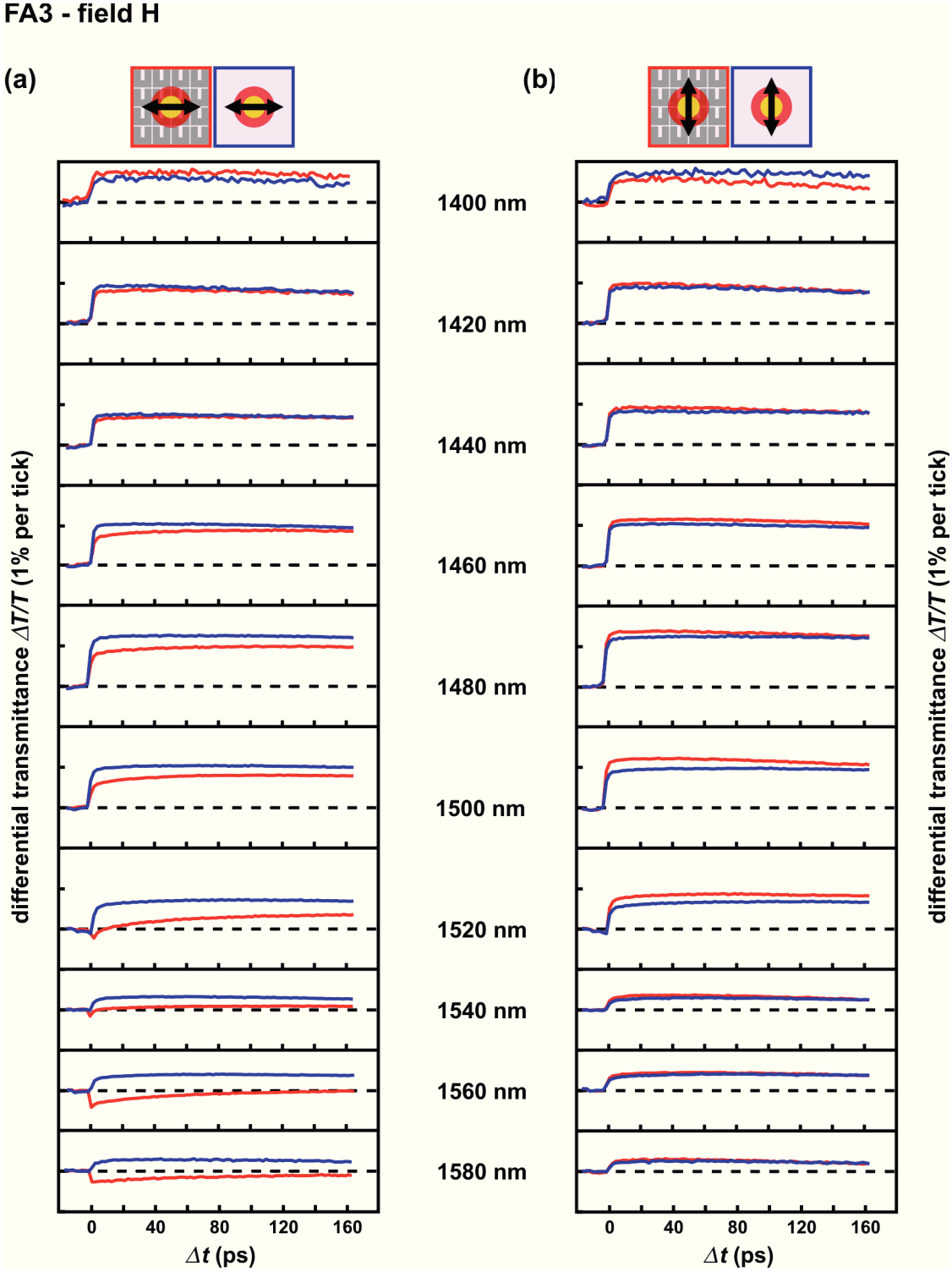
FA3 - field H
(a)
(b)
1400 nm
1420 nm
1440 nm
1460 nm
1480 nm
1500 nm
1520 nm
1540 nm
1560 nm
1580 nm
differential transmittance ΔT/T (1% per tick)
differential transmittance ΔT/T (1% per tick)
0
40
80
120
160
Δt (ps)
Δt (ps)

Sample NA7 (HSG 37)

FTIR Spectra

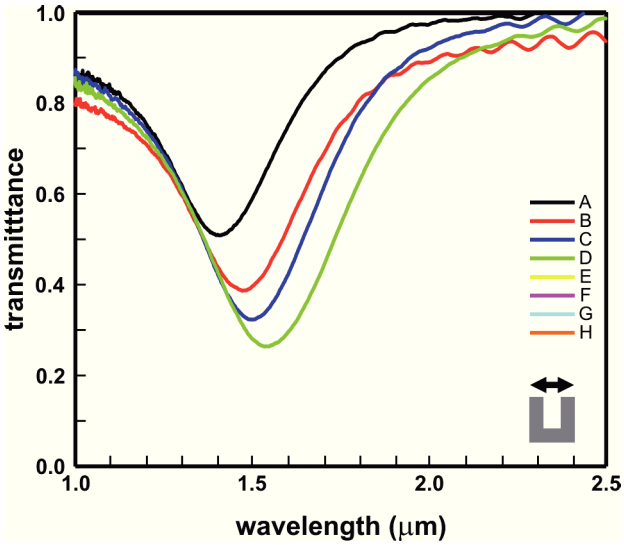

SEM Micrographs

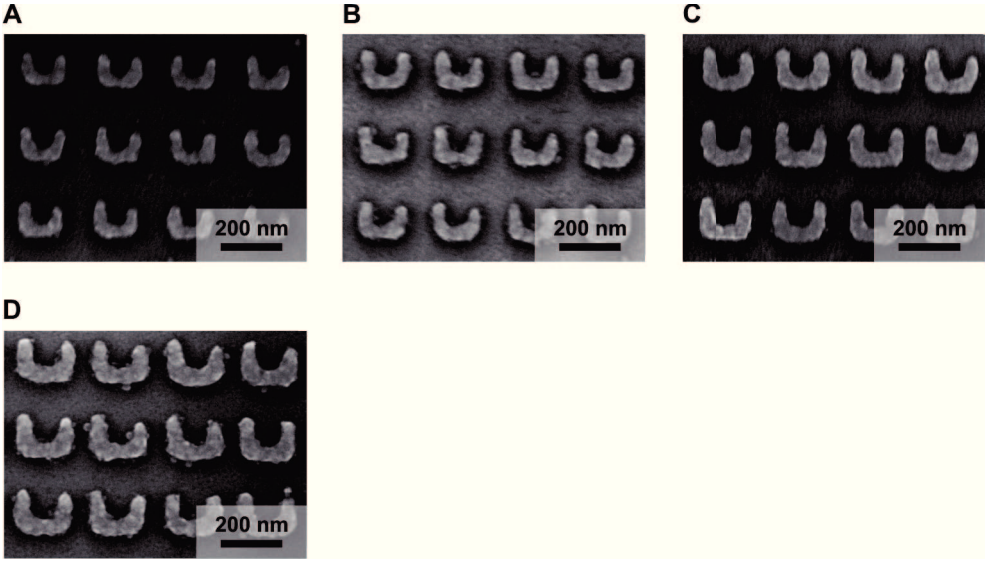

Pump-Probe Data

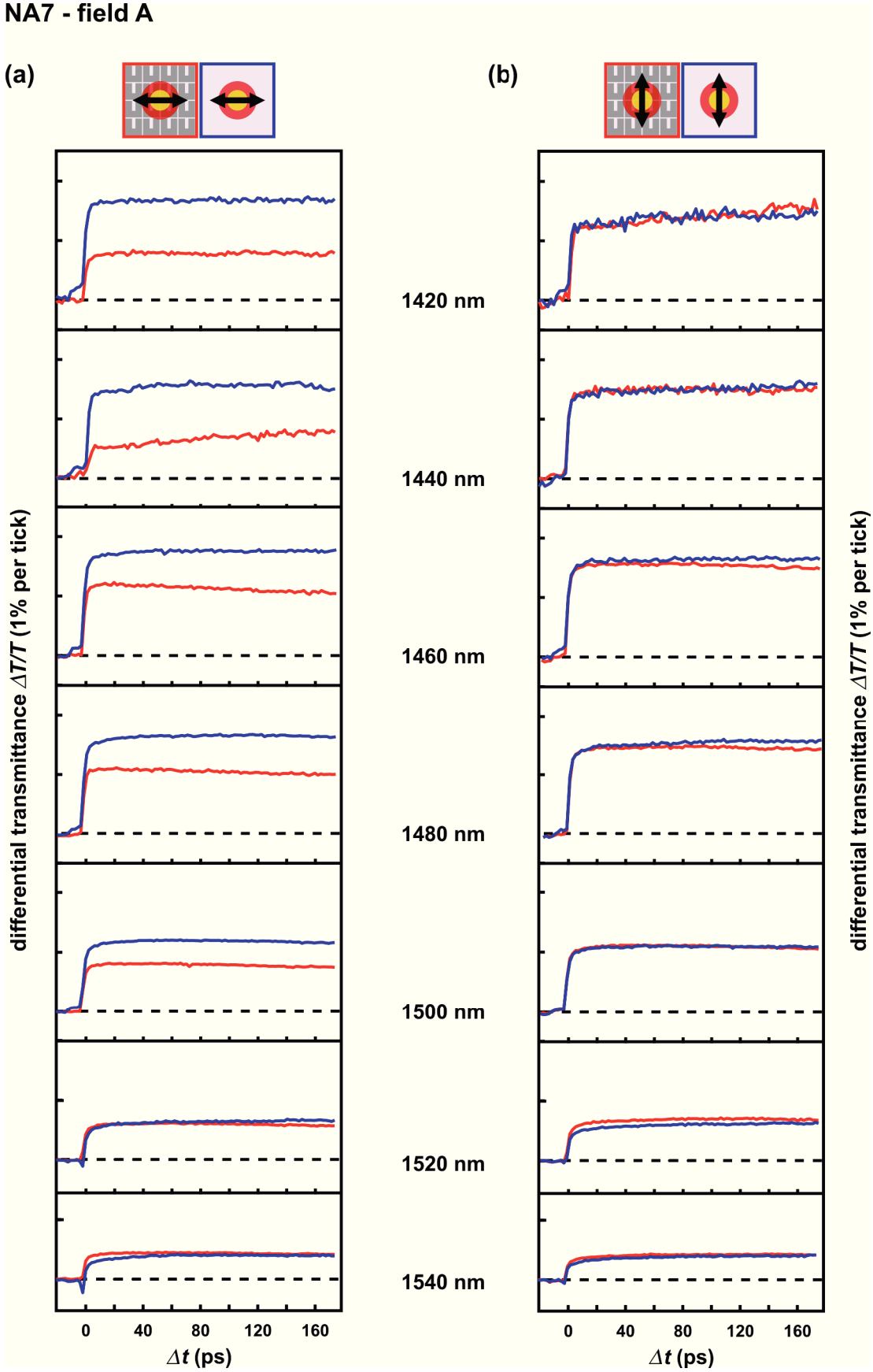

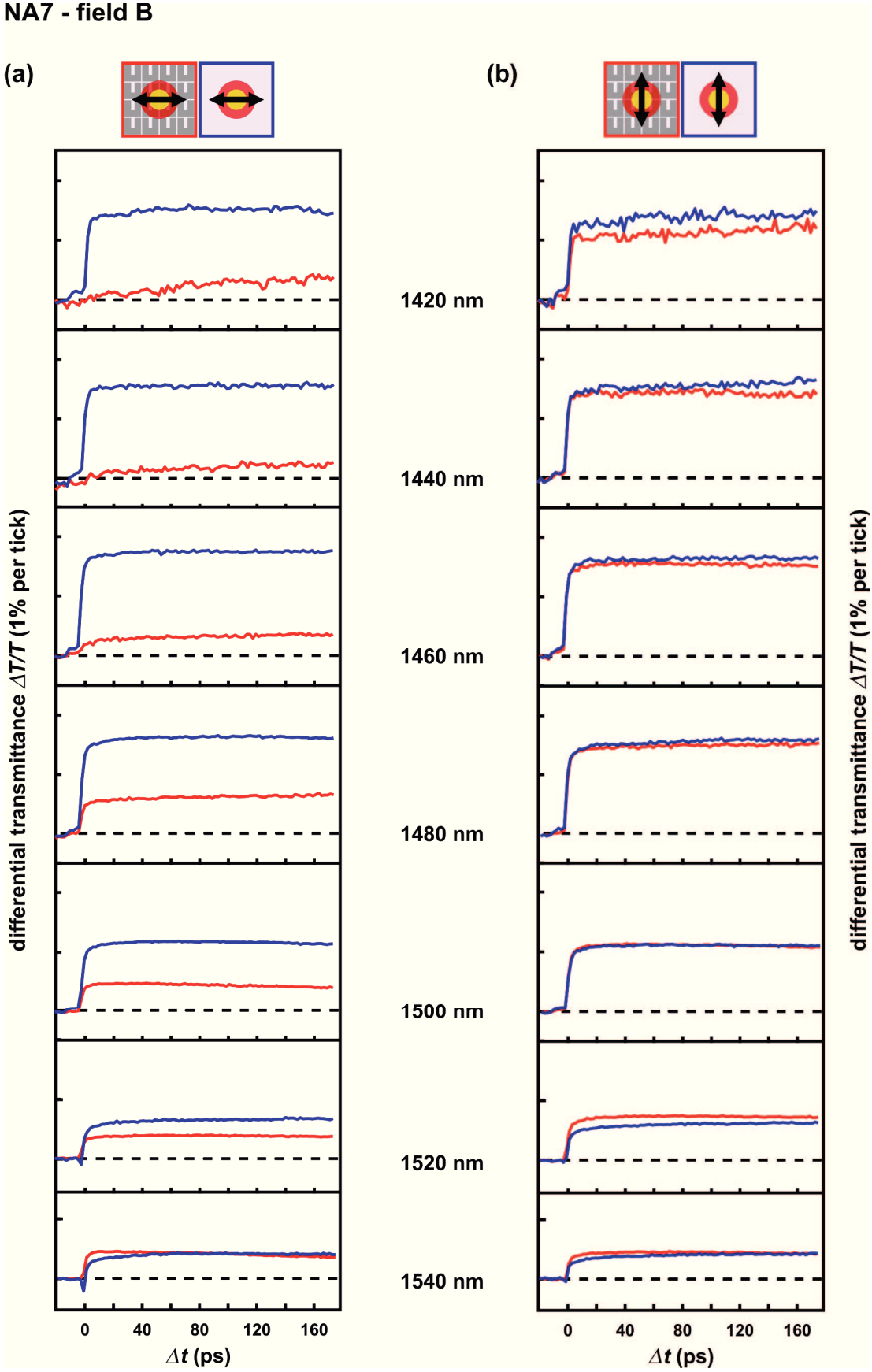
NA7 - field B
(a)
(b)
1420 nm
1440 nm
1460 nm
1480 nm
1500 nm
1520 nm
1540 nm
differential transmittance ΔT/T (1% per tick)
differential transmittance ΔT/T (1% per tick)
0
40
80
120
160
Δt (ps)
0
40
80
120
160
Δt (ps)

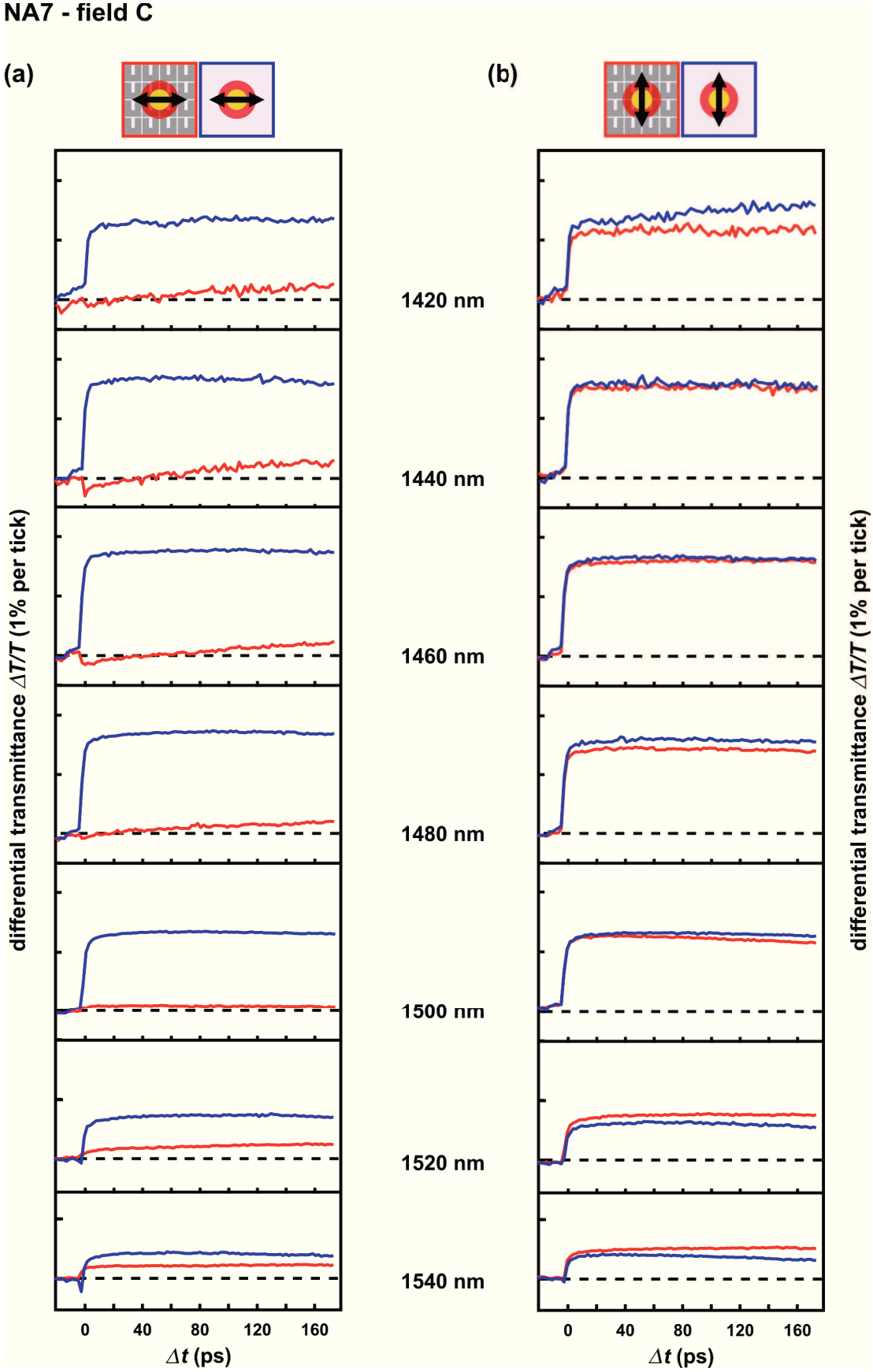
NA7 - field C
(a)
(b)
1420 nm
1440 nm
1460 nm
1480 nm
1500 nm
1520 nm
1540 nm
differential transmittance ΔT/T (1% per tick)
differential transmittance ΔT/T (1% per tick)
0
40
80
120
160
Δt (ps)
0
40
80
120
160
Δt (ps)

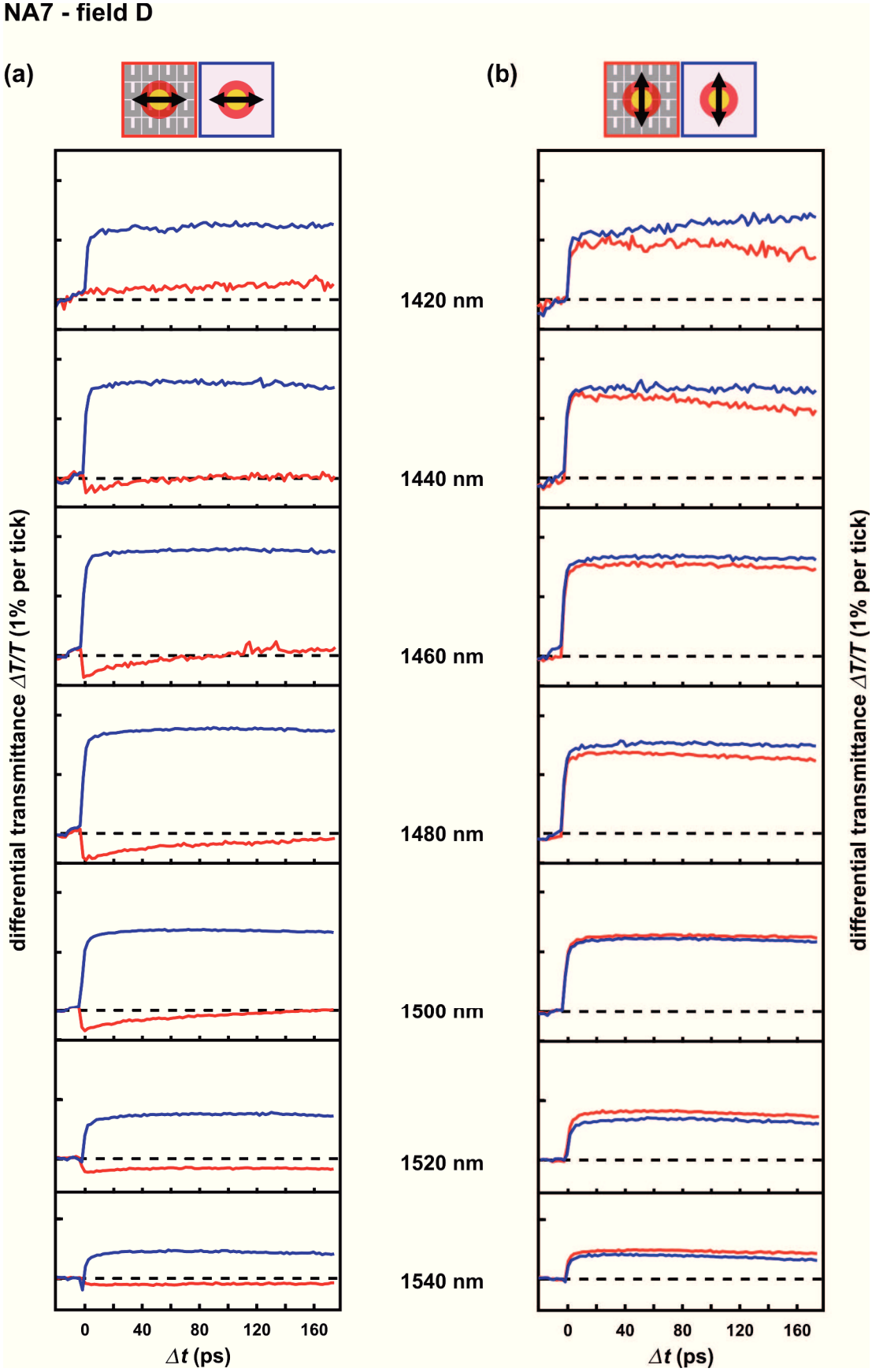
NA7 - field D
(a)
(b)
1420 nm
1440 nm
1460 nm
1480 nm
1500 nm
1520 nm
1540 nm
differential transmittance ΔT/T (1% per tick)
differential transmittance ΔT/T (1% per tick)
0
40
80
120
160
Δt (ps)
0
40
80
120
160
Δt (ps)

Sample NA5 (HSG 37)

FTIR Spectra

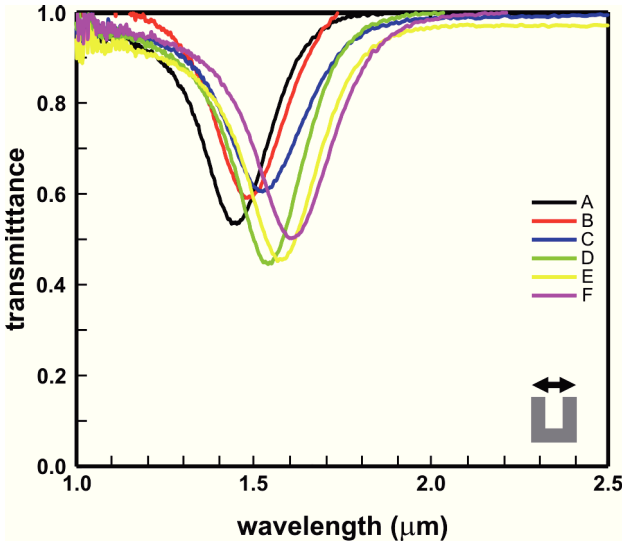

SEM Micrographs

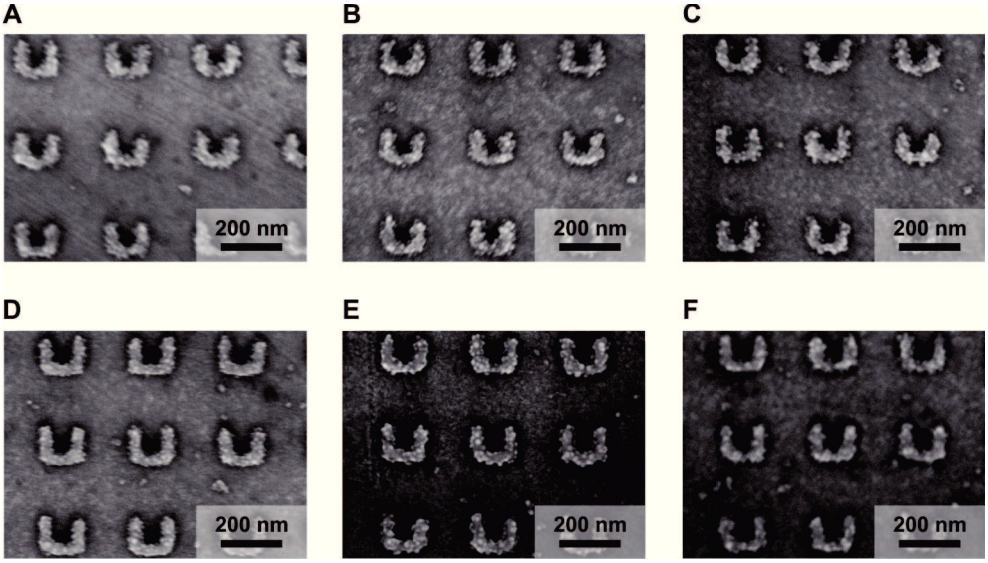

Pump-Probe Data

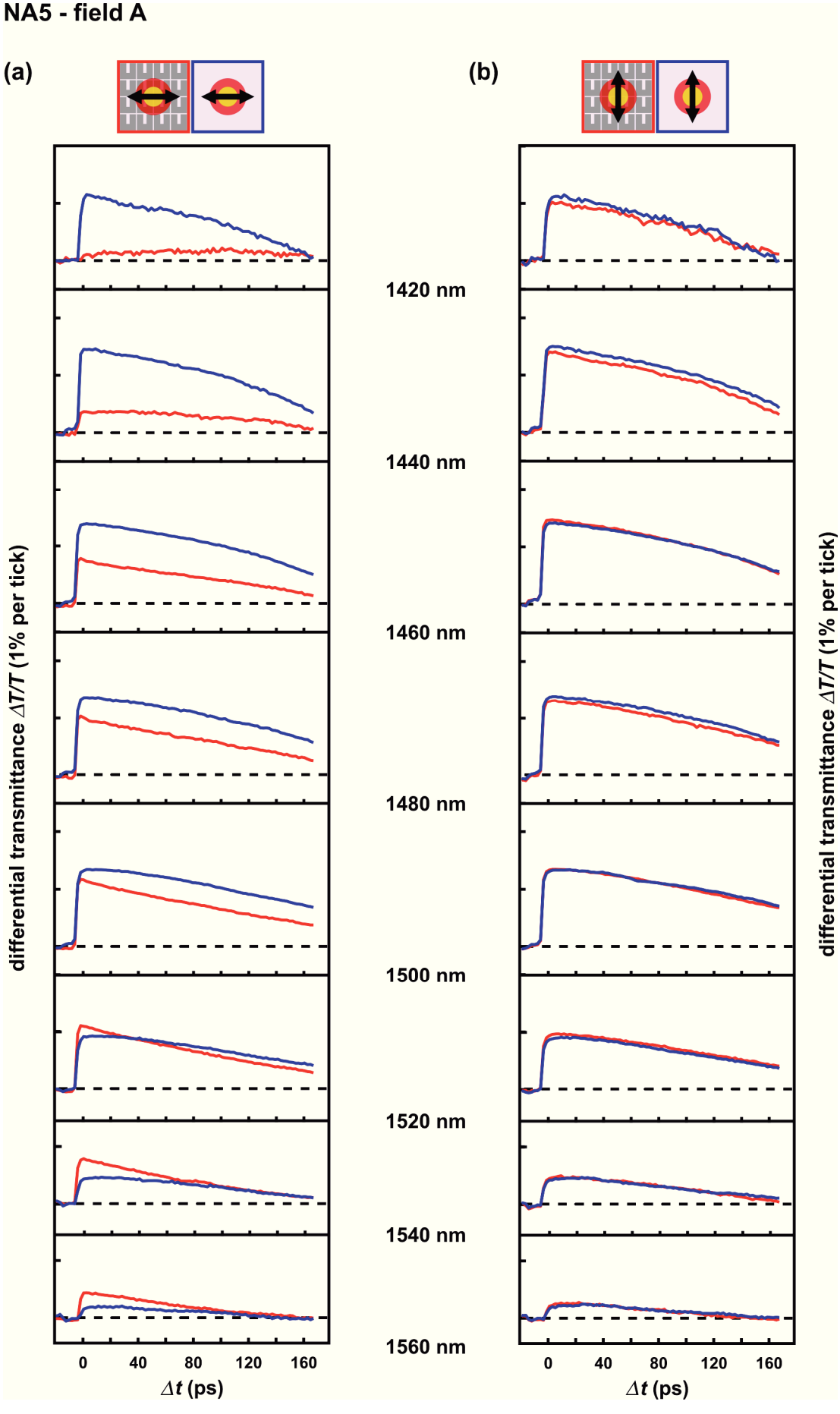

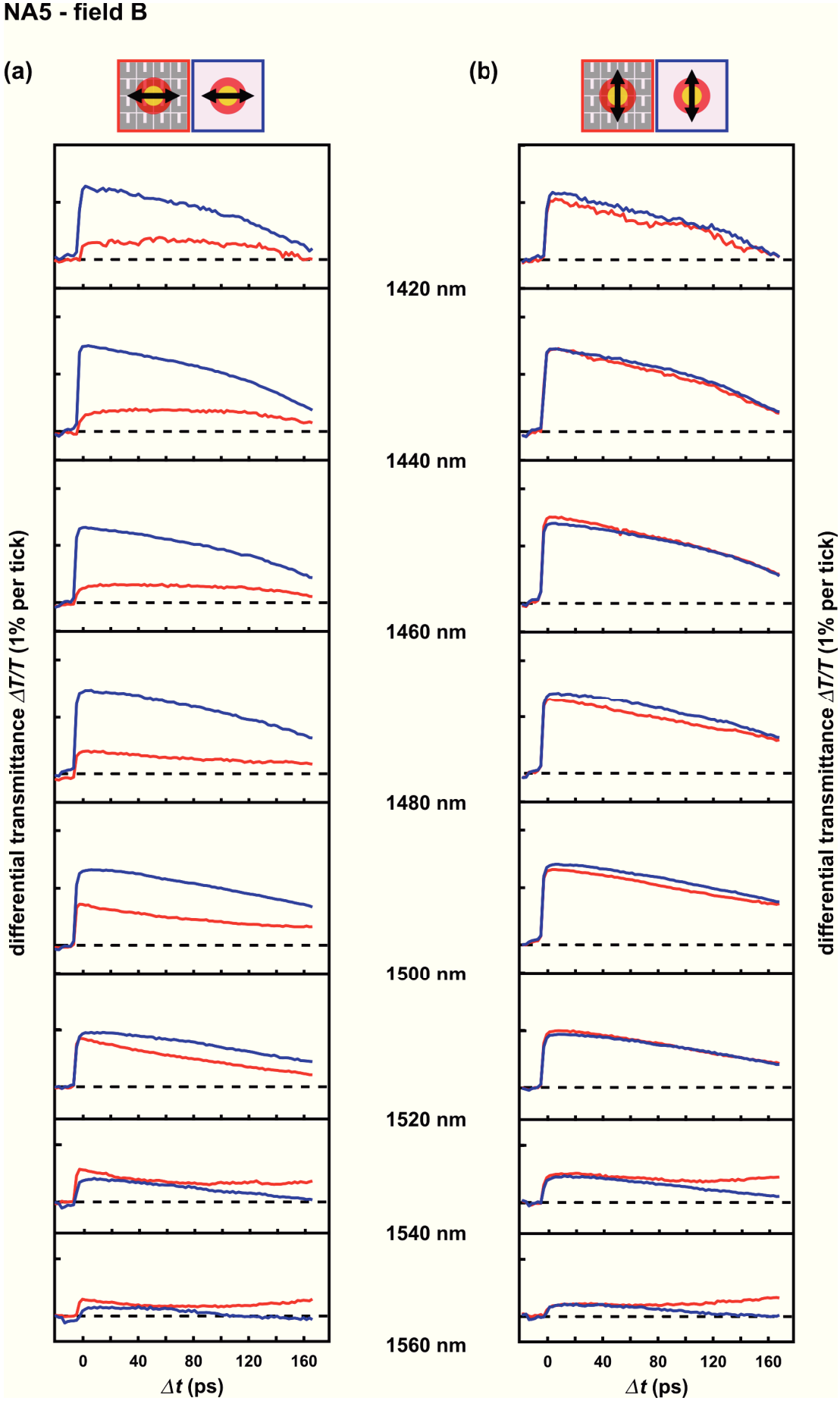
NA5 - field B
(a)
(b)
1420 nm
1440 nm
1460 nm
1480 nm
1500 nm
1520 nm
1540 nm
1560 nm
differential transmittance ΔT/T (1% per tick)
differential transmittance ΔT/T (1% per tick)
0
40
80
120
160
Δt (ps)
0
40
80
120
160
Δt (ps)

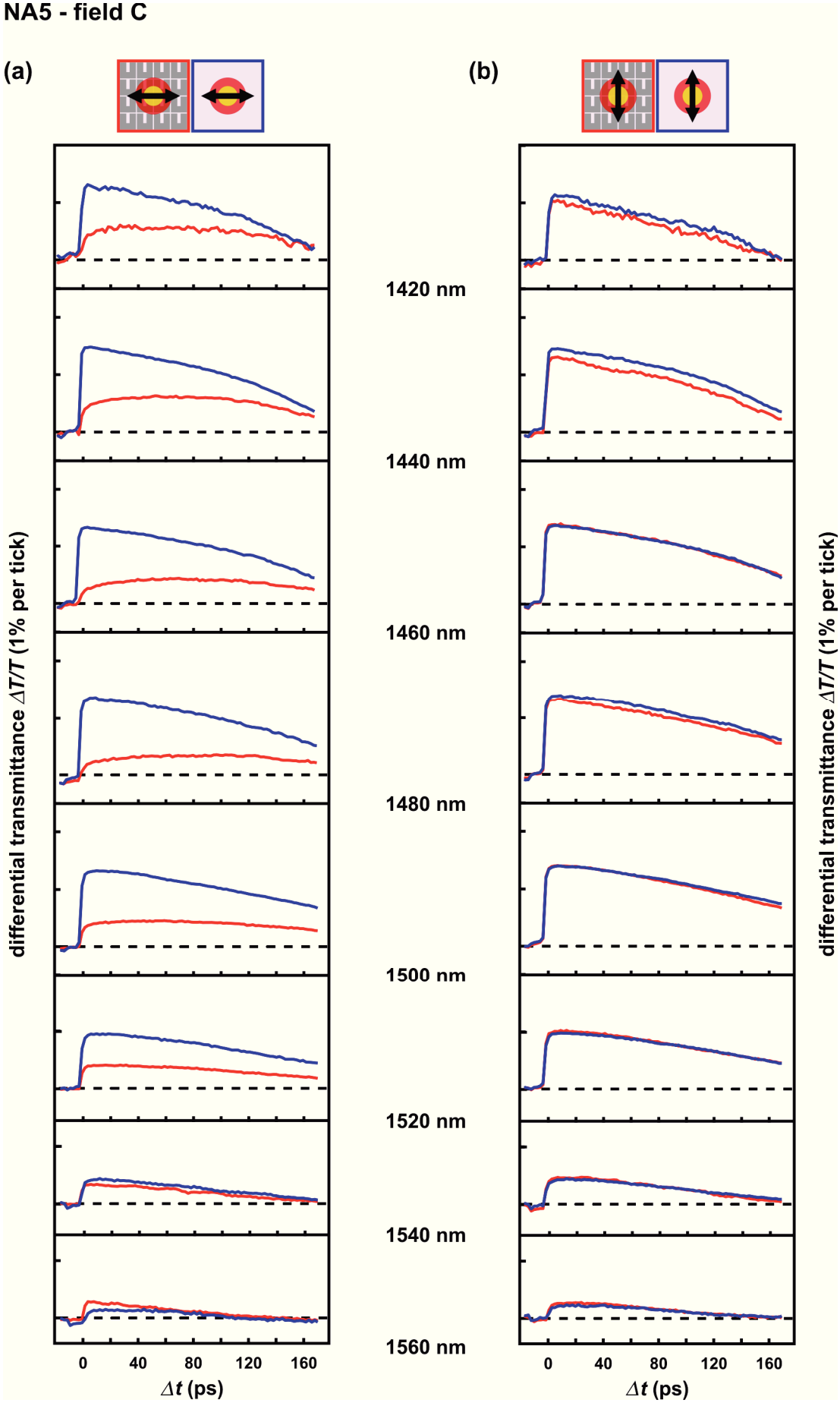
NA5 - field C
(a)
(b)
1420 nm
1440 nm
1460 nm
1480 nm
1500 nm
1520 nm
1540 nm
1560 nm
differential transmittance ΔT/T (1% per tick)
differential transmittance ΔT/T (1% per tick)
0
40
80
120
160
Δt (ps)
0
40
80
120
160
Δt (ps)

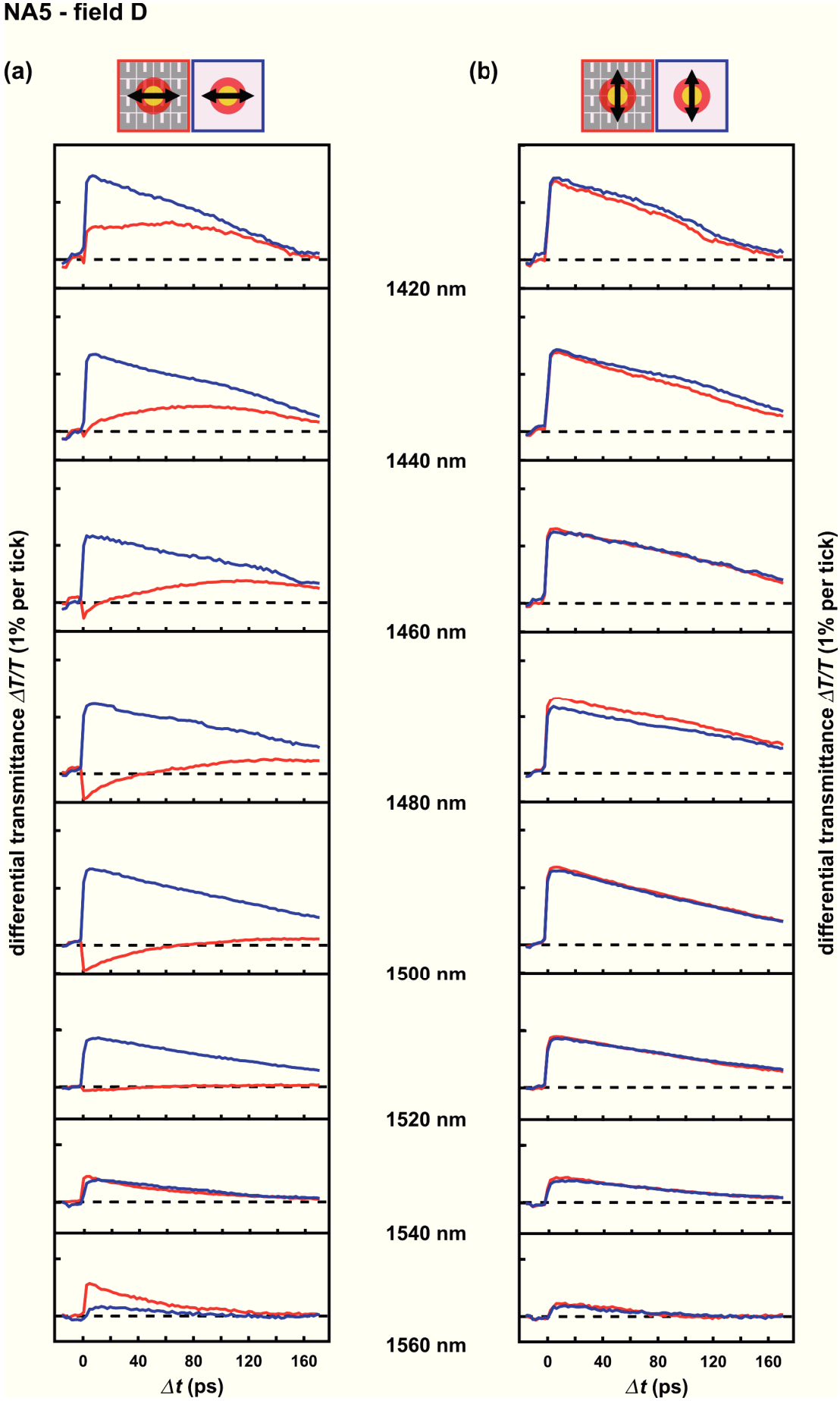
NA5 - field D
(a)
(b)
1420 nm
1440 nm
1460 nm
1480 nm
1500 nm
1520 nm
1540 nm
1560 nm
differential transmittance ΔT/T (1% per tick)
differential transmittance ΔT/T (1% per tick)
0
40
80
120
160
Δt (ps)
0
40
80
120
160
Δt (ps)

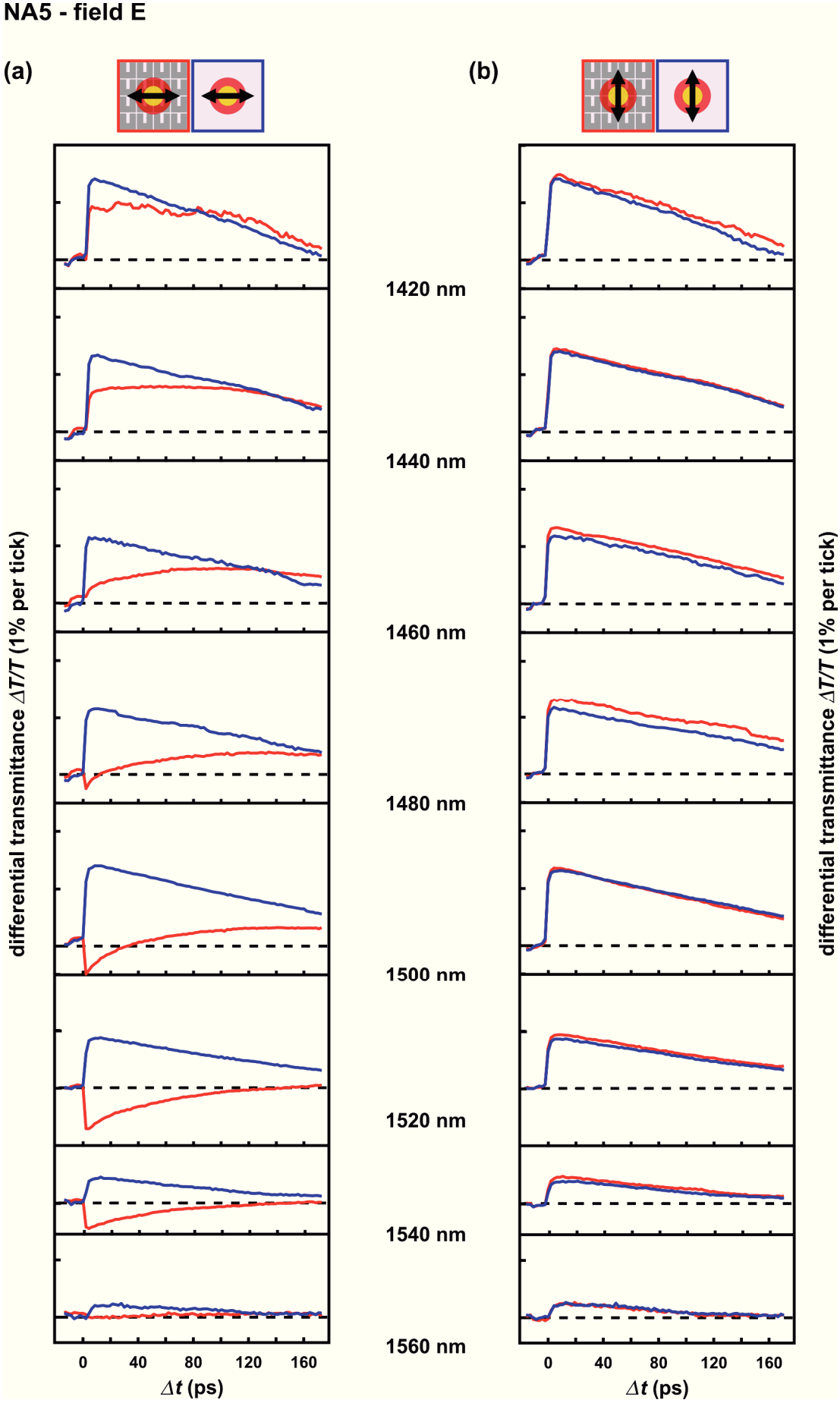
NA5 - field E
(a)
(b)
1420 nm
1440 nm
1460 nm
1480 nm
1500 nm
1520 nm
1540 nm
1560 nm
differential transmittance ΔT/T (1% per tick)
differential transmittance ΔT/T (1% per tick)
0
40
80
120
160
Δt (ps)
0
40
80
120
160
Δt (ps)

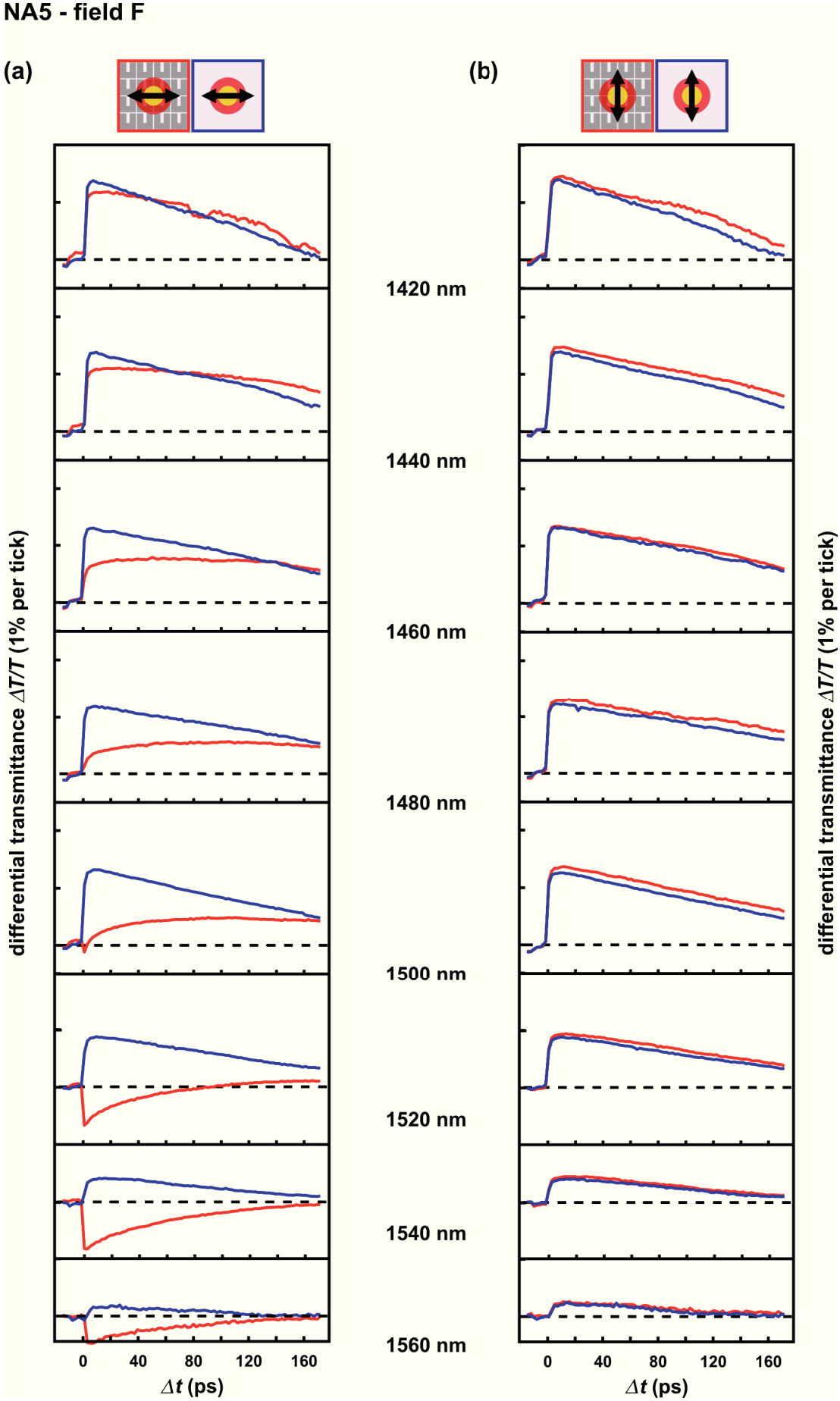
NA5 - field F
(a)
(b)
1420 nm
1440 nm
1460 nm
1480 nm
1500 nm
1520 nm
1540 nm
1560 nm
differential transmittance ΔT/T (1% per tick)
differential transmittance ΔT/T (1% per tick)
0
40
80
120
160
Δt (ps)
0
40
80
120
160
Δt (ps)

Sample NA62 (HSG 37)

FTIR Spectra

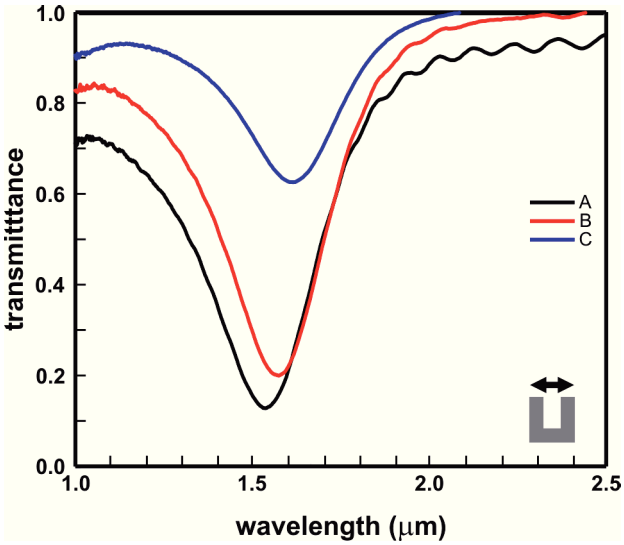

SEM Micrographs

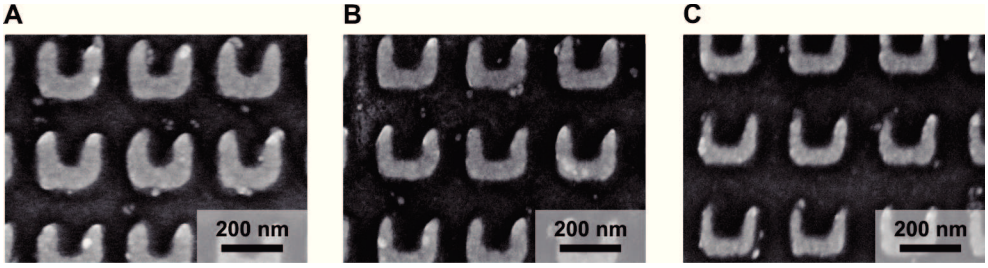

Pump-Probe Data

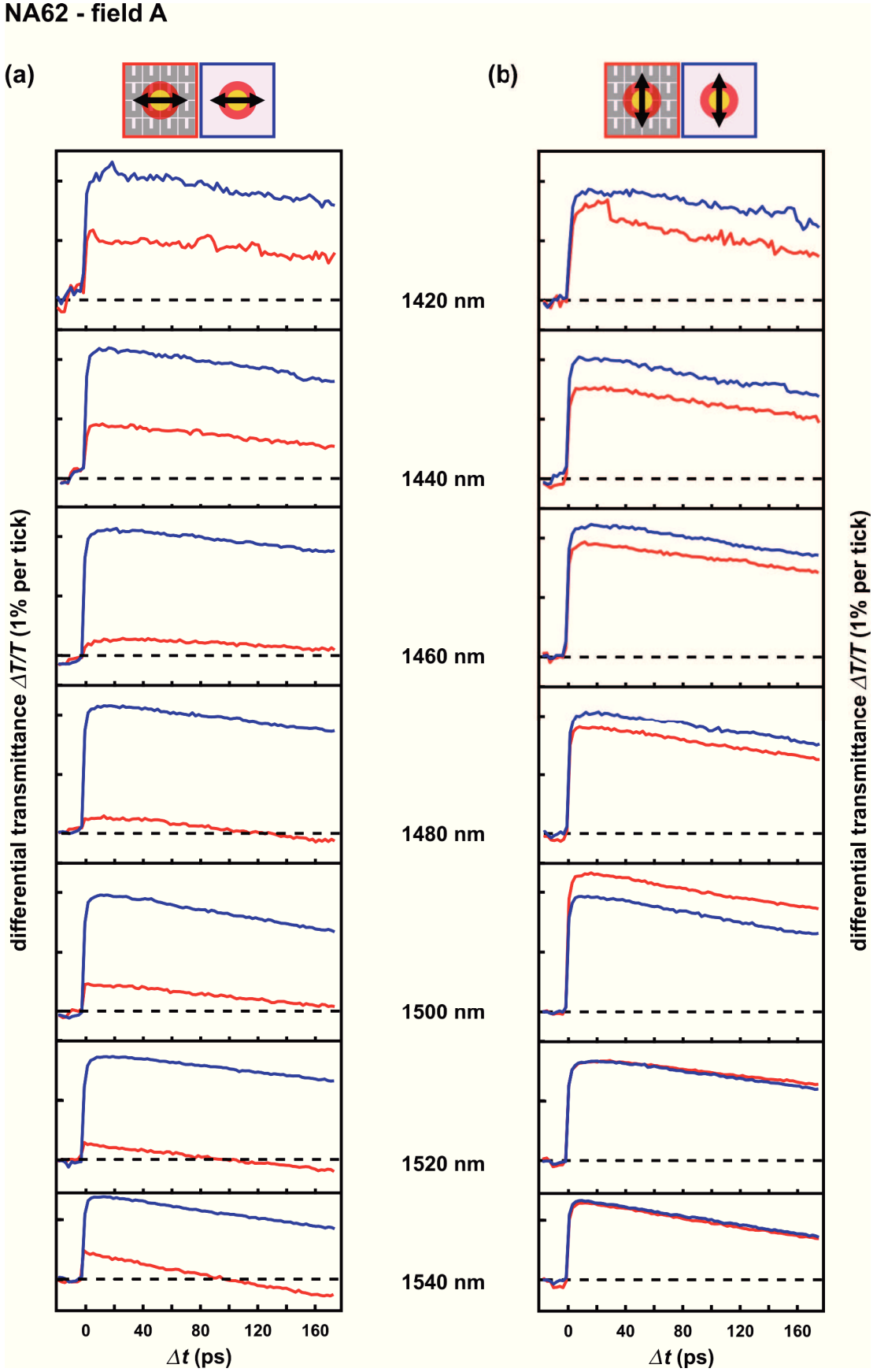

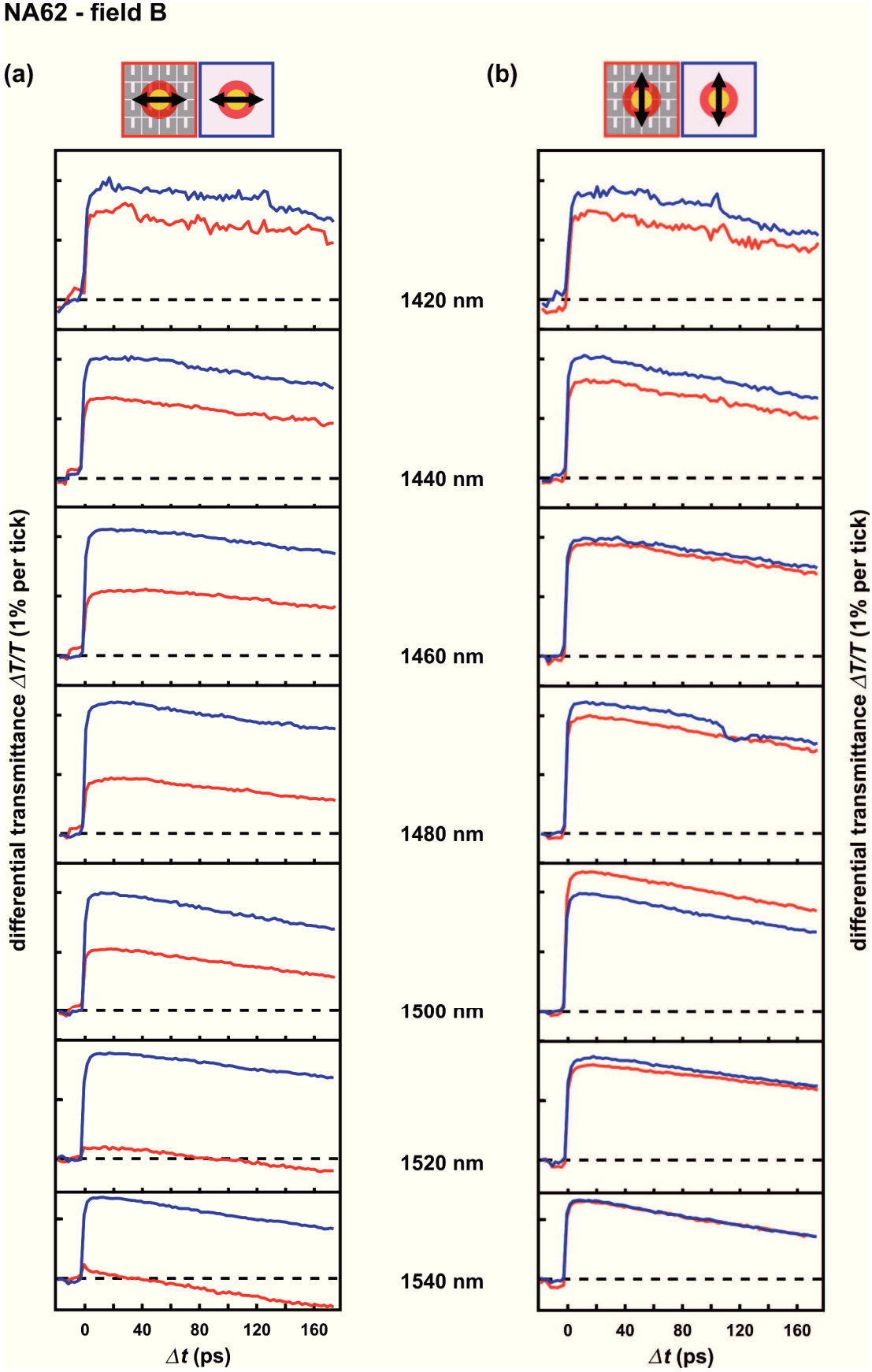
NA62 - field B
(a)
(b)
1420 nm
1440 nm
1460 nm
1480 nm
1500 nm
1520 nm
1540 nm
differential transmittance ΔT/T (1% per tick)
differential transmittance ΔT/T (1% per tick)
0
40
80
120
160
Δt (ps)
0
40
80
120
160
Δt (ps)

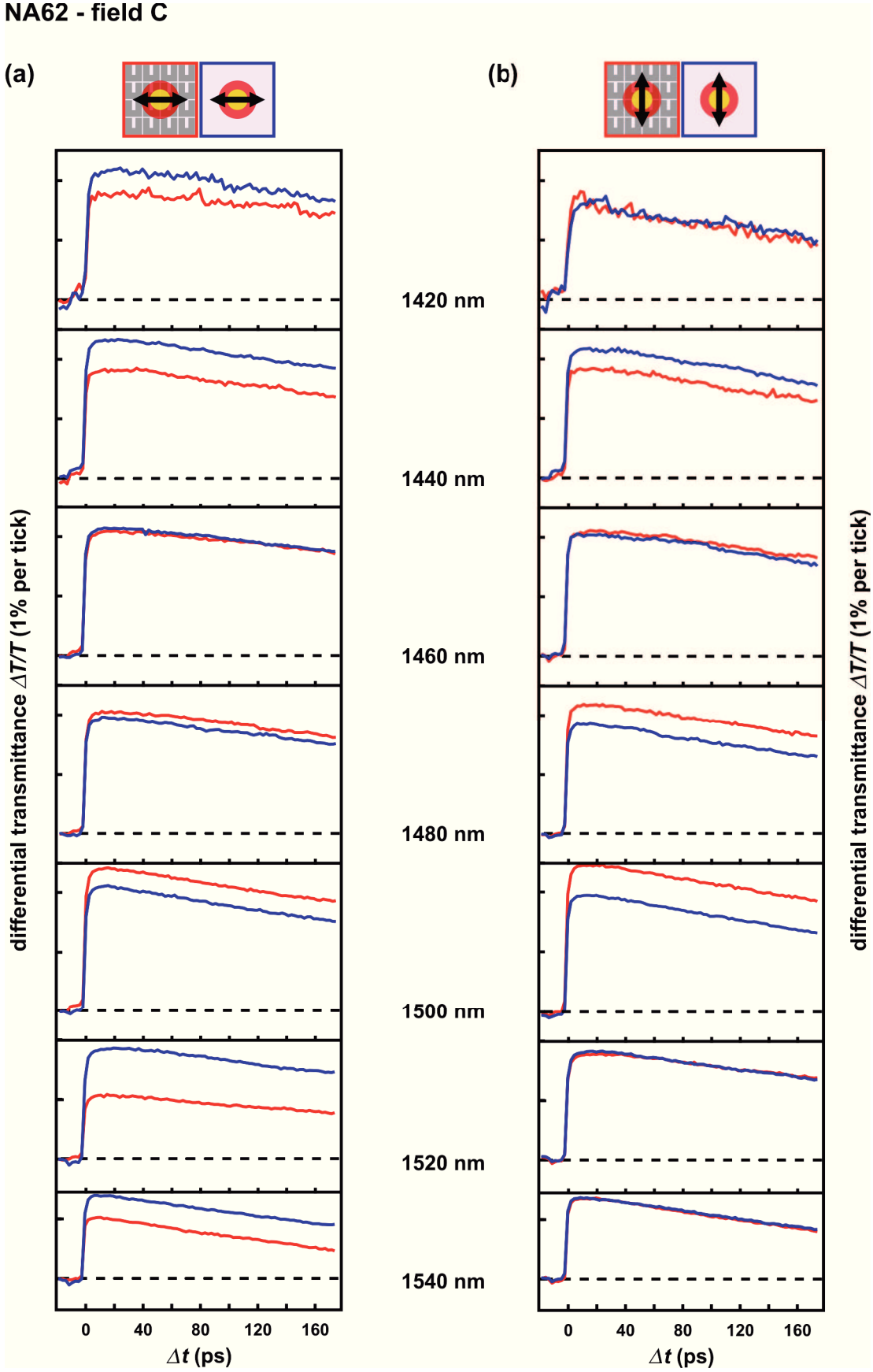
NA62 - field C
(a)
(b)
1420 nm
1440 nm
1460 nm
1480 nm
1500 nm
1520 nm
1540 nm
differential transmittance ΔT/T (1% per tick)
differential transmittance ΔT/T (1% per tick)
0
40
80
120
160
Δt (ps)
0
40
80
120
160
Δt (ps)

Bibliography

[1] K. Busch, G. von Freymann, S. Linden, S.F. Mingaleev, L. Tkeshelashvili, and M. Wegener, *Periodic nanostructures for photonics*, Phys. Rep. **444**, 101 (2007).

[2] Costas M. Soukoulis, Stefan Linden, and Martin Wegener, *Negative Refractive Index at Optical Wavelengths*, Science **315**, 47 (2007).

[3] Vladimir M. Shalaev, *Optical negative-index metamaterials*, Nature Photon. **1**, 41 (2007).

[4] J. B. Pendry, *Negative Refraction Makes a Perfect Lens*, Phys. Rev. Lett. **85**, 3966 (2000).

[5] J. B. Pendry, D. Schurig, and D. R. Smith, *Controlling Electromagnetic Fields*, Science **312**, 1780 (2006).

[6] D. Schurig, J. J. Mock, B. J. Justice, S. A. Cummer, J. B. Pendry, A. F. Starr, and D. R. Smith, *Metamaterial Electromagnetic Cloak at Microwave Frequencies*, Science **314**, 977 (2006).

[7] Costas M. Soukoulis and Martin Wegener, *Optical Metamaterials - More Bulky and Less Lossy*, Science **330**, 1633 (2010).

[8] Alexandra Boltasseva and Harry A. Atwater, *Low-Loss Plasmonic Metamaterials*, Science **331**, 290 (2011).

[9] D. A. Bobb, G. Zhu, M. Mayy, A. V. Gavrilenko, P. Mead, V. I. Gavrilenko, and M. A. Noginov, *Engineering of low-loss metal for nanoplasmonic and metamaterials applications*, Appl. Phys. Lett. **95**, 151102 (2009).

[10] Durdu Ö. Güney, Thomas Koschny, and Costas M. Soukoulis, *Reducing ohmic losses in metamaterials by geometric tailoring*, Phys. Rev. B **80** (r), 125129 (2009).

[11] N. M. Lawandy, *Localized surface plasmon singularities in amplifying media*, Appl. Phys. Lett. **85**, 5040 (2004).

[12] A. Fang, Th. Koschny, M. Wegener, and C. M. Soukoulis, *Self-consistent calculation of metamaterials with gain*, Phys. Rev. B **79**, 241104 (2009).

[13] Sebastian Wuestner, Andreas Pusch, Kosmas L. Tsakmakidis, Joachim M. Hamm, and Ortwin Hess, *Overcoming Losses with Gain in a Negative Refractive Index Metamaterial*, Phys. Rev. Lett. **105**, 127401 (2010).

[14] E. Plum, V. A. Fedotov, P. Kuo, D. P. Tsai, and N. I. Zheludev, *Towards the lasing spaser: controlling metamaterial optical response with semiconductor quantum dots*, Opt. Express **17**, 8548 (2009).

[15] K. Tanaka, E. Plum, J. Y. Ou, T. Uchino, and N. I. Zheludev, *Multifold Enhancement of Quantum Dot Luminescence in Plasmonic Metamaterials*, Phys. Rev. Lett. **105**, 227403 (2010).

[16] Shumin Xiao, Vladimir P. Drachev, Alexander V. Kildishev, Xingjie Ni, Uday K. Chettiar, Hsiao-Kuan Yuan, and Vladimir M. Shalaev, *Loss-free and active optical negative-index metamaterials*, Nature **466**, 735 (2010).

[17] Anika Kinkhabwala, Zongfu Yu, Shanhui Fan, Yuri Avlasevich, Klaus MÃ¼llen, and W. E. Moerner, *Large single-molecule fluorescence enhancements produced by a bowtie nanoantenna*, Nature Photon. **3**, 654 (2009).

[18] Alberto G. Curto, Giorgio Volpe, Tim H. Taminiau, Mark P. Kreuzer, Romain Quidant, and Niek F. van Hulst, *Unidirectional Emission of a Quantum Dot Coupled to a Nanoantenna*, Science **329**, 930 (2010).

[19] Darrick E. Chang, Anders S. SÃ¸rensen, Eugene A. Demler, and Mikhail D. Lukin, *A single-photon transistor using nanoscale surface plasmons*, Nature Phys. **3**, 807 (2007).

[20] D.J. Bergman and M.I. Stockman, *Surface Plasmon Amplification by Stimulated Emission of Radiation: Quantum Generation of Coherent Surface Plasmons in Nanosystems*, Phys. Rev. Lett. **90**, 027402 (2003).

[21] Mark I. Stockman, *Spasers explained*, Nature Photon. **2**, 327 (2008).

[22] M. A. Noginov, G. Zhu, A. M. Belgrave, R. Bakker, V. M. Shalaev, E. E. Narimanov, S. Stout, E. Herz, T. Suteewong, and U. Wiesner, *Demonstration of a spaser-based nanolaser*, Nature **460**, 1110 (2009).

[23] N.I. Zheludev, S.L. Prosvirinin, N. Papasimakis, and V.A. Fedotov, *Lasing Spaser*, Nature Photon. **2**, 351 (2008).

[24] V.G. Veselago, *The electrodynamics of substances with simultaneously negative values of ϵ and μ*, Sov. Phys. Uspekhi **10**, 509 (1968).

[25] Mark Fox, *Optical Properties of Solids* (Oxford University Press, 2001), first edition.

[26] Eugene Hecht, *Optics* (Addison Wesley, 2002), fourth edition.

[27] P. B. Johnson and R. W. Christy, *Optical Constants of the Noble Metals*, Phys. Rev. B **6**, 4370 (1972).

[28] Paul Drude, *Zur Elektronentheorie der Metalle*, Ann. Physik **306**, 566 (1900).

[29] John David Jackson, *Classical Electrodynamics* (John Wiley & Sons, Inc., 1999), third edition.

[30] Stefan A. Maier, *Plasmonics: Fundamentals and Applications* (Springer-Verlag, 2007), first edition.

[31] Gustav Mie, *Beiträge zur Optik trüber Medien, speziell kolloidaler Metallösungen*, Ann. Physik **330**, 377 (1908).

[32] D. R. Smith, Willie J. Padilla, D. C. Vier, S. C. Nemat-Nasser, and S. Schultz, *Composite Medium with Simultaneously Negative Permeability and Permittivity*, Phys. Rev. Lett. **84**, 4184 (2000).

[33] T.A. Klar, A.V. Kildishev, V.P. Drachev, and V.M. Shalaev, *Negative-Index Metamaterials: Going Optical*, IEEE J. Sel. Top. Quantum Electronics **12**, 1106 (2006).

[34] Shuang Zhang, Wenjun Fan, N. C. Panoiu, K. J. Malloy, R. M. Osgood, and S. R. J. Brueck, *Experimental Demonstration of Near-Infrared Negative-Index Metamaterials*, Phys. Rev. Lett. **95**, 137404 (2005).

[35] Shuang Zhang, Wenjun Fan, K. J. Malloy, S.R. Brueck, N. C. Panoiu, and R. M. Osgood, *Near-infrared double negative metamaterials*, Opt. Express **13**, 4922 (2005).

[36] Gunnar Dolling, Christian Enkrich, Martin Wegener, Costas M. Soukoulis, and Stefan Linden, *Low-loss negative-index metamaterial at telecommunication wavelengths*, Opt. Lett. **31**, 1800 (2006).

[37] G. Dolling, C. Enkrich, M. Wegener, J. F. Zhou, C. M. Soukoulis, and S. Linden, *Cut-wire pairs and plate pairs as magnetic atoms for optical metamaterials*, Opt. Lett. **30**, 3198 (2005).

[38] Vladimir M. Shalaev, Wenshan Cai, Uday K. Chettiar, Hsiao-Kuan Yuan, Andrey K. Sarychev, Vladimir P. Drachev, and Alexander V. Kildishev, *Negative index of refraction in optical metamaterials*, Opt. Lett. **30**, 3356 (2005).

[39] D.J. Robbins J.B. Pendry, A.J. Holden and W.J. Stewart, *Magnetism from Conductors and Enhanced Nonlinear Phenomena*, IEEE Trans. Microw. Theory Tech. **47**, 2075 (1999).

[40] Stefan Linden, Christian Enkrich, Martin Wegener, Jiangfeng Zhou, Thomas Koschny, and Costas M. Soukoulis, *Magnetic Response of Metamaterials at 100 Terahertz*, Science **306**, 1351 (2004).

[41] S. Linden, C. Enkrich, G. Dolling, M. W. Klein, J. Zhou, T. Koschny, C. M. Soukoulis, S. Burger, F. Schmidt, and M. Wegener, *Photonic Metamaterials: Magnetism at Optical Frequencies*, IEEE J. Sel. Top. Quantum Electronics **12**, 1097 (2006).

[42] N. Katsarakis, T. Koschny, M. Kafesaki, E. N. Economou, and C. M. Soukoulis, *Electric coupling to the magnetic resonance of split ring resonators*, Appl. Phys. Lett. **84**, 2943 (2004).

[43] Jonathan Grandidier, Gérard Colas des Francs, Sébastien Massenot, Alexandre Bouhelier, Laurent Markey, Jean-Claude Weeber, Christophe Finot, and Alain Dereux, *Gain-Assisted Propagation in a Plasmonic Waveguide at Telecom Wavelength*, Nano Lett. **9**, 2935 (2009).

[44] C. Sönnichsen, T. Franzl, T. Wilk, G. von Plessen, J. Feldmann, O. Wilson, and P. Mulvaney, *Drastic Reduction of Plasmon Damping in Gold Nanorods*, Phys. Rev. Lett. **88**, 077402 (2002).

[45] Michael Ricci, Nathan Orloff, and Steven M. Anlage, *Superconducting metamaterials*, Appl. Phys. Lett. **87** (3), 034102 (2005).

[46] A. Tsiatmas, A. R. Buckingham, V. A. Fedotov, S. Wang, Y. Chen, P. A. J. de Groot, and N. I. Zheludev, *Superconducting plasmonics and extraordinary transmission*, Appl. Phys. Lett. **97** (11), 111106 (2010).

[47] M G Blaber, M D Arnold, and M J Ford, *Optical properties of intermetallic compounds from first principles calculations: a search for the ideal plasmonic material*, J.Ph.-Condens. Mat. **21**, 144211 (2009).

[48] Marinko Jablan, Hrvoje Buljan, and Marin Soljaćić, *Plasmonics in graphene at infrared frequencies*, Phys. Rev. B **80**, 245435 (2009).

[49] Martin Wegener, Juan Luis García-Pomar, Costas M. Soukoulis, Nina Meinzer, Matthias Ruther, and Stefan Linden, *Toy model for plasmonic metamaterial resonances coupled to two-level system gain*, Opt. Express **16**, 19785 (2008).

[50] Nina Meinzer, Matthias Ruther, Stefan Linden, Costas M. Soukoulis, Galina Khitrova, Joshua Hendrickson, Joshua D. Olitzky, Hyatt M. Gibbs, and Martin Wegener, *Arrays of Ag split-ring resonators coupled to InGaAs single-quantum-well gain*, Opt. Express **18**, 24140 (2010).

[51] Mark I. Stockman, *Criterion for Negative Refraction with Low Optical Losses from a Fundamental Principle of Causality*, Phys. Rev. Lett. **98**, 177404 (2007).

[52] P. Kinsler and M. W. McCall, *Causality-Based Criteria for a Negative Refractive Index Must Be Used With Care*, Phys. Rev. Lett. **101**, 167401 (2008).

[53] R. N. Hall, G. E. Fenner, J. D. Kingsley, T. J. Soltys, and R. O. Carlson, *Coherent Light Emission From GaAs Junctions*, Phys. Rev. Lett. **9**, 366 (1962).

[54] Shuji Nakamura, Masayuki Senoh, Shin ichi Nagahama, Naruhito Iwasa, Takao Yamada, Toshio Matsushita, Yasunobu Sugimoto, and Hiroyuki Kiyoku, *Room-temperature continuous-wave operation of InGaN multi-quantum-well structure laser diodes*, Appl. Phys. Lett. **69**, 4056 (1996).

[55] Andrey K. Sarychev and Gennady Tartakovsky, *Magnetic plasmonic metamaterials in actively pumped host medium and plasmonic nanolaser*, Phys. Rev. B **75**, 085436 (2007).

[56] L. Esaki and R. Tsu, *Superlattice and Negative Differential Conductivity in Semiconductors*, IBM Journal of Research and Development **14**, 61 (1970).

[57] Neil W. Ashcroft and N. David Mermin, *Festkörperphysik* (Oldenbourg Wissenschaftsverlag, 2005).

[58] Claus F. Klingshirn, *Semiconductor Optics* (Springer-Verlag, 2007), second edition.

[59] Peter Y. Yu and Manuel Cardona, *Fundamentals of Semiconductors - Physics and Materials Properties* (Springer-Verlag, 2010), fourth edition.

[60] J.P. Pocholle, M. Razeghi, J. Raffy, M. Papuchon, C. Weisbuch, C. Puech, A. Vandenborre, J.L. Bezy, L. Heinrich, and J.E. Vimont, *Observation d'états excitoniques à température ambiante dans les semiconducteurs à puits quantiques de type InGaAs/InP (Applications)*, Rev. Phys. Appl. (Paris) **22**, 1239 (1987).

[61] Claude Cohen-Tannoudji, Bernard Diu, and Franck Laloe, *Quantenmechanik, Teil 1* (de Gruyter, 1999), second edition.

[62] Nasser Peyghambarian, Stephan W. Koch, and Andre Mysyrowicz, *Introduction to Semiconductor Optics*, Series in Solid State Physical Electronics (Prentice Hall, 1993), first edition.

[63] S. Jorda and U. Rössler, *Group Theory of Electron States in Quantum Wells and Heterostructures*, Superlattice Microst. **8**, 481 (1990).

[64] Wilfried Schäfer and Martin Wegener, *Semiconductor Optics and Transport Phenomena* (Springer-Verlag, 2002), first edition.

[65] E.M. Purcell, *Proceedings of the American Physical Society*, Phys. Rev. **69**, 674 (1946).

[66] Marlan O. Scully and M. Suhail Zubairy, *Quantum Optics* (Cambridge University Press, 1997), fifth edition.

[67] Stefan A. Maier, *Plasmonic field enhancement and SERS in the effective mode volume picture*, Opt. Express **14**, 1957 (2006).

[68] A. F. Koenderink, *On the use of Purcell factors for plasmon antennas*, Opt. Lett. **35**, 4208 (2010).

[69] R Ruppin, *Electromagnetic energy density in a dispersive and absorptive material*, Phys. Lett. A **299**, 309 (2002).

[70] Theodor Förster, *Zwischenmolekulare Energiewanderung und Fluoreszenz*, Ann. Physik **437**, 55 (1948).

[71] Peter Atkins and Julio de Paula, *Atkins' Physical Chemistry* (Oxford University Press, 2002), seventh edition.

[72] Kurt Busch, Michael König, and Jens Niegemann, *Discontinuous Galerkin Methods in Nano-Photonics*, Laser & Photon. Rev. **5**, n/a (2011).

[73] J. C. Maxwell Garnett, *Colours in Metal Glasses and in Metallic Films*, Philos. T. Roy. Soc. A **203**, pp. 385 (1904).

[74] J. C. Maxwell Garnett, *Colours in Metal Glasses, in Metallic Films, and in Metallic Solutions. II*, Philos. T. Roy. Soc. A **205**, pp. 237 (1906).

[75] M. Wegener, I. Bar-Joseph, G. Sucha, M. N. Islam, N. Sauer, T. Y. Chang, and D. S. Chemla, *Femtosecond dynamics of excitonic absorption in the infrared $In_xGa_{1-x}As$ quantum wells*, Phys. Rev. B **39**, 12794 (1989).

[76] D. E. Chang, A. S. Sørensen, P. R. Hemmer, and M. D. Lukin, *Quantum Optics with Surface Plasmons*, Phys. Rev. Lett. **97**, 053002 (2006).

[77] A. V. Akimov, A. Mukherjee, C. L. Yu, D. E. Chang, A. S. Zibrov, P. R. Hemmer, H. Park, and M. D. Lukin, *Generation of single optical plasmons in metallic nanowires coupled to quantum dots*, Nature **450**, 201 (2007).

Acknowledgements

Praise the bridge that carried you over. (G. Colman)

The bridge that carried me over the last few years has often spanned troublesome waters but it turned out to be solid enough to ensure a safe journey to the other side. It is therefore my pleasure to now take some time and thank all the people who helped build this bridge and who have thus contributed to the successful outcome of this thesis in one way or another.

I want to thank my advisor, Prof. Martin Wegener, who gave me the opportunity to work on the versatile topic of metamaterials coupled to optical gain and who provided an ideal experimental infrastructure to us all. He also helped revive the low-temperature equipment in the laboratory and his broad and deep knowledge of semiconductor physics has often been the crucial factor towards understanding our data.
This thesis took part in the framework of the junior group of my co-advisor Prof. Stefan Linden. He was of great assistance while assembling the pump-probe setup and has contributed to countless discussions along the way. To him I am especially grateful because he always had an open ear for the issues I was dealing with and for supporting me in my daily work.
Prof. Kurt Busch deserves my thanks for kindly agreeing to co-referee this work. The numerical calculations used in this thesis were performed in his nanophotonics group and he always took interest in my project over the years.
I am indebted to Prof. Galina Khitrova and Prof. Hyatt M. Gibbs at the University of Arizona. They have not only provided us with countless (actually 37) quantum-well and quantum-dot wafers of the highest quality but have also contributed to numerous discussions and at times have shared in the project like a second set of advisors, for which I am very grateful. They even allowed me to stay in their house when they invited me to Tucson, where I had the pleasure of meeting all their pigs.

The group of Prof. Wegener is a very vivid place to work in where group members contribute to a pleasant, industrial atmosphere where working days can be fruitful, yet enjoyable. For creating these conditions I would like to thank all my colleagues, but some of them deserve to be named separately for the role they have played in my working life over the last years:
Dr. Matthias Ruther initially shared the gain project and performed most of the electron-beam lithography of the samples we have used over the years, although unfortunately only few of them are presented in the final version of this thesis. He also made large contributions to the toy model together with Dr. Juan-Luis García-Pomar who was a visiting scientist in our group at the time.
Despite not being in the group of Prof. Wegener but in that of Prof. Busch I also want to mention Michael König here. He performed the near-field calculations for this thesis and

contributed to discussions on decay-rate enhancements. Interestingly, Michael and I have been friends throughout our time at university, have worked together for both our diploma and PhD theses and do now finish the latter on the same day. It is therefore a pleasure to thank him for all his work.
Dr. Manuel Decker, Dr. Nils Feth, Dr. Isabelle Staude, Joachim Fischer and Martin Husnik were my partners in many discussions on various aspects of this project. Many of our conversations have helped me gain a clearer picture of a complicated system and often spawned new ideas on what steps to take next. They were also very helpful when it came to analysing and solving experimental problems regarding both optics and fabrication.
Special thanks goes to Joachim Fischer with whom I shared a laboratory for almost two years. Although the noise level in the lab, together with my headphones, was usually in the way of proper conversation, his enthusiasm and company made very long days in the dark - or yellow - just that necessary bit more bearable.
My diploma student Johannes Kaschke unfortunately only worked on the outskirts of my thesis topic at a time when I was very busy with my own work. Still, the time we shared in the laboratory, in discussion or at the metamaterial summer school was very delightful.
I also want to thank all the critical readers of this thesis, Dr. Stefan Linden, Dr. Isabelle Staude, Martin Husnik and Michael König and especially my sister, Sabrina Feickert, for applying the last drops of varnish to the text.
Furthermore, thank you to Natalie who has had a crucial role in the success of this thesis.

We scientists could never perform our work were it not for all the people who provide us with technical and administrative assistance. In this sense I want to thank our former technician Thorsten Kuhn and his successor Johann Westhauser; the secretariat at the Insitute of Applied Physics, headed by Renate Helfen, and the one at the Insitute for Nanotechnology in person of Erika Schütze; the electronics workshop consisting of the recently-retired Heinz Hoffmann, Werner Gilde and Helmuth Lay; the mechanical workshop headed by Werner Wagner and Franz Hartlieb who is responsible for the helium reprocessing.

Finally, I want to express my gratitude and love to my friends - inside and outside of the Wegener group - and my family for their incessant and unconditional support in all aspects of my life. They have built the bridge from my earliest interest in science and technology all the way to taking this PhD and they have always kept me going, even through the hardest of times.